PhD-FSTM-2023-116
The Faculty of Science, Technology and Medicine

NNT : 2023AIXM0001
Faculté des Sciences

DISSERTATION

Defence held on 22/09/2023 in Esch-sur-Alzette.

to obtain the degree of

DOCTEUR DE L'UNIVERSITÉ DU LUXEMBOURG

EN Sciences de l'Ingénieur

AND

DOCTEUR DE L'UNIVERSITÉ D'AIX-MARSEILLE

IN Sciences de l'Ingénieur : Spécialité Mécanique des Solides

by

Camilo Andrés SUAREZ AFANADOR
Born on 04 January 1991 in NEIVA, COLOMBIE

ESTIMATION DES CONTRAINTES INTERNES DANS LES PIECES COMPOSITES IMPRIMES PAR DEPOT DE FILAMENT POLYMERE.

Dissertation defence committee

Dr Renald BRENNER, Chairman
Directeur de recherche, Sorbone Université
Dr Emanuela BOSCO
Associate Professor, Eindhoven University of Technology (TU/e)
Dr Pierre SUQUET, Vice-Chairman
Directeur de recherche émérite, Aix-Marseille Université
Dr Lars BEEX
Research Scientist, Université du Luxembourg
Dr Noël LAHELLEC
Professeur, Aix-Marseille Université
Dr Stéphane Pierre-Alain BORDAS
Professeur, Université du Luxembourg

Affidavit

I, undersigned, Camilo Andrés SUAREZ AFANADOR, hereby declare that the work presented in this manuscript is my own work, carried out under the scientific supervision of Noël LAHELLEC, Aurélien MAUREL and Stéphane P.A. BORDAS, in accordance with the principles of honesty, integrity and responsibility inherent to the research mission. The research work and the writing of this manuscript have been carried out in compliance with both the french national charter for Research Integrity and the Aix-Marseille University charter on the fight against plagiarism.

This work has not been submitted previously either in this country or in aother country in the same or in a similar version to any other examination body.

Esch-sur-Alzette le 26 juin 2023

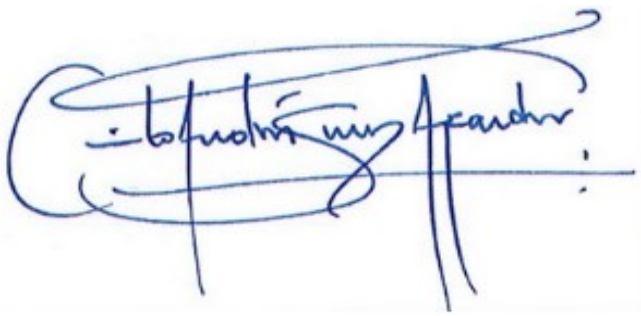

Publications list

i. Camilo Suarez Afanador et al. “Mean-Field Approximations in Effective Thermo-viscoelastic Behavior for Composite Parts Obtained via Fused Deposition Modeling Technology”. In: AIP Conference Proceedings 2425 (1 Apr. 2022).

ii. C. A. Suarez-Afanador, Lukas Jakabcin, N. Lahellec, A. Maurel-Pantel, D. Boussaa and S. P. A. Bordas. “Effective thermo-viscoelastic behavior of short fiber rein- forced thermo-rheologically simple polymers: An application to high temperature fiber reinforced additive manufacturing.” In: Eur. J. Mech. A Solids. 1.2 (2022), p. 18.

iii. Camilo A. Suarez-Afanador, Noel Lahellec, and Martín I. Idiart. “Mean-field descrip- tions for the viscoelastic response of thermorheologically complex reinforced solids”. In: Eur. J. Mech. A Solids. 98 (2023), p. 104859. issn: 0997-7538.

Conferences attendance list

i. International Conference of Numerical Analysis and Applied Mathematics ICNAAM Rhodes 2020. Oral presentation of the first advances in the PhD work at the mini-symposium MS 51: "Advanced methods of computational mechanics and simulation oriented to civil and industrial engineering"

ii. FabAddComp 2020 "Fabrication additive des composites" Lorient, France / AMAC Association pour les matériaux composites. Oral presentation : Estimation du comportement thermo-viscoélastique effectif des pièces composites obtenues par impression 3D-FDM.

iii. ICTAM Milano 2020+1 – 25th International congress of theoretical and applied mechanics. Oral presentation at the mini-symposium in additive manufacturing during the conference: Estimating thermomechanical residual stresses in FDM 3D printed composite parts.

iv. JNC Besançon 2023 Journées Nationales sur les Composites. Oral presentation at the mini-symposium M1 - Modélisation multi-échelle: Estimation des contraintes résiduelles dans des pièces composites imprimées 3D HT- FDM.

Résumé

Ce travail considère l'étude des contraintes résiduelles dans une pièce composite à matrice polymère qui est obtenue en utilisant la procédure de manufacture dénommée high-temperature fused deposition modeling (HT-FDM). Ce type d'impression 3D utilise des polymères à haute performance comme matière primaire. Durant la procédure d'impression, on observe l'apparition de plusieurs types des défauts en raison du fort gradient thermique qui subit la pièce en construction, en général, ils représentent le manque de précision dimensionnelle par rapport au modèle 3D utilisé pour coder les trajectoires d'impression. Cette distorsion est en fait une déformation résiduelle associée aux contraintes résiduelles dans la pièce en réponse à la distribution de température au cours de l'impression jusqu'à que chaque point matériel atteint la température ambiante. L'estimation des contraintes résiduelles dans un polymère composite imprimé n'est pas triviale puisque le matériau comporte plusieurs échelles d'hétérogénéité. Si l'on souhaite traiter le problème multiéchelle d'une façon déterministe en utilisant une méthode de calcul générique telle que les éléments finis (FEM) on observe que le phénomène de séparation d'échelle impose des tailles caractéristiques de maille qui sortent d'une démarche de calcul raisonnable en termes du temps vis-à-vis des ressources computationnelles actuels, et dans une telle démarche, il faut prendre en compte que le cout des simulations augmente de façon exponentielle en raison du volume total de la pièce étudiée. C'est pourquoi on propose une méthodologie basée sur l'homogénéisation en mécanique des matériaux [1, 2, 3] pour remonter au comportement macroscopique qui permet de considérer la pièce imprimée comme étant représentée par un modèle continu qui, à l'échelle de l'observateur, se comporte de façon équivalente à sa contrepartie hétérogène, ce que l'on traite par une méthodologie d'homogénéisation à deux étapes.

La première échelle, la micro-échelle, est traitée en utilisant une méthode d'homogénéisation en champ moyen décrite dans une publication précédente des auteurs [4], dans laquelle l'estimation est obtenue par extension des méthodes d'homogénéisation de champ moyen conventionnelles (dérivées du problème d'Eshelby dans le contexte the la thermoélasticité) en utilisant l'extension du principe de correspondance [5] dans des variations continues de la température pour un matériau thermo-viscoélastique dit *thermorhéologiquement simple*, et en utilisant une description probabiliste des paramètres microstructuraux associés aux fibres. Il faut aussi mentionner que l'on a dédié un chapitre pour l'estimation du comportement effective dans le cas des matériaux *thermorhéologiquement complexes* par une technique de réduction de modèle du problème d'homogénéisation en champ moyen étant déjà publiées dans [6]. La mésoéchelle est traitée par une méthode numérique d'homogénéisation de champ complet basé sur les éléments finis conventionnels, le calcul des propriétés thermo-viscoélastiques effectives est réalisé à travers de simulations dynamiques à régime établi sur un espace de fréquence pertinent aux conditions de service de la pièce pour après subir une procédure d'identification selon [7] ce qui conserve une représentation conventionnelle des fonctions qui caractérisent la réponse du matériau dans un contexte expérimentale d'identification.

Après d'avoir vérifié la qualité des approximations obtenues avec des comparaisons purement numériques on compare ce que l'on obtient avec la réalité physique. L'expérience de référence est celle du refroidissement d'une plaque mince obtenue par superposition des couches unidirectionnelles d'impression, l'orientation des couches est [0,0,90,90]. La pièce est refroidie dans la chambre d'impression et l'on mesure la déflexion de la plaque, étant conséquence de l'évolution de la température et la distribution asymétrique des porosités alignées dans les couches imprimées. L'objective est donc de prédire la déflexion de la plaque avec un modèle numérique avec des propriétés étant obtenues suivant la méthodologie que l'on propose dans ce travail de thèse. Sachant que l'on est confronté à la réalité, plusieurs mesures expérimentales qui servent à l'identification

des paramètres nécessaires ont été effectués, ainsi que des analyses de microtomographie des deux échelles caractéristiques.

Abstract

This thesis deals with the study of residual stresses in a polymer matrix composite part obtained using the High Temperature Fused Deposition Modeling (HT-FDM) manufacturing process. This type of 3D printing uses high performance polymers as the primary material. During the printing process, several types of defects are observed due to the strong thermal gradient that the part under construction undergoes, generally representing the lack of dimensional accuracy with respect to the 3D model used to encode the printing paths. This distortion is in fact a residual deformation associated with residual stresses in the part in response to the temperature distribution during printing until each point of the material reaches room temperature.

Estimating residual stresses in a printed polymer composite is not trivial because the material contains multiple scales of heterogeneity. If we want to treat the multiscale problem in a deterministic way using a generic computational method such as Finite Element Analysis (FEA), we observe that the phenomenon of scale separation imposes characteristic mesh sizes that are beyond the scope of a reasonable computational approach in terms of time versus current computational resources, and in such an approach we have to take into account that the cost of simulations increases exponentially due to the total volume of the part studied. For this reason, we propose a methodology based on homogenization in the mechanics of materials [1, 2, 3] to trace back to the macroscopic behavior, which allows to consider the printed part as represented by a continuous model that, at the scale of the observer, behaves equivalently to its heterogeneous counterpart, which we treat through a two-stage homogenization methodology.

The first scale, the microscale, is treated using a mean-field homogenization method described in a previous publication by the authors [4], where the estimation is obtained by extending conventional mean-field homogenization methods (derived from the Eshelby problem in the context of thermoelasticity) using the extension of the correspondence principle [5] in continuous temperature variations for a thermo-viscoelastic material known as *thermorheologically simple*, and using a probabilistic description of the microstructural parameters associated with the fibers. It should also be mentioned that we have dedicated a chapter to the estimation of the effective behavior in the case of *thermorheologically complex* materials by a model reduction technique of the mean-field homogenization problem being already published in [6]. The mesoscale is treated by a full-field numerical homogenization method based on conventional finite elements, the calculation of the effective thermo-viscoelastic properties is carried out by steady-state dynamic simulations over a frequency space relevant to the part's operating conditions of the part, and then undergoes an identification procedure according to [7], which maintains a conventional representation of the functions characterizing the material's response in an experimental identification context.

After checking the quality of the approximations obtained with purely numerical comparisons, we compare what we have obtained with physical reality. The reference experiment is that of cooling a thin plate obtained by superimposing unidirectional printing layers, the orientation of the layers being [0,0,90,90]. The part is cooled in the printing chamber and the deflection of the plate is measured, as a consequence of the temperature evolution and the asymmetric distribution of the porosities aligned in the printed layers. The objective is therefore to predict the plate deflection using a numerical model with properties obtained using the methodology proposed in this thesis. Since we are confronted with reality, several experimental measurements have been carried out to identify the necessary parameters, as well as microtomographic analyses of the two characteristic scales.

Contents

List of Figures

List of Tables

Introduction

The present work is the result of a doctoral fellowship funded by the French Ministry of Higher Education and Research through the Doctoral School of Engineering of the University of Aix-Marseille [1] (ED353) with hosting laboratory, the *Laboratoire de Mechanique et d'Acoustique de Marseille* (LMA). The research subject was conceived in the framework of the scientific support of the SPRING project financed by DGA-RAPID (DGA-2103404513) of the French Ministry of Defense. The main objective of this major project was to evaluate the applicability of the FDM 3D printing technology to the industry as functional parts integrating mechanical systems. A cotutelle with the University of Luxembourg is systematically established at the beginning of this project with the Doctoral School of Science and Engineering [2] (DSSE) with host laboratory the *Legato team* who financed the last part of the time dedicated to the research. The first published manifestation of the present work was given by the Mini-Symposium of Mathematics for Industry and Manufacturing held during the International Conference of Numerical Analysis and Applied Mathematics ICNAAM 2020 [8]. To date, two articles have been published in high impact journals [4, 6] and three others are in preparation for submission to high impact journals as well

Additive manufacturing, commonly referred to as 3D printing, is an emerging technology that spans a broad spectrum of applications [9, 10]. One specific variant of this technology is Fused Deposition Modeling (FDM), which predominantly utilizes thermoplastic polymer filaments as the primary raw material for part construction [11]. The focus of this thesis is on FDM. Its objective is to advance the development of engineering simulation tools that assist in mechanical design. This encompasses material selection, the determination of printing trajectories, and the application of heat treatments both during and post-printing. The central goal is to maintain

[1] https://ecole-doctorale-353.univ-amu.fr
[2] https://wwwen.uni.lu/fstm

dimensional accuracy and minimize residual stresses.

To understand the significance and intrigue surrounding additive manufacturing and to establish the relevance of this project, it's beneficial to delve briefly into its history. The roots of additive manufacturing trace back to the 1980s, when Hideo Kodama presented a seminal paper on a photopolymer rapid prototyping system [12]. This paper set the stage for the development of stereolithography (SLA), a pioneering form of additive manufacturing. This technology was further solidified in 1984 by Charles Hull [13]. Hull co-founded 3D Systems[3] and introduced the market to the first commercial 3D printer. In retrospect, while this technology's origins may seem dated, its true potential and widespread adoption have only recently been realized. This trajectory is unsurprising, considering the technology's inherent promise: the capacity to use nearly any material to craft almost any form.

In 1989, Scott and Lisa Crump, co-founders of Stratasys[4], pioneered what is now known as Fused Deposition Modeling (FDM). The first commercial iteration of an FDM-based 3D printer made its debut in 1992. This technique functions by extruding thermoplastic materials through a heated nozzle, subsequently depositing them layer by layer to form a three-dimensional object. This innovation was groundbreaking, especially considering its ease of implementation, which was rooted in knowledge derived from its precursor, injection molding. Notably, FDM can utilize materials that are transformable at temperatures beyond conventional industrial ranges.

The burgeoning community interest in this domain is evident, a sentiment accentuated by the meteoric rise of the open-source movement over the past two decades. A testament to this is Adrian Bowyer's spearheading of the RepRap[5] project. Bowyer's visionary concept revolved around low-cost 3D printers with the unique ability to replicate themselves, essentially "printers printing other printers" [14].

As we transition further into our discussion, it's crucial to delve into a more nuanced category. While we've established the relative simplicity of constructing a 3D printer and producing 3D parts, significant questions emerge concerning the properties of these parts. Specifically, in which contexts can their application be deemed "safe"? Within the scope of this thesis, our central inquiry becomes:

[3] https://www.3dsystems.com
[4] https://www.stratasys.com
[5] https://reprap.org

How might one harness the potential of this adaptable manufacturing method, in synergy with materials science, continuum mechanics, and computational mechanics, to engineer 3D printed components suitable for integration into industrial and commercial mechanical systems, beyond just prototyping?

In addressing the aforementioned question, one could adopt the classic trial-and-error methodology, iterating through various printers, printing techniques, and materials, complemented by mechanical testing, until the desired outcomes are achieved. Naturally, the exploration of potential combinations is constrained by our existing knowledge in engineering sciences, particularly when identifying a class of materials apt for a specific application.

For the purpose of this study, our primary focus will be on the thermomechanical properties of 3D printed components. However, it's essential to acknowledge that numerous materials already exhibit other valuable properties, such as biocompatibility and corrosion resistance [15]. Indeed, the drive to enhance the thermomechanical attributes of thermoplastic polymers stems from the aspiration to incorporate these qualities into functional mechanical systems, potentially replacing metallic components while preserving their operational integrity.

When seeking to enhance the mechanical performance of high-grade thermoplastic polymers, our attention naturally shifts to a precursor in the field: composite materials. Specifically, we focus on fiber-reinforced thermosets. These materials, celebrated for their exceptional strength-to-weight ratio, have been instrumental in driving advancements in aerospace since the 1930s. Following World War II, from the 1950s to '60s, their application proliferated across various sectors of mechanical engineering, including automotive, marine, and construction.

Drawing inspiration from these composites in thermoplastics is intuitive. The concept of fiber-reinforced thermoplastic polymers, or filled filaments, emerged around 2010 under the umbrella of FRAM (Fiber Reinforced Additive Manufacturing). Early studies by Lopes et al. [16] explored the feasibility of integrating filled filaments into FDM 3D printing procedures. Their research set the stage for subsequent inquiries into short fiber-reinforced polymers.

We now approach the crux of this research project. Over the past decade, efforts to advance FRAM technologies—aimed at converting 3D printed components into functional parts—have culminated in the emergence of HT-FRAM, or High Temperature Fiber Reinforced Additive Manufacturing. This "high temperature" descriptor arises from the materials chosen for crafting the composite filament. The goal: to elevate the thermomechanical performance and broaden

the operational temperature range of a component.

A key metric guiding the selection of materials is the glass transition temperature. This parameter denotes the temperature at which a material undergoes a pronounced shift in its mechanical properties [17, 18, 19, 20], transitioning from a quasi-conservative to a quasi-dissipative state (a state unfavorable for structural elements) and vice versa.

Examples of polymers boasting high glass transition temperatures (signifying robust thermal stability) include the poly-ether-imide PEI, commercially branded as Ultem®, and the poly-ether-ketone-ketone PEKK, recognized as Kepstan. Both are prevalently employed in HT-FRAM applications.

However, this narrowed focus on thermally stable materials introduced a manufacturing challenge: ensuring the extrusion of materials at elevated temperatures without compromising the integrity of the 3D printer components or the quality of the printed part [21]. While this issue is not entirely resolved, several companies, including Stratasys, have presented and continue to unveil solutions tailored to this context.

At this juncture, we find a selection of materials each paired with its FDM solution, all nested under the HT-FRAM category. The subsequent steps in evaluating the applicability of a 3D printed component within a functional context involve:

i) Choosing materials from this group along with their specific reinforcements for the filament, ii) designing the printing program—which is characterized by a combination of plane trajectories and printing velocities that depend on the filament's viscosity at its extrusion temperature—and iii) selecting the thermal treatment, which is delineated by temperature profiles over time, spanning the commencement of extrusion to the moment the completed part acclimates to room temperature post-printing.

The prospect of making these decisions arbitrarily is both daunting and potentially wasteful. To devise a pragmatic strategy, we harness the scientific understanding of the relevant physical phenomena for this class of materials. This is coupled with numerical estimations to formulate a methodology for modeling the thermomechanical response of a 3D printed component. It is here that we've carved our niche: simplifying the simulation task by approximating its macroscopic mechanical behavior. This approximation leans heavily on pre-existing knowledge of the material's characteristic scales, with "scales" referring to specific lengths where noticeable property fluctuations occur—fluctuations that inevitably influence the desired behavior of a part when

viewed at an observational scale.

In summary, given the intricacies outlined previously, this technology poses substantial engineering challenges. The task is twofold: developing both hardware and software capable of maintaining an optimal thermal environment for layer consolidation and the extrusion process. Such endeavors necessitate high-performance thermostable materials alongside precise electronics. Addressing these challenges is a pressing concern in modern technology. Consequently, current manufacturing systems on the market cannot consistently ensure peak performance. Many produced parts often suffer from defects, including geometrical distortions, delamination, warping [22], and surface inconsistencies. The root cause of most of these defects lies in internal stresses [23], which emerge due to temperature fluctuations within the printing chamber. Therefore, it becomes imperative for engineers to predict internal stress distributions in 3D printed components, considering both the temperature field history and the printing program (print trajectories). The ultimate goal is enhancing specific properties by finely tuning the print settings of available hardware.

The diagram provided below offers a visual breakdown. This figure elucidates the critical temperatures associated with FDM 3D printing, pivotal in understanding the defects previously discussed. First and foremost, we have the printing temperature T_p, which, for HT-FRAM, is approximately 400°C, closely aligning with the material's melting point. Following this is the printing bed temperature T_b, the surface that supports the incrementally building part. Ideally, T_b should exceed the glass transition temperature to mitigate the impact of the initial drastic temperature shift. Given that modern hardware can handle up to 250°C, this temperature shift averages about 100°C [6]. Lastly, we have the chamber temperature T_c, reaching highs of 270°C in current 3D printers. Ideally, T_c should maintain uniformity throughout its volume during the printing process, hovering around the glass transition temperature. This would prevent significant temperature variations and the premature onset of internal stresses, stemming from the polymer's inconsistent thermodynamic state within the growing part. Unfortunately, with the limitations of contemporary technologies, there's an inability to ensure this ideal thermal environment consistently during printing. As a result, the produced geometries often differ from their original blueprints, introducing internal stresses that modify their mechanical behaviors when subjected to the operational loads in the mechanical systems they're integrated into.

[6] https://qualup.com

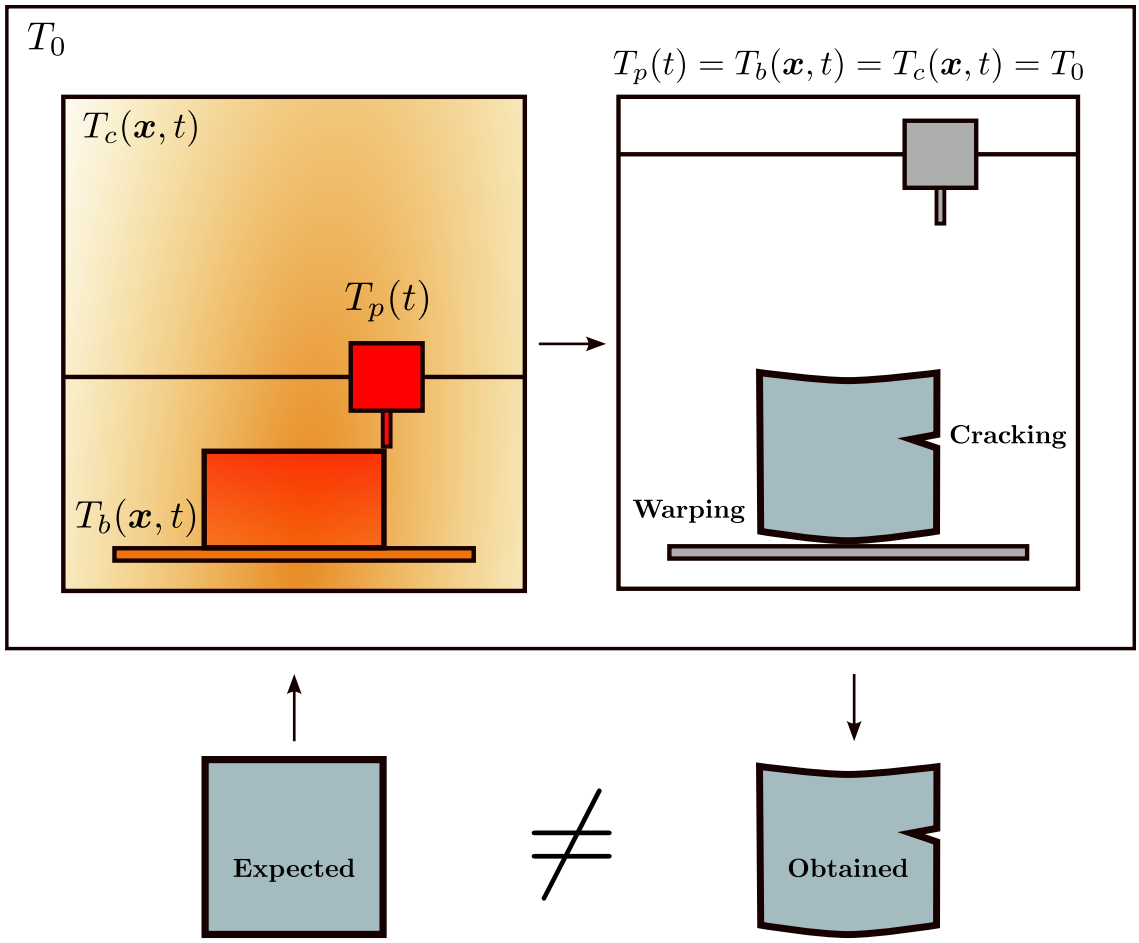

Figure 1: Graphical representation of the technological problem.

One can quickly recognize the intricacy involved in fabricating a functional part via FDM 3D printing; indeed, it emerges as a multiscale challenge. Initially, there's the composite filament, reinforced with short fibers (usually glass or carbon fibers, borrowed from the domain of composite thermosets). This fiber reinforcement augments the filament's rigidity, thus boosting its mechanical prowess, marking our introduction to the first level of heterogeneity, termed the *microscale* here. In our study, the matrix material under consideration is the glassy amorphous polymer (PEI in the application sections), which essentially mirrors a continuous matrix compared to its sibling, the semi-crystalline polymers. As the printing process progresses, the filament, heated to its melting temperature, is methodically laid upon the printing bed, layer by layer. The resultant near-cylindrical shape of the adjoining filaments forms a porous lattice, representing our second level of heterogeneity, which we label as the *mesoscale*. Referencing Fig. 2, we see an illustrative depiction of our target material. Moving from right to left, we encounter the *microscale*, showcasing short fibers nestled within a polymer matrix. Then, the *mesoscale*

manifests as a porous region, birthed from the layer-over-layer construction process. Lastly, we have the *macroscale*—the scale perceptible to the human observer, typically continuous given our visual limits and predicated on the assumption that the printer retains a precision within a 20-50 µm range in tolerances.

Presently, the estimation of these internal stresses primarily involves the application of finite element methods in commercial software [24, 25]. These software solutions address the thermo-mechanical structural problem by integrating thermo-viscoelastic behavior laws tailored for the polymer material [26, 27]. Given the material's multiscale nature, virtual prototyping and simulations emerge as a notably time-intensive endeavor. In a broad simulation context, the necessary discretization strategies mandate selection criteria that can precisely capture the heterogeneity shapes at the most refined scale. Such a requirement often leads to extensive simulations, which are nearly unfeasible without resorting to high-performance computing resources. Notably, the literature provides various simulation methodologies aiming to circumvent the need for such intricate meshing [28, 29]. Nevertheless, regardless of the chosen approach, it's a computationally expensive procedure. Homogenization techniques aspire to substitute complex heterogeneous bodies with a homogeneous counterpart that mirrors the same macroscopic characteristics. The majority of these techniques find their roots in linear thermoelastic behavior models [1, 2]. Regarding application expense, homogenization can be executed both analytically (like mean-field methods) and computationally (such as full-field methods) [4, 6]. The time commitment for analytical methods is a fraction of that required by computational ones. However, the efficacy of these analytical methods hinges on the availability of suitable analytical delineations of heterogeneity in both geometry and distribution, and the adaptability of the underlying mathematical frameworks of the considered material laws to align with the homogenization paradigm.

This study introduces a two-step homogenization methodology to predict residual stresses in 3D printed parts, as visually depicted in Fig.2. The material of the cat illustrated on the left is characterized by two distinct scales. Our goal is to apply homogenization techniques to derive a continuous equivalent for the cat's material. Initially, the composite filament shown on the right of Fig.2, consisting of a polymer matrix reinforced with short glass fibers, undergoes an analytical homogenization. This step results in a continuum representation, which becomes the input for the material properties at the mesoscale. Subsequently, the layered porous structure illustrated in the center of Fig.2 is addressed using a homogenization process tailored for periodic

microstructures, implemented via classical finite element simulations. This output sets the stage for the material properties at the cat's macroscopic scale. It's worth noting that one trade-off of these averaged models is their inability to capture highly localized phenomena. The repercussions of this approximation within the realm of 3D printing will be thoroughly explored and evaluated. Upcoming sections will delve into the specific methodologies employed as we examine each scale. Ultimately, the derived macroscopic behavior is utilized to gauge the deflection in an actual 3D printed part, serving as a primary validation criterion.

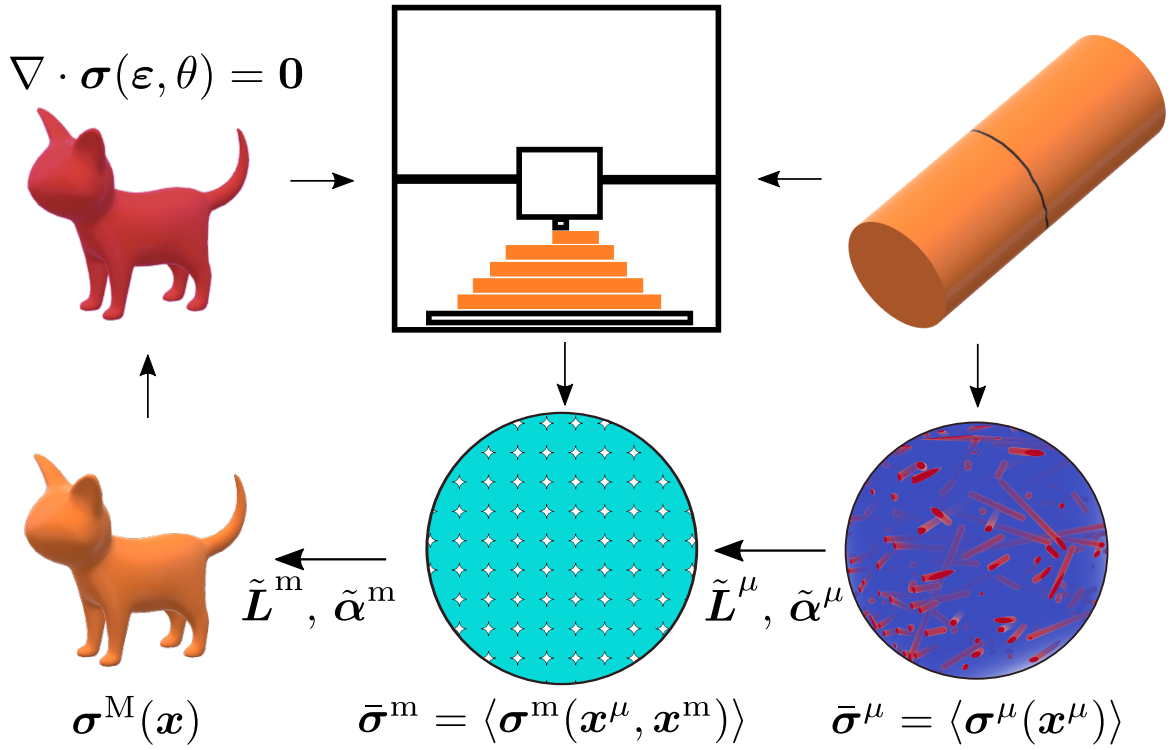

Figure 2: Schematic representation of the multiscale problem, the superscript $(.)^{\mu}$ stands for microscale quantities, $(.)^{\mathrm{m}}$ for those of the mesoscale and $(.)^{\mathrm{M}}$ for the macroscale.

Up to this point, readers have been acquainted with the research's scope without diving deep into its theoretical and experimental nuances. These details will be incrementally introduced, maintaining an inductive approach to the overarching topic. In subsequent sections, our initial focus lies in identifying and detailing a suitable polymer matrix, specifically the PEI or more precisely, the commercially known Sabic Ultem® 1010 resin. This material serves as the benchmark for the mathematical modeling of our target behavior, emphasizing the characterization of residual stresses and deformations, two classical mechanical variables, and their time-temperature dependency. The ensuing section pivots to estimating the effective properties

of a composite filament reinforced with short glass fibers. Given that this material is categorized as a *thermorheologically simple material* [30], an additional chapter will broach the microscale homogenization problem when selecting *thermorheologically complex* [31] matrix materials for the filament. This sets the stage for an exploration of the effective behavior of the porous network using rudimentary computational mesostructures. Concluding this chapter, we will present an experimental validation study, aiming to assess the precision of the suggested methodology within a controlled, real-world setting.

An additional chapter is provided, focusing on a numerical study that extrapolates the macroscopic behavior of 3D printed parts. This study utilizes data-driven models founded on CNN networks and Bayesian methods, using data generated by our proposed methodology which factors in a microstructural parameter map. This is presented as a pioneering exploration into the latest predictive algorithm developments. Furthermore, to expedite data generation and reduce costs, we will employ alternative strategies to conventional finite element approximations, notably the Extended Finite Element Methods (XFEM) and CutFEM. The closing sections will offer conclusions, remarks, and insights into the strengths and constraints of our proposed approach, coupled with discussions on application contexts and potential adaptations for more intricate scenarios. Each chapter will culminate with its own set of conclusions. Lastly, the sequence in which information is relayed does not reflect the chronological development of the work, as the theoretical and experimental components often ran concurrently.

Chapter 1

Thermo-viscoelasticity : Theoretical background and modeling

In this opening chapter, we will revisit the foundational theories that underpin our approach for calculating the thermomechanical response of thermo-viscoelastic polymers. In essence, we'll cover: i) The thermodynamic formulation of the polymer, both in its integral and differential forms. ii) The time-temperature superposition principle for thermorheologically simple polymers and its extension for continuous temperature variations. And iii) the mathematical depiction of mechanical and thermal expansion behaviors, represented through Prony series.

This section marks the commencement of our in-depth exploration of the multiscale problem. Beginning with the microscale, we identify two distinct phases: the elastic fibrous inclusion domain and the matrix, the predominant phase that houses the stiff fibers. This matrix is an amorphous (or glassy) polymer. A popular matrix material for such considerations is polyetherimide (PEI), our reference material for this study. Commercially recognized as Ultem®, PEI boasts a commendable balance of thermal and mechanical properties. Its high glass transition temperature ($T_g > 210, °C$) stands as a testament to its robust thermal stability. However, this trait also demands higher printing temperatures ($T_p > 350, °C$), introducing challenges in the printing process.

From a modeling perspective, representing the thermomechanical behavior of the elastic fibers is straightforward as it falls within the conventional realm of thermoelastic materials. This

simplicity is advantageous since many of their properties remain constant throughout the temperature spectrum of the printing process. In contrast, the matrix's thermomechanical behavior exhibits thermo-viscoelastic characteristics. This implies that the mathematical depiction of its property evolution is dependent on both time and temperature. A polymer's solid state can be perceived as a phase where the Brownian motion rate of its structural chains is diminished, but it never truly ceases. Essentially, a polymer can be viewed as a conglomerate of perpetually mobile molecular chains. Temperature variations influence the pace of these polymer chains, with heightened temperatures correlating to rapid molecular movements. As such, the matrix material necessitates a somewhat non-traditional mathematical model within the domain of homogenization theory. Indeed, the intricate study of such materials is enshrined in a dedicated scientific discipline known as *rheology*.

Numerous studies have delved into the challenges presented by viscoelastic materials, a unique class that simultaneously exhibits viscous and elastic behaviors. The historical origin of such material studies can be traced back to James Clerk Maxwell in 1867 [32]. His *rheological model* used a spring (an elastic component) and a dashpot (a viscous component) connected in series, modeling the relaxation response of polymers. Later, in 1890, both Voigt and Lord Kelvin independently proposed an alternate model wherein a spring and dashpot were connected in parallel [33]. This Kelvin-Voigt model was adept at predicting creep behavior. Recognizing the limitations of the existing models, the standard solid model was introduced, adeptly capturing a polymer's asymptotic stress and deformation responses. Zener was credited with this model [34], and it was seen as a complement to earlier models. Specifically, it incorporated an elastic spring either in parallel with a Maxwell model's viscoelastic model or in series with a Kelvin-Voigt model, enabling it to predict both creep and relaxation behaviors. These initial models, with their single viscoelastic units, however, had limitations regarding the range of viscoelastic materials they could represent. To address this, the 1950s saw the emergence of generalized versions for both Maxwell and Kelvin-Voigt models [35]. The 1970s ushered in more intricate models based on fractional operators dealing with non-integer order derivatives, leading to fractional versions of the generalized models, which allowed for even more precise and adaptable representations [36]. For the purposes of this work, our focus will be on the traditional generalized Zener models, deemed sufficiently accurate for the materials in question.

In the realm of temperature-dependent viscoelasticity—or "thermo-viscoelasticity", as we term it—the foundational study by Williams, Landel, and Ferry in 1955 stands as a pioneering effort to phenomenologically depict the nuanced interplay between relaxation mechanisms in amorphous polymers and temperature [37]. This groundbreaking model, frequently referenced as the WLF (Williams-Landel-Ferry) model, was instrumental in delineating the relationship between a polymer's viscoelastic properties and temperature, thereby paving the way for subsequent thermo-viscoelastic models. The journey to formulating a cohesive theory of thermo-viscoelasticity saw its inception in the late 1950s, with significant contributions from researchers such as Biot in 1958, who delved into the linear thermodynamics of viscoelastic solids [38, 26], followed by Hunter in 1961 [39], Schapery in 1964 [40], Christensen and Naghdi in 1967 [41], Crochet and Naghdi in 1969 [30] and Bouc in 1977 [42]. Each of these works embarked on the mission of crafting a thermodynamically consistent formulation. A more consolidated discussion of these studies can be found in R. M. Christensen's 1982 publication, "Theory of Viscoelasticity" [43]. This text offers a thorough breakdown of thermo-viscoelasticity in linear viscoelastic materials and serves as our primary touchstone for understanding the theoretical nuances of thermo-viscoelastic behavior.

1.1 Integral form of the state equations in linear thermo-viscoelasticity

We now shift our focus to the mathematical framework that underpins the initial homogenization step. The most fitting approach to express the evolution of the polymer's state as a function of time and temperature is undoubtedly a thermodynamic formulation. Such a formulation seamlessly integrates mechanical occurrences with thermal interactions, providing a spatial representation of the temperature field. This is crucial, as the polymer's structural state at a specific moment is intrinsically tied to its preceding temperature history. While our primary reference for these formulations remains [43], it's essential to acknowledge other seminal contributions that have furthered our understanding of the theory, including works like [5, 44, 45, 35]. Let's delve deeper into the constitutive equations that capture the thermo-mechanical essence of the material:

$$\boldsymbol{\sigma} = \boldsymbol{\sigma}_0 + \left[\mathbb{L}(T,\cdot) \circledast \boldsymbol{\varepsilon} - \mathbb{L}(T,\cdot) \circledast \boldsymbol{\alpha}(T,\cdot) \circledast \theta\right](t) \tag{1.1}$$

$$s = s_0 + \left[\mathbb{L} \circledast \boldsymbol{\alpha}(T,\cdot) \circledast \boldsymbol{\varepsilon} + m(T,\cdot) \circledast \theta\right](t). \tag{1.2}$$

The equations under consideration pertain to the second order symmetric stress tensor, denoted by $\boldsymbol{\sigma}$, and the specific entropy, represented by s. Both of these are functions of their initial states: $\boldsymbol{\sigma}_0$ and s_0. They also depend on state variables, which include the second order strain tensor $\boldsymbol{\varepsilon}$ and the temperature variation, θ, relative to an initial temperature of the reference state, T_0. Additionally, these equations factor in material properties: the fourth order stiffness tensor, $\mathbb{L}$; the second order thermal dilatation tensor, $\boldsymbol{\alpha}$; and the heat capacity at constant strain, denoted as m. Notably, each of these properties is a function of both time and temperature. The upcoming thermodynamic formulation aligns with the constitutive equations above as detailed in Appendix B.1 of [43].

The thermodynamic representation of the thermomechanical state of the polymer is given by two energetic potentials, the Helmholtz free energy and the dissipation potential, and a coupling equation representing the interactions between the temperature fields and the dissipation of energy. The time dependent nature of viscoelastic materials is represented mathematically by the Boltzmann superposition principle, which translates the fact that the state of a polymer at a given time depends on each previous state of the polymer, this imposes the presence of Stieltjes convolution operators ($\circledast$) relating the quantities of each monomial in the energy formulation (see: A.1). Let's take a first look at the equations describing the thermomechanical state of the polymer: first, the Helmholtz specific free energy,

$$w = w_0 + \boldsymbol{\sigma}_0 \cdot \boldsymbol{\varepsilon} - s_0\theta + \left[\frac{1}{2}\mathbb{L}(T,\cdot) \circledast \boldsymbol{\varepsilon} \circledast \boldsymbol{\varepsilon} - \mathbb{L}(T,\cdot) \circledast \boldsymbol{\alpha} \circledast (T,\cdot)\boldsymbol{\varepsilon} \circledast \theta - \frac{1}{2}m(T,\cdot) \circledast \theta \circledast \theta\right](t), \tag{1.3}$$

the associated dissipation potential,

$$\varphi = -\left[\frac{1}{2}\frac{\partial}{\partial t}\mathbb{L}(T,\cdot) \circledast \boldsymbol{\varepsilon} \circledast \boldsymbol{\varepsilon} + \frac{\partial}{\partial t}(\mathbb{L}(T,\cdot) \circledast \boldsymbol{\alpha}(T,\cdot)) \circledast \boldsymbol{\varepsilon} \circledast \theta + \frac{1}{2}\frac{\partial}{\partial t}m(T,\cdot) \circledast \theta \circledast \theta\right](t), \tag{1.4}$$

and the thermal coupling inequality,

$$\varphi - [\boldsymbol{\lambda}(T,\cdot) \circledast \boldsymbol{\nabla}\theta](t) \geq 0, \tag{1.5}$$

and finally a suitable form of the conservation of energy equation in a first order theory of thermo-viscoelasticity,

$$r - T_0 \frac{\partial}{\partial t} [\mathbb{L}(T,\cdot) \circledast \boldsymbol{\alpha}(T,\cdot) \circledast \boldsymbol{\varepsilon} + m(T,\cdot) \circledast \theta](t) + \nabla [\boldsymbol{\lambda}(T,\cdot) \circledast \nabla\theta](t) = 0. \tag{1.6}$$

This theoretical formulation is obtained using the first and second thermodynamic principles, where w_0 is the initial free energy, $\boldsymbol{\lambda}$ is the second order thermal conductivity tensor and r is an external heat source; further information on the derivation of the integral form of state equations can be found in B.1. As it was mentioned earlier, the $\circledast$ operator represents the Stieltjes convolution product, for more information and properties, see A.2. These equations allow to describe the evolution of the thermomechanical state of the polymer as a function of the reference state, the strain energy, the dilatation energy, the heat capacity, and a description of the effect of the heat flux in the energy balance equation. We will use these equations to derive the methodology for the effective behavior of the 3D printed polymer parts, as such equations must be solved during the simulation of a printing process. We end here by rewriting the constitutive equations in Eq. 1.2 for a body assumed to be in an initial reference state, free of stress and in thermodynamic equilibrium at the reference temperature T_0, noting that we will give a particular interest to the first one of the stress tensor, since it is the target variable to be evaluated microscopically in the 3D printed composite part.

$$\boldsymbol{\sigma} = [\mathbb{L}(T,\cdot) \circledast \boldsymbol{\varepsilon} - \mathbb{L}(T,\cdot) \circledast \boldsymbol{\alpha}(T,\cdot) \circledast \theta](t) \tag{1.7}$$

$$s = [\mathbb{L} \circledast \boldsymbol{\alpha}(T,\cdot) \circledast \boldsymbol{\varepsilon} + m(T,\cdot) \circledast \theta](t). \tag{1.8}$$

1.2 Thermomechanical modeling of isotropic thermorheologically simple polymers

Now, we will start to specialize the formulation for the particular case of the reference material subject of the validation experiments. The PEI is considered as an isotropic material, which

means that the fourth order relaxation tensor is entirely defined by two viscoelastic coefficients by means of the fourth order orthogonal projectors $\mathbb{J}$ and $\mathbb{K}$ [46], then, for the case of an isotropic polymer $\mathbb{L}$ can be written as (A.4):

$$\mathbb{L}(t, T(t)) = 3\kappa(t, T(t))\mathbb{J} + 2\mu(t, T(t))\mathbb{K}, \tag{1.9}$$

with $\kappa(t, T(t))$ and $\mu(t, T(t))$ being the compressibility and shear relaxation moduli respectively. In the same fashion as consequence of the isotropic character, the representation of $\boldsymbol{\alpha}(t, T(t))$ and $\boldsymbol{\lambda}(t, T(t))$ reads :

$$\boldsymbol{\alpha}(t, T(t)) = \alpha(t, T(t))\boldsymbol{I}, \quad \text{and} \quad \boldsymbol{\lambda}(t, T(t)) = \lambda(t, T(t))\boldsymbol{I}, \tag{1.10}$$

With $\boldsymbol{I}$ being the second order identity tensor.

Our primary focus in this work is to accurately depict the volumetric changes of the polymer in response to temperature and time variations. To this end, we find it apt to introduce a representation of $\alpha(t, T(t))$ that can capture the prolonged effects of temperature shifts on the final volume of the part. Delving a little into history—albeit briefly—it is crucial for our study's objective. This historical journey starts with the pioneering work of A. J. Kovacs in 1964 [47]. He delivered a sequence of papers focusing on experimental and phenomenological investigations into glassy polymers, ultimately formulating a theory surrounding the isobaric volume and enthalpy recovery of glasses [48]. He extensively developed this theory, with its applications rooted in what he termed "isothermal recovery". These experiments, based on rapid temperature variations on PVAc or polyvinyl acetate samples, effectively captured the thermal expansion's long-term (or viscoelastic) behavior.

A subsequent development in this area was made by Knauss and Emri in 1981 [49, 50]. They highlighted the striking resemblance between the creep function and the time-responsive thermal dilation function. Knauss took Kovacs' differential formulation of the free volume fraction, transforming it into its integral form, and aptly tagged $\alpha(t, T(t))$ as a thermal creep function. Although this model isn't extensively utilized, it finds its niche application in fields like shape memory alloys [51, 52, 53]. In these contexts, similar models are employed to provide a rheological description of thermal expansion.

In this study, we're guided by Kovacs' foundational theories to elucidate and quantify the isotropic thermal creep function. It's worth noting that such a portrayal of thermal expansion is already hinted at by [43] and can be discerned in the fifth term of Eq. (1.3). We introduce $\beta(t, T(t))$ as the second-order thermal strain tensor, the equation of which is

$$\boldsymbol{\beta}(t, T(t)) = [\boldsymbol{\alpha}(T, \cdot) \circledast \theta]\,(t), \tag{1.11}$$

and for the case of the isotropic PEI matrix,

$$\boldsymbol{\beta}(t, T(t)) = \beta(t, T(t))\boldsymbol{I} = [\alpha(T, \cdot) \circledast \theta]\,(t)\boldsymbol{I}. \tag{1.12}$$

1.2.1 Time-temperature superposition principle

Earlier in this section, we delved into the initial historical explorations surrounding thermo-viscoelasticity. Significantly, these pioneering studies were predominantly focused on a unique category of polymers termed as *thermorheologically simple materials*. This nomenclature was introduced in the influential work by Williams, Landel, and Ferry in 1955 [37]. The delineation of such materials offered two-fold advantages. For engineers, it facilitated the construction of a master curve, enabling them to extrapolate long-term behavioral predictions from short-term experimental data. Concurrently, for materials scientists, it streamlined the experimental process by reducing the requisite number of tests to adequately characterize a given material sample.

The implications of these observations were indeed more general, and thermodynamic studies of this time-temperature superposition showed that in this class, temperature variations cause structural uniform changes in the polymer. As a consequence, the time spectrum of the properties is contracted or expanded by a unique *shift factor*, here noted as a_T. In terms of experimental observations, what they noticed was that when plotted on a logarithmic scale, the results of relaxation experiments at different temperatures appeared to be the same, but shifted in time, and their shift magnitude with respect to an arbitrary reference temperature T_r was a function of the given temperature, this is the shift factor [37, 54, 55, 56, 57].

To illustrate this phenomenon, consider the internal dynamics of a "solid" polymer. Although we perceive a polymer as a solid, it's essentially a solution wherein polymer chains are in perpetual

motion. Its solid-like appearance stems from the sluggish rate of polymer chain movement. This apparent stasis results from the exceedingly high viscosity exhibited by the polymer solution. Consequently, when subjected to a constant load, the polymer takes a significant amount of time to manifest discernible shape alterations, thus earning its "solid" moniker. Now, imagine elevating the temperature of the polymer sample uniformly. At this higher temperature, the polymer's response time quickens. Deformations that would have previously occurred at a time t_1 now transpire at a quicker moment t_2 (where $t_2<t_1$). Thus, events seem to be "shifted" in time.

When examining this phenomenon from the localized perspective of a polymer chain, the role of temperature becomes more evident. As the temperature rises, Brownian motion intensifies, accelerating the movement of the polymer chains. Beyond a certain temperature threshold, these movements become so rapid that an external observer would struggle to track the events occurring within the polymer chain in real-time. From the vantage point of the polymer chain, external events appear to transpire sluggishly. Now, to understand the implications of this principle for our model, let's examine the effects on $\mathbb{L}(t, T(t))$ and $\boldsymbol{\alpha}(t, T(t))$. Owing to the unique shift factor, when $T(t) = \mathrm{T} \neq \mathrm{T}_r$, the following relationship can be derived:

$$\mathbb{L}(t, \mathrm{T}) = \mathbb{L}_{\mathrm{r}}\left(\frac{t}{a_T(\mathrm{T}, \mathrm{T}_r)}\right) = 3\kappa_{\mathrm{r}}\left(\frac{t}{a_T(\mathrm{T}, \mathrm{T}_r)}\right)\mathbb{J} + 2\mu_{\mathrm{r}}\left(\frac{t}{a_T(\mathrm{T}, \mathrm{T}_r)}\right)\mathbb{K}, \tag{1.13}$$

$$\boldsymbol{\alpha}(t, \mathrm{T}) = \boldsymbol{\alpha}_{\mathrm{r}}\left(\frac{t}{a_T(\mathrm{T}, \mathrm{T}_r)}\right) = \alpha_{\mathrm{r}}\left(\frac{t}{a_T(\mathrm{T}, \mathrm{T}_r)}\right)\boldsymbol{I}, \tag{1.14}$$

where the subscript $(.)_{\mathrm{r}}$ indicates that the function is constructed as a "master property" or reference property by shifting it horizontally while constructing the function of the shift factor a_T being, which by construction is equal to 1 at the reference temperature T_r. Note that in the rest of the text, since multiple indices are used in the formulations, this distinction of the reference master curve of the property is not shown.

1.2.2 Time temperature superposition principle in continuous variations of temperature : The "internal time"

The problem for us now is that the time-temperature superposition principle was derived for constant temperature states, which is obviously not the case for a 3D printed part. In order to deal with continuous temperature variations, the notion of "internal time" (ξ) is introduced as the "time variable" replacing the observer time (t) in the argument of the material functions; this notion is widely used and is considered as a common practice in modeling and simulation of polymers [45, 43, 58]. As mentioned above, the TTS is defined for constant temperature states. To be able to define the form of the "internal time" explicitly, an extension of this principle is needed. From there, one can consider the case of a material under test at a fixed initial reference temperature T_1 for a period of Δt_1 units of observer time (for instance, seconds). Then an infinitesimal temperature step is introduced ($\mathrm{T}_2 = \mathrm{T}_1 + \Delta\mathrm{T}$) and it is hold for a period of Δt_2. Let's check the differences between the total elapsed time of the observer, and the "internal time" of the polymer.

$$\begin{aligned} t &= \Delta t_1 + \Delta t_2, \\ \xi &= \Delta\xi_1 + \Delta\xi_2 = \frac{\Delta t_1}{a_T(\mathrm{T}_1, \mathrm{T}_r)} + \frac{\Delta t_1}{a_T(\mathrm{T}_2, \mathrm{T}_r)}. \end{aligned} \tag{1.15}$$

The notion of time inside the polymer can be considered as a relative variable with respect to temperature. The generalization to a continuous form of the "internal time" is obtained by applying N succesive infinitesimal temperature steps ($\Delta T_i \to 0$):

$$\xi(t) = \lim_{N\to\infty} \sum^{N} \frac{\Delta t_i}{a_T(T_i, \mathrm{T}_r)} = \lim_{N\to\infty} \sum^{N} \frac{\Delta t_i}{a_T(T(t_i), \mathrm{T}_r)} = \int_0^t \frac{du}{a_T(T(u), \mathrm{T}_r)} \tag{1.16}$$

1.2.3 thermo-viscoelasticity in the "internal time" domain

As we have shown in the previous sections, the mechanical response of a polymer is a function of time and temperature and this dependence is represented by the time temperature superposition principle, which in the case of continuous variations of temperature can be unified using the notion of "internal time" (Section 1.2.2). Based on the previous works [59, 60], which proposes the application of the correspondence principle [5] for viscoelastic composite mean-field estimates, which takes the advantage of the analogy of the linear elastic problem as Stieltjes convolution

products are transformed into conventional products in the Laplace-Carson domain, we aim here to apply a similar methodology in Section 4.2, but by extending it to the case of a thermo-viscoelastic composite.

To start the discussion, we will use the stress constitutive relation in Eq. (1.8), the time temperature superposition representation by means of the shift factor function a_T as it is presented in Eq. (1.13) and Eq. (1.14) with the corresponding extension to continuous variations of temperature by means of the "internal time" ξ in Eq. (1.16). Then, by writing the explicit form of the modified Stieltjes integral (see: A.2) for the constitutive relation, we can see the real problem regarding the application of the correspondence principle to continuous variations of temperature:

$$\boldsymbol{\sigma}(t) = \int_{-\infty}^{t} \mathbb{L}(\xi(t) - \xi(v)) \cdot \dot{\boldsymbol{\varepsilon}}(v) dv - \int_{-\infty}^{t} \int_{-\infty}^{v} \mathbb{L}(\xi(t) - \xi(v)) \cdot \dot{\boldsymbol{\alpha}}(\xi(v) - \xi(s)) \dot{\theta}(s) ds dv. \quad (1.17)$$

As can be seen in the previous expression the arguments of the integrals are different, this is: material functions ($\mathbb{L}$ and α) are function of the internal time ξ while the observable and state variables ($\boldsymbol{\varepsilon}$, θ and $\boldsymbol{\sigma}$) are function of the observer's times t; which does not allow the application of the correspondence principle since these integrals are no longer of the Stieltjes type. In order to ensure a representation that is equivalent to the aforementioned principle we perform a change of variables in the state ($\boldsymbol{\varepsilon}$, θ) and observable ($\boldsymbol{\sigma}$) variables to match the time space of the material properties which is the internal time ξ, noting that the new set of functions mapped from the internal time take the same exact values at different instants with correspondence known from the bijection defined in Eq. (1.16), which allows to easily define the inverse map $h \equiv f^{-1}$. Taking this into account this, the notation used for the new set of observed state variables will be the same, and their correspondence will be carried implicitly. This abuse of notation seek to alleviate the writing of the analytical forms developed in the following chapters, and to make the expressions more readable. Nevertheless, for the sake of clarity, we will use a special notation just once in the following definition, where the superscript $(.)^{\xi}$ denotes the state and observable variables, which are now mapped to internal time instants within an observation interval $t \in [0, t_f]$.

$$
\begin{aligned}
t \in [0, t_f] \qquad & (\boldsymbol{\varepsilon} \circ h)(\xi) \equiv \boldsymbol{\varepsilon}^{\xi} : [0, \xi_f] \to \Re^6 \\
\boldsymbol{\varepsilon} : [0, t_f] \to \Re^6 \qquad & (\theta \circ h)(\xi) \equiv \theta^{\xi} : [0, \xi_f] \to \Re \\
\theta : [0, t_f] \to \Re \qquad & \boldsymbol{\sigma}^{\xi} : [0, \xi_f] \to \Re^6 \\
\xi \equiv f : [0, t_f] \to [0, \xi_f] \qquad & \boldsymbol{\beta}^{\xi} : [0, \xi_f] \to \Re^6 \\
f^{-1} \equiv h : [0, \xi_f] \to [0, t_f] \qquad & \boldsymbol{\sigma}(t) = \left(\boldsymbol{\sigma}^{\xi} \circ f\right)(t) \\
& \boldsymbol{\beta}(t) = \left(\boldsymbol{\beta}^{\xi} \circ f\right)(t)
\end{aligned}
$$

This change of variables allows homogenizing the arguments, ensuring the Stieltjes representation of the integrals in the second line of Eq. (1.17), and thus the applicability of the correspondence principle. Considering now, the distributivity property of the Stieltjes convolution (see: A.2) and recalling that for the rest of this chapter the internal time forms (i.e., the starred forms) of the state and observable variables will be the same as those of their observer's time counterparts which only distinction will be identified on the argument of the functions (e.g., $\theta^{\xi}(\xi) \equiv \theta(\xi)$) we can rewrite Eq. (1.17) as follows:

$$
\boldsymbol{\sigma}(\xi) = \int_{-\infty}^{\xi} \mathbb{L}(\xi - v) \left(\dot{\boldsymbol{\varepsilon}}(v) - \dot{\boldsymbol{\beta}}(v)\right) dv = \left[\mathbb{L} \circledast (\boldsymbol{\varepsilon} - \boldsymbol{\beta})\right](\xi), \tag{1.18}
$$

with $\boldsymbol{\beta}$:

$$
\boldsymbol{\beta}(\xi) = \boldsymbol{I} \int_{-\infty}^{\xi} \alpha(\xi - v) d\theta(v) = \boldsymbol{I} \left[\alpha \circledast \theta\right](\xi), \tag{1.19}
$$

recalling, $\boldsymbol{\sigma}(\xi)$ is the second order stress tensor, $\mathbb{L}(\xi)$ is the fourth order relaxation tensor, $\boldsymbol{\varepsilon}(\xi)$ is the second order strain tensor, $\boldsymbol{\beta}(\xi)$ is the second order thermal strain tensor, $\alpha(\xi)$ is the isotropic thermal creep function, and $\theta(\xi) = T(\xi) - T_0$, the change of temperature from the initial temperature T_0, all of them now defined in the internal time domain ξ. This way of representing the stress response is a suitable form, as can be easily compared to the conventional forms of linear thermoelasticity, the reference theory for the estimation of the effective behavior computation in Section 4.2.

1.3 Prony series representation for viscoelastic spectra

As mentioned before, we use a Generalized Zener model of the Maxwell kind [35, 45, 44, 61] to approximate the continuous spectra for viscoelastic properties of the polymer for us, $\kappa(t)$ and

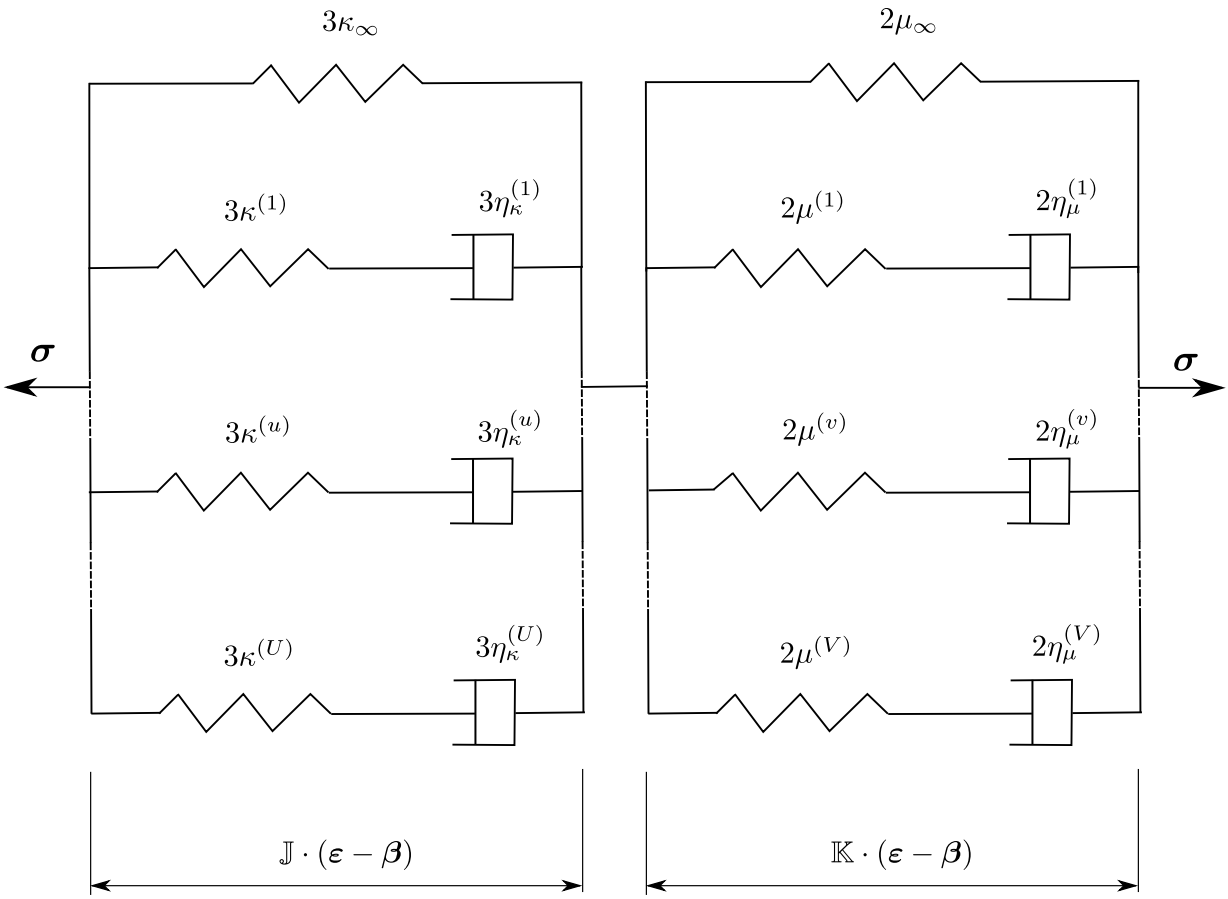

Figure 1.1: Generalized Maxwell standard solid rheological model for isotropic materials.

$\mu(t)$, this can be observed in the graphical representation of Fig. 1.1. The viscoelastic spectra are then approximated by a linear combination of weighted exponential functions called Prony series expansion, which in the case of the master properties at reference temperature (T_r) takes the following form:

$$\begin{aligned}\kappa(t) &= \kappa_\infty + \sum_{u=1}^{U} \kappa^{(u)} \exp\left(\frac{-t}{\tau_\kappa^{(u)}}\right) = \kappa_\mathrm{g} - \sum_{u=1}^{U} \kappa^{(u)} \left(1 - \exp\left(\frac{-t}{\tau_\kappa^{(u)}}\right)\right), \\ \mu(t) &= \mu_\infty + \sum_{v=1}^{V} \mu^{(v)} \exp\left(\frac{-t}{\tau_\mu^{(v)}}\right) = \mu_\mathrm{g} - \sum_{v=1}^{V} \mu^{(v)} \left(1 - \exp\left(\frac{-t}{\tau_\mu^{(v)}}\right)\right),\end{aligned} \tag{1.20}$$

with $\kappa_\mathrm{g} = \kappa_\infty + \sum_{u=1}^{U} \kappa^{(u)}$ and $\mu_\mathrm{g} = \mu_\infty + \sum_{v=1}^{V} \mu^{(v)}$, being the glassy or instantaneous moduli obtained by adding the weights $\kappa^{(u)}$ and $\mu^{(v)}$ with their respective long-term or rubbery moduli κ_∞ and μ_∞. By construction, the set of characteristic times $\tau_\kappa^{(u)}$ and $\tau_\mu^{(v)}$ is obtained by relating a set of discrete constant stiffness coefficients and their corresponding temperature dependent viscosity (rheological interpretation from the free volume theory [62]), for instance, $\tau_\kappa^{(u)}(T) =$

$\eta_\kappa^{(u)}(T)/\kappa^{(u)}$, with $\eta_\kappa^{(u)}$ being the compressibility viscosity of a given branch in the rheological model. In Eq. (1.13) due to the modeling choice, the shift factor a_T, appears to be related to the set of discrete characteristic times, this association is interpreted from the notion of activation of relaxation mechanisms and observed as a decrease on the viscosity as a consequence of the increase in temperature, which is reflected in an earlier activation of the relaxation mechanism due to the augmentation of Brownian motion in the polymer chains and promoting the viscous flow locally. Taking into account this representation and considering Eq. (1.13) and Eq. (1.20) for temperatures different from T_r, the interpretation of the shift factor for thermo-rheologically simple materials is related to the discrete viscosity spectra as follows:

$$a_T(T,\mathrm{T}_r) = \frac{\tau_\kappa^{(u)}(T)}{\tau_\kappa^{(u)}(T_\mathrm{r})} = \frac{\eta_\kappa^{(u)}(T)}{\eta_\kappa^{(u)}(T_\mathrm{r})} = \frac{\tau_\mu^{(v)}(T)}{\tau_\mu^{(v)}(T_\mathrm{r})} = \frac{\eta_\mu^{(v)}(T)}{\eta_\mu^{(v)}(T_\mathrm{r})}. \tag{1.21}$$

From the foregoing equation, one can note that, as a consequence of the thermorheologically simple material assumption, the time temperature superposition principle ensures the uniqueness of the shift factor not only when considering any of the elements in the discrete time sets, but also between the moduli characterizing the mechanical response of the polymer. One of the objectives of the present work is to experimentally validate this assumption for the chosen material, PEI - Ultem® 1010. Despite the theory chosen to derive the existence of an internal time ξ, which are indeed complementary, keeping a material support from the phenomenological consideration of the rheological model, the internal time forms of the isotropic relaxation moduli reads:

$$\begin{aligned}
\kappa(\xi) &= \kappa_\infty + \sum_{u=1}^{U} \kappa^{(u)} \exp\left(\frac{-\xi}{\tau_\kappa^{(u)}}\right) = \kappa_\mathrm{g} - \sum_{u=1}^{U} \kappa^{(u)} \left(1 - \exp\left(\frac{-\xi}{\tau_\kappa^{(u)}}\right)\right), \\
\mu(\xi) &= \mu_\infty + \sum_{v=1}^{V} \mu^{(v)} \exp\left(\frac{-\xi}{\tau_\mu^{(v)}}\right) = \mu_\mathrm{g} - \sum_{v=1}^{V} \mu^{(v)} \left(1 - \exp\left(\frac{-\xi}{\tau_\mu^{(v)}}\right)\right),
\end{aligned} \tag{1.22}$$

therefore,

$$\begin{aligned}
&\mathbb{L}(t,T(t)) = \mathbb{L}(\xi) = 3\kappa(\xi)\mathbb{J} + 2\mu(\xi)\mathbb{K}, \\
&\boldsymbol{\sigma}(t,T(t)) = \boldsymbol{\sigma}(\xi) = \left[\mathbb{L} \circledast (\boldsymbol{\varepsilon} - \boldsymbol{\beta})\right](\xi) = \left[3\kappa \circledast \mathbb{J} \cdot (\boldsymbol{\varepsilon} - \boldsymbol{\beta}) + 2\mu \circledast \mathbb{K} \cdot (\boldsymbol{\varepsilon} - \boldsymbol{\beta})\right](\xi).
\end{aligned} \tag{1.23}$$

1.4 The spectral form of the thermal deformations

To derive the time dependent form of the isotropic thermal expansion coefficient, we will follow [47, 48, 63]. The thermodynamic formulation of the volume variations will consider just isobaric transformations. The exact differential of the volume v is defined as :

$$dv = \left(\frac{\partial v}{\partial T}\right)_{q^{(n)}...q^{(N)}} dT + \sum^{N} \left(\frac{\partial v}{\partial q^{(n)}}\right)_{T,q^{(j)}\neq q^{(n)}} dq^{(n)}, \tag{1.24}$$

With q_i a set of ordering parameters that complete the description of the thermodynamic state. The instantaneous and established response of the volume variation as a consequence of an instantaneous variation in temperature are characterized by the glassy expansion modulus α_g and rubbery modulus α_l, these two quantities being definition :

$$\alpha_g = \frac{1}{v}\left(\frac{\partial v}{\partial T}\right)_{q^{(n)}...q^{(N)}}, \tag{1.25}$$

$$\alpha_l = \frac{1}{v_\infty}\left(\frac{\partial v_\infty}{\partial T}\right), \tag{1.26}$$

where v_∞ is the equilibrium volume at a given temperature. Now, considering that the equilibrium of a thermodynamic system is defined as the state that is uniquely determined by the temperature T and the pressure P of the system (note that here we are considering just isobaric transformations), we can rewrite Eq. (1.24) for both the volume differential dv and the differential of the equilibrium volume dv_∞:

$$dv = v\alpha_g dT + \sum^{N} \left(\frac{\partial v}{\partial q^{(n)}}\right)_{T,q^{(j)}\neq q^{(n)}} dq^{(n)} \tag{1.27}$$

$$dv_\infty = v_\infty \alpha_l dT \tag{1.28}$$

From the fact that $dv = dv_\infty$ when the equilibrium is achieved by comparison of the above two expression, we can write :

$$\left(\frac{dv_\infty}{dT}\right) = v_\infty(\alpha_g + \sum^{N} \alpha^{(n)}) = v_\infty \alpha_l \tag{1.29}$$

This gives a physical sense to the set of internal set of parameters as a set of creep weighted functions controlling the evolution of the expansion coefficient from its glassy state to its equilibrium

value or *rubbery plateau*. Let's introduce the *free volume fraction* variable, $\delta = v_\infty^{-1}(v - v_\infty)$ as the fraction of the volume that is not in equilibrium at a given instantaneous temperature, and related to the thermal deformation by means of the following expression:

$$\delta = \frac{\beta_{kk}}{3} - \alpha_l \theta, \tag{1.30}$$

with β_{kk} being the trace of the thermal strain tensor, we now aim to obtain an explicit form of the differential of δ:

$$d\delta = \frac{v_\infty dv - v dv_\infty}{v_\infty^2} = -(\delta + 1)\sum^{N} \alpha^{(n)} dT + \sum^{N} \left(\frac{\partial \delta}{\partial q^{(n)}}\right)_{T, q^{(j\neq n)}} dq^{(n)} \tag{1.31}$$

Considering that for the range of polymers that we work the values of $\delta < 0.0025$ [47] are negligible compared to the unity, we have neglected it here in the latter expression. Now we take the derivative with respect to time of the free volume fraction to try to give a form to its evolution after an instantaneous infinitesimal step of temperature :

$$\frac{d\delta}{dt} = -\sum^{N} \alpha^{(n)} \frac{dT}{dt} + \sum^{N} \left(\frac{\partial \delta}{\partial q^{(n)}}\right)_{T, q^{(j\neq n)}} \frac{dq^{(n)}}{dt}, \tag{1.32}$$

now, considering that this must be true for all values of $\dot{T}$, if we take the isothermal recovery experience in which the temperature is constant: $T(t) = \mathrm{T}\ \forall t > 0^+$. The first term in the above equation vanishes, and assuming proportional causality and individual contributions of the ordering parameters $q^{(n)}$ we can write:

$$\frac{d\delta}{dt} = \sum^{N} \frac{d\delta^{(n)}}{dt}, \tag{1.33}$$

$$\frac{d\delta^{(n)}}{dt} = \left(\frac{\partial \delta}{\partial q^{(n)}}\right)_{T, q^{(j\neq n)}} \frac{dq^{(n)}}{dt} = -\frac{\delta^{(n)}}{a_T(\mathrm{T}, \mathrm{T}_r)\tau_\alpha^{(n)}}, \tag{1.34}$$

by using this definition in its precedent we obtain a set of ODEs characterizing the evolution of the free volume fraction δ, recalling that $\dot{T} = \dot{\theta}$:

$$\frac{d\delta^{(n)}}{dt} + \frac{\delta^{(n)}}{a_T(\mathrm{T}, \mathrm{T}_r)\tau_\alpha^{(n)}} = -\alpha^{(n)} \frac{d\theta}{dt}. \tag{1.35}$$

With this set of evolution laws we can rewrite the expression of $\frac{\beta_{kk}}{3} = \beta$:

$$\beta(t) = \alpha_l \theta(t) + \sum^{N} \delta^{(n)}(t). \tag{1.36}$$

This last statement is sufficient proof of the suitable mathematical representation of the time dependent expansion coefficient, since, despite the physical context of the parameters, it is an exact analogy of the evolution law of Prony systems when simulating creep behavior in polymers[45]. If one wants to see this by an explicit equation, the form of the thermal creep function can be obtained by means of the Laplace-Carson transform of Eq. (1.35) and to insert it into the corresponding transform of Eq. (1.36). The spectral form of the thermal expansion coefficient is then:

$$\alpha(t, \mathrm{T}) = \alpha_l - \sum^{N} \alpha^{(n)} \exp\left(\frac{-t}{a_T(\mathrm{T}, \mathrm{T}_r)\tau_\alpha^{(n)}})\right) = \alpha_g + \sum^{N} \alpha^{(n)} \left(1 - \exp\left(\frac{-t}{a_T(\mathrm{T}, \mathrm{T}_r)\tau_\alpha^{(n)}}\right)\right). \tag{1.37}$$

Finally, considering the time temperature superposition principle in continuous variations of temperature for thermorheologically simple materials presented earlier (see: 1.2.2), we can then write the internal time form of Eq. (1.37) considering the definition in Eq. (1.16) as:

$$\alpha(t, T(t)) = \alpha(\xi) = \alpha_l - \sum^{N} \alpha^{(n)} \exp\left(\frac{-\xi}{\tau_\alpha^{(n)}})\right) = \alpha_g + \sum^{N} \alpha^{(n)} \left(1 - \exp\left(\frac{-\xi}{\tau_\alpha^{(n)}}\right)\right), \tag{1.38}$$

and the correspondent internal time form of the thermal strains isotropic invariant β:

$$\beta(t, T(t)) = \beta(\xi) = \alpha_l \theta(\xi) - \sum^{N} \delta^{(n)}(\xi). \tag{1.39}$$

with the explicit form of the evolution of the fractional contributions $\delta^{(n)}$ in the internal time domain as:

$$\frac{d\delta^{(n)}}{d\xi} + \frac{\delta^{(n)}}{\tau_\alpha^{(n)}} = \alpha^{(n)} \frac{d\theta}{d\xi}. \tag{1.40}$$

This closes the particular remarks about the material modeling for the properties of the PEI, the rest of the thermal properties will be explored as the experimental section is presented.

1.5 Differential form of the state equations in linear thermo-viscoelasticity for the generalized Zener model of the Maxwell kind

Now, taking into account the previous considerations regarding the modeling of the relaxation spectra, it seems appropriate to introduce a different but equivalent form of the state equations. This representation of the state and stress equations will be used in the Chapter 5. Before entering into details, we will use for the following steps a simplified version of the rheological model presented in Fig. 1.1. The simplification is achieved by imposing equal characteristic times sets for both the compressibility and shear spectra. This is a common practice when modeling viscoelastic behavior, as it reduces the number of internal variables associated with viscous strains; and is for example the only way of defining time dependent viscoelastic behavior using Prony series in Abaqus CAE, which is only possible for isotropic materials with a maximum length of 13 elements (these limitations are avoided using UMAT subroutines). This simplification is in fact made for the validation examples in Chapters 4 and 5, and the first round of numerical validation experiments in Chapter 6. And it made us recall that as it was already mentioned at the end of the introduction the experimental work was being done in parallel with the modeling, in consequence the material laws were not completed at most of the stages of the research pushing us to use a support for simulation, viscoelastic spectra that were indeed artificial, with some of them holding direct physical meaning (the shift factor and the shear spectrum) and others furbished using material data from the producers and partial experiments at hand. Despite this fact, we must insist that this does not affect the implications of the conclusions of the formulations, since the mathematical structures of the material laws are preserved. We then adopted this simplified form for the artificial matrix material laws used in the validation examples of the following two chapters. With this in mind, we should start rewriting the fourth order relaxation tensor $\mathbb{L}(\xi)$ from Eq. (1.22):

$$\begin{aligned}\mathbb{L}(\xi) &= (3\kappa_\infty \mathbb{J} + 2\mu_\infty \mathbb{K}) + \sum_{u=1}^{U} (3\kappa^{(u)} \mathbb{J} + 2\mu^{(u)} \mathbb{K}) \exp\left(\frac{-\xi}{\tau_L^{(u)}}\right) \\ &= \mathbb{L}_\infty + \sum_{u=1}^{U} \mathbb{L}^{(u)} \exp\left(\frac{-\xi}{\tau_L^{(u)}}\right) = \sum_{u=0}^{U} \mathbb{L}^{(u)} \exp\left(\frac{-\xi}{\tau_L^{(u)}}\right),\end{aligned} \tag{1.41}$$

with $\mathbb{L}^{(0)} = \mathbb{L}_\infty$ and $\tau_L^{(0)} = \infty$. The correspondent rheological representation of this simplified version of Fig. 1.1 is shown below.

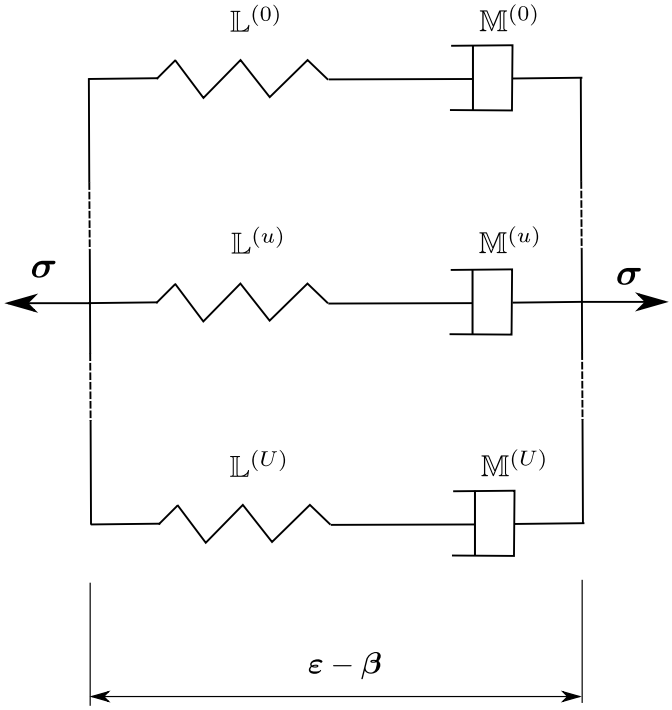

Figure 1.2: Simplified generalized Maxwell standard solid rheological model for isotropic materials.

Let's now recall the form of the stress constitutive relation from Eq. (1.18):

$$\boldsymbol{\sigma} = [\mathbb{L} \circledast (\boldsymbol{\varepsilon} - \boldsymbol{\beta})](\xi), \tag{1.42}$$

this way of representing the stress by means of the associative property of the Stieltjes product (see A.2) can be seen as equivalent to instead of choosing as state variable the observable deformation $\boldsymbol{\varepsilon}$, we choose the mechanical deformation $\boldsymbol{\varepsilon}_m = \boldsymbol{\varepsilon} - \boldsymbol{\beta}$ as state variable. Now we perform the Laplace-Carson transform (see: A.3) on the later expression in the previous equation noting the transformed quantities by using the starred notation, $(.)^*$, and taking into account the Prony series representation of $\mathbb{L}$ to obtain the internal variables representation of the Stieltjes integral of the stress:

$$\boldsymbol{\sigma}^* = \sum_{u=1}^{U} \mathbb{L}^{(u)} \frac{p}{p + 1/\tau_L^{(u)}} \cdot (\boldsymbol{\varepsilon}^* - \boldsymbol{\beta}^*) = \sum_{u=1}^{U} \mathbb{L}^{(u)} \cdot (\boldsymbol{\varepsilon}^* - \boldsymbol{\beta}^* - \boldsymbol{q}^{(u),*}) \tag{1.43}$$

with,

$$\boldsymbol{q}^{(u)*} = \frac{1}{p + 1/\tau_L^{(u)}} \frac{(\boldsymbol{\varepsilon}^* - \boldsymbol{\beta}^*)}{\tau_L^{(u)}}, \tag{1.44}$$

the internal variable accounting for the "viscous strains" or the dissipative part of the strain. By performing the correspondent inverse Laplace-Carson transform of the two precedent equation we obtain an internal time formulation of the thermo-viscoelastic constitutive law lying in the internal variables formulation:

$$\boldsymbol{\sigma}(\xi) = \sum_{u=1}^{U} \mathbb{L}^{(u)} \cdot (\boldsymbol{\varepsilon}(\xi) - \boldsymbol{\beta}(\xi) - \boldsymbol{q}^{(u)}(\xi)) \tag{1.45}$$

with,

$$\frac{d}{d\xi}\boldsymbol{q}^{(u)} + \frac{1}{\tau_L^{(u)}}\boldsymbol{q}^{(u)} = \frac{(\boldsymbol{\varepsilon}(\xi) - \boldsymbol{\beta}(\xi))}{\tau_L^{(u)}}, \tag{1.46}$$

Therefore, we can write the expression of the potential w considering that the latter expression of $\boldsymbol{\sigma}$ is derived from it, which lies in the standard solids framework [26, 6, 64, 65]:

$$w = \sum_{u=1}^{U} \frac{1}{2}\mathbb{L}^{(u)} \cdot (\boldsymbol{\varepsilon} - \boldsymbol{\beta} - \boldsymbol{q}^{(u)}) \cdot (\boldsymbol{\varepsilon} - \boldsymbol{\beta} - \boldsymbol{q}^{(u)}) - f(\theta), \tag{1.47}$$

with f accounting for the pure thermal contributions to the free energy. To derive the expression of the dissipation potential, we start by considering the correspondent form of the dissipation potential of Eq. (1.4):

$$\varphi = -\frac{1}{2}\frac{\partial \mathbb{L}}{\partial \xi} \circledast (\boldsymbol{\varepsilon} - \boldsymbol{\beta}) \circledast (\boldsymbol{\varepsilon} - \boldsymbol{\beta}) + g(\theta), \tag{1.48}$$

with g the pure thermal contributions to the dissipation. Now, by taking the explicit form of the partial time derivative of $\mathbb{L}$:

$$\frac{\partial \mathbb{L}}{\partial \xi} = -\sum_{u=1}^{U} \frac{1}{\tau_L^{(u)}} \mathbb{L}^{(u)} \exp\left(-\frac{\xi}{\tau_L^{(u)}}\right), \tag{1.49}$$

and considering the equivalency regarding the integrals in w we can write φ in function of the

internal variables $\boldsymbol{q}^{(u)}$:

$$\varphi = \frac{1}{2}\sum_{u=1}^{U} \mathbb{L}^{(u)} \cdot \frac{(\boldsymbol{\varepsilon} - \boldsymbol{\beta} - \boldsymbol{q}^{(u)})}{\tau_L^{(u)}} \cdot (\boldsymbol{\varepsilon} - \boldsymbol{\beta} - \boldsymbol{q}^{(u)}) + g(\theta). \tag{1.50}$$

Finally, by considering the expression of $\boldsymbol{q}^{(u)}$ above, we can rewrite the dissipation as a function of the time derivative of the internal variables $\dot{\boldsymbol{q}^{(u)}}$:

$$\varphi = \frac{1}{2}\sum_{u=1}^{U} \mathbb{L}^{(u)}\tau_L^{(u)} \cdot \dot{\boldsymbol{q}}^{(u)} \cdot \dot{\boldsymbol{q}}^{(u)} + g(\theta) = \frac{1}{2}\sum_{u=1}^{U} \mathbb{M}^{(u)} \cdot \dot{\boldsymbol{q}}^{(u)} \cdot \dot{\boldsymbol{q}}^{(u)} + g(\theta). \tag{1.51}$$

At this point, it should be noted that the matrix formulation matches perfectly into the standard solids framework (see Equations (5.4)-(5.6)), verifying by construction the constitutive laws introduced at the beginning of Section 5.1 and their correspondence with the integral form presented at the beginning of this chapter. The reader can argue that this differential form does not consider the terms associated with the heat capacity m within the formulation, this has two direct reasons: i) all the application examples are based on the assumption of prior knowledge of the temperature history, and ii) the linear thermo-viscoelastic theory assumes that the fields $\boldsymbol{\varepsilon}$ and $\frac{\theta}{T_0}$ are infinitesimal, this is quietly ensured for the strain field $\boldsymbol{\varepsilon}$, but as it can be inferred values of $\frac{\theta}{T_0}$ are of the order of 1 suggesting that this linear approximation with respect to the second order term in θ may be insufficient to map the nonlinearity induced by these temperature variations. We have just proofed the equivalency of the integral (Eqs. 1.3 and 1.4) and differential formulation which modeling choices lie in the internal variables framework and interpreted as viscous strains in the decomposing the macroscopic strain in the case of the mechanical internal variables, and pseudo temperatures or fictive temperatures in the case of the decomposition of the thermal strain. We can now pass to study the experimental observations serving to feed the models presented above.

Chapter 2

Matrix Reference material (PEI): Experimental identification

This chapter focuses on the experimental identification of the thermo-viscoelastic behavior following Chapter 1 for the reference material used in this work, the comercial PEI-Ultem 1010. This work is the result of a collaboration with the *Centre de mise en forme des matériaux* (CEMEF-Mines Paristech Sophia Antipolis). The experimental protocol within the identification of thermomechanical parameters is presented. This work is on preparation for publication with target journal: *Journal of Polymer Science and Engineering.* In summary, we present: Dynamical mechanical tests and creep experiments for the determination of the master curves representing the mechanical properties of the isotropic polymer matrix using injection molded samples. Differential scanning calorimetry to measure the isobare heat capacity and the glass transition temperature. Further comments are made when considering the determination of the thermal expansion coefficients, since it was an unproductive experimental campaign and others related to the determination of the compressibility modulus and its lack of consistency.

In the following sections, the experimental methodology, results, and model identification will be presented. The present section aims to describe the experimental campaign followed for the identification of the material parameters needed to describe the thermo-viscoelastic response of PEI - Ultem® 1010 already described in the latter section, in addition, this study is extended to experimentally characterize thermal parameters needed for the case of coupled simulations in which the heat and entropy equation are involved (*e.g.* simulation of the printing process itself).

2.1 Materials

As mentioned above, For this study, poly-ether-imide (Ultem® 1010 grade) supplied by Sabic was used for this study. Recalling that the key parameter regarding the thermal stability of such polymers is the glass transition temperature. In the literature, the glass transition of the PEI 1000 has been reported at a temperature of 220°C [66], in the case of our reference material, in [67] a temperature of 215°C is reported, but its source comes from the information given by the commercial supplier Stratasys as we can observe when considering the Table. 2.1, in [68, 69] a temperature of 217°C is reported, but again this corresponds to commercial suppliers (the first in the table below) and the measure was not performed. From the outputs of our research, there are no journal publications reporting this value as a result of an experimental campaign and then, we will answer to this during the thermal measures. The samples used for the experiments were injection molded at high temperature in order to obtain plates of 10 cm in side and 1 mm in thickness.

Table 2.1: Material data from commercial suppliers and material web's datasheet.

	E(GPa)	Tg(°C)	C.T.E. (m/m°C)	Conductivity (W/m°C)	diffusivity(mm^2/s)
3DXTECH (Filament)	2.500	217	-	-	-
STRATASYS (Resin)	3.040	209.37	0.00003608	0.24	0.14
AMCO (Resin)	3.199	215	0.00005220	0.22	-
SABIC (Resin)	3.200	215	0.00005200	0.22	-
XYOMETRY(Resin)	2.770	216	-	-	-
MAT DATA CENTER (Resin)	3.200	215	-	0.22	-
MATWEB (Resin)	3.200	215	0.00005000	0.21	-

2.2 Methods

2.2.1 Static tensile tests at different constant temperatures

This study was performed as a preliminary step of the tensile creep experiments. As creep tests are observations of the evolution of the deformation of the specimen as a function of time in response to an "instantaneous" load at a given temperature, the mechanical properties are subjected to variations due to the variations of temperature (time-temperature superposition principle). It is then necessary to perform a primal study to estimate admissible levels of stress, relying on the infinitesimal deformations theory in the linear viscoelastic framework. Then, tensile static tests were performed for each chosen isotherm of the creep experiments (i.e. $\{150, 170, 190, 210, 230\}$°C). The experimental program was performed at controlled displacement conditions with an axial displacement rate of 0.1 mm s^{-1}, until the samples reach the nominal elongation of about 30 mm. Results of these experiments are reported in Fig. 2.1.

As expected, below the glass transition temperature (T_g) the magnitude of the admissible loads are on the range of conventional measurement systems. In contrast, when regarding the last two isotherms, the decrease in the magnitude of the stiffness is significant, characterizing the drastic transition around T_g. As it can be observed, the curve of the static response at 230°C shows a very low values of stress compared to the others, considering that the given temperature is around a dozen degrees above the transition. Regarding the coherence of the computed modulus as function of temperature, we see a monotonous decreasing of the Young modulus as a function of temperature, which is expected. The values below the glass transition happened to be greater than the ones reported from Sabic® with a value of 3.2 GPa against values around 2.38 GPa noting that reported external values of Table. 2.1 are given for room temperature, and the greatest value is computed for a temperature of 150°C, this suggests an overestimation of the Young modulus considering the corresponding value in Section 2.2.3 that is close. In the same way, these results sustain the affirmation about the machine dependent variation reported in the Young modulus when performing DMA experiments (Section 2.2.3) with a value of 2.46 GPa, and showing consistency between the measures and the reported values from external sources.

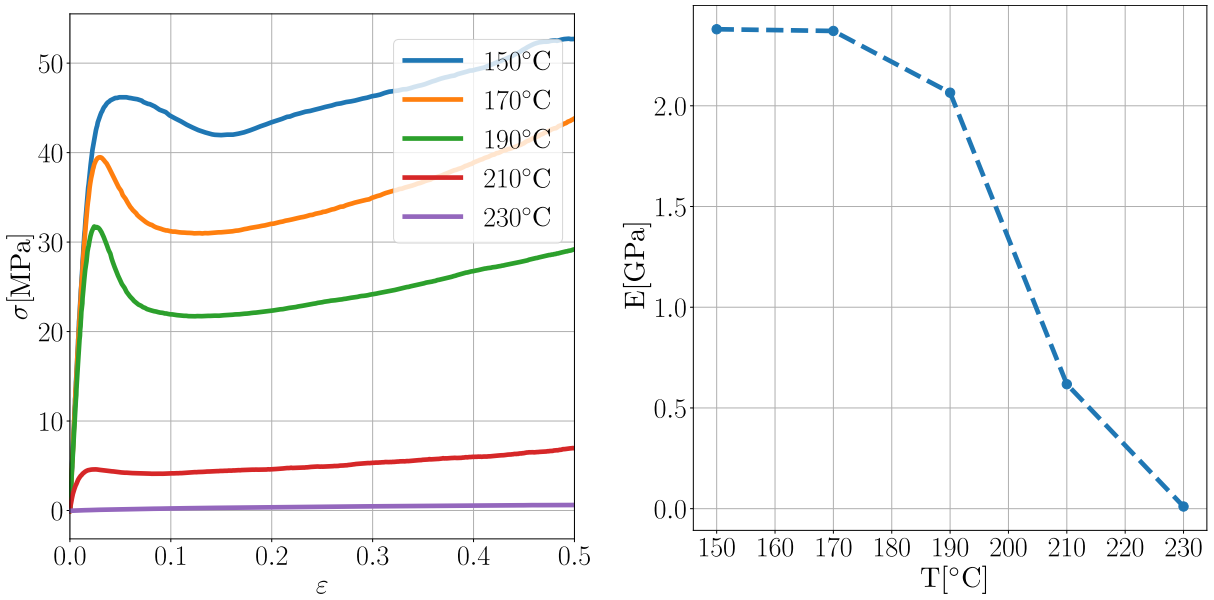

(a) Axial rational stress vs. Hencky axial deformation

(b) Instantaneous Young modulus (E) vs. Temperature

Figure 2.1: Static tensile tests : On the load magnitude to determine the admissible stress for linear experiments.

2.2.2 Creep tests

In this section, two kinds of creep experiments are performed. The first part of this campaign was performed in order to obtain a verification concerning the magnitude of the Young modulus after the inconsistencies reported in the dynamical experiments in Section 2.2.3. The second experiments aim to the determination of the thermo-viscoelastic bulk modulus through what's called confined compression tests. The latter was proposed to get an additional confirmation between the measured modulus as for the case of an isotropic material, two coefficients are enough to characterize the full fourth order relaxation tensor as can be noted from Eq. (1.9), then it must exist an equivalence between them to ensure the validity of the acquired data. These kinds of experiments are suitable when studying the differed response of a polymer to an "instantaneous" load in function of temperature. Indeed, the relaxation experiments are slightly more complicated as are performed in imposed displacement, something that becomes a challenge considering that the sample is actively being deformed by the temperature variation.

Tensile experiments

In this study, creep tests were performed to establish a master curve of PEI in the time domain. It consists of applying a stress step σ_0 to the sample, that is adjusted for each value of temperature, taking into account the static tests of the previous section, ensuring that measurements are performed within the linear viscoelastic domain, and measuring its strain response $\varepsilon(t)$ as a function of time while maintaining the stress. When the applied stress is in the linear range, the sample tensile modulus $E(t)$ can be calculated as:

$$E(t) = \frac{\sigma_0}{\varepsilon(t)} \tag{2.1}$$

Experimentally, in order to build creep master curves, successive creep tests are carried out on the same sample at different temperatures. For a given isotherm, the experimental protocol consists of 4 successive steps (see Fig. 2.2):

i. Loading the sample to the stress σ_0 at a traverse speed of $0.1\,\mathrm{mm.s^{-1}}$.

ii. Maintaining the stress σ_0 and measuring the sample strain for a time $\mathrm{t_{creep}} = 1\,\mathrm{h}$, the end of one creep measurement.

iii. Unloading the sample with a traverse speed of $0.1\,\mathrm{mm.s^{-1}}$. The previous step to the transition between an isotherm T_i and its following value T_{i+1}.

iv. Measurement of the sample strain during a time $\mathrm{t_{relax.}} = 1\,\mathrm{h}$. This "waiting time" between each creep measurement is intended to avoid the superposition of the pure mechanical response and the dilatation due to the increase of temperature in the sample.

Thereafter, the sample is heated to the next isotherm at a temperature ramp of $1\,\mathrm{°C.min^{-1}}$ and the creep protocol is repeated.

Creep tests were performed on dumbbell shaped samples using an Instron 30 kN tensile facility. During the tests, the strain field is determined locally by stereo image correlation using VIC–3D software. Isotherms were selected around the glass transition temperature of PEI. Due to the time required to perform each creep test ($\approx 2\,\mathrm{h}$), only five isotherms were investigated: 150 °C, 170 °C, 190 °C, 210 °C and 230 °C. Moreover, in order to stay in the linear domain for

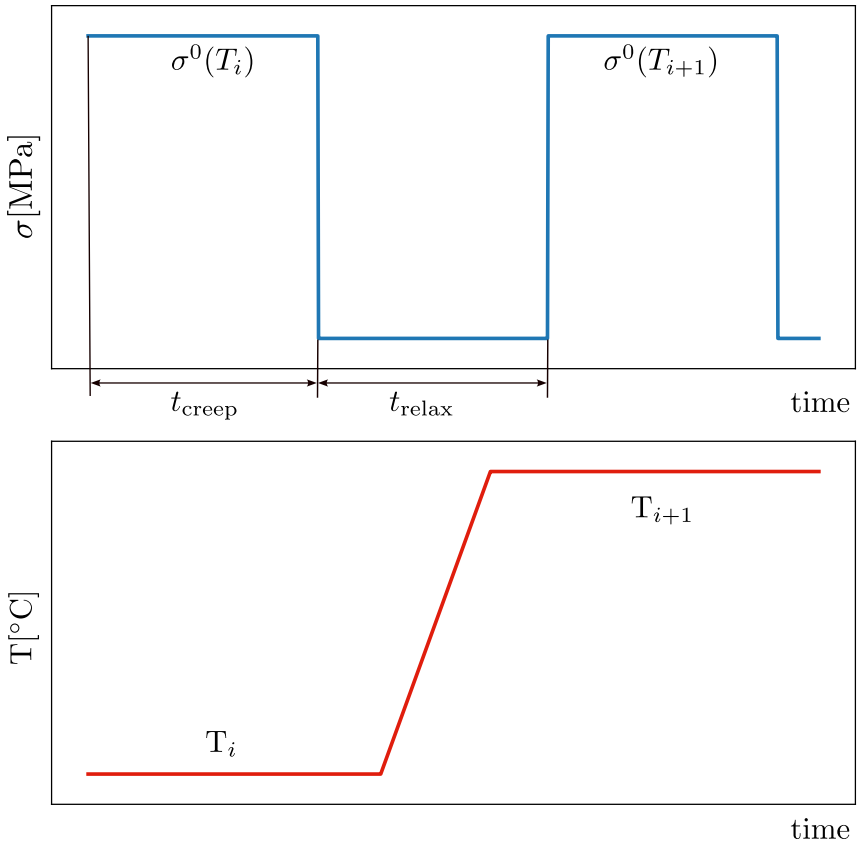

Figure 2.2: Graphical representation of the creep experiments protocol

each isotherm, while preserving a good signal-to-noise ratio, the applied stress σ_0 is 2.5 MPa in glassy state (i.e., first four isotherms) and 0.25 MPa in rubbery state (i.e., last isotherm).

Fig. 2.3a presents the PEI creep curves obtained for each isotherm. For the 150 °C isotherm, data show a quasi-constant modulus as a function of time. The tensile modulus at this temperature is around 2.3 GPa, this value is consistent with the one measured by DMA (see Section 2.2.3) at the same temperature in tensile tests ($E'(150\,°C) = 2.46$ GPa), rectangular torsion ($E'_{shear}(150\,°C) = 2.91$ GPa) and the values reported in the preliminary static tests ($E(150\,°C) = 2.38$ GPa). As the temperature increases, a change in PEI creep behavior as a function of time is observed. This change is due to glass transition of PEI which goes from glassy to rubbery state. This is particularly reflected in a significant tensile modulus decrease of about three decades.

Fig. 2.3b shows the master curve built from isothermal creep curves. The reference temperature T_{ref} used to build this curve is 210 °C. As expected, the data suggest different behavior as a function of time. At short time, PEI exhibits a quasi-constant tensile modulus associated with the glassy plateau. Thereafter, a drastic decrease in modulus is observed, which is associated

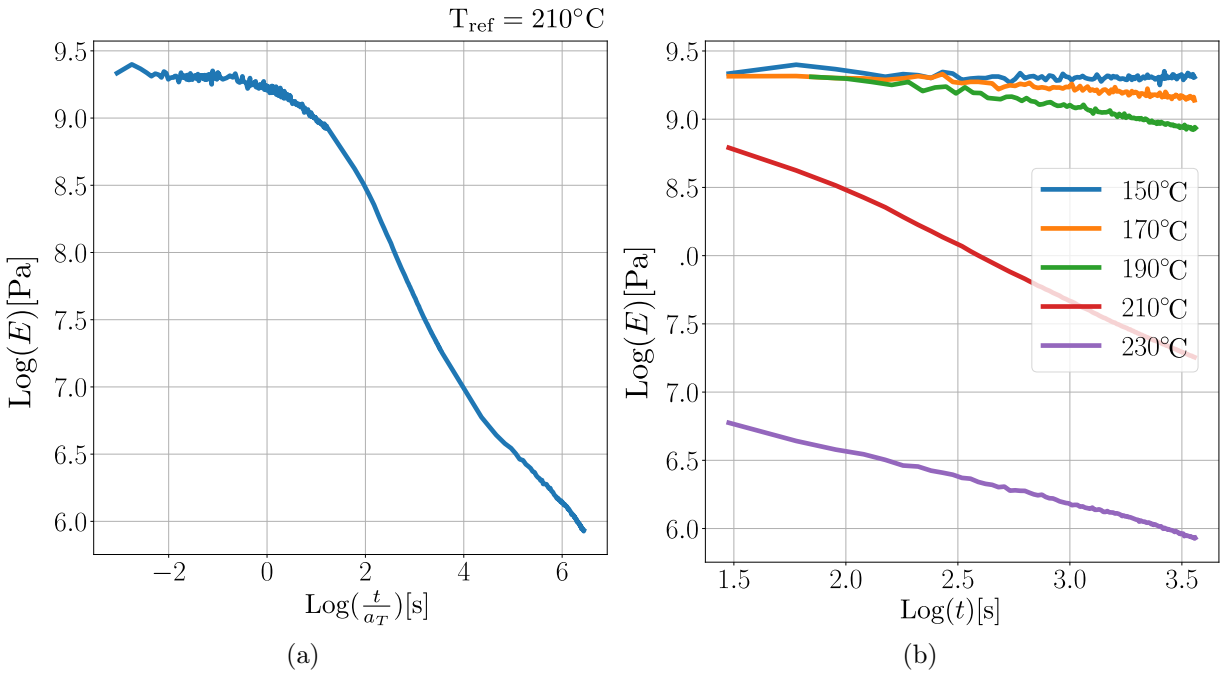

Figure 2.3: PEI creep master curve **(a)** and PEI creep curves as a function of isothermal temperatures **(b)** .

with the mechanical manifestation of the glass transition. At long time, PEI shows a rubbery plateau over a reduced time range: a rubbery modulus of about 3 MPa can be determined from this master curve. At the end of the curve (above 10^6 s), the beginning of the viscous flow of the polymer can be guessed. In resume, the observed behavior as a function of time is classical for an amorphous thermoplastic polymer, and confirms the relevancy of the executed experimental creep protocol. Nevertheless, due to the reduced number of isotherm, just a few number of shift factors can be determined and therefore, it is difficult to analyze their temperature dependency. The values of the shift factor a_T computed from these experiments are presented in Fig. 2.7. As can be observed, the values computed are close to those of the tensile DMA with non-negligible gaps for low temperatures, suggesting an influence of the experimental facilities and a lack of consistency between samples used to perform experiments.

2.2.3 Dynamical mechanical tests

Dynamic Mechanical Analysis (DMA) was used to analyze the thermo-viscoelastic behavior of PEI. DMA experiments were performed in two geometries : tensile and rectangular torsion, allowing to determine experimentally either tensile E^* and shear G^* complex moduli as function of frequency and temperature.

DMA tests in tensile geometry were performed on a DMA1 manufactured by Perkin Elmer and sample dimensions are 20 mm×4 mm×2 mm. For rectangular torsion, tests were performed on a ARES G1 manufactured by TA Instruments and sample dimensions are 35 mm×10 mm×2 mm. For both geometries, measurements were performed in the linear domain with a strain of 0.04 %. For each geometry, two types of tests were performed : during a temperature ramp at a constant frequency (i.e., thermogram) and as a function of frequency during isotherms (i.e., DMA master curves and shift factor). The experimental parameters used for both geometries and each type of test are summarized in Table 2.2.

Table 2.2: Experimental parameters used for both geometries and each type of DMA tests.

	Dynamic tensile tests		Rectangular torsion tests	
	Thermogram	Master Curves	Thermogram	Master Curves
Temperature range	[30 ; 300] °C	[150 ; 300] °C	[30 ; 240] °C	[30 ; 240] °C
Temperature ramp or step	1 °C.min^{-1}	10 °C	1 °C.min^{-1}	5 °C
Frequency	1 Hz	[0.1 ; 10] Hz	1 Hz	[0.1 ; 10] Hz

Mechanical behavior as a function of temperature

Fig. 2.4a and Fig. 2.4b show the storage and loss moduli of PEI as a function of temperature in dynamic tensile and rectangular torsion mode, respectively.

Both figures show a classical dynamic mechanical behavior of an amorphous high-performance thermoplastic polymer: a quasi-constant storage modulus over a wide temperature range followed by a two decades drop at a temperature of 220 °C, approximately. This phenomenon, named α, is associated with the mechanical manifestation of the PEI glass transition, the polymer going from the glassy state to rubbery state. On the loss moduli, it results in a mechanical dissipation peak.

At lower temperature, loss shear modulus G'' exhibits a second relaxation phenomenon, named β, characterized by a broad peak with a maximum at around 80 °C and linked to localized molecular motions of benzene rings on the polymer main chain [70, 71]. Due to low signal-to-noise ratio of dynamic tensile mode in glassy state, the β relaxation is hardly observed on the thermogram. Above glass transition, dynamic tensile test reaches a rubbery plateau over a narrow temperature range, beyond which a gradual decrease in modulus with temperature is observed

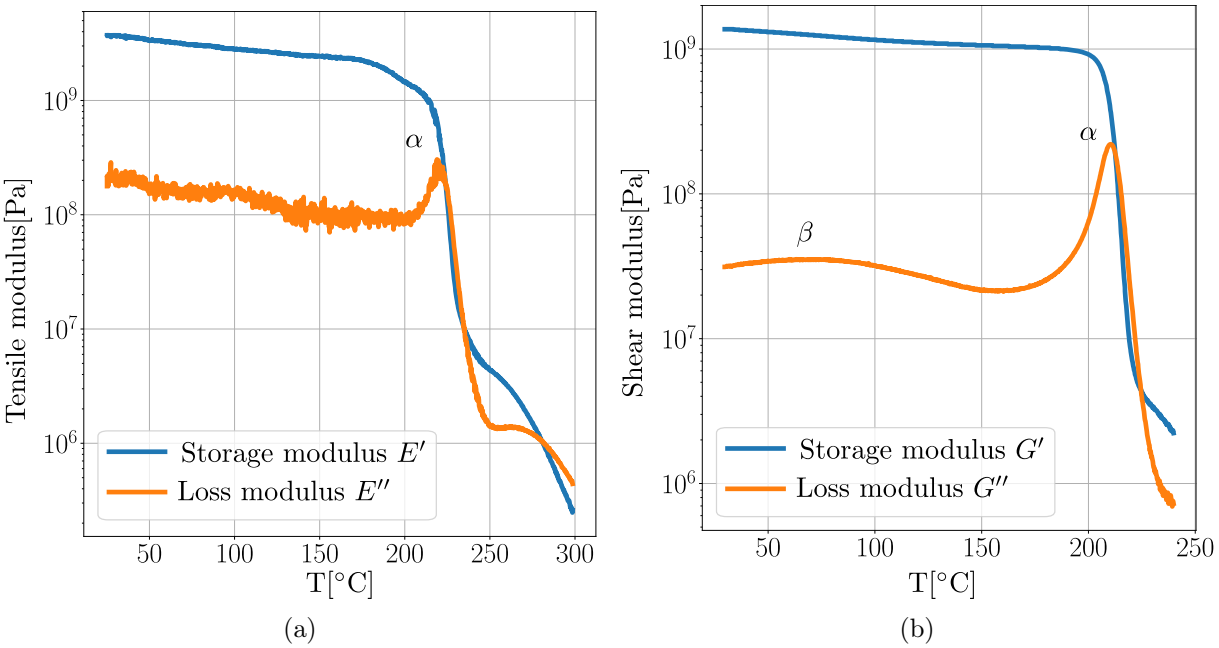

Figure 2.4: Dynamic mechanical analysis thermograms of PEI in dynamic tensile test **(a)** and in rectangular torsion test **(b)**.

(close to a purely dissipative behavior). This decrease is also visible on the tensile storage modulus E' in the thermogram. As PEI is an amorphous polymer, its mechanical strength on the rubbery plateau is only allowed by the presence of physical entanglements. Above a certain temperature (around 260 °C), these entanglements are no longer sufficient to retain the macromolecules: the polymer flows. This polymer flow is not observed in rectangular torsion mode due to a torque too low to be reliably measured by the ARES G1 facility.

Observing the glassy behavior from the thermograms, the magnitude of the storage modulus are as follows: at 25 °C, E' is about 3.72 GPa which is in agreement with values in Table 2.1, and G' is about 1.36 GPa, while at 150 °C, E' is about 2.46 GPa and G' is about 1.07 GPa. In order to compare the consistency of these values with respect to external sources, we use the low temperature values to compute the Poisson's ratio and compare it to 0.36 from [72] for PEI at room temperature. The calculated value of $\nu = (E'/2G') - 1$ is 0.3677, which is consistent with the reported values.

Building of master curves in the frequency domain

As we have already discussed, the ability to construct such master curves comes from the aforementioned time-temperature superposition (TTS) principle, which makes it possible to map the

behavior of a polymer over a wide range of frequencies (i.e., time) by performing experiments at a reduced interval and changing the constant temperature of the test. As a consequence of the TTS, the behavior at a given time for a constant temperature greater than room temperature can be interpreted as the behavior at the initial temperature but earlier, in other words, due to temperature the behavior appears to be horizontally shifted (and we now know the origin of the name of the shift factor, a_T). The same interpretation in time is given by frequency, remembering that in this context low frequencies are associated with long term responses and high temperatures, while high frequency values are associated with short term responses and low temperatures.

Data in the frequency domain at different isotherms can be observed in Fig. 2.5. This is the data used for building the master-curve of the tensile relaxation modulus ($E^* = E' + jE''$) in Fig. 2.6a. As can be inferred, the construction of the master curves happens in parallel with the definition of the numerical values, given by maximizing the overlap between two subsequent isotherms by shifting it a distance given by a_T (see 2.7).

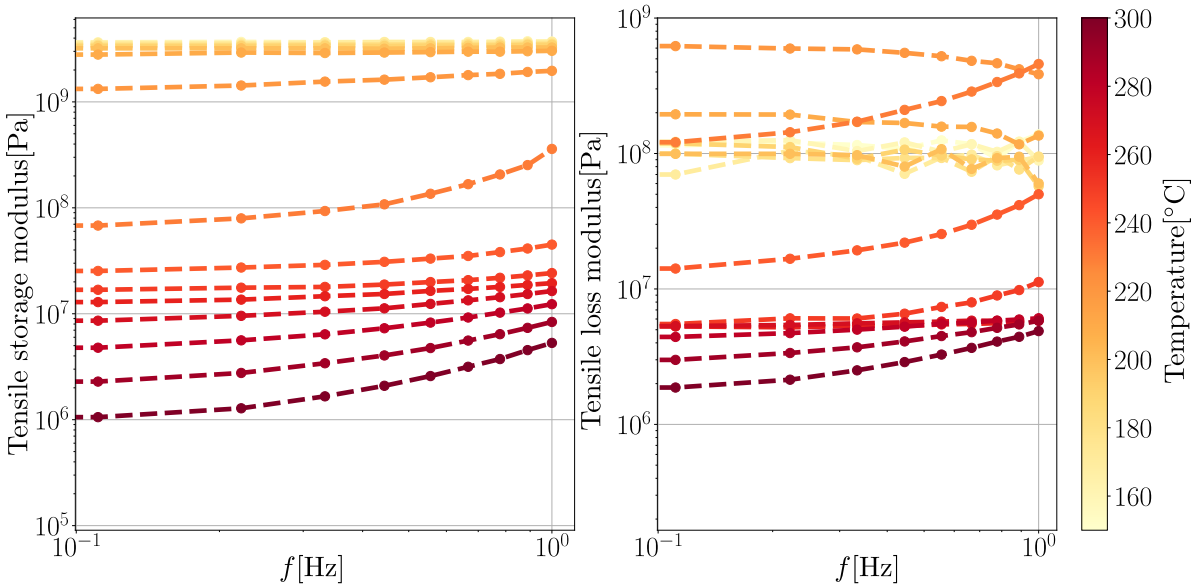

Figure 2.5: Example of raw data for building master curve in dynamic tensile behavior.

In order to study the PEI behavior over a wide frequency range, master curves has been built for both dynamic tensile test and rectangular torsion test by using the Time-Temperature Superposition (TTS) principle. Fig. 2.6a and Fig. 2.6b show the master curves obtained for tensile moduli and for shear moduli, respectively. The reference temperature T_{ref} used to build master curves is close to α relaxation temperature and is indicated in the top right corner of

each figure. As observed on DMA thermograms (Fig. 2.4a and Fig. 2.4b), dynamic tensile

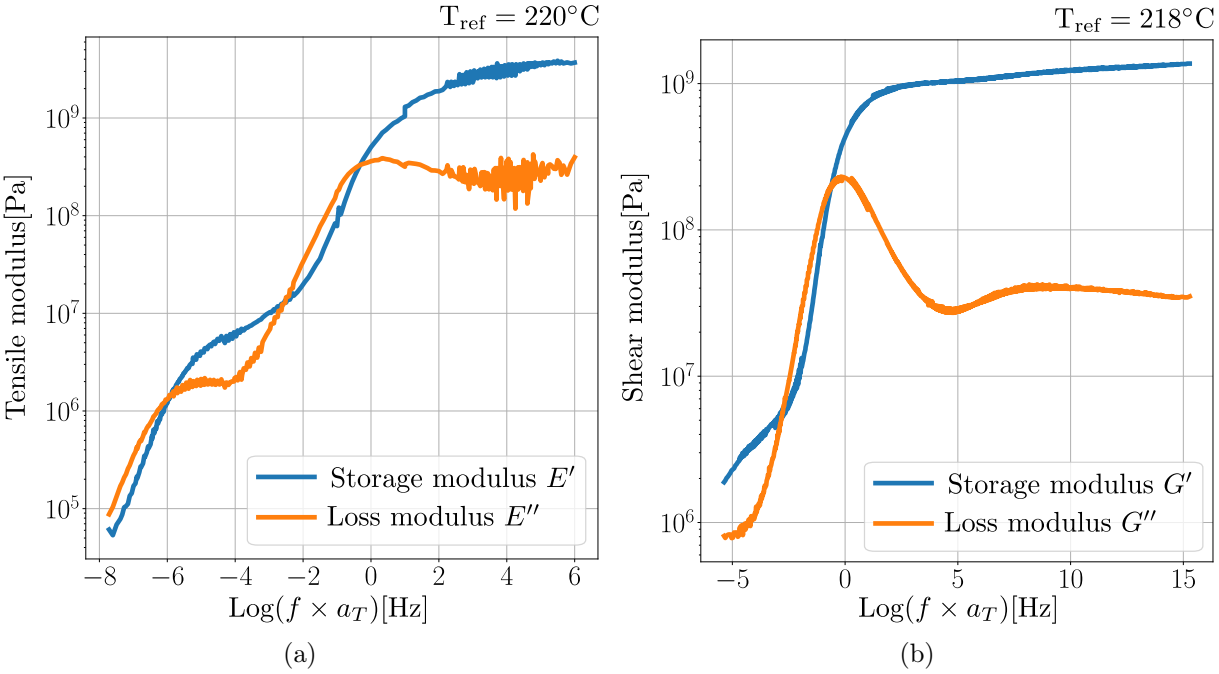

Figure 2.6: PEI master curves in dynamic tensile **(a)** and in rectangular torsion **(b)**.

test allows studying the polymer behavior in rubbery and liquid state (i.e., at high temperature an analogy of low frequency) while the rectangular torsion test allows a good signal-to-noise in glassy state (i.e., at low temperature an analogy of high frequency). Therefore, depending on the measurement geometry, the accessible temperature ranges for shift factors are not the same.

From the construction of these master curves using TTS principle, shift factors a_T has been extracted. Fig. 2.7 reports, as a function of temperature, the logarithm of shift factors obtained for both dynamic tensile test and rectangular torsion test.

These data can be divided into three temperature ranges corresponding to different temperature dependencies: [30 ; 70] °C, [100 ; 180] °C and [220 ; 300] °C (i.e., above T_α).

Below α relaxation, temperature dependency of shift factors a_T were fitted by an Arrhenius law as following:

$$\log(a_T(T, T_{ref})) = \frac{E_a(T)}{R\ln(10)}\left(\frac{1}{T} - \frac{1}{T_{ref}}\right) \tag{2.2}$$

Where E_a is the relaxation activation energy (J.mol^{-1}) and R the universal gas constant (J.K^{-1}.mol^{-1}). In Fig. 2.7 a graphical representation for Arrhenius equations is presented for both tensile and shear DMA experiments, with numerical values reported in Table 2.3.

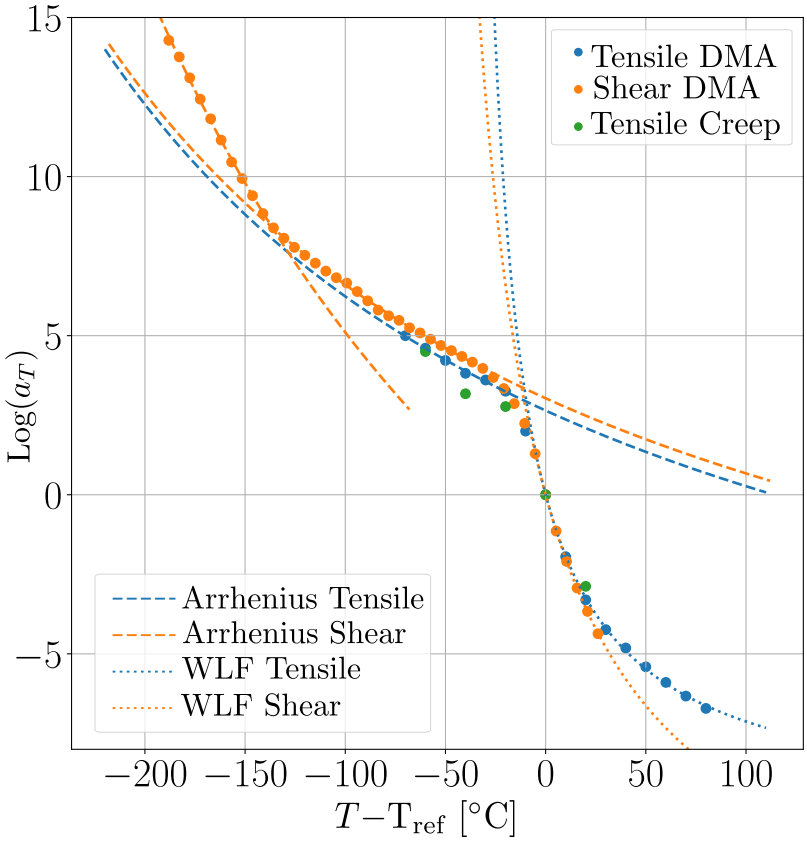

Figure 2.7: Temperature dependency of PEI $\log(a_T)$ in creep and DMA experiments. Dashed lines represent WLF fit of data for $T > T_g$.

Above α relaxation, WLF (Williams-Landel-Ferry) equation was used to describe the temperature dependency of shift factor a_T in rubbery state [37]:

$$\log(a_T(T, T_{ref})) = \frac{-C_1(T - T_{ref})}{C_2 + (T - T_{ref})} \tag{2.3}$$

Where C_1 (unitless) and C_2 (°C) are parameters characteristic of the material, and T_{ref} is the reference temperature used to build master curves. It is possible to link these two parameters to VTF law parameters which describe the temperature dependency of α relaxation time: $C_2 = T_{ref} - T_\infty$ and $\alpha_f = 1/(C_1 C_2)$ [73].

Fit parameters are reported for each temperature ranges and each measurement geometries in Table. 2.3. WLF fit above α relaxation are plotted as well in Fig. 2.7 for each measurement geometries.

In glassy state, a slope break is observed at temperature of 80 °C which corresponds to peak maximum temperature of the β relaxation as observed on DMA thermograms. In rectangular

Table 2.3: Parameters obtained from the fit of $\log(a_T)$ for the different temperature ranges and geometries.

	[30 ; 70] °C	[100 ; 180] °C	[220 ; 300] °C	
	E_a (kJ.mol^{-1})	E_a (kJ.mol^{-1})	C_1	C_2(°C)
Tensile	∅	133	10.2	44
Rectangular torsion	240	131	15.5	67

torsion, the activation energy E_a given by the Arrhenius fit above the slope break is 131 kJ.mol^{-1}. In dynamic tensile test, an activation energy of 133 kJ.mol^{-1} is calculated over this temperature range. In the literature, the activation energy of β relaxation was measured by mechanical at 134 ± 6 kJ.mol^{-1} [71]. This confirms that on this temperature range, the shift factor temperature dependency is controlled by the β molecular motions. Below 80 °C, the fit gives an activation energy of 240 kJ.mol^{-1}. The literature reports a second sub-glass relaxation named γ at about -100 °C and associated with molecular motions due to absorbed water [70]. However, the activation energy of this relaxation was determined by Fontanella *et al.* through Thermally Stimulated Depolarization Current analysis at a value of about 40 kJ.mol^{-1} [74]. Thus, it seems that the PEI behavior on this temperature range is controlled by another process.

In rubbery state, above glass transition manifestation, the shift factor temperature dependency follows a WLF behavior. Fit of both dataset gives quite different values for C_1 and C_2 (Table 2.3). These values are close to the ones given by the WLF model ($C_1 = 17.4$ and $C_2 = 51.6$ °C). In the literature, different values can be found for PEI like: $C_1 = 6.7$ and $C_2 = 46.4$ °C determined by DMA in dynamic tensile [75] or $C_1 = 17.0$ and $C_2 = 37.5$ °C by volume recovery [76]. Concerning dynamic tensile, the reported results are consistent with those reported for the same solicitation geometry by Biddlestone *et al.* in [75]. These results tend to show that shift factors a_T in rubbery state, and their temperature dependency, can be dependent on the experimental technique used to build the master curve. Alves *et al.* [77] reported the same trend, but to a much greater extent, in PMMA between master curves build from DMA or creep tests. The authors explained this behavior by the superposition of α ($T_\alpha \approx 125$ °C) and β ($T_\beta \approx 25$ °C) relaxations of PMMA at the considered temperatures: this superposition depends on the solicitation frequency, therefore, if the characteristic frequency of both techniques is being different, then shift factors discrepancies are observed. This hypothesis could explain the shift factor divergence observed for PEI.

2.3 Thermal analysis

2.3.1 Specific heat determination by Differential Scanning Calorimetry

Differential Scanning Calorimetry (DSC) was used in order to measure the specific heat of PEI as a function of temperature. Measurements were carried out on a DSC 8500 manufactured by PerkinElmer. Samples were analyzed under nitrogen flow during a temperature ramp. During the analysis, the instrument will maintain the reference and the sample at the same temperature by adjusting the oven power (Eq. (2.4)).

$$W = W_{ech} - W_{ref} = \frac{dH}{dt} = q\frac{dH}{dT} = qmC_P \tag{2.4}$$

With W the power difference required to keep the two ovens at the same temperature in W, H the enthalpy (J), q the temperature ramp rate (°C.min^{-1}), m the sample weight (g) and C_P the sample specific heat at constant pressure (J.g^{-1}.K^{-1}).

The specific heat of samples was determined by the sapphire method. It consists of measuring the heat flux in three different configurations: an empty aluminum pan, the same pan containing the sapphire reference and the same pan containing the sample. The sample specific heat $C_{P,sample}$ at a temperature T is then calculated as follows:

$$C_{P,sample}(T) = \frac{H(T)}{h(T)} \times \frac{m_{sapphire}}{m_{sample}} \times C_{P,sapphire}(T) \tag{2.5}$$

With H the heat flow difference between sample and empty pan (W), h the heat flow difference between sapphire and empty pan (W), $m_{sapphire}$ the sapphire weight (g), m_{sample} the sample weight (g) and $C_{P,sapphire}$ the specific heat of sapphire (J.g^{-1}.K^{-1}) calculated using Eq. (2.4). Fig. 2.8 presents the specific heat measured for PEI Ultem 1010 as a function of temperature.

This figure highlights the influence of glass transition on the temperature behavior of specific heat : a specific heat jump, characteristic of this transition, is observed as well as a change in the slope between $C_{P,glass}$ and $C_{P,liquid}$. In order to include this data into the model, the temperature dependence of $C_{P,glass}$ and $C_{P,liquid}$ was described with a linear fit. Theoretically, the temperature behavior of $C_{P,glass}$ is not supposed to be linear [78]. However, over the temperature

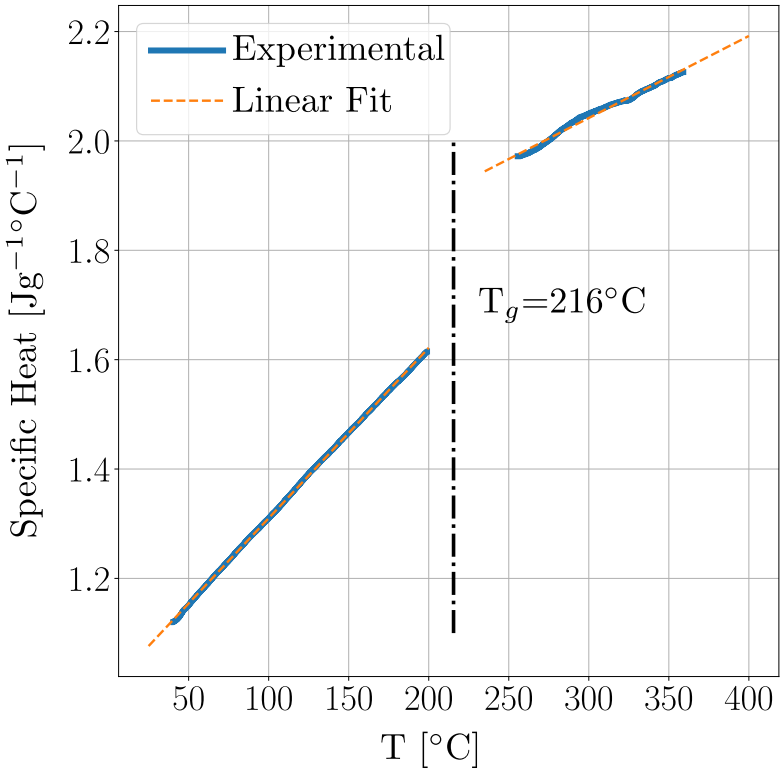

Figure 2.8: Specific heat of PEI ULTEM 1010 as a function of temperature.

range studied, a linear approximation of $C_{P,glass}$ is adequate. The two equations obtained are as follows:

$$C_{P,glass}\ (\mathrm{J.g^{-1}.K^{-1}}) = 0.14 + 3.1 \times 10^{-3}\mathrm{T(K)} \tag{2.6}$$

$$C_{P,liquid}\ (\mathrm{J.g^{-1}.K^{-1}}) = 1.2 + 1.5 \times 10^{-3}\mathrm{T(K)} \tag{2.7}$$

2.3.2 Expansion coefficient

This section is devoted to the observation of free deformations induced by a variation in temperature. This includes the calculation of the isotropic *thermal expansion coefficient*, α. As we discussed in Chapter 1, more precisely Section 1.4, the target mathematical representation of the expansion coefficient is a Prony series and is denoted as *thermal creep function*.

Several problems have been encountered in the performance of isothermal recovery experiments, due to the fact that the specimens used for such experiments exhibit a violent response when heated due to the relaxation of internal stresses generated during injection molding, and it

was also observed the appearance of an additional phase made of bubbles in consequence of outgassing. The experiments were not carried out by the partners of our project, but by an external contractor, and due to budget limitations, further research on this matter was not possible.

In the absence of reliable data, we then performed dilatation experiments using image correlation for samples subjected to slow cooling ($\dot{\theta} = -0.05°\text{C}s^{-1}$) from 225°C to 100°C. In fact, we also observed inconsistencies of volume variation during the heating of the sample with unexpected contractions presented during the glass transition and is why the measurements of the coefficient of expansion were finally carried out during the cooling and which associated coefficient of expansion values are consistent with those given by commercial suppliers and shown in table 2.1. Below, in Fig. 2.9 the outputs of these experiments are presented.

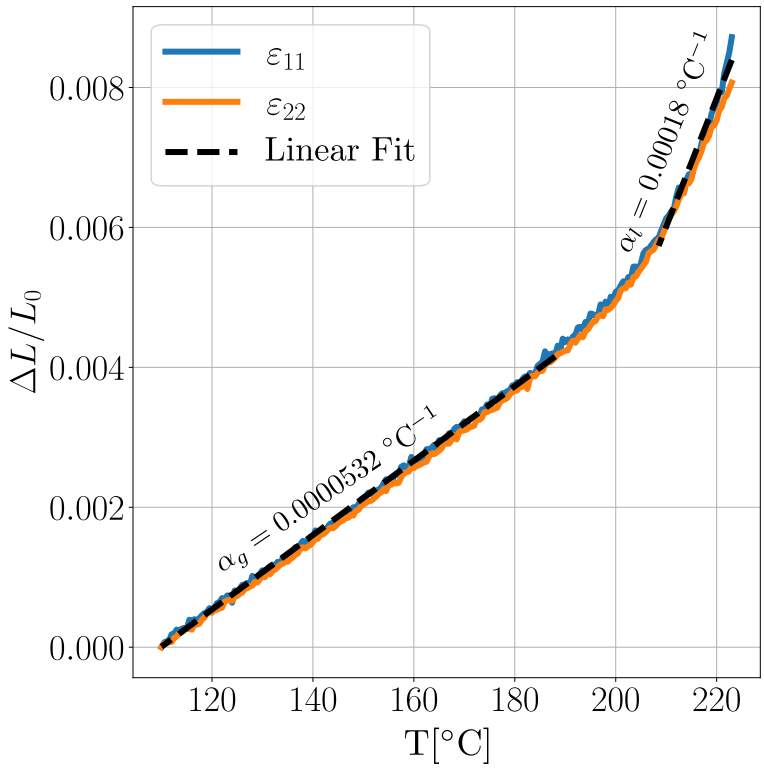

Figure 2.9: Isotropic dilatation coefficient measured at constant linear cooling $-0.5°\text{C}s^{-1}$.

Looking at this figure, we can see how the isotropic nature of the thermal expansion is verified, with the axial and transverse contractions being almost superposed. The low temperature thermal expansion coefficient, $\alpha_g = 5.32 \times 10^{-5}\text{mm/mm/°C}$ matches almost exactly with values given in the table at the first of this chapter. The increase in temperature causes an increase of the molecular motions of the polymer chains favoring the dilatation of the amorphous phase of the polymer sample, therefore an increase of the measured dilatation coefficient is observed [79].

The computed value of the high temperature thermal expansion coefficient, $\alpha_l = 1.83 \times 10^{-4}$ mm/mm/°C is consistent with the latter affirmation. We were then able to give a reliable estimation of the asymptotic values of our isotropic thermal creep function in the absence of a proper estimate of its spectrum.

2.4 Data analysis and identification

This section aims to the identification of the material parameters characterizing the thermo-viscoelastic response of the chosen material. As it was already mentioned, due to the fact that the material is isotropic, only two moduli are enough to build the fourth order thermo-viscoelastic tensor. Therefore, the redundancy in the number of identified moduli allows having an additional confirmation about the representativity of the measured data. Furthermore, the measures reported in this work are compared with data from literature and industry suppliers.

2.4.1 DMA data

The numerical procedure implemented for the approximation of discrete viscoelastic spectra is the one proposed in [7]. This framework corresponds to the Krein Nudelman method [80] combined with the Honerkamp and Weese method [81], that was introduced in [7] for the identification of viscoelastic parameters given frequency domain data. The highlight of this methodology is that it allows the approximation of the time spectra as a part of the numerical implementation, rather than imposing arbitrary distributions as is done in classical collocation methods.

As can be seen from the figures showing the DMA-data (i.e., Fig. 2.6a, Fig. 2.6b) the signals obtained from experiments are noisy, which is not suitable for the identification procedure. To overcome this, two smoothing steps are implemented: i) on the raw data, a procedure of locally estimated scatterplot smoothing is implemented (or Savitzky-Golay filter). ii) The filtered data is resampled using Hermitian interpolation of the first order to avoid local outliers and to limit the number of data points in the identification step. The outputs of the preprocessing step are shown in Fig. 2.10.

As can be inferred, the ideal case to effectively denoise the data is to know a priori the nature of the noise, unfortunately this task was not achieved during the experimental campaign, and the lack of sufficient redundancy in the experimental data make it a hard task to identify a

good candidate for the noise representation. The decision was then made to perform this local filter represented by a conjunction of the moving average technique with polynomial regression, allowing a progressive smoothing based on a local moving neighborhood. As we can see from this figure, the filter seems to smooth the curves properly, but since the nature of the noise is not known, it is not possible to say that the desired phenomenon we want to observe is now the only one present in the processed data. In fact, it is possible that a part of the real expected data is lost due to this arbitrary filter, lying in the outliers and in the smoothness.

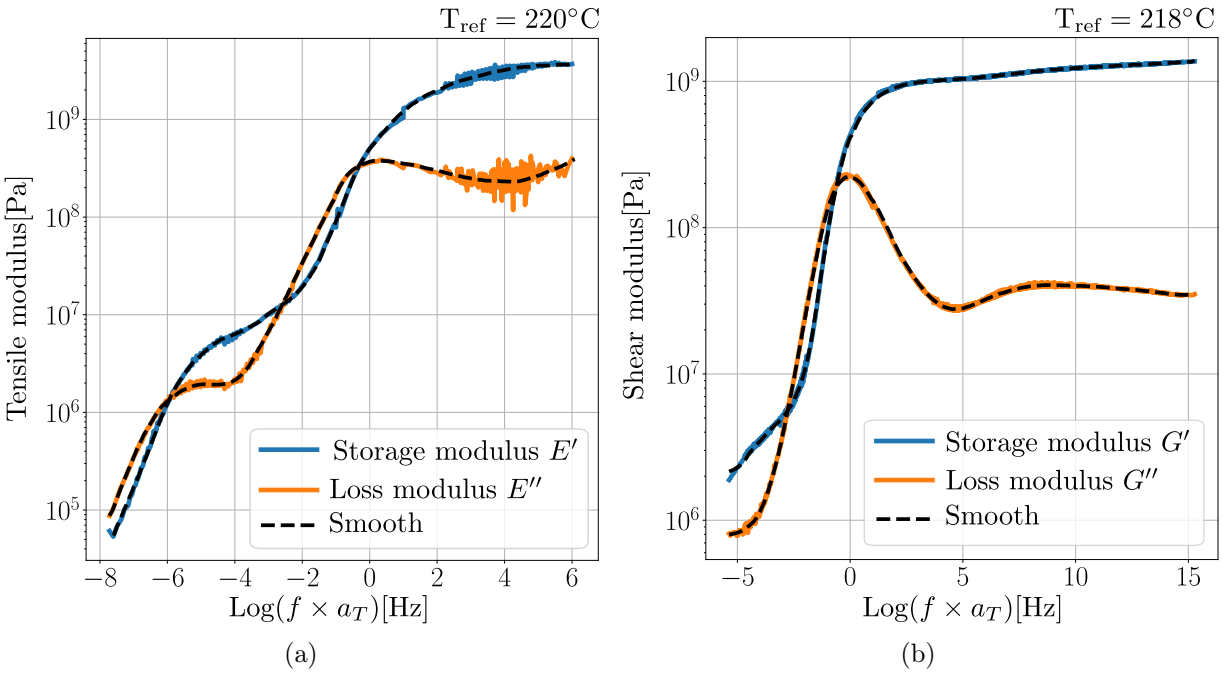

Figure 2.10: Filtered data for dynamic tensile test **(a)** and rectangular torsion test **(b)**.

Regarding the identification step, which outputs are shown in Fig. 2.11, the estimated coefficients are good enough to capture the storage moduli for both, tensile and shear moduli, but not good enough to characterize the dissipation (i.e., loss moduli). As mentioned in [7], the identification methodology exhibits a remarkable behavior when not noisy data are entered, this was confirmed in [4, 6], where artificial data were feeding the application examples, in those cases, the methodology was able to approximate the coefficients of the macroscopic effective response with a negligible associated error, which is not the case here. The latter can be observed when comparing the fitted behavior of the tensile and torsion tests; the noise on the first is more important, this makes it more difficult to reliably identify the coefficients associated with the actual behavior covered by the noise, therefore, the nature of the filter applied could suggest

that its output erases part of the true behavior. The fitted coefficients can be found in C.1.

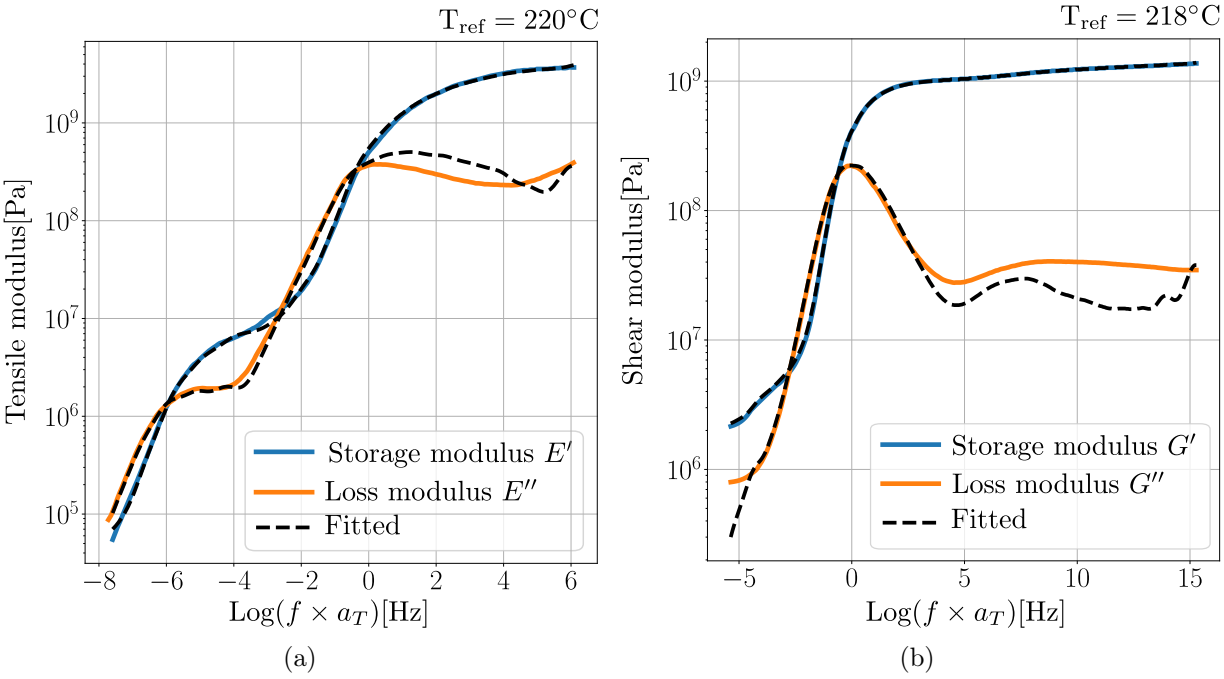

Figure 2.11: Fitted data for dynamic tensile test **(a)** and rectangular torsion test **(b)**.

2.5 Final comments

The identified moduli appear to be consistent with observed data in similar measurements from industry, pertinent sources were presented within the content of the present chapter. Concerning the dilatation experiments and the compressibility and dilatation spectra, the lack of consistency from experimental observations that were indeed very limited in terms of sampling did not allow identifying the proper coefficients associated to the corresponding Prony series. To fulfill the identification task for the experimental validation in Chapter 6 further assumptions were considered to shape the evolution of the missing spectra.

Chapter 3

Preamble to the problem of homogenization in mechanics of composites materials

In this part, we aim to give to the reader a global idea behind the notion of homogenization in mechanics of materials in order to facilitate the understanding of the formulations as well as the intuition from which it derives. Recall that, as we have already said during the introduction and previous chapters, the strategy here is to test this effective medium theory on the approximation of the macroscopic response of a 3D printed part. The following content is inspired by [1] mixed with our own taste.

3.1 Brief history

The foundations of homogenization can be traced back to the early 1900s, with the works of pioneering scientists such as Albert Einstein [82] and Marian Smoluchowski [83], who made fundamental contributions to the understanding of the effective properties of heterogeneous materials while trying to give a consistent definition around the theory of Brownian motion (sounds fun this, as we use this theory as support for the definition of the internal time inside the polymer). To give a bit more about how this papers contribute to the idea of homogenization, let's talk a little bit about Einsteins works. The main goal of this early work was to demonstrate that

bodies in suspensions perform motions as a consequence of thermal molecular motions (related to Brownian motion). The contribution to heterogeneous materials domain is then given by his way of defining locally the osmotic pressure, by introducing a subset of a sample volume limited by a semi-permeable membrane and, in which the dissolve substance is represented by the solvent within a group of suspended spheres that can not cross the membrane arguing that it was difficult for him to not think that from the molecular kinetics theory point of view an "invisible" particle field should produce osmotic pressure in the same way as the visible one. From this starting idea he was able to obtain a macroscopic definition of the diffusion coefficient (for him D) for a collection of suspended non-interacting bodies, proving that at great dilutions the ideas of dissolved and suspended particles are superposed.

With Einstein at the core of all the knowledge we've used in this thesis, let's move on to the hall of stars of homogenization of solid composites. First, in the period between the 60s and 80s, the homogenization technique gained significant momentum during this period, with contributions from researchers such as **John D. Eshelby** [84], the father of the modern homogenization techniques in mechanical engineering and his famous works on the inhomogeneous ellipsoidal inclusion merged into an unbounded infinite body, the well known dilute approximation. Rodney Hill [85] another pioneer of these techniques, we actually use his anisotropic basis to represent the effective behavior at the microscale, and he was one of the first aiming to generalize the effective properties up to any arbitrary concentration of the inclusions. Zvi Hashin (who introduced the concept of "concentration/localization tensor") and Shmuel Shtrikman [86, 87], who defined the variational bounds of the homogenization problems for linear elastic materials. And finally we should include Erwin Kröner [88] for the formulation of the statistical theory of heterogeneous materials contributing to the understanding of the concept of effective properties in heterogeneous media; most of his works in this field are referred to within his lectures at CISM (Centre International des Sciences Mécaniques in Udine, Italy, 1971).

The period between the 80s to the first decade of the century is characterized by a considerable improvement of the computing capabilities of computer systems. This advances in computational power and numerical methods during this period led to the development of computational micromechanics, which focused on modeling the local response of materials at the microscale level. John R. Willis's work on variational principles for the homogenization of heterogeneous materials [89, 90] and his studies on the mechanics of random media [91] made important contributions to

this field. Pierre Suquet's work on homogenization techniques for inelastic materials [92]. And finally, the development of the "variational asymptotic method" by Sanchez-Palencia and his co-workers [93]. Furthermore, Bensoussan, Lions, and Papanicolaou introduced the homogenization theory for partial differential equations, giving a formal statement to the theory of effective medium. For now this is enough history, more details will be given during the application of the homogenization theory in the context of the present thesis.

3.2 Formulation

Let's start by considering again Fig. 2. From the previous content and the figure itself, we already know that this is a composite material in which we have identified two scales (*microscale* and *mesoscale*) of heterogeneity as being the reference scales from which the macroscopic behavior should be estimated. To illustrate the generalities of a homogenization procedure, let's take just the transition from the *microscale* to the *mesoscale*, which in other words is: to find a continuous equivalent of the composite filament.

In general, to ensure the applicability of the homogenization theory, we must ensure the separation of the scales considered characterizing the heterogeneous medium; this is: the size of the local volume at which we observe the heterogeneity must be greater than the size of the heterogeneity itself (i.e., the size of the local volume must be large enough to contain as much as heterogeneities as needed for the description of the observed scale) and moreover the size of the total volume must be considerable larger and able to contain multiple local volumes (i.e., multiple representative elementary volumes or REVs).

We can divide the homogenization methodology into two steps: i) The representation step: in which the choice of the REV is made as the unit containing the material, geometrical and statistical information describing the observed scale, for example in our example case, this should be a volume containing enough fibers spatially distributed in a way that is representative of the whole volume in terms of their microstructural parameters (for instance, length and orientation distributions). This REV will be used to solve the homogenization problem. ii) The homogenization, starting by the localization, where modeling choices are made taking into account the microstructure and the expected behavior to relate microscopic fluctuant fields and their homogeneous correspondent counterparts, this is a difficult and critical task as this step must consider

the statistical description of the heterogeneous body (i.e., its spatial distribution) for some observable variables, such as the second order strain tensor $\boldsymbol{\varepsilon}$ and second order stress tensor $\boldsymbol{\sigma}$. Finally, following the localization, the effective behavior is computed, this gives the explicit analytical forms of the homogenized (or effective) medium in the case of mean-field homogenization, or numerical values associated to it, in the case of full-field homogenization techniques.

Effective behavior

Assuming that the first step is fulfilled, we now proceed to describe the mathematical formulation of the homogenization step. To do so, let's start by considering the macroscopic effective medium that we sought to be continuous, noting that, for the following forms, the linear thermoelastic case is considered and in this case the local behavior is: $\sigma(\boldsymbol{x}) = \mathbb{L}(\boldsymbol{x}) \cdot (\boldsymbol{\varepsilon}(\boldsymbol{x}) - \boldsymbol{\alpha}(\boldsymbol{x})\theta(\boldsymbol{x}))$. If this medium is subjected to a macroscopic homogeneous load, for instance $\bar{\boldsymbol{\varepsilon}}$, the mechanical response is expected to be homogeneous too, this is :

$$\bar{\boldsymbol{\sigma}} = \widetilde{\mathbb{L}} \cdot \left(\bar{\boldsymbol{\varepsilon}} - \widetilde{\boldsymbol{\alpha}}\bar{\theta}\right), \tag{3.1}$$

in other words we aim to write the mechanical problem of a heterogeneous body as it is done for the case of a homogeneous one by finding an appropriate explicit form for the fourth order effective elastic tensor $\widetilde{\mathbb{L}}$ (characterizing the effective medium), which by comparison will exhibit an equivalent macroscopic behavior of its counterpart. We now assume that the macroscopically observable fields can be expressed as :

$$\bar{\boldsymbol{\sigma}} = \langle \boldsymbol{\sigma} \rangle = \frac{1}{|\Omega|} \int_{\Omega} \boldsymbol{\sigma}(\boldsymbol{x}) d\Omega, \text{ and } \bar{\boldsymbol{\varepsilon}} = \langle \boldsymbol{\varepsilon} \rangle = \frac{1}{|\Omega|} \int_{\Omega} \boldsymbol{\varepsilon}(\boldsymbol{x}) d\Omega. \tag{3.2}$$

This imposes the macroscopic fields as being, by definition, the volume average (i.e., the spatial average) of the correspondent microscopic fields within a representative elementary volume (Ω). The localization step is achieved by constructing a fourth order localization tensor from a set of test macroscopic homogeneous fields ($\bar{\boldsymbol{\varepsilon}}^0$ or $\bar{\boldsymbol{\sigma}}^0$) by solving the set of correspondent equilibrium problems, for instance (the pure elastic problem):

$$\begin{aligned} &\nabla \cdot \boldsymbol{\sigma}(\boldsymbol{x}) = 0 \text{ and } \boldsymbol{\sigma}(\boldsymbol{x}) = \mathbb{L}(\boldsymbol{x}) \cdot \boldsymbol{\varepsilon}(\boldsymbol{x}) \quad \forall \boldsymbol{x} \in \Omega, \text{ with } \quad \langle \boldsymbol{\varepsilon} \rangle = \bar{\boldsymbol{\varepsilon}}^0, \text{ or,} \\ &\nabla \cdot \boldsymbol{\sigma}(\boldsymbol{x}) = 0 \text{ and } \boldsymbol{\sigma}(\boldsymbol{x}) = \mathbb{L}(\boldsymbol{x}) \cdot \boldsymbol{\varepsilon}(\boldsymbol{x}) \quad \forall \boldsymbol{x} \in \Omega, \text{ with } \quad \langle \boldsymbol{\sigma} \rangle = \bar{\boldsymbol{\sigma}}^0. \end{aligned} \tag{3.3}$$

From the foregoing equation we can see that for the case of linear elasticity, the complementary problems will differ in the choice of the elementary macroscopic fields to impose. Here, when considering such macroscopic quantities, we choose the macroscopic strain field $\bar{\boldsymbol{\varepsilon}}$ as it is related to the macroscopic stiffness instead of the macroscopic stress $\bar{\boldsymbol{\sigma}}$ associated to the computation of the macroscopic compliance, recalling that these two problems are equivalent as the macroscopic stiffness must be equal to the inverse of its correspondent compliance, for the following considerations we will refer to the strain imposed problem.

Choice of the appropriate set of boundary conditions

As the reader can note, the problems in Eq. (3.3) are ill-posed as there are no boundary conditions associated to it. We overcome this by introducing the notion of homogeneous strain field on the boundary ($\partial\Omega$) that is in fact to apply the displacement $\boldsymbol{u}^d = \bar{\boldsymbol{\varepsilon}}^0 \cdot \boldsymbol{x}$, the consistency of such boundary conditions can be verified by considering the expression of the volume average of the strain field $\langle\boldsymbol{\varepsilon}\rangle$:

$$
\begin{aligned}
\langle\boldsymbol{\varepsilon}\rangle &= \frac{1}{|\Omega|}\int_\Omega \boldsymbol{\varepsilon}(\boldsymbol{x})d\Omega = \frac{1}{2|\Omega|}\left[\int_\Omega \left(\nabla\cdot\boldsymbol{u}(\boldsymbol{x}) + \boldsymbol{u}^T(\boldsymbol{x})\cdot\nabla^T\right)d\Omega\right] \\
&= \frac{1}{2|\Omega|}\left[\left(\int_{\partial\Omega}\boldsymbol{u}(\boldsymbol{x})\boldsymbol{n}(\boldsymbol{x})d\partial\Omega\right) + \left(\int_{\partial\Omega}\boldsymbol{n}^T(\boldsymbol{x})\boldsymbol{u}^T(\boldsymbol{x})d\partial\Omega\right)\right] \\
&= \frac{1}{2|\Omega|}\left[\bar{\boldsymbol{\varepsilon}}^0\cdot\left(\int_{\partial\Omega}\boldsymbol{x}\cdot\boldsymbol{n}(\boldsymbol{x})d\partial\Omega\right) + \left(\int_{\partial\Omega}\boldsymbol{n}^T(\boldsymbol{x})\cdot\boldsymbol{x}^T d\partial\Omega\right)\cdot\bar{\boldsymbol{\varepsilon}}^{0T}\right] \\
&= \frac{1}{2|\Omega|}\left[\bar{\boldsymbol{\varepsilon}}^0\cdot\boldsymbol{I}\left(\int_\Omega d\Omega\right) + \left(\int_\Omega d\Omega\right)\boldsymbol{I}\cdot\bar{\boldsymbol{\varepsilon}}^{0T}\right] \\
&= \bar{\boldsymbol{\varepsilon}}^0,
\end{aligned}
\tag{3.4}
$$

with $(.)^T$ representing the transpose. The foregoing expressions are indeed implications of the *Green's theorem* (see [1]). If one aims to solve the homogenization problem by imposing homogeneous stress fields on the boundaries of the REV, this is achieved by applying the stress vector $\boldsymbol{t}^d = \bar{\boldsymbol{\sigma}}^0\cdot\boldsymbol{n}$, with $\boldsymbol{n}$ being the outer normal on $\partial\Omega$. Let's show the consistency of such choice to solve the second problem in Eq. (3.3) similarly as we just have done above, but we will substitute the argument of the integral being $\boldsymbol{\sigma}$, by $\nabla\cdot(\boldsymbol{\sigma}\cdot\boldsymbol{x})$, since $\nabla\cdot(\boldsymbol{\sigma}\cdot\boldsymbol{x}) = (\nabla\cdot\boldsymbol{\sigma})\cdot\boldsymbol{x} + \boldsymbol{\sigma}\cdot(\nabla\cdot\boldsymbol{x}) = \boldsymbol{\sigma}$,

with $\nabla \cdot \boldsymbol{\sigma} = 0$ from Eq. (3.3), and $\nabla \cdot \boldsymbol{x} = \boldsymbol{I}$:

$$\begin{aligned}\langle \boldsymbol{\sigma} \rangle &= \frac{1}{|\Omega|}\int_{\Omega} \boldsymbol{\sigma}(\boldsymbol{x}) d\Omega = \frac{1}{|\Omega|}\int_{\Omega} \nabla \cdot (\boldsymbol{\sigma} \cdot \boldsymbol{x}) d\Omega = \frac{1}{|\Omega|}\int_{\partial\Omega} (\boldsymbol{\sigma} \cdot \boldsymbol{x}) \cdot \boldsymbol{n} d\partial\Omega \\ &= \bar{\boldsymbol{\sigma}}^0 \left(\frac{1}{|\Omega|}\int_{\partial\Omega} \boldsymbol{x} \cdot \boldsymbol{n} d\partial\Omega \right) = \bar{\boldsymbol{\sigma}}^0 \left(\frac{1}{|\Omega|}\int_{\Omega} \nabla \cdot \boldsymbol{x} d\Omega \right) = \bar{\boldsymbol{\sigma}}^0 \left(\frac{1}{|\Omega|}\int_{\Omega} \boldsymbol{I} d\Omega \right) \\ &= \bar{\boldsymbol{\sigma}}^0.\end{aligned} \tag{3.5}$$

We have then demonstrated the pertinence of these homogeneous test fields to remove the ill-posedness of the problems in Eq. (3.3). The other type of consistent boundary conditions are those of the *periodic composites* (often the case when modeling textiles) denoted *periodic boundary conditions*, for which the REV is characterized by a unit cell that is a pattern that is periodically repeated in some particular the directions denoted as directions of the periodicity. In this framework, as a consequence of the periodicity of the local field $\boldsymbol{u}$ can be decomposed in a part derived from a macroscopic homogeneous field and fluctuating part, $\boldsymbol{u} = \bar{\boldsymbol{\varepsilon}}^0 \cdot \boldsymbol{x} + \boldsymbol{u}'$, the associated local strain field is then derived by means of the linearity of the nabla operator with respect to addition, $\boldsymbol{\varepsilon} = \bar{\boldsymbol{\varepsilon}}^0 + \boldsymbol{\varepsilon}(\boldsymbol{u}')$. The macrohomogenity condition by construction forces the fluctuating field $\boldsymbol{\varepsilon}(\boldsymbol{u}')$ to vanish at the observer scale, thus $\langle \boldsymbol{\varepsilon} \rangle = \bar{\boldsymbol{\varepsilon}}^0 + \langle \boldsymbol{\varepsilon}(\boldsymbol{u}') \rangle = \bar{\boldsymbol{\varepsilon}}^0$.

This confirms the applicability of the periodic boundary conditions for solving the homogenization problem for such microstructures. In terms of applications, in the present work we use periodic boundary conditions in Chapter 6 to solve numerically the homogenization problem at the mesoscale (see Fig. 2), the appropriate way of imposing the periodic boundary conditions is not unique, one could think about solving the problem for the composed local field $\boldsymbol{u}$ enforcing locally its periodicity, or instead of this, to solve the problem for the fluctuant part and to globally enforce the mean of $\boldsymbol{u}'$ to vanish in the REV. The introduction of the appropriate choice of the cinematic boundary conditions will be addressed in Chapter 6.

Homogenization

For now, we can rewrite the well-posed form of the homogenization problem for the thermoelastic case :

$$\begin{cases} \nabla \cdot \boldsymbol{\sigma}(\boldsymbol{x}) & = \mathbf{0} & \forall \boldsymbol{x} \in \Omega, \\ \boldsymbol{\sigma}(\boldsymbol{x}) & = \mathbb{L}(\boldsymbol{x}) \cdot (\boldsymbol{\varepsilon}(\boldsymbol{x}) - \boldsymbol{\alpha}(\boldsymbol{x})\theta(\boldsymbol{x})) & \forall \boldsymbol{x} \in \Omega, \\ \boldsymbol{u}(\boldsymbol{x}) & = \bar{\boldsymbol{\varepsilon}}^0 \cdot \boldsymbol{x} & \forall \boldsymbol{x} \in \partial\Omega \\ \theta(\boldsymbol{x}) & = \bar{\theta} & \forall \boldsymbol{x} \in \Omega \end{cases} \tag{3.6}$$

As we can note, the thermoelastic homogenization problem above consider a homogeneous temperature field $\bar{\theta}$ in the REV, the fact that the estimation of effective properties is achieved through the testing macroscopic fields in equilibrated representative elementary volumes, the implications of homogeneous temperature fields on the boundaries is the uniform temperature in each material point. We now introduce $\mathbb{A}(\boldsymbol{x})$ and $\boldsymbol{a}(\boldsymbol{x})$ as the strain localization tensors relating the microscopic and macroscopic strain fields of the thermoelastic problem. By solving all the set of problems associated to the set of appropriate homogeneous test fields $\bar{\boldsymbol{\varepsilon}}^0$, and an arbitrary $\bar{\theta}$, we are able to fill the elements of the fourth order localization tensor $\mathbb{A}(\boldsymbol{x})$ and the second order localization tensor $\boldsymbol{a}(\boldsymbol{x})$, completing the following relation:

$$\boldsymbol{\varepsilon}(\boldsymbol{x}) = \mathbb{A}(\boldsymbol{x}) \cdot \bar{\boldsymbol{\varepsilon}} + \boldsymbol{a}(\boldsymbol{x})\bar{\theta} \tag{3.7}$$

Finally, since we were able to compute the elements in $\mathbb{A}$, the output of the localization step, we can now pass to the estimation of the effective elastic stiffness in our example case, to do so we now take the definition of the macroscopic stress and rewrite it by taking into account the foregoing definition of the local strain $\boldsymbol{\varepsilon}(\boldsymbol{x})$:

$$\begin{aligned} \bar{\boldsymbol{\sigma}} &= \frac{1}{|\Omega|} \int_\Omega \mathbb{L}(\boldsymbol{x}) \cdot \left[\mathbb{A}(\boldsymbol{x}) \cdot \bar{\boldsymbol{\varepsilon}} - (\boldsymbol{\alpha}(\boldsymbol{x}) - \boldsymbol{a}(\boldsymbol{x}))\bar{\theta} \right] d\Omega \\ &= \left(\frac{1}{|\Omega|} \int_\Omega \mathbb{L}(\boldsymbol{x}) \cdot \mathbb{A}(\boldsymbol{x}) d\Omega \right) \cdot \bar{\boldsymbol{\varepsilon}} - \left(\frac{1}{|\Omega|} \int_\Omega \mathbb{L}(\boldsymbol{x}) \cdot (\boldsymbol{\alpha}(\boldsymbol{x}) - \boldsymbol{a}(\boldsymbol{x})) d\Omega \right) \bar{\theta} \\ &= \widetilde{\mathbb{L}} \cdot \bar{\boldsymbol{\varepsilon}} - \widetilde{\mathbb{L}} \cdot \widetilde{\boldsymbol{\alpha}} \bar{\theta}, \end{aligned} \tag{3.8}$$

with $\widetilde{\mathbb{L}}$ and $\widetilde{\boldsymbol{\alpha}}$ being the fourth order effective stiffness tensor and second order of effective thermal dilatation coefficients respectively. As can be observed, the computation of explicit analytical forms of this effective behavior is limited by the knowledge of the explicit forms defining $\mathbb{A}$ and $\boldsymbol{a}$. In fact, most of the widely used localization tensors forms are known for trivial symmetries and trivial behaviors and even though this simple cases are observed it is almost sure that we will need further assumptions to get an analytical form of it as the description of the fluctuations of the microscopic fields represents a difficult task; all of this give us an idea of the level of simplification in such approximations. Nevertheless, in the last 30 years these techniques have being tested extensively in the literature, showing a good agreement when considering engineering applications. This way of formulating the homogenization problem will indeed be the reference for the formulations presented in Chapter 4 where different forms of the localization tensors will be tested in order to compute the effective behavior by means of the expression above. In Chapter 5 the numerical solutions of the homogenization problem will be presented for the case of periodic structures.

Now to obtain an equivalent variational formulation of the homogenization problem in Eq.3.6 let's start by introducing the suitable Sobolev space in which the solution field $\boldsymbol{u}(\boldsymbol{x})$ exists.

$$\mathcal{K} = \left\{ \boldsymbol{u} \text{ regular in } \Omega \text{ and } \boldsymbol{\varepsilon}(\boldsymbol{u}) = 0.5(\nabla \cdot \boldsymbol{u} + \boldsymbol{u}^T \cdot \nabla^T) \quad / \boldsymbol{u} = \bar{\boldsymbol{\varepsilon}} \cdot \boldsymbol{x} \text{ on } \partial\Omega \right\}.$$

The variational form of the homogenization problem is formulated by considering that $\boldsymbol{\sigma}$ derive from a potential (which is ensured in the case of our example), for instance the Helmholtz free energy $w.$ with the effective behavior computed as :

$$\bar{w}(\bar{\boldsymbol{\varepsilon}}, \bar{\theta}) = \inf_{\boldsymbol{u} \in \mathcal{K}(\bar{\boldsymbol{\varepsilon}})} \left\langle w(\boldsymbol{\varepsilon}(\boldsymbol{u}(\boldsymbol{x})), \bar{\theta}) \right\rangle = \frac{1}{2} \bar{\boldsymbol{\varepsilon}} \cdot \widetilde{\mathbb{L}} \cdot \bar{\boldsymbol{\varepsilon}} - \widetilde{\mathbb{L}} \cdot \widetilde{\boldsymbol{\alpha}} \bar{\theta} \cdot \bar{\boldsymbol{\varepsilon}}, \tag{3.9}$$

thus,

$$\bar{\boldsymbol{\sigma}} = \frac{\partial \bar{w}}{\partial \bar{\boldsymbol{\varepsilon}}} = \widetilde{\mathbb{L}} \cdot \bar{\boldsymbol{\varepsilon}} - \widetilde{\mathbb{L}} \cdot \widetilde{\boldsymbol{\alpha}} \bar{\theta}. \tag{3.10}$$

Finally, it is important to note that the effective computed behavior from the above variational formulation is equivalent to the obtained from solving Eq.3.6, exhibiting the difference that by construction the variational forms ensures the symmetry of the fourth order stiffness tensor $\widetilde{\mathbb{L}}$.

To observe the latter in particular, let's take a look at the derived form, that by virtue of the Hill's Lemma [1] takes the following form.

$$\begin{aligned}\bar{w}(\bar{\boldsymbol{\varepsilon}},\bar{\theta}) &= \frac{1}{2}\bar{\boldsymbol{\varepsilon}}\cdot\langle\mathbb{A}^{\mathrm{T}}(\boldsymbol{x})\cdot\mathbb{L}(\boldsymbol{x})\cdot\mathbb{A}(\boldsymbol{x})\rangle\cdot\bar{\boldsymbol{\varepsilon}} - \bar{\theta}\langle\mathbb{L}(\boldsymbol{x})\cdot(\boldsymbol{\alpha}(\boldsymbol{x})-\boldsymbol{a}(\boldsymbol{x}))\cdot\mathbb{A}(\boldsymbol{x})\rangle\cdot\bar{\boldsymbol{\varepsilon}} \\ &= \frac{1}{2}\bar{\boldsymbol{\varepsilon}}\cdot\widetilde{\mathbb{L}}\cdot\bar{\boldsymbol{\varepsilon}} - \widetilde{\mathbb{L}}\cdot\widetilde{\boldsymbol{\alpha}}\bar{\theta}\cdot\bar{\boldsymbol{\varepsilon}}.\end{aligned} \tag{3.11}$$

This last presented form of the homogenization problem will be the starting point of the formulations presented in Chapter 5. For now, this is all we need to move on to the estimation of the residual stresses in our 3D printed part at the scale of the observer. We should recall that, here, when considering multiscale problems we do not solve the problem simultaneously for all the scales considered, our methodology as already mentioned is a two-step homogenization methodology in which the effective behavior computed from lower scales serves as input of the matrix (or continuous phase) of the upper scales.

Mean-field v.s. Full-field

Considering the solution of the problem in Eq. 3.6 we distinguish the two major category of mean-field and full-filed techniques, a distinction made on the nature of the solution, one being purely analytical including a set of complementary assumptions allowing to represent all the elements in the problem in an analytical way, and the second one, which is achieved by solving the problem numerically, by solving the associated set of PDEs in a weak sense and finally giving a numerical approximation that is specific to the characteristics of the computational REV.

Each of these techniques has its own advantages, from one side mean-field techniques are much lighter in cost, since the solution is represented by a set of symbolic expressions of the microstructural parameters, meaning that these expressions can be used in similar situations with some restrictions. The clear limitation of this technique is that we need to find suitable functions for the representation step, judging their pertinence by their closeness to the physical parameter that we are trying to model and the existence of analytical forms to the integrals of the volume averaged quantities.

The second one is much more flexible in terms of representation, since a computational REV covers a much wider range of geometries mapping the heterogeneities, since no analytical representation of the geometry is needed and a discrete map from, for example microphotography

is sufficient to create a computational domain that matches the actual microstructure with a high degree of accuracy. As mentioned before, the cost of these computations is higher compared to their analytical counterparts and the quality of the approximation is a function of the quality of the numerical map and the numerical strategy that we have chosen to solve the homogenization problem in the REV.

In the case of mean-fields, in general we assume that the localization tensors are constant per phase which reduces the computation of the integrals in the second line of Eq. 3.8 to the computation of a finite linear combination which weights are the volume fractions, we can then write the expressions of the effective behavior considering the following decomposition applied to the volume integrals under the assumption of perfect interphases for a REV Ω with $N+1$ phases: $\Omega = \cup_{r=0}^{N}\Omega^{(r)}$, thus, $\int_\Omega f(\boldsymbol{x})d\Omega = \sum_{r=0}^{N}\int_{\Omega^{(r)}} f(\boldsymbol{x})\chi(\boldsymbol{x})^{(r)}d\Omega^{(r)}$, with $\chi(\boldsymbol{x})^{(r)}$ the level set function, being 1 inside the phase $\Omega^{(r)}$ and 0 otherwise.

$$\begin{aligned}\widetilde{\mathbb{L}} &= \frac{1}{|\Omega|}\int_\Omega \mathbb{L}(\boldsymbol{x})\cdot\mathbb{A}(\boldsymbol{x})d\Omega = \sum_{r=0}^{N}\frac{1}{|\Omega|}\int_{\Omega^{(r)}}\mathbb{L}^{(r)}\cdot\mathbb{A}^{(r)}\chi(\boldsymbol{x})^{(r)}d\Omega^{(r)} \\ &= \sum_{r=0}^{N}\frac{1}{|\Omega|}\mathbb{L}^{(r)}\cdot\mathbb{A}^{(r)}\int_{\Omega^{(r)}}\chi(\boldsymbol{x})^{(r)}d\Omega^{(r)} = \sum_{r=0}^{N}\frac{|\Omega^{(r)}|}{|\Omega|}\mathbb{L}^{(r)}\cdot\mathbb{A}^{(r)} = \sum_{r=0}^{N}c^{(r)}\mathbb{L}^{(r)}\cdot\mathbb{A}^{(r)},\end{aligned} \tag{3.12}$$

and,

$$\begin{aligned}\widetilde{\mathbb{L}}\cdot\widetilde{\boldsymbol{\alpha}} &= \frac{1}{|\Omega|}\int_\Omega \mathbb{L}(\boldsymbol{x})\cdot(\boldsymbol{\alpha}(\boldsymbol{x})-\boldsymbol{a}(\boldsymbol{x}))d\Omega = \frac{1}{|\Omega|}\sum_{r=0}^{N}\int_{\Omega^{(r)}}\mathbb{L}^{(r)}\cdot(\boldsymbol{\alpha}^{(r)}-\boldsymbol{a}^{(r)})\chi(\boldsymbol{x})^{(r)}d\Omega \\ &= \frac{1}{|\Omega|}\sum_{r=0}^{N}\mathbb{L}^{(r)}\cdot(\boldsymbol{\alpha}^{(r)}-\boldsymbol{a}^{(r)})\int_{\Omega^{(r)}}\chi(\boldsymbol{x})^{(r)}d\Omega = \sum_{r=0}^{N}c^{(r)}\mathbb{L}^{(r)}\cdot(\boldsymbol{\alpha}^{(r)}-\boldsymbol{a}^{(r)}),\end{aligned} \tag{3.13}$$

with $c^{(r)}$ being the volume fraction of the phase $\Omega^{(r)}$.

As mentioned above, the computation of the effective behavior by means of full-field technique implies the computation of the numerical solution of the homogenization problem, which no longer need the restriction of homogeneous per phase localization tensors to compute the effective behavior. The full-field solution of the homogenization problem gives a numerical approximation of the local field $\boldsymbol{u}(\boldsymbol{x}) \in \mathcal{K}(\bar{\boldsymbol{\varepsilon}})$ in solving the weak form associated to Eq. 3.8; the local strain and stress fields, $\boldsymbol{\varepsilon}(\boldsymbol{u})$ and $\boldsymbol{\sigma}(\boldsymbol{u})$, are then computed as a post-processing step. Let's take a look

at the expression of the average stress $\bar{\boldsymbol{\sigma}}$ in this case :

$$\begin{aligned}
\bar{\sigma} &= \frac{1}{|\Omega|}\int_{\Omega}\boldsymbol{\sigma}(\boldsymbol{u}(\boldsymbol{x}))d\Omega = \frac{1}{|\Omega|}\sum_{r=0}^{N}\int_{\Omega^{(r)}}\mathbb{L}^{(r)}\cdot\left(\boldsymbol{\varepsilon}(\boldsymbol{u}(\boldsymbol{x})) - \boldsymbol{\alpha}^{(r)}\bar{\theta}\right)d\Omega \\
&= \frac{1}{|\Omega|}\sum_{r=0}^{N}\mathbb{L}^{(r)}\cdot\int_{\Omega^{(r)}}\boldsymbol{\varepsilon}(\boldsymbol{u}(\boldsymbol{x}))d\Omega - \sum_{r=0}^{N}c^{(r)}\mathbb{L}^{(r)}\cdot\boldsymbol{\alpha}^{(r)}\bar{\theta} \\
&= \sum_{r=0}^{N}\mathbb{L}^{(r)}\cdot\left[\left(\frac{1}{|\Omega|}\int_{\Omega^{(r)}}\mathbb{A}(\boldsymbol{x})d\Omega\right)\cdot\bar{\boldsymbol{\varepsilon}} + \left(\frac{1}{|\Omega|}\int_{\Omega^{(r)}}\boldsymbol{a}(\boldsymbol{x})d\Omega\right)\bar{\theta}\right] - \sum_{r=0}^{N}c^{(r)}\mathbb{L}^{(r)}\cdot\boldsymbol{\alpha}^{(r)}\bar{\theta} \\
&= \sum_{r=0}^{N}\mathbb{L}^{(r)}\cdot\langle\mathbb{A}\rangle^{(r)}\cdot\bar{\boldsymbol{\varepsilon}} - \sum_{r=0}^{N}\mathbb{L}^{(r)}\cdot\left(c^{(r)}\boldsymbol{\alpha}^{(r)} - \langle\boldsymbol{a}\rangle^{(r)}\right)\bar{\theta} = \widetilde{\mathbb{L}}\cdot\bar{\boldsymbol{\varepsilon}} - \widetilde{\mathbb{L}}\cdot\widetilde{\boldsymbol{\alpha}}\bar{\theta}.
\end{aligned} \tag{3.14}$$

From above, as we mentioned, the computed localization tensors for the phase $\Omega^{(r)}$ with no prior restrictions are in fact the approximation of the volume average of the localization tensor in that phase and noted $\langle(\cdot)\rangle^{(r)}$. We will use this technique to solve the homogenization problem at the mesoscale (see Chapter 6).

The thermo-viscoelastic homogenization problem

As it was presented in the previous chapters, since the printed material is a polymer composite, its mathematical representation is a function of the time and the temperature, which is an implicit function of time itself. The homogenization problem for this case reads :

$$\begin{cases}
\nabla\cdot\ \boldsymbol{\sigma}(\boldsymbol{x},\bar{\theta},t) & = \mathbf{0} & \forall\boldsymbol{x}\in\Omega, \\
\boldsymbol{\sigma}(\boldsymbol{x},\bar{\theta},t) & = \left[\mathbb{L}^{(r)}\circledast\left(\boldsymbol{\varepsilon}(\boldsymbol{x},\cdot) - \boldsymbol{\beta}^{(r)}(\bar{\theta},\cdot)\right)\right](t) & \forall\boldsymbol{x}\in\Omega^{(r)}, \\
\boldsymbol{\beta}^{(r)}(t) & = \left[\boldsymbol{\alpha}^{(r)}(\bar{\theta},\cdot)\circledast\bar{\theta}\right](t), & \\
\langle\boldsymbol{\varepsilon}(\boldsymbol{x},t)\rangle & = \bar{\boldsymbol{\varepsilon}}(t), &
\end{cases} \tag{3.15}$$

This is the starting point for the following chapters devoted to the estimation of the effective behavior. This concludes the discussion in this preamble. In the newt chapter, we will solve this problem for the case of a single polymer composite (SPC) where the polymer phase is modeled using the extension of the internal time technique for continuous variations of temperature (see 1.2.2) which allows using the correspondence principle in this context [4].

Chapter 4

Microscale Analysis : thermorheologically simple material

This chapter is devoted to the estimation of the effective behavior of the fiber-reinforced filament, and it is already published in the *European journal of Mechanics - A/Solids* [4]. To adresse this task a consistent artificial material law inspired on the PEI is used. The effective behavior at this scale is computed analytically by considering the extension of the correspondence principle to continuous variations of temperature, allowing an straighforward implementation of the wide developped mean-field analytical approximation for lineart thermoelastic materials.

The scale characterizing the heterogeneity of the reinforced thermoplastic filament is the scale of glass fibers (around 100 μm length and 10 μm diameter) and is much lower than the scale of the printed part (the composite structure of the PEI filament reinforced with glass fibers is observed by means of three-dimensional computerized tomography scans (CT-scans) as shown in Fig. 4.1). As we were mentioning before, due to this separation of scales it is no longer possible to use conventional codes based on the finite element method to take into account the effect of the reinforcement on the behavior of the printed composite filament inside the part, as it becomes too expensive to predict. During the introduction, we pointed out that there are several works proposing multiple analytical and numerical alternatives to deal with this computation (see for instance [3, 2, 1]). The macroscopic behavior can be given as a result of numerical simulations in the case of full-field methods (see for instance [94, 95, 96, 97, 98]). In case of

complex microstructures (meaning by complex the fact that there is not an optimal analytical representation of the heterogeneity shape), the estimates given by the mean field methods are no longer accurate and require numerical calculations to be approximated (see [99] and [100] in the case of poly-crystals). Full-field methods can handle a lot of complexities not only in geometry but in constitutive laws describing their behavior (non-linearity, plasticity, aging. . .), the problem is that they only give the response of the composite for a particular loading path. This requires a large amount of computations on many REVs (Representative Elementary Volume) with different distributions of inclusions to get an appropriate estimation of the effective behavior.

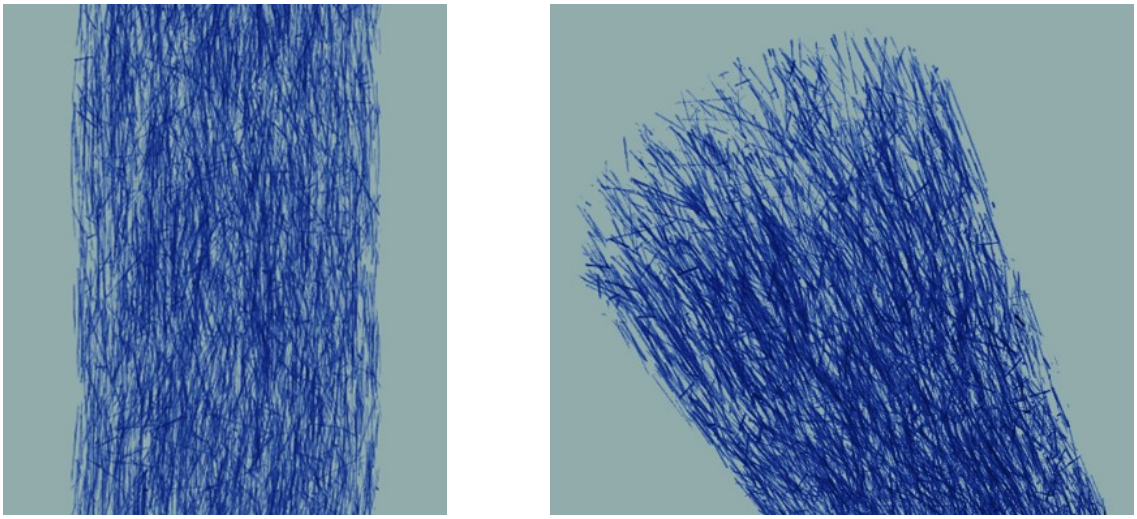

(a) lateral view (b) sectional view

Figure 4.1: 3D reconstruction of CT-scans acquisitions performed on the PEI FDM glass fiber reinforced filament with a volume fraction of 10%. The scanning step used an X-ray source with a voxel size of 2.67 μm, a voltage of 150 kv and a current of 18 µA. The imager has a resolution of 1920 $\times$ 1536 pixels. The device used is an EasyTom XL Ultra 150/160 (µCT) produced by RX Solution. The pictures describe the volume rendering of fibers embedded in the PEI matrix.

Considering that previous works in fibrous composites homogenization have shown that the analytical representation of fibers as prolate spheroids is a good approximation of the finite cylinder-like shape of the fiber, we follow this fashion choosing as target framework the *Mean-field homogenization* methodology (see among others [84, 101, 102, 103, 104, 105, 106]) intending an extension of the classical well described methodologies for the case of linear thermo-viscoelastic theory. In linear viscoelasticity framework, by using the correspondence principle, several authors like [107] or [60] among others, find some estimates in closed form for the macroscopic behavior of isotropic composites with microstructures following the Hashin-Shtrikman lower bound. Gupta et al. [108] has investigated a Mori-Tanaka (MT) approach to predict the elastic effective properties

of a 3D-printed composite material, assuming that the matrix (thermoplastic polymer) and fibers (carbon fiber) are linearly elastic and homogeneous, to predict the elastic effective properties of 3D-printed composite material. Hessman et al. [109] has confronted different mean field homogenization schemes to predict elastic effective properties for short fiber reinforced composites using a fiber length distribution and an orientation distribution in Advani and Tucker form [110]. The authors show that reasonable predictions for effective elastic properties are possible even with limited microstructural information. Muliana [111] has proposed a micromechanical model to predict thermal properties and thermo-viscoelastic response of a functionally graded material idealized as solid spherical particles spatially distributed in a homogeneous matrix. Both constituents are considered thermo-viscoelastic. Although mean-field approximations are more difficult to obtain for complex constituents behaviors, certain non-linearities exhibited by polymer matrices can be accounted for, see the case of an elastoplastic matrix in [112, 113].

Then here we propose to predict the residual thermal internal stresses during the cooling of this HT-FRAM 3D-printed composite filament by means of mean field homogenization technique and correspondence principle to estimate the effective behavior of a thermo-viscoelastic amorphous polymer matrix (PEI) reinforced with a transverse isotropic distribution of the elastic inclusions (short Glass Fibers (GF)) for us, the microscale. Because of some limitations during the experimental campaign, the results that we will be presenting here are obtained from a polymer matrix that is artificial but which behavior preserves the mathematical structure of the property model, more details about the precise coefficients will be given in the following section, recalling that from Chapter 2, the matrix in which the short glass fibers are embedded is an amorphous polymer assumed to belong to the group of thermorhelogically simple materials [54]. The polymer follows the time temperature superposition principle (TTS) [55] and the material functions describing its behavior are presented using the notion of "internal time" [45, 43]. The PEI-like matrix thermo-viscoelastic model parameters are identified (and some of them estimated) with the experimental data taken from the precedent section and data-sheet from SABIC [114]. In Section 4.2, the procedure to perform mean-field homogenization in *single polymer composite* (SPC) with elastic fibrous reinforcements is presented. Probabilistic description of the Representative Elementary Volume (REV) and supplementary identification step to ensure the same mathematical structure for the matrix and the composite are presented as well. In Section 4.3, first, the internal variables' approach to rewrite the local thermo-viscoelastic

problem is given, as well as its incremental scheme to update the residual stress. Three different scenarios are considered to compare the accuracy of the presented mean-field homogenization procedure with respect to Fast Fourier Transform (FFT) based full-field homogenization simulations. The reference solutions are computed using REVs that are statistically equivalent to the distribution parameters chosen for the microstructure iterations that are used in the mean-field computations. Convergence studies for the reference solutions are presented as well. Finally, a comparative analysis is performed for each scenario.

4.1 Amorphous polymer matrix behavior

Now let's take a look at the thermo-viscoelastic model used to describe the behavior of the PEI-like amorphous polymer, recalling that as it was told during the introduction, the advances of the work in terms of its particular goals were not completed sequentially, and for the analysis of the reinforced filament we were able to get reliable data just for the shear behavior and its correspondent shift function. The PEI-like model's parameters are then complemented by using data given by the material supplier SABIC [114], and other supplementary assumptions to circumvent the lack of experimental data. Numerical values are given in C.2, correspondent to the material constitutive models presented in Eq. (1.9) and Eq. (1.10). As we start discussing at the end of the Chapter 1, we impose shared characteristic times for the viscoelastic spectra in $\mathbb{L}$ and can be noted in Figure.4.2a in which we can observe the moduli $\kappa^{(u)}$ and $\mu^{(u)}$ for the different relaxation times $\tau_L^{(u)}$. Fig. 4.2b shows the evolution of the relaxation moduli κ and μ, with respect to time at the reference temperature, the *master curves* of the isotropic relaxation moduli.

The explicit form of the shift factor function a_T for polymers varies in literature with the range of temperature of the observed material [62]. The most widely used formulations are the WLF (Williams-Landel-Ferry [57]) that we have used previously in the experiments and commonly used for temperatures above the glass transition, the VFTH (Vogel-Fulcher-Tamman-Hesse) equation, and the Arrhenius equation for terminal flow [62] that we've implemented as well. In view of the experimental results available on PEI matrix of the 3D-printed filament, it was found that, the best one is the model VFTH as we can conserve the same mathematical structure and define a shift function that have discontinuous coefficients which evolution is a step

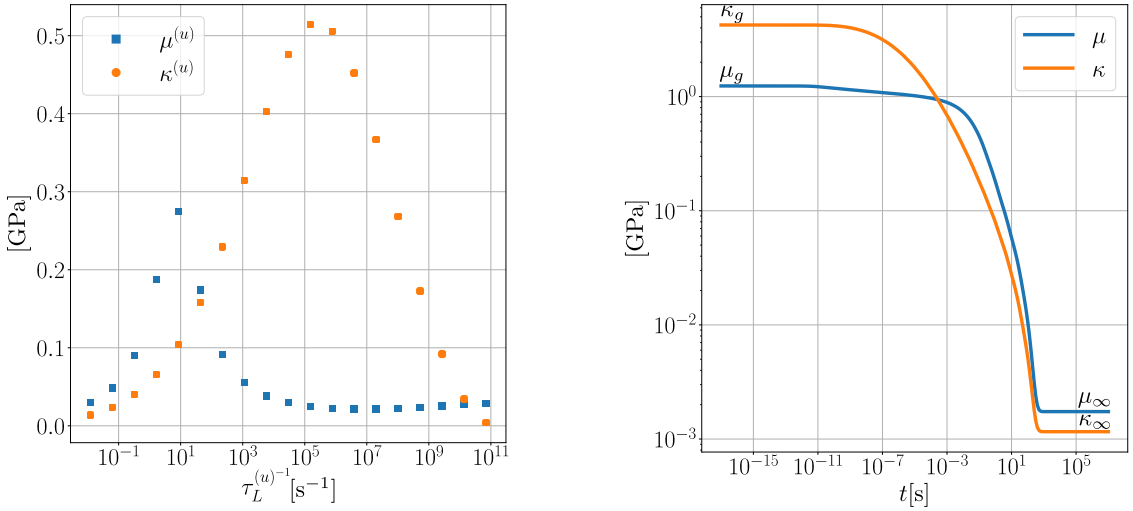

(a) Moduli distributions with shared times.

(b) Relaxation moduli vs. time.

Figure 4.2: Relaxation spectra characterizing the linear viscoelastic behavior of a PEI-like polymer matrix used in the present work.

function with zero on the "split" temperature value T_s chosen to improve the numerical accuracy of the approximation, the form of the a_T function is then:

$$\log_{10} a_T(T, \mathrm{T}_r) = a + \frac{b}{c + (T - T_r)}, \tag{4.1}$$

with a, b and c, three material parameters. This function is implemented in the whole characteristic range of temperature with piecewise constant coefficients (with T_s characterizing the discontinuity) from either side of the glass transition temperature $T_\mathrm{g} = T_\mathrm{r} = 216°\mathrm{C}$, which give the evolution plotted on Fig. 4.3a. Numerical values of the material parameters are shown in Table. 4.1.

Table 4.1: Piece-wise constant coefficients of the VFTH function

T_s=205.099	T<T_s	T>T_s
a	-3.58611	-17.0449
b	1882.297	1129.382
c	288.3494	66.36251

In Fig. 4.3b, the above-mentioned shift factor is used to show an example of the TTS principle on the compressibility relaxation modulus. In Fig. 4.4, examples of internal time and computed matrix' artificial material thermal isotropic dilatation are shown for various linear

cooling histories. To close this section, we can say that at this point of the formulation as we have ensured the applicability of the correspondance principle in the context of continuous variations of temperature for thermorheologically simple polymers (see : Section 1.2.3), the applicability of the mean-field homogenization methods as it is performed in [**Hashin65** , 60] is also ensured, we can now pass to show the methodology followed to obtain the effective thermo-viscoelastic behavior of the composite filament.

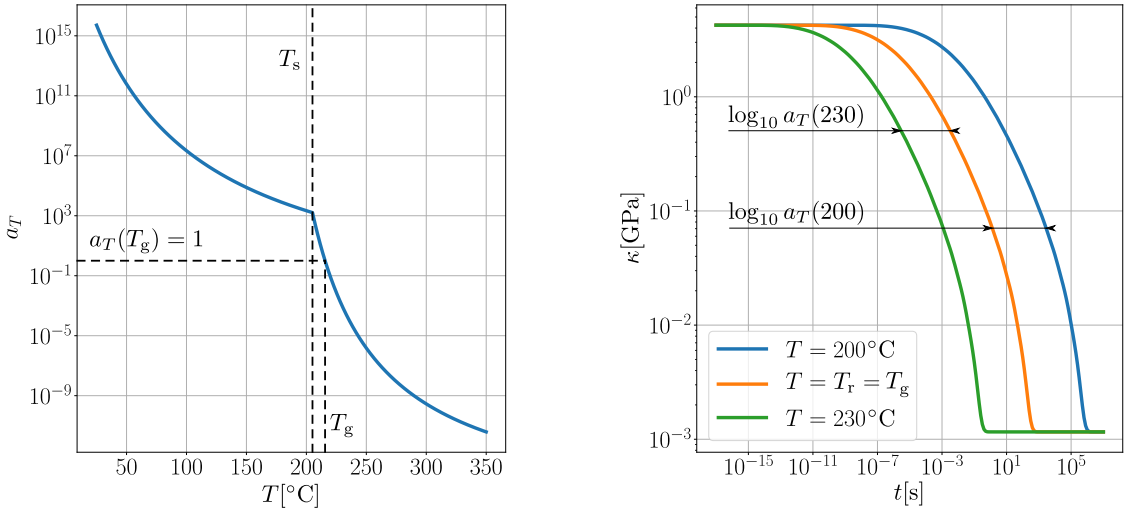

(a) VFTH shift function with piecewise constant coefficients.

(b) Time-temperature superposition in compressibility modulus.

Figure 4.3: Time temperature superposition principle for the PEI-like matrix.

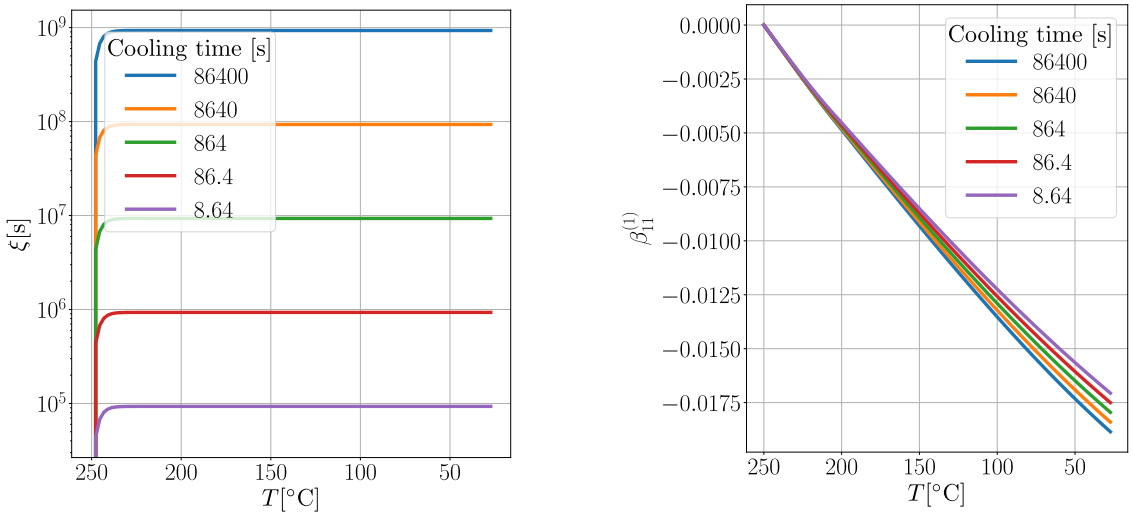

(a) ξ vs. T.

(b) matrix' thermal strain $\beta_{11}^{(1)}$.

Figure 4.4: Computed internal time and thermal strains of the amorphous polymer matrix, identified with a superscript (1) (i.e. $\{\cdot\}^{(1)}$) for various linear cooling rates.

4.2 Effective thermo-viscoelastic behavior of the reinforced filament

This section presents the mean-field homogenization procedure. The objective is to give an estimation of the macroscopic stress, $\bar{\boldsymbol{\sigma}}$, for given histories of the macroscopic, strain and temperature, $\bar{\boldsymbol{\varepsilon}}$ and $\bar{T}$ respectively, and for a given Representative Elementary Volume, Ω. To do so, we have extended the well-known correspondence principle [59, 60, 5, 44, 45, 35] to thermo-mechanical loading by using the fact that, in our case, all the materials constituting the REV share the same internal time ξ. This property is verified under the following assumptions: i) In the considered REV, only the matrix is thermo-viscoelastic, the fibers are purely elastic and therefore time-independent. ii) The matrix is thermo-rheologically simple, with its behavior given by the equations (1.18) and (1.19). iii) For coupled thermo-mechanical homogenization problem, at the REV scale, the mechanical problem has to be solved by considering a homogeneous temperature field $\bar{T}$ which is the average in the REV of the temperature field $T(\boldsymbol{x})$ solving the heat equation in the REV, i.e. $\bar{T} = \langle T(\boldsymbol{x})\rangle = \frac{1}{|\Omega|}\int_\Omega T(\boldsymbol{x})d\Omega$. This had been demonstrated by [115] for periodic composites by using asymptotic homogenization in the framework of thermo-viscoelasticity. The effective thermo-viscoelastic response to a thermo-mechanical loading is then given by: $\bar{\boldsymbol{\sigma}}(\xi) = \langle \boldsymbol{\sigma}(\boldsymbol{x},\xi)\rangle$, with $\boldsymbol{\sigma}(\boldsymbol{x},\xi)$ solving the following equations in Ω:

$$\begin{cases} \nabla\cdot\ \boldsymbol{\sigma}(\boldsymbol{x},\xi) & = \mathbf{0} & \forall \boldsymbol{x}\in\Omega, \\ \boldsymbol{\sigma}(\boldsymbol{x},\xi) & = \left[\mathbb{L}^{(r)} \circledast \left(\boldsymbol{\varepsilon}(\boldsymbol{x},\cdot) - \boldsymbol{\beta}^{(r)}\right)\right](\xi) & \forall \boldsymbol{x}\in\Omega^{(r)}, \\ \boldsymbol{\beta}^{(r)}(\xi) & = \left[\boldsymbol{\alpha}^{(r)} \circledast \bar{\theta}\right](\xi), & \\ \langle\boldsymbol{\varepsilon}(\boldsymbol{x},\xi)\rangle & = \bar{\boldsymbol{\varepsilon}}(\xi), & \end{cases} \tag{4.2}$$

with $\Omega^{(r)}$ being the volume occupied by phase r in the REV ($\Omega = \cup_{r=1}^{R}\Omega^{(r)}$). Boundary conditions and compatibility conditions on $\boldsymbol{\varepsilon}$ must complete this problem. The implementation of mean-field schemes is achieved by using the correspondence principle [5, 45], that utilizes the Laplace-Carson transform to rewrite (4.2) as a symbolic equivalent of a linear thermoelastic composite. The explicit form of the Laplace-Carson transform ($\mathcal{LC}\{\cdot\}$) is defined as follows (see: A.3):

$$f^*(p) = \mathcal{LC}\{f\}(p) = p\mathcal{L}\{f\}(p) = p\int_0^\infty f(\xi)e^{-p\xi}d\xi, \tag{4.3}$$

and recalling the property for the Stieltjes convolution product $f \circledast g$,

$$\mathcal{LC}\{f \circledast g\}(p) = p\mathcal{L}\{f\}(p)p\mathcal{L}\{g\}(p) = f^*(p)g^*(p), \tag{4.4}$$

as all the mechanical quantities in (4.2) are defined in terms of the internal time domain, ensuring the applicability of the property in Eq. (4.4) to the constitutive equations in (4.2), the implication of the TTS are indeed grater which is the fact that the TTS principle definitions for an SPC filament will remain the same as the matrix, and this is actually verified for another experimental work we have conducted and that is on the way of being published. In the Laplace domain, the symbolic homogenization problem reads

$$\begin{cases} \nabla \cdot \boldsymbol{\sigma}^*(\boldsymbol{x}, p) & = \mathbf{0} & \forall \boldsymbol{x} \in \Omega, \\ \boldsymbol{\sigma}^*(\boldsymbol{x}, p) & = \mathbb{L}^{*(r)}(p) \cdot \left(\boldsymbol{\varepsilon}^*(\boldsymbol{x}, p) - \boldsymbol{\beta}^{*(r)}(p)\right) & \forall \boldsymbol{x} \in \Omega^{(r)}, \\ \boldsymbol{\beta}^{*(r)}(p) & = \boldsymbol{\alpha}^{*(r)}(p)\bar{\theta}^*(p) & \forall \boldsymbol{x} \in \Omega^{(r)}, \\ \langle \boldsymbol{\varepsilon}^*(\boldsymbol{x}, p) \rangle & = \bar{\boldsymbol{\varepsilon}}^*(p), \end{cases} \tag{4.5}$$

with compatibility and boundary conditions.

Based on the theory of effective moduli [1, 91, 3], an approximated solution of the linear problem in (4.5) is sought using mean-field approaches, that are widely applied to randomly distributed microstructures [109, 116, 117, 118, 119, 120]. In this context, localization tensors ($\mathbb{A}^{*(r)}(p)$ and $\boldsymbol{a}^{*(r)}(p)$) are characterized as linear operators relating the local strain of a given phase r of volume fraction $c^{(r)}$, and the macroscopic strain imposed on the REV by assuming strain fields that are uniform per phase ($\boldsymbol{\varepsilon}^{*(r)}(p) = \mathbb{A}^{*(r)}(p) \cdot \bar{\boldsymbol{\varepsilon}}^*(p) + \boldsymbol{a}^{*(r)}(p)\bar{\theta}^*(p)$). By considering the relation given in [91] between the concentration tensors $\mathbb{A}^{*(r)}(p)$ and $\boldsymbol{a}^{*(r)}(p)$, the effective behavior ($\tilde{\mathbb{L}}^*(p)$, $\tilde{\boldsymbol{\alpha}}^*(p)$) of an R-phases composite in the Laplace-Carson domain is obtained through the following relationships, noting that, in order to lighten the writing, the dependency on the complex variable p of every transformed quantity is not presented explicitly, but it can be understood in every starred variable, $\{\cdot\}^*$.

$$\bar{\boldsymbol{\sigma}}^* = \tilde{\mathbb{L}}^* \cdot (\bar{\boldsymbol{\varepsilon}}^* - \tilde{\boldsymbol{\alpha}}^* \bar{\theta}^*), \tag{4.6}$$

with

$$\begin{aligned}\tilde{\mathbb{L}}^* &= \left(\mathbb{L}^{*(1)} + \sum_{r=2}^{R} c^{(r)} \left(\mathbb{L}^{*(r)} - \mathbb{L}^{*(1)}\right) \cdot \mathbb{A}^{*(r)}\right), \text{ and} \\ \tilde{\boldsymbol{\alpha}}^* &= \left(\tilde{\mathbb{L}}^*\right)^{-1} \cdot \left(\mathbb{L}^{*(1)} \cdot \boldsymbol{\alpha}^{*(1)} + \sum_{r=2}^{R} c^{(r)} \left(\mathbb{A}^{*(r)}\right)^T \cdot \left(\mathbb{L}^{*(r)} \cdot \boldsymbol{\alpha}^{*(r)} - \mathbb{L}^{*(1)} \cdot \boldsymbol{\alpha}^{*(1)}\right)\right),\end{aligned} \tag{4.7}$$

where the superscript $^{(1)}$ denotes the matrix. Three mean-field schemes are implemented: Mori-Tanaka, Lielens and IDD (Interaction Direct Derivative), each of them with a particular form of $\mathbb{A}^{*(r)}$. It must be noted that in the present work, all chosen schemes involve the mean over the phases of some quantities inside its formulation of the localization tensor. Details about the choices made are presented in Appendix B.2.

4.2.1 Short-fibers description

A microstructure like the one presented in the microtomography in Fig. 4.1, should be considered as a heterogeneous medium with $R-1$ linear thermoelastic phases embedded in a thermo-viscoelastic matrix (each phase corresponds to a family of elastic fibers sharing the same microstructural parameters (i.e. length and orientation)). The fibrous inclusions of the engineering thermoplastic polymers are commonly made of carbon (transverse isotropic) or glass (isotropic). In the next definitions, transverse-isotropic symmetry will be used for both, the inclusions' and matrix' properties, since an isotropic material can be represented in any transverse-isotropic basis with arbitrary orientation vector $\boldsymbol{n}$ of the symmetry axis [46]. The chosen 4th order tensor basis is the Hill basis $\{\mathbb{H}^{(1)}, .., \mathbb{H}^{(b)}, .., \mathbb{H}^{(6)}\}(\boldsymbol{n})$ (Appendix A.5). Constitutive equations of the fibrous inclusions (defined in the internal time), denoted by the superscript $^{(\mathrm{f})}$, are presented directly in the Laplace-Carson domain as the explicit form of the fibers' properties remains the same after transformation (i.e. $\boldsymbol{L}^{*(\mathrm{f})} = \mathbb{L}^{(\mathrm{f})}$, $\boldsymbol{\alpha}^{*(\mathrm{f})} = \boldsymbol{\alpha}^{(\mathrm{f})}$).

$$\begin{aligned}\boldsymbol{\sigma}^{*(\mathrm{f})}(p) &= \mathbb{L}^{(\mathrm{f})}(\boldsymbol{n}) \cdot (\boldsymbol{\varepsilon}^*(p) - \boldsymbol{\beta}^*(p)) = \sum_{b=1}^{6} l^{(b,\mathrm{f})} \mathbb{H}^{(b)}(\boldsymbol{n}) \cdot (\boldsymbol{\varepsilon}^*(p) - \boldsymbol{\beta}^*(p)), \\ \boldsymbol{\beta}^{*(\mathrm{f})}(p) &= \boldsymbol{\alpha}^{(\mathrm{f})} \theta^*(p) = \left(\alpha_{11}^{(\mathrm{f})} \boldsymbol{\Theta} + \alpha_{33}^{(\mathrm{f})} \boldsymbol{\mathcal{N}}\right) \theta^*(p),\end{aligned} \tag{4.8}$$

with, $\alpha_{11}^{(\mathrm{f})}$ and $\alpha_{33}^{(\mathrm{f})}$, being the transverse and longitudinal fibers' expansion coefficients associated to the second order tensor basis $\boldsymbol{\mathcal{N}} = \boldsymbol{n} \otimes \boldsymbol{n}$ and $\boldsymbol{\Theta} = \boldsymbol{I} - \boldsymbol{\mathcal{N}}$ in terms of the orientation vector

$\boldsymbol{n}$ (Appendix A.5).

Probabilistic approach to account the presence of fibers:

In the present study, instead of a deterministic description of the fibers, a continuous distributions approach is implemented for the microstructural parameters [110, 109]. To illustrate this, only the effective mechanical behavior ($\tilde{\mathbb{L}}^*$) is presented, as it is enough to show the impact of this technique in the thermo-mechanical macroscopic response. Since it is sought a binary representation of the composite (polymer matrix + fibers), the superscript $^{(1)}$ is substituted by $^{(\mathrm{m})}$ as the matrix identification character in Eq. (4.7). The volume fraction of the polymer matrix is then expressed by: $c^{(1)} = c^{(\mathrm{m})} = 1 - \sum_{r=2}^{R} c^{(r)} = 1 - c^{(\mathrm{f})}$. With $c^{(\mathrm{f})}$ being the fibers' total volume fraction. Then, $\tilde{\mathbb{L}}^*$ from Eq. (4.7) is rewritten by considering the explicit form of $\boldsymbol{L}^{*(\mathrm{f})}$ in Eq. (4.8) to write both, matrix and inclusions' mechanical properties in the fibers' basis.

$$\tilde{\mathbb{L}}^* = \mathbb{L}^{*(\mathrm{m})} + c^{(\mathrm{f})} \sum_{b=1}^{6} \left(l^{*(b,\mathrm{f})} - l^{*(b,\mathrm{m})} \right) \sum_{r=2}^{R} \frac{c^{(r)}}{c^{(\mathrm{f})}} \mathbb{H}^{(b)}(\boldsymbol{n}^{(r)}) \cdot \mathbb{A}^{*(r)}(\boldsymbol{n}^{(r)}, w^{(r)}). \tag{4.9}$$

The above presentation is possible because the fiber families differ only in their orientation ($\boldsymbol{n}^{(r)}$) and length (i.e. aspect ratio $w^{(r)} = l^{(r)}/d$), so their only differences are in the explicit forms of the Hill basis and the localization tensor. Considering as it is shown in [46] for spheroidal inclusions, that the localization tensor of a fiber family with orientation $\boldsymbol{n}^{(r)}$ can be written down in the same basis as its mechanical properties ($\mathbb{A}^{*(r)} = \sum_{b=1}^{6} a^{*(r)}(w^{(r)}) \mathbb{H}^{(b)}(\boldsymbol{n}^{(r)})$), and by introducing the relative volume fraction of a family of fibers with respect to the total number of fibers $c_{\mathrm{f}}^{(r)} = c^{(r)}/c^{(\mathrm{f})}$ (with $\sum_{r=2}^{R} c_{\mathrm{f}}^{(r)} = 1$), Eq. (4.9) reads,

$$\begin{aligned} \tilde{\mathbb{L}}^* &= \boldsymbol{L}^{*(\mathrm{m})} + c^{(\mathrm{f})} \sum_{b=1}^{6} \left(l^{*(b,\mathrm{f})} - l^{*(b,\mathrm{m})} \right) \sum_{r=2}^{R} c_{\mathrm{f}}^{(r)} \mathbb{H}^{(b)}(\boldsymbol{n}^{(r)}) \cdot \sum_{v=1}^{6} a^{*(v,r)}(w^{(r)}) \mathbb{H}^{(v)}(\boldsymbol{n}^{(r)}) \\ &= \mathbb{L}^{*(\mathrm{m})} + c^{(\mathrm{f})} \sum_{b=1}^{6} \sum_{v=1}^{6} \left(l^{*(b,\mathrm{f})} - l^{*(b,\mathrm{m})} \right) \left\langle a^{*(v,r)}(w^{(r)}) \left(\mathbb{H}^{(b)}(\boldsymbol{n}^{(r)}) \cdot \mathbb{H}^{(v)}(\boldsymbol{n}^{(r)}) \right) \right\rangle_{\Omega \setminus \Omega^{(\mathrm{m})}}. \end{aligned} \tag{4.10}$$

The expression between angle brackets in the foregoing equation represents the volume average over the space of orientations and lengths of the concerned quantities. For the case of an REV with a finite number of fibers, Eq. (4.10) can be computed explicitly in a deterministic way, however this approach limits the number of fibers describing the distribution of the microstructural parameters. As it is mentioned in [110], The most general description of the fibers' state

is the probability distribution function, in which it is possible to consider an infinite number of fibers covering in a more accurate way the distribution of parameters in the composite. The probabilistic approach is then introduced as the number of fibers in Ω tends to infinity, therefore its microstructural parameters are no longer defined in a discrete way but characterized by a continuous distribution of the observed parameter.

$$\begin{aligned}\left\langle a^{*(v,r)}(w^{(r)})\left(\mathbb{H}^{(b)}(\boldsymbol{n}^{(r)})\cdot\mathbb{H}^{(v)}(\boldsymbol{n}^{(r)})\right)\right\rangle_{\Omega\setminus\Omega^{(\mathrm{m})}} &= \frac{1}{|\Omega\setminus\Omega^{(\mathrm{m})}|}\int_{\Omega\setminus\Omega^{(\mathrm{m})}} a^{*(v,r)}(w^{(r)})\left(\mathbb{H}^{(b)}(\boldsymbol{n}^{(r)})\cdot\mathbb{H}^{(v)}(\boldsymbol{n}^{(r)})\right)d\Omega \\ &= \int_{w_{min}}^{w_{max}} f_w(w)a^{*(v)}(w)dw\int_S f_{\boldsymbol{n}}(\boldsymbol{n})\left(\mathbb{H}^{(b)}(\boldsymbol{n})\cdot\mathbb{H}^{(v)}(\boldsymbol{n})\right)dS.\end{aligned} \tag{4.11}$$

The mean over the distribution of lengths is characterized by the integral of the normalized distribution function ($f_w(w)$), that depends on the aspect ratio ($w = l/d \in [w_{min}, w_{max}]$) being a function of the fiber length ($l \in [l_{min}, l_{max}]$) under the hypothesis of constant fibers' diameter (d). The mean over the orientations is computed by integrating over the unit sphere (S) the distribution function ($f_{\boldsymbol{n}}(\boldsymbol{n})$), depending on the unit direction vector ($\boldsymbol{n}$).

For the simulation examples of the present work, glass fiber inclusions are considered, in consequence $\mathbb{L}^{*(r)}$ is independent of the orientation vector $\boldsymbol{n}$ of the fiber as it is isotropic and can be represented in any arbitrary transverse isotropic basis $\{\mathbb{H}^{(b)}\}(\boldsymbol{n})$, therefore in Eq. (4.10) only the localization tensor $\mathbb{A}^{*(r)}(w^{(r)}, \boldsymbol{n}^{(r)})$ is different for each family of fibers. This fact reduces the computation of the distribution averages to the computation of the mean coefficients $\{a_\star^{*(v,f)}\}$ and associated mean Hill basis tensors $\{\mathbb{H}_\star^{(v,f)}\}$ (Eqs. (A.40) - (A.42)). Considering this, Eq. (4.10) under the continuous distribution representation (Eq. (4.11)) reads

$$\begin{aligned}\tilde{\mathbb{L}}^* &= \mathbb{L}^{*(m)} + c^{(f)}\left(\mathbb{L}^{*(f)} - \mathbb{L}^{*(m)}\right)\cdot\sum_{v=1}^{6}\int_{w_{min}}^{w_{max}} f_w(w)a^{*(v)}(w)dw\int_S f_{\boldsymbol{n}}(\boldsymbol{n})\mathbb{H}^{(v)}(\boldsymbol{n})dS \\ &= \mathbb{L}^{*(m)} + c^{(f)}\left(\mathbb{L}^{*(f)} - \mathbb{L}^{*(m)}\right)\cdot\sum_{v=1}^{6} a_\star^{*(v,f)}\mathbb{H}_\star^{(v,f)} = \mathbb{L}^{*(m)} + c^{(f)}\left(\mathbb{L}^{*(f)} - \mathbb{L}^{*(m)}\right)\cdot\mathbb{A}_\star^{*(f)},\end{aligned} \tag{4.12}$$

with $\mathbb{A}_\star^{*(f)}$ being the distribution averaged fibers' localization tensor. The two-phases like version of the effective thermo-viscoelastic behavior (Eq.4.7) for the case of isotropic linear elastic glass

fibers inclusions is given by:

$$\begin{aligned}
\tilde{\mathbb{L}}^* &= \mathbb{L}^{*(m)} + c^{(f)} \left(\mathbb{L}^{*(f)} - \mathbb{L}^{*(m)} \right) \cdot \mathbb{A}_\star^{*(f)}, \\
\tilde{\boldsymbol{\alpha}}^* &= \bar{\boldsymbol{\alpha}} + \left(\mathbb{S}^{*(f)} - \mathbb{S}^{*(m)} \right)^{-1} \cdot \left(\tilde{\mathbb{S}}^* - \bar{\mathbb{S}}^* \right) \cdot \left(\boldsymbol{\alpha}^{*(f)} - \boldsymbol{\alpha}^{*(m)} \right),
\end{aligned} \tag{4.13}$$

where $\tilde{\mathbb{S}}^*$ and $\bar{\mathbb{S}}^* = c^{(m)}\mathbb{S}^{*(m)} + c^{(f)}\mathbb{S}^{*(f)}$, are the effective and average, transformed creep moduli tensor ($\mathbb{S}^* = (\mathbb{L}^*)^{-1}$) respectively. $\boldsymbol{\alpha}^{*(m)}$, $\boldsymbol{\alpha}^{*(f)}$, are the matrix' and fibers' thermal expansion second order tensors, respectively. The second equation in Eq. (4.13) is equivalent to the well-known Levin's equation (Hashin-Rosen, [121, 120]). The choices made for the explicit form of $f_w(w)$ and $f_{\boldsymbol{n}}(\boldsymbol{n})$ are presented below.

Weibull's law for length distributions:

The chosen length probability density function ($f_w(w)$) is the Weibull's law, used in the literature in the context of injection molding thermoplastic composites, where it was demonstrated its accuracy compared to the deterministic approach [51]. The explicit form of the function reads

$$\begin{aligned}
&f_w(w) = \mathrm{W}\left(wp(w)\right), \text{ with} \\
&p(w) = \frac{c_w}{w_0}\left(\frac{w}{w_0}\right)^{c_w-1} e^{-\left(\frac{w}{w_0}\right)^{c_w}}, \text{ and } \mathrm{W} = \left(\int_{w_{min}}^{w_{max}} wp(w)dw\right)^{-1},
\end{aligned} \tag{4.14}$$

where c_w, w_0 are the Weibull's law parameters to be fitted from data statistics obtained from image processing (e.g. microtomography Fig. 4.1). Examples of the parameters range chosen for the present study are presented in Fig. 4.5. From this figure, it can be noted that the value of w_0 represents the mean aspect ratio. Furthermore, by increasing the value of c_w at a given w_0 the number of fibers with aspect ratio w_0 is increased.

Advani and Tucker law for orientation distributions:

Primal observations of filament microtomography (Fig. 4.1) suggest an axisymetric distribution of the fibers' orientation about the filament axis. For this case, the Advani-Tucker's law is proposed in [110] in the context of injection molding composites. In the axisymetric case, this law is characterized by a single parameter (m_{AT}) to be computed from microphotography analysis.

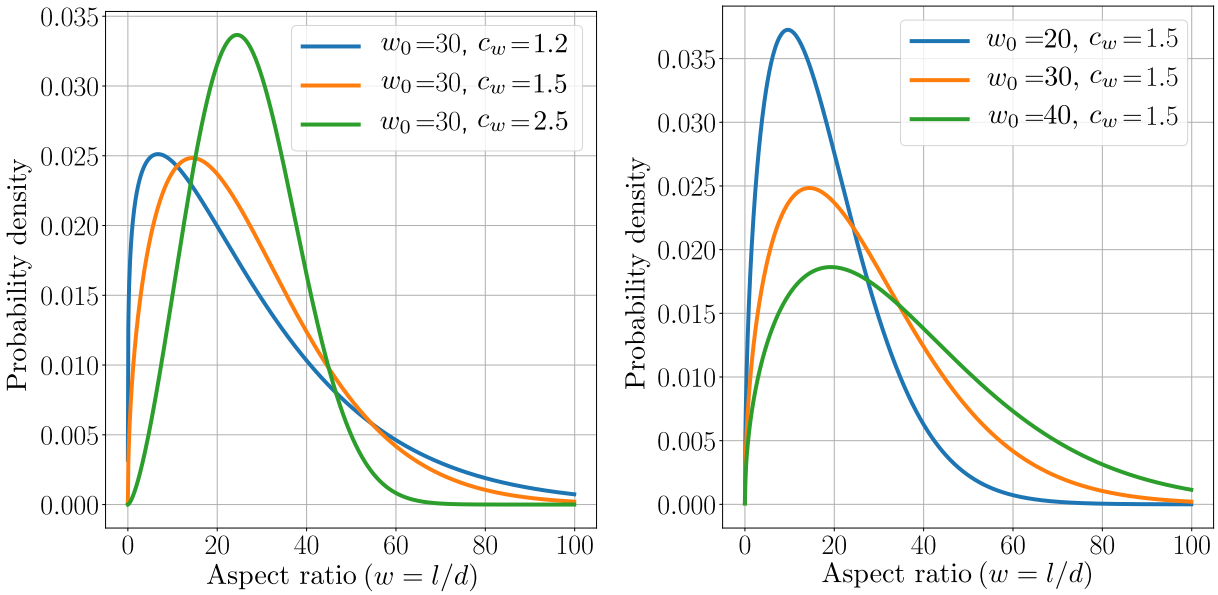

(a) Probability density plot for a given $w_0 = 30$ and various c_w

(b) Probability density plot for a given $c_w = 1.5$ and various w_0.

Figure 4.5: Weibull's probability density ($p(w)$) plots for various combinations of the parameters (c_w, w_0) used in the present study.

The explicit form of the distribution law is presented below.

$$f_{\boldsymbol{n}}(\theta, \phi) = K \sin^{m_{\mathrm{AT}}}(\theta) \cos^{m_{\mathrm{AT}}}(\phi), \tag{4.15}$$

where K is a normalization constant and, θ and ϕ are the direction angles characterizing the orientation deviation of a fiber from the filament axis. The implementation of this approach is simplified by using the mean orientation tensors ($\boldsymbol{\eta}_2$ and $\boldsymbol{\eta}_4$) as it is done in [110]. This procedure is of particular interest in the case of composites holding material symmetries that enables to write down the effective behavior in a particular choice of basis. Information about the application of the law and computation of orientations tensors can be found in A.6. Some examples of the orientation distributions used in the present work are presented in Fig. 4.6. As can be noted from this figure, the number of fibers, oriented in the principal filament's axis direction, increases as m_{AT} becomes greater. Indeed, the unidirectional case corresponds to the limit $m_{\mathrm{AT}} \to \infty$.

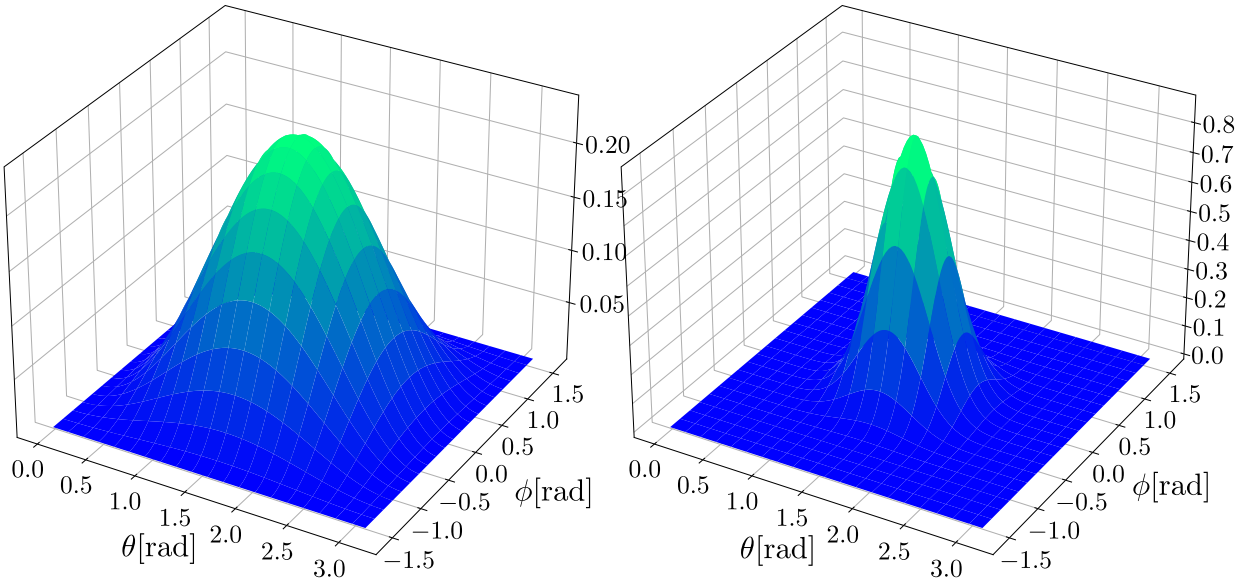

(a) Probability density plot for $m_{\mathrm{AT}} = 2$

(b) Probability density plot for $m_{\mathrm{AT}} = 10$

Figure 4.6: Advani-Tucker probability density $f_{\boldsymbol{n}}(\boldsymbol{n})$ for deviation angles $\theta \in [0, \pi]$ and $\phi \in [-\pi/2, \pi/2]$

4.2.2 Effective Prony series

To ensure the same mathematical representation of the effective behavior as it was presented for the matrix in the time domain (Prony-series), this study considers a supplementary identification step. In Eq. (4.13), the effective thermo-viscoelastic behavior is given in the Laplace-Carson domain ($\tilde{\mathbb{L}}^*$, $\tilde{\boldsymbol{\alpha}}^*$). In function of the length of the Prony-series of the polymer matrix and the choice of mean-field scheme, the complexity of the rational polynomials of the elements in $\tilde{\mathbb{L}}^*$ and $\tilde{\boldsymbol{\alpha}}^*$ varies, therefore the analytical inversion of the Laplace-Carson transform is sometimes too expensive in terms of computational time or is not giving a sum of weighted exponential functions (Prony-series) as it is desired. Since a complex relaxation moduli tensor $\mathbb{L}(j\omega)$ is equivalent to the above defined Laplace-Carson transform of the relaxation moduli tensor [122, 45], artificial dynamical mechanical analysis (DMA) is performed, and then processed using KN-HW identification procedure from [7] to obtain an approximation of the discrete spectra (Appendix A.7). The advantage of this method in contrast with the collocation methods is that it includes an accurate approximation of the characteristic discrete time spectrum. This is performed identically for both, mechanical and thermal Prony-series, differing only on the physical meaning of the identified coefficients. The expected explicit form of $\tilde{\mathbb{L}}^*$ and $\tilde{\boldsymbol{\alpha}}^*$ after

parameters' identification reads

$$\tilde{\mathbb{L}}^* = \tilde{\mathbb{L}}_{\mathrm{g}} - \sum_{b=1}^{6} \sum_{n_b=1}^{N_b} \frac{\tilde{l}^{(b,n_b)}/\tau_L^{(n_b)}}{p + (\tau_L^{(n_b)})^{-1}} \mathbb{H}_\star^{(b)}, \tag{4.16}$$

$$\tilde{\boldsymbol{\alpha}}^* = \tilde{\boldsymbol{\alpha}}_{\mathrm{g}} + \sum_{m=1}^{M} \frac{\tilde{\alpha}_{11}^{(m)}/\tau_\alpha^{(m)}}{p + (\tau_\alpha^{(m)})^{-1}} \boldsymbol{\Theta}_\star + \sum_{o=1}^{O} \frac{\tilde{\alpha}_{33}^{(o)}/\tau_\alpha^{(o)}}{p + (\tau_\alpha^{(o)})^{-1}} \boldsymbol{\mathcal{N}}_\star. \tag{4.17}$$

Here, $\tilde{\mathbb{L}}_{\mathrm{g}}$ is the effective glassy 4th order stiffness tensor, $\tilde{\boldsymbol{\alpha}}_{\mathrm{g}}$ is the glassy 2nd order thermal expansion tensor, $\boldsymbol{\Theta}_\star = \boldsymbol{I} - \boldsymbol{\eta}_2$ is the second-order tensor that characterizes the orthogonal behavior, $\boldsymbol{\mathcal{N}}_\star = \boldsymbol{\eta}_2$ is the second-order tensor that characterizes the symmetry axis behavior (see: Appendix A.5.2), N_b is the length of the Prony-series of the relaxation modulus $\tilde{l}^{*(b)}$, and, M and O are the lengths of the Prony-series of the effective thermal creep functions $\tilde{\alpha}_{11}^*$ and $\tilde{\alpha}_{33}^*$, respectively.

4.3 Simulation results

The modeling of the matrix thermo-viscoelastic behavior for the specific range of temperatures of the 3D-FDM printing have been presented in Section 4.1, where linear viscoelasticity, time-temperature superposition principle and the internal time technique were introduced. Section 4.2 presents the methodology to obtain the effective behavior. The homogenization procedure via mean-field schemes is achieved based on the validity of the applicability of the correspondence principle (Laplace-Carson transform) in continuous variations of temperature for thermo-rheologically simple polymers. Mean-field schemes were presented in a general shared formulation, differing only in the form of the localization tensor $\mathbb{A}^*(\boldsymbol{n}^{(r)}, w^{(r)})$ in function of the chosen scheme (Appendix B.2). Probabilistic approach to account for the variability of lengths and orientations of the fibers was introduced as a powerful tool able to map distributions over greater spaces and being very simple in terms of implementation. Finally, the methodology to identify the coefficients of the effective properties of the composite was introduced, ensuring that the composite is represented in the same way as the matrix. This Prony-series representation allows applying directly the internal variables' formulation [5, 26, 60] for the incremental scheme in the computation of stress as a function of time and temperature. In this section, the accu-

racy of the presented methodology will be compared to extensive heterogeneous simulations in computational REVs using the FFT-based full field homogenization method.

4.3.1 Internal variables' technique for stress computation

The stress computation problem can be formulated as follows:

$$\text{Given } \tilde{\mathbb{L}}(t),\ \tilde{\boldsymbol{\alpha}}(t),\ a_T(T),\ \bar{\boldsymbol{\varepsilon}}(t) \text{ and } \bar{\theta}(t) = \bar{T}(t) - \bar{T}_0, \text{ compute } \bar{\boldsymbol{\sigma}}(t).$$

First, $\xi(t)$ is computed by using Eq. (1.16) in function of $\bar{T}(t)$ and the total observation time of the simulation. Then, a simple way to start the procedure to compute the evolution of the macroscopic stress $\bar{\boldsymbol{\sigma}}(t)$ is by considering the explicit form of the Laplace-Carson transform of the stress function (Eq. (1.18)) for the case of a transverse isotropic homogenized material (Eqs. (4.16) - (4.17)), noting that, in order to lighten the writing, the implicit form of the thermal strains is conserved, and its computation is treated separately. It must be note that as [59, 60], the following formulation allows a simple and natural definition of the internal variables forms avoiding integral operations, and reducing the formulation to algebraic operations in rational polynomials.

$$\begin{aligned}
\bar{\boldsymbol{\sigma}}^*(p) &= \left(\tilde{\mathbb{L}}_{\mathrm{g}} - \sum_{b=1}^{6} \sum_{n_b=1}^{N_b} \frac{\tilde{l}^{(b,n_b)}/\tau_L^{(n_b)}}{p + (\tau_L^{(n_b)})^{-1}} \mathbb{H}_\star^{(b)} \right) \cdot \left(\bar{\boldsymbol{\varepsilon}}^*(p) - \tilde{\boldsymbol{\beta}}^*(p) \right) \\
&= \bar{\boldsymbol{\sigma}}_{\mathrm{g}}^*(p) - \sum_{b=1}^{6} \sum_{n_b=1}^{N_b} \tilde{l}^{(b,n_b)} \frac{\mathbb{H}_\star^{(b)} \cdot \left(\bar{\boldsymbol{\varepsilon}}^*(p) - \tilde{\boldsymbol{\beta}}^*(p) \right)}{\tau_L^{(n_b)} \left(p + (\tau_L^{(n_b)})^{-1} \right)},
\end{aligned} \tag{4.18}$$

with

$$\begin{aligned}
\tilde{\boldsymbol{\beta}}^*(p) &= \left(\tilde{\boldsymbol{\alpha}}_{\mathrm{g}} + \sum_{m=1}^{M} \frac{\tilde{\alpha}_{11}^{(m)}/\tau_\alpha^{(m)}}{p + (\tau_\alpha^{(m)})^{-1}} \boldsymbol{\Theta}_\star + \sum_{o=1}^{O} \frac{\tilde{\alpha}_{33}^{(o)}/\tau_\alpha^{(o)}}{p + (\tau_\alpha^{(o)})^{-1}} \boldsymbol{\mathcal{N}}_\star \right) \bar{\theta}^*(p) \\
&= \tilde{\boldsymbol{\beta}}_{\mathrm{g}}^*(p) + \sum_{m=1}^{M} \frac{\tilde{\alpha}_{11}^{(m)} \bar{\theta}^*(p)}{\tau_\alpha^{(m)} \left(p + (\tau_\alpha^{(m)})^{-1} \right)} \boldsymbol{\Theta}_\star + \sum_{o=1}^{O} \frac{\tilde{\alpha}_{33}^{(o)} \bar{\theta}^*(p)}{\tau_\alpha^{(o)} \left(p + (\tau_\alpha^{(o)})^{-1} \right)} \boldsymbol{\mathcal{N}}_\star,
\end{aligned} \tag{4.19}$$

where $\bar{\boldsymbol{\sigma}}_{\mathrm{g}}^*(p)$ and $\tilde{\boldsymbol{\beta}}_{\mathrm{g}}^*(p)$ are the Laplace-Carson transform of the glassy responses in terms of stress and thermal strains, respectively. Introducing three sets of second order tensor internal

variables $\{\boldsymbol{q}_L^{*(n_b)}\}$, $\{\boldsymbol{q}_{\alpha_1}^{*(m)}\}$ and $\{\boldsymbol{q}_{\alpha_3}^{*(o)}\}$ the foregoing equations reads:

$$
\begin{aligned}
&\bar{\boldsymbol{\sigma}}^*(p) = \bar{\boldsymbol{\sigma}}_{\mathrm{g}}^*(p) - \sum_{b=1}^{6}\sum_{n_b=1}^{N_b} \tilde{l}^{(n_b)}\mathbb{H}_\star^{(b)} \cdot \boldsymbol{q}_L^{*(n_b)}(p), \qquad \boldsymbol{q}_L^{*(n_b)}(p) = \frac{\bar{\boldsymbol{\varepsilon}}^*(p) - \tilde{\boldsymbol{\beta}}^*(p)}{\tau_L^{(n_b)}\left(p + (\tau_L^{(n_b)})^{-1}\right)},\\
&\tilde{\boldsymbol{\beta}}^*(p) = \tilde{\boldsymbol{\beta}}_{\mathrm{g}}^*(p) + \sum_{m=1}^{M} \boldsymbol{q}_{\alpha_1}^{*(m)}(p) + \sum_{o=1}^{O} \boldsymbol{q}_{\alpha_3}^{*(o)}(p), \qquad \boldsymbol{q}_{\alpha_1}^{*(m)}(p) = \frac{\tilde{\alpha}_{11}^{(m)}\bar{\theta}^*(p)\boldsymbol{\Theta}_\star}{\tau_\alpha^{(m)}\left(p + (\tau_\alpha^{(m)})^{-1}\right)},\\
&\boldsymbol{q}_{\alpha_3}^{*(o)}(p) = \frac{\tilde{\alpha}_{33}^{(o)}\bar{\theta}^*(p)\boldsymbol{\mathcal{N}}_\star}{\tau_\alpha^{(o)}\left(p + (\tau_\alpha^{(o)})^{-1}\right)}.
\end{aligned}
\tag{4.20}
$$

Reordering the expressions of the internal variables and performing the inverse transform of the equations in Eq. (4.20) we obtain equivalent forms to those presented in [60]. the internal-time forms and the associated O.D.E's of the internal variables are obtained as follows:

$$
\begin{aligned}
&\bar{\boldsymbol{\sigma}}(\xi) = \bar{\boldsymbol{\sigma}}_{\mathrm{g}}(\xi) - \sum_{b=1}^{6}\sum_{n_b=1}^{N_b} \tilde{l}^{(n_b)}\mathbb{H}_\star^{(b)} \cdot \boldsymbol{q}_L^{(b,n_b)}(\xi), \qquad \frac{d}{d\xi}\boldsymbol{q}_L^{(n_b)}(\xi) + \frac{1}{\tau_L^{(n_b)}}\boldsymbol{q}_L^{(n_b)}(\xi) = \frac{\bar{\boldsymbol{\varepsilon}}(\xi) - \tilde{\boldsymbol{\beta}}(\xi)}{\tau_L^{(n_b)}},\\
&\tilde{\boldsymbol{\beta}}(\xi) = \tilde{\boldsymbol{\beta}}_{\mathrm{g}}(\xi) + \sum_{m=1}^{M} \boldsymbol{q}_{\alpha_1}^{(m)}(\xi) + \sum_{o=1}^{O} \boldsymbol{q}_{\alpha_3}^{(o)}(\xi), \quad \frac{d}{d\xi}\boldsymbol{q}_{\alpha_1}^{(m)}(\xi) + \frac{1}{\tau_\alpha^{(m)}}\boldsymbol{q}_{\alpha_1}^{(m)}(\xi) = \frac{\tilde{\alpha}_{11}^{(m)}\bar{\theta}(\xi)\boldsymbol{\Theta}_\star}{\tau_\alpha^{(m)}},\\
&\frac{d}{d\xi}\boldsymbol{q}_{\alpha_3}^{(o)} + \frac{1}{\tau_\alpha^{(o)}}\boldsymbol{q}_{\alpha_3}^{(o)} = \frac{\tilde{\alpha}_{33}^{(o)}\bar{\theta}(\xi)\boldsymbol{\mathcal{N}}_\star}{\tau_\alpha^{(o)}}.
\end{aligned}
\tag{4.21}
$$

The computed stress is then obtained in the internal-time domain. Thanks to the mapping $t \mapsto \xi$, quantities measured in the internal time take the same values in the correspondent observer times, in fact since the values of ξ are computed as an initial step for a given temperature at a given instant, the return to the observer time is trivial. For the simulation examples, the non-homogeneous ODE's characterizing the evolution of the internal variables are solved numerically by implementing the Taylor's integration scheme [58]. This methodology is based on the assumption of a linear evolution of the right-hand side of the ODE's for the computation of its particular solution. The discrete evolution equation for an ODE relating second order tensorial functions (Eq. (4.21)), for instance, an arbitrary internal variable $\boldsymbol{q}(\xi)$, and a right-hand side

$\frac{\boldsymbol{\Upsilon}(\xi)}{\tau}$, is written down as follows:

$$\forall \xi_k \in \{0, \xi_2, ..., \xi_k, ..., \xi_K\}, \quad \text{and,} \quad \Delta\xi_{k+1} = \xi_{k+1} - \xi_k$$
$$\boldsymbol{q}(\xi_{k+1}) = \boldsymbol{q}(\xi_k) e^{-\frac{\Delta\xi_{k+1}}{\tau}} + \boldsymbol{\Upsilon}(\xi_k)\left(1 - e^{-\frac{\Delta\xi_{k+1}}{\tau}}\right) + (\boldsymbol{\Upsilon}(\xi_{k+1}) - \boldsymbol{\Upsilon}(\xi_k))\left(1 - \frac{\tau}{\Delta\xi_{k+1}}(1 - e^{-\frac{\Delta\xi_{k+1}}{\tau}})\right) \tag{4.22}$$

4.3.2 Problems setting

Macroscopic loading:

Three scenarios of simulation are presented. All these situations consider a linear cooling while different mechanical constraints are applied to the REV. Five constant cooling rate ($\dot{\bar{\theta}}$) are studied, from very fast (8.64s) to slow cooling (24h). The cooling rate iterations are given by $\Delta\bar{T}/t_c$, with t_c being the cooling times, previously presented in Fig. 4.4, and ΔT the total variation of temperature, here, -225°C. Numerical values are presented below.

$$\dot{\bar{\theta}} \in \{-0.00260417, -0.0260417, -0.260417, -2.60417, -26.0417\}[\text{°C s}^{-1}].$$

For the mechanical constraints, three different cases are considered: the strains-free case, this is, $\bar{\boldsymbol{\varepsilon}}(t) = \mathbf{0}$ (**load case 1**). The second case is the stress-free case, this is, $\bar{\boldsymbol{\sigma}}(t) = \mathbf{0}$ (**load case 2**). Finally, the mixed conditions' case is implemented, this is, $\bar{\boldsymbol{\sigma}}_{22}(t) = 0$ and $\bar{\boldsymbol{\varepsilon}}_{33}(t) = \bar{\boldsymbol{\varepsilon}}_{11}(t) = 0$ (**load case 3**), which corresponds to the case of a laminate composed by two thin plates with an angle of relative deviation of the material's symmetry axis of 90° with $\boldsymbol{e}_2$ being the stacking direction of the laminate.

Sensibility to the starting temperature:

The study range of the temperature characterizing the FDM 3D-printing of a PEI filaments is between 355°C to room temperature ($\approx$ 25°C). Primary studies of the amorphous PEI-like matrix used in the present work have suggested the quasi-pure dissipative behavior between 355 and 250°C, reflected by a negligible amount of residual stress produced within this temperature interval. This can be identified easily by observing the values of $a_T(T)$ associated to high temperatures, it is observed that, the amount of viscous strain is increased at high temperatures

as most of the relaxation mechanisms are activated simultaneously. The influence of the starting temperature on the magnitude of the residual stress is presented in Fig. 4.7. This analysis was performed at maximum cooling rate as it is the one giving the highest levels of stress. From this figure, it is clear that the generation of stress at high temperature is negligible compared to the level produced as the glass transition temperature ($T_g = 216°C$) is closer and below it. The maximum relative error on the stress is close to 2%. For the interest of the present work, low stages of stress are not displayed. In conclusion, the starting temperature is set to $T(0) = 250°C$, which imposes the before mentioned $\Delta T = -225°C$.

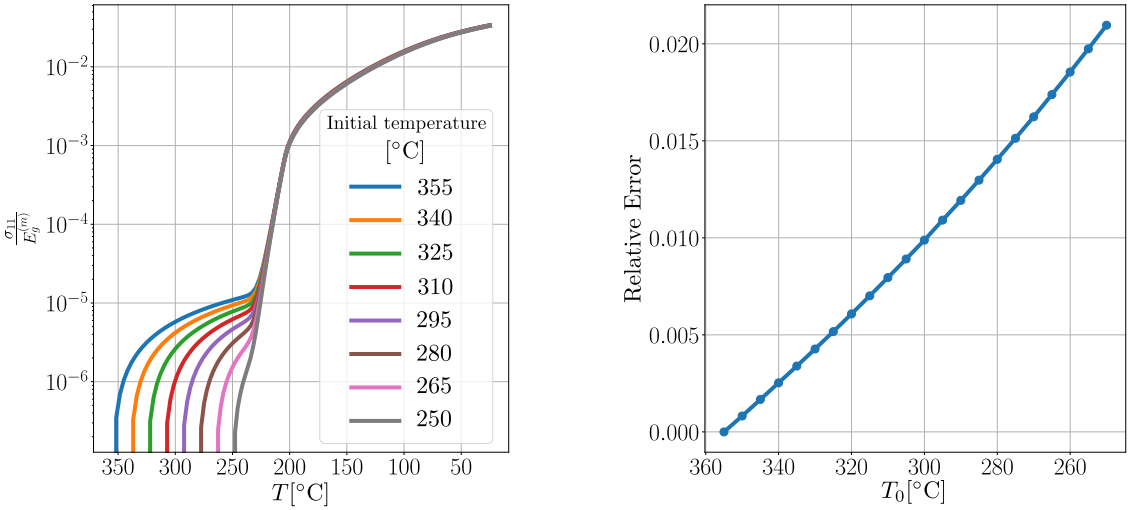

(a) stress component σ_{11} vs. temperature T (b) Relative error on σ_{11}^{∞} vs. initial temperature T_0.

Figure 4.7: Influence of the starting temperature T_0 of the simulation on the magnitude of the residual stress at minimum cooling time (8.64[s]). Study performed for the load case 1 (Section 4.3.4).

4.3.3 Numerical considerations

Reference solutions are obtained from FFT-based full-field homogenization [95] by using the in-house code Craft[1]. This method uses 3D images discretized in voxels for the REVs (Fig. 4.8). The fibers' are represented by long capsules (cylinders with hemispherical ends), that is closer to the actual geometry of the fibers. In contrast, mean-field schemes uses prolate spheroids as representation for the fibers. For this study, it is considered a spheroid that preserves the quadratic moment of the capsule used in the full-field simulations instead of keeping the same aspect ratio [119], this is, $w_0 = w_0^{\text{ref}}(2/\sqrt{3})$. Comparison data of the consequences of the

[1] http://craft.lma.cnrs-mrs.fr/

precedent choice is presented in Fig. 4.9. In this figure, the error is measured just on the Lielens scheme, comparing the closeness of the asymptotic stress with the reference solutions. Finally, the simulations used for these plots consider the case of maximum volume fraction ($c^{(f)} = 40\%$) as it represents a greater influence of the presence of fibers on the macroscopic behavior.

The computational 3D REVs for the simulations are generated using the probability distribution functions described in Section 4.2. The generation task has to ensure the non superposition of fibers as priority, in consequence the distributions are exposed to violations during the sampling process, this is why after generation, the distribution parameters are refitted from the generated microstructures to avoid the loss of accuracy when comparing the mean-field data (in results, only theoretical values of the distribution parameters are displayed).

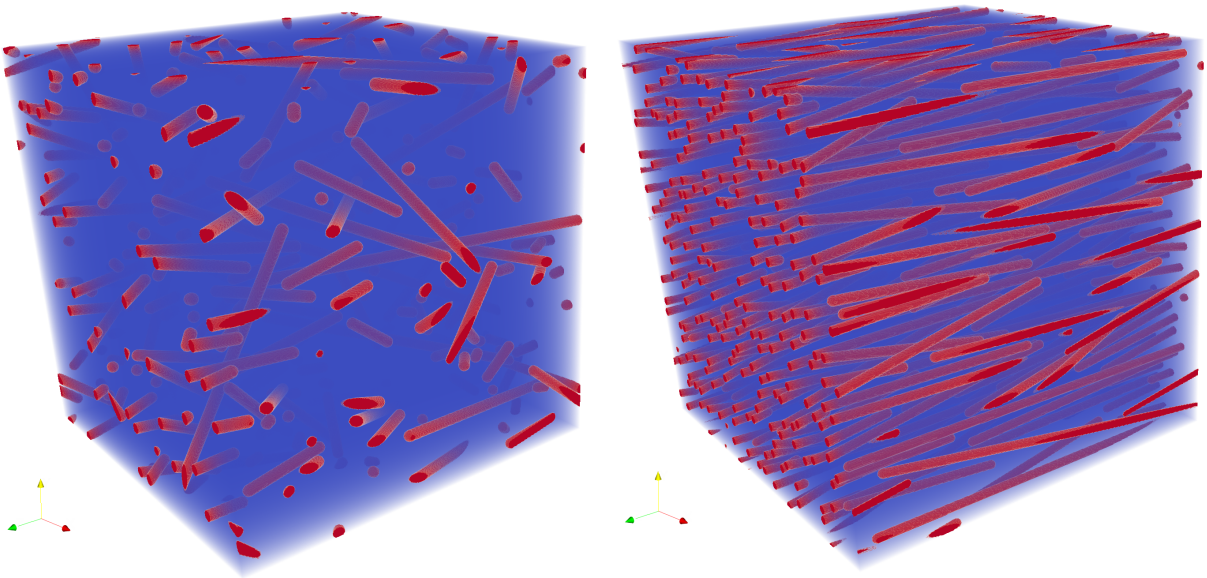

(a) $m_{\mathrm{AT}} = 2$, $c_w = 0.5$ and $w_0 = 20$.

(b) $m_{\mathrm{AT}} = 60$, $c_w = 2.5$ and $w_0 = 40$.

Figure 4.8: Examples of computer generated representative elementary volumes (REV) used in the computation of reference solutions. The volume fraction of fibers in the displayed microstructures is $c^{(f)} = 10\%$. On the left side, the more disoriented case with a higher variability of lengths. On the right side, the most oriented and less variable lengths.

Discretization and Sampling convergence: Due to the high cost in terms of computation time of references solutions, the discretization of the REVs is limited by the computation capabilities of the available hardware. This is why a study of discretization convergence is performed to improve the time of computations. By imposing a maximum admissible error of 1.0×10^{-4}, the microstructure discretization is set to $300 \times 300 \times 300$ voxels. On the other hand, a study characterizing the convergence in terms of the number of inclusions is performed too. This is

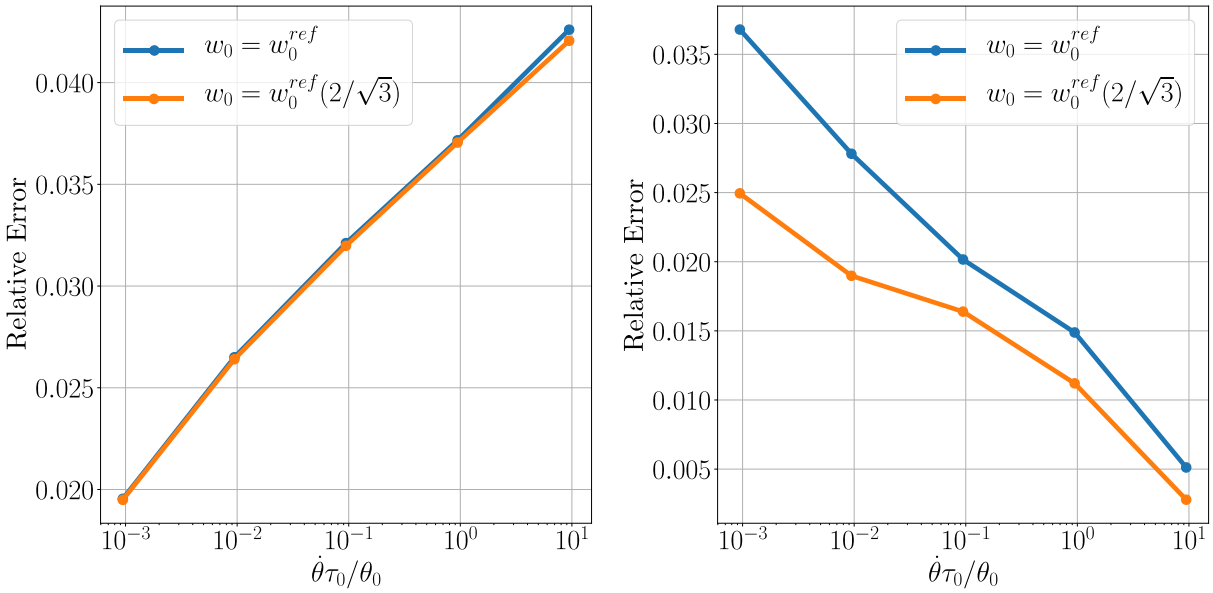

(a) Error on σ_{11}^{∞}.

(b) Error on σ_{33}^{∞}.

Figure 4.9: Relative error of the inclusions' representation, measured on the asymptotic stress for Lielens' scheme vs. normalized cooling rate. volume fraction $c^{(f)} = 40\%$. Distribution parameters, $m_{\text{AT}} = 60$, $c_w = 2.5$ and $w_0 = 40$.

equivalent to the study of the size of the REV, as the dimensions of the fibers are obtained by relative sizing from the total volume and the volume fraction; this study characterizes the accuracy of the representation of the REV with respect to the whole composite volume. Similarly, by imposing the maximum error in the number of fibers to 1.5×10^{-4}, the number of inclusions for the simulations is set to 300 fibers. Results of the Convergence studies are presented in Fig. 4.10. In addition, in Table. 4.2 the times for reference and mean-field solutions' computations are presented, the values correspond to the "faster" FFT simulation and its correspondent obtained through mean-field schemes. In the case of the reference solutions, each simulation was obtained in two computational nodes with 56 cores and 128 Gigabytes of RAM.

For mean-field computations, a machine with 16 cores and 128 Gigabytes of RAM was used. As can be noted from the table, even under less computational power conditions, the time for mean-field computations is always negligible compared to the full-field reference solutions. In fact, as the effective behavior is in an explicit form, the computation of effective behavior (in the Laplace-Carson domain) is a fraction of the time shown in the table. Most of the time is consumed in approximating effective Prony series and computing each simulation scenario.

Table 4.2: Time of computations for effective residual stress simulations

Method	Time (h.m.s)
FFT(300x300x300)	05:11:17
FFT(400x400x400)	08:04:21
FFT(500x500x500)	12:19:03
Mean-field	00:02:46

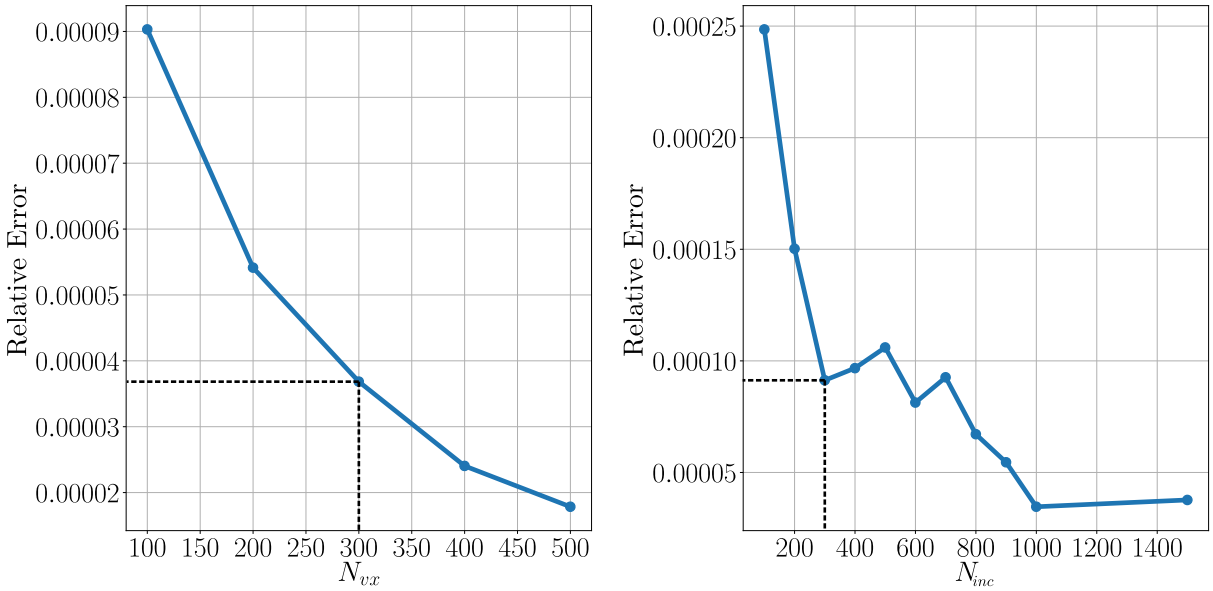

(a) Error on $\bar{\boldsymbol{\sigma}}^{\infty}$ vs number of voxels per edge (N_{vx}). (b) Error on $\bar{\boldsymbol{\sigma}}^{\infty}$ vs number of inclusions (N_{inc}).

Figure 4.10: Convergence study for reference solutions. volume fraction $c^{(f)} = 40\%$. Distribution parameters, $m_{\mathrm{AT}} = 60$, $c_w = 2.5$ and $w_0 = 40$.

4.3.4 Comparisons

Here, results are presented for the simulations settings specified in Section 4.3.2. The solutions are obtained for multiple combination of microstructural parameters, that are, the volume fraction $c^{(f)}$, the orientation distribution parameter m_{AT}, and length distribution parameters w_0 and c_w. Numerical values of the parameters are presented in the Table. 4.3. All combinations of parameters have been tested, and as can be noted this represents a large amount of data. For the sake of clarity in comparisons, just some representative combinations are presented for each load case.

Simulation results are presented as follows: First, for each load case, the evolution of the computed mechanical quantities is presented in function of the temperature (figures Fig. 4.11, Fig. 4.16 and Fig. 4.21). Each of these figures shows the evolution for three different values

of the imposed cooling rate, from the slowest (blue lines) passing by a middle velocity (green lines), to the fastest (purple lines). As can be noted from the gaps in each group, they are almost consistent in each figure, this fact verifies the ability of the method to predict residual stress in a wide range of cooling rates. Then, having this initial figures for each load case, the influence of the microstructural parameters is studied by presenting the asymptotic value of the mechanical quantities as a function of the microstructural parameters by sweeping in one parameter while the rest of them remains constant and equal to the values of the evolution plots: Figures Fig. 4.12, Fig. 4.17 and Fig. 4.22 showing the influence of the volume fraction $c^{(f)}$, figures Fig. 4.13, Fig. 4.18 and Fig. 4.23 presents the influence of the Advani-Tucker orientation parameter m_{AT}. To study the influence of the length distribution parameters (Weibull's law), Figures Fig. 4.14, Fig. 4.19 and Fig. 4.24 show the influence of c_w, and figures Fig. 4.15, Fig. 4.20 and Fig. 4.25 present the influence of w_0. Regarding the plotted stress, it is normalized by the elastic response of the matrix $\boldsymbol{\sigma}^{(m),e}$.

From all these figures, the high accuracy of the proposed methodology is verified noting that, Lielens' scheme is almost always slightly closer to the reference solutions, but despite this fact the magnitude of the gaps are negligible between the implemented mean-field schemes. The closeness of the responses of the Mori–Tanaka and IDD schemes is explained from the fact that the IDD approximation was computed using a unique spatial distribution cell which aspect ratio is very close to the fiber's mean aspect ratio ($w^{(D,r)} = 0.8w_0$). A better use of the capabilities of this scheme should consider a non-uniformly distributed spatial distribution cell ($\Omega^{(D,r)}$) space using a probabilistic distribution, as it was for example implemented for the variation in the fiber lengths and suggested in [118]. As inferred in [117], the Lielens' scheme is able to improve the approximation of the effective behavior at higher volume fractions of the fibrous phase by considering the computation of localization tensors as an interpolation of the Mori–Tanaka scheme and another one obtained by considering the same estimate but in a case in which the fibers become the continuous phase and the matrix the dispersed one. The latter justifying why this approximation shows better results when comparing the asymptotic responses as a function of the volume fraction (Fig. 4.12, Fig. 4.17 and Fig. 4.22), anyway considering the volume fraction interval in the present work, that is representative of the charge of fibers in composite filaments for HT-FRAM technology, the gaps between the mean-field schemes are not so significant which explains the closeness between all of them. In the same fashion, the effects

of the variations of the microstructural parameters (i.e. length and orientation distributions) representing the particular state of the fibers inside the composite filament are enhanced by Lielens approach. Regarding the effect of the variation of the orientation parameter m_{AT}, in Fig. 4.13, Fig. 4.18 and Fig. 4.23, the mean-field approach exhibits consistency in all cases when going from the more disoriented distribution (more isotropic) to the more filament axis aligned distribution (increasing the stiffness in the axis direction). However, the proposed methodology and the reference solutions are slightly closer in the cases where the fiber orientation disorder increases (lower values of the Advani and Tucker parameter). Finally, considering the variation of the length parameters w_0 and c_w, representing the mean length and intensification of the distribution around this value respectively. The simulation results are still consistent when considering combinations resulting in microstructures of long fibers and more or less homogeneous in distribution, with those that have a distribution of different lengths. The variations of the gaps are always on the same order, and as pointed out before, Lielens' scheme is always better at accounting the effect of these variations when comparing with reference solutions. From the aforementioned, one can conclude that any of these three methods could be a good choice, however it must be noted that if one aims to make an objective choice based on the quality and the complexity of the implementation, the choice should be the Mori-Tanaka Scheme.

Parameter	Values			
m_{AT}	2	10	60	-
c_w	0.5	1.5	2.5	-
w_0	20	30	40	-
$c^{(f)}$	0.1	0.2	0.3	0.4

Table 4.3: Microstructural parameters for simulations

Load case 1:

Due to the fact that the imposed macroscopic strain is $\bar{\boldsymbol{\varepsilon}}(t) = \mathbf{0}$, this case presents the highest levels of stress. The figure Fig. 4.12 showing the normalized asymptotic stress in function of the volume fraction allows seeing the effect of the reinforcement in the macroscopic behavior, then from the left to the right side the values of the normalized stress are always increasing as the effective relaxation moduli tensor increases in magnitude. The figure Fig. 4.13, showing the normalized asymptotic stress on-plane and on-axis, allows seeing the level of anisotropy in terms

of the principal directions $\boldsymbol{e}_1$ and $\boldsymbol{e}_3$. from the less to the most oriented, one can see how the level of isotropy decrease as the fibers become more organized around the filament axis, the ability of the probabilistic approach to map these variations is then verified because the gap between reference and mean-field solutions is almost consistent. From these figures, one can note that it is difficult to differentiate the gap between the different mean-field schemes implemented in the comparisons. Indeed, it seems that the three of them are giving high quality approximations. To be able to compare between them. The figure Fig. 4.14 and Fig. 4.15 showing the influence of the length distribution parameters shows small variations of the observed stress as these parameters varies; regarding Fig. 4.14 and considering that the fixed value of m_{AT} is 10 which represents a larger number of fibers in the filament axis direction (Fig. 4.6), one can note how the fact of increasing the number of fibers with a length that is close to the mean value $w_0 = 30$, significantly increases the asymptotic response of the stress in the filament axis direction compared to the behavior in the transverse plane. Looking at the variations of the asymptotic stress as a function of the mean length w_0, and holding the distribution parameter c_w to 1.5, a decrease in the asymptotic stress is observed as w_0 increases, this can be interpreted supported by Fig. 4.5 in which this fact gives as output a "more distributed" population of fibers but always being notably higher to the side of the shorter fibers, then as the diameter of fibers is considered constant the fact that shorter fibers are populating the REV gives an effective stiffness that is lower, ergo it is reasonable that the asymptotic stress decrease. From all the figures showing the asymptotic response, it is confirmed that despite the scheme chosen for the approximations, all of them are very close to the reference solutions. Anyway, Lielens scheme is always slightly better in all situations.

Load case 2:

In this case, the macroscopic stress $\bar{\boldsymbol{\sigma}}$ is set to $\mathbf{0}$ in the REV, therefore the corresponding strain solution is equal to the macroscopic thermal strain, since it is the only source of deformation in the REV. As can be noted from the figures of this case (Figs. 4.16-4.20), the computed macroscopic strains remain inside the linear domain, which validates the material model adopted in the present work, that is linear viscoelastic. The figure Fig. 4.16 showing the evolution of the strain elements in function of temperature confirms the consistency of the methodology when computing stress or strain. Similarly to the load case 1, in figure Fig. 4.18 the degree of anisotropy is controlled

via the values of m_{AT}, the effect of the reinforcement in the macroscopic strain presented in Fig. 4.17 shows the high accuracy of the proposed procedure as the solutions are very close to the reference (FFT), specially when regarding the filament axis direction ($\boldsymbol{e}_3$). When looking figures Fig. 4.19 and Fig. 4.20 one can note how the macroscopic strain decreases as the parameters increases, this represents the fact that the mean length of the fibers increases and the number of fibers associated to this value increases.

Load case 3:

This is the case of mixed macroscopic constraints, here the laminate case, in which the stacking direction is $\boldsymbol{e}_2$. Results are presented in the same way as the precedent load cases, Fig. 4.21 shows the evolution of the showing the non-zero elements of the mechanical response ($\bar{\varepsilon}_{22} = \bar{\varepsilon}_{11}$ and $\bar{\sigma}_{33}$) in function of temperature. In agreement with the precedent cases, the solutions plotted show remarkable accuracy compared to reference solutions in both, stress and strain. Similarly to the precedent load cases, the influence of the microstructural parameters in presented in figures Fig. 4.22- 4.25. In the same way as for the precedent load cases, Lielens schemes seems to be slightly better when estimating both, macroscopic stress or strain.

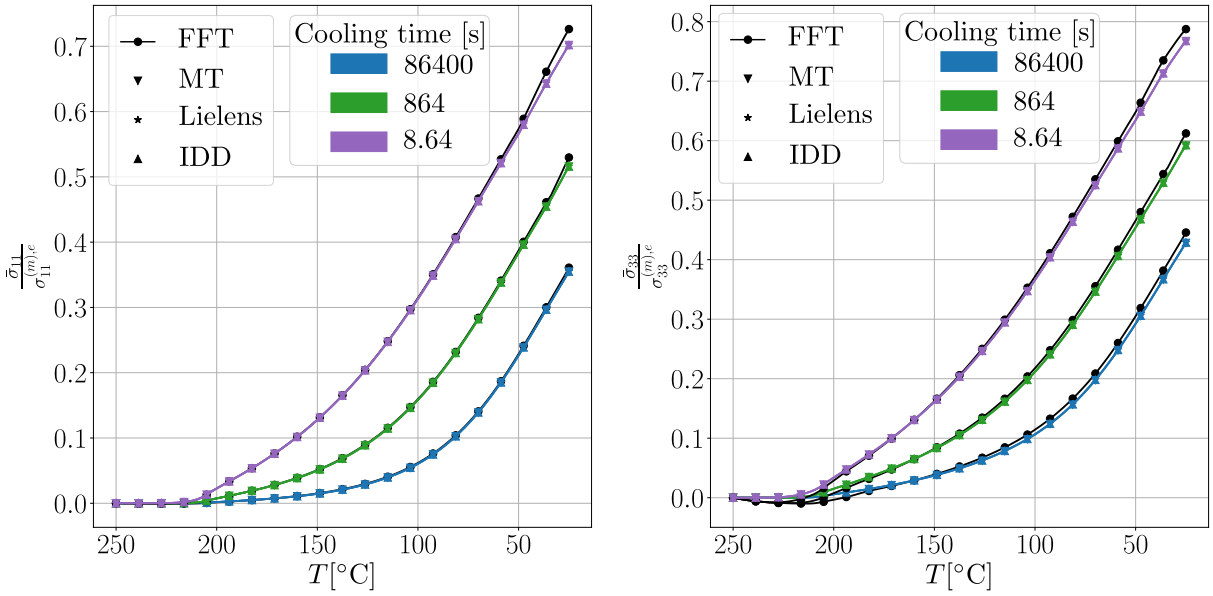

(a) On-plane residual stress (σ_{11}). (b) Filament axis residual stress (σ_{33}).

Figure 4.11: Normalized stress vs. temperature (T), computed for load case 1, $c^{(f)} = 0.2$, $m_{\mathrm{AT}} = 10$, $c_w = 1.5$ and $w_0 = 30$.

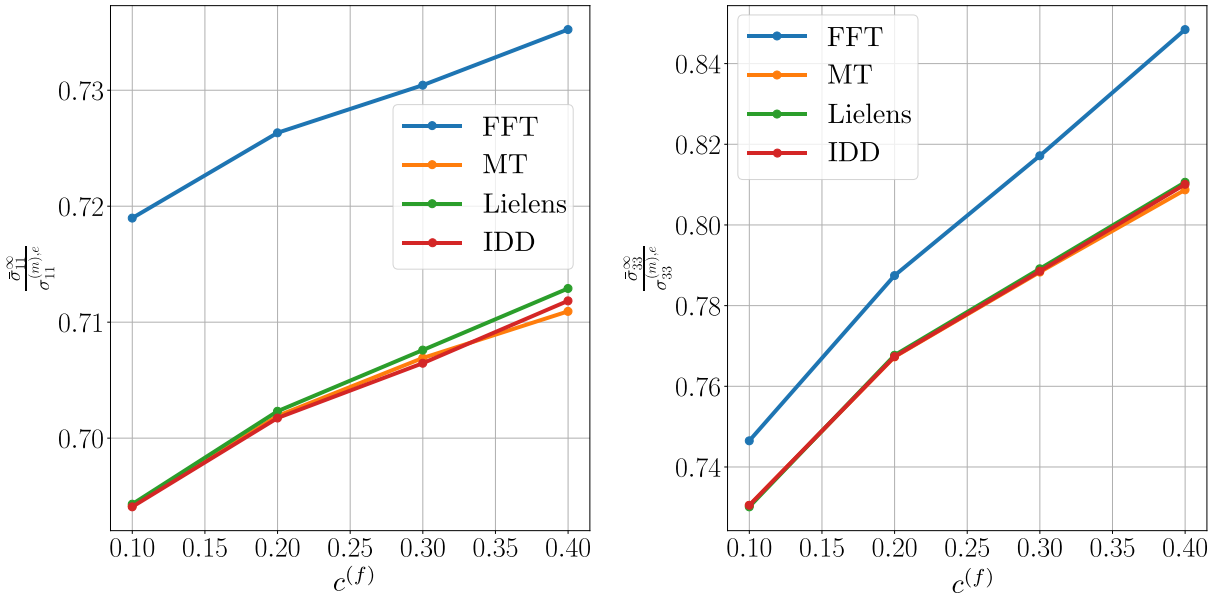

(a) On-plane residual stress (σ_{11}). (b) Filament axis residual stress (σ_{33}).

Figure 4.12: Asymptotic normalized stress vs. the volume fraction ($c^{(f)}$), computed for load case 1, Cooling time = 8.64[s], $m_{\text{AT}} = 10$, $c_w = 1.5$ and $w_0 = 30$.

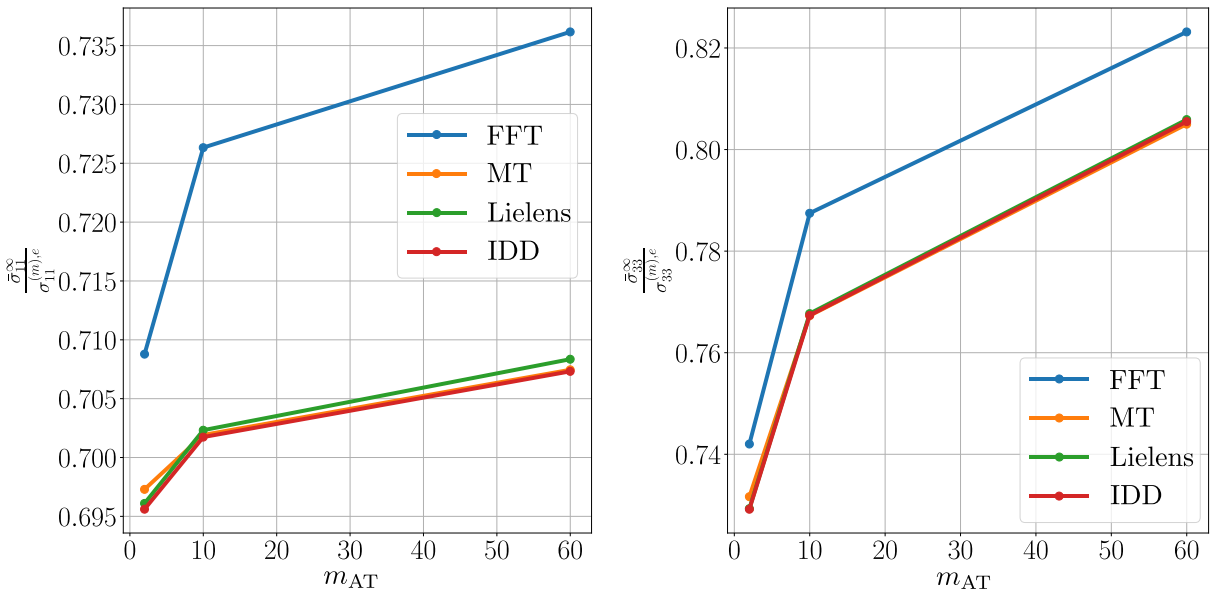

(a) On-plane residual stress (σ_{11}). (b) Filament axis residual stress (σ_{33}).

Figure 4.13: Asymptotic normalized stress vs. the Advani-Tucker parameter m_{AT}, computed for load case 1, Cooling time = 8.64[s], $c^{(f)} = 0.2$, $c_w = 1.5$ and $w_0 = 30$.

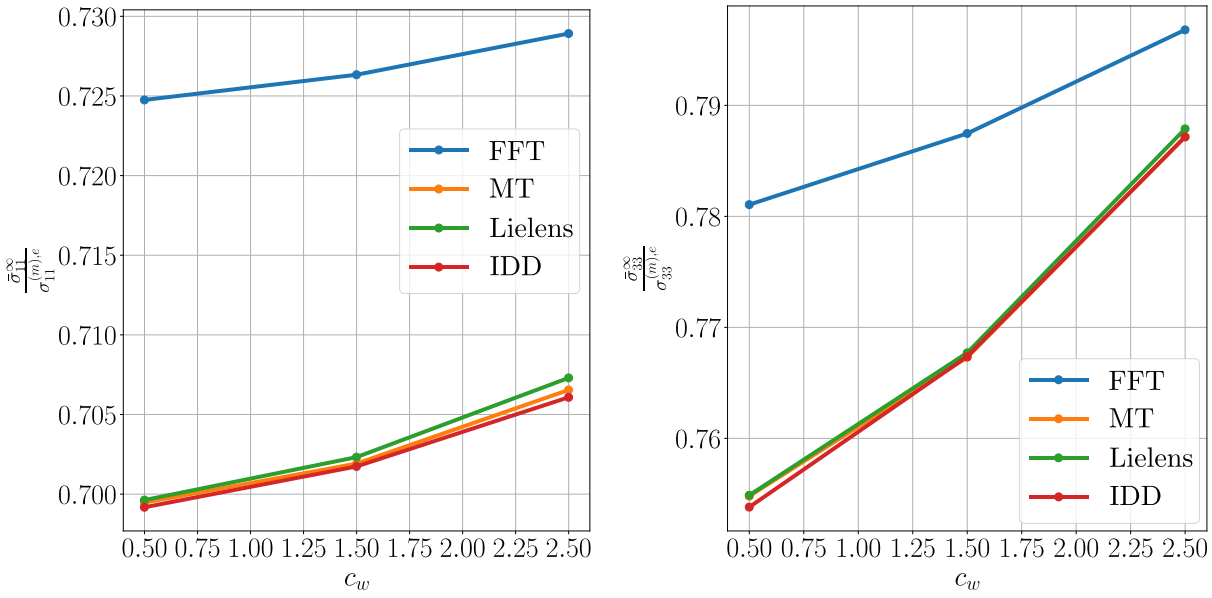

(a) On-plane residual stress (σ_{11}). (b) Filament axis residual stress (σ_{33}).

Figure 4.14: Asymptotic normalized stress vs. the Weibull's parameter c_w, computed for load case 1, Cooling time = 8.64[s], $c^{(f)} = 0.2$, $m_{\text{AT}} = 10$ and $w_0 = 30$.

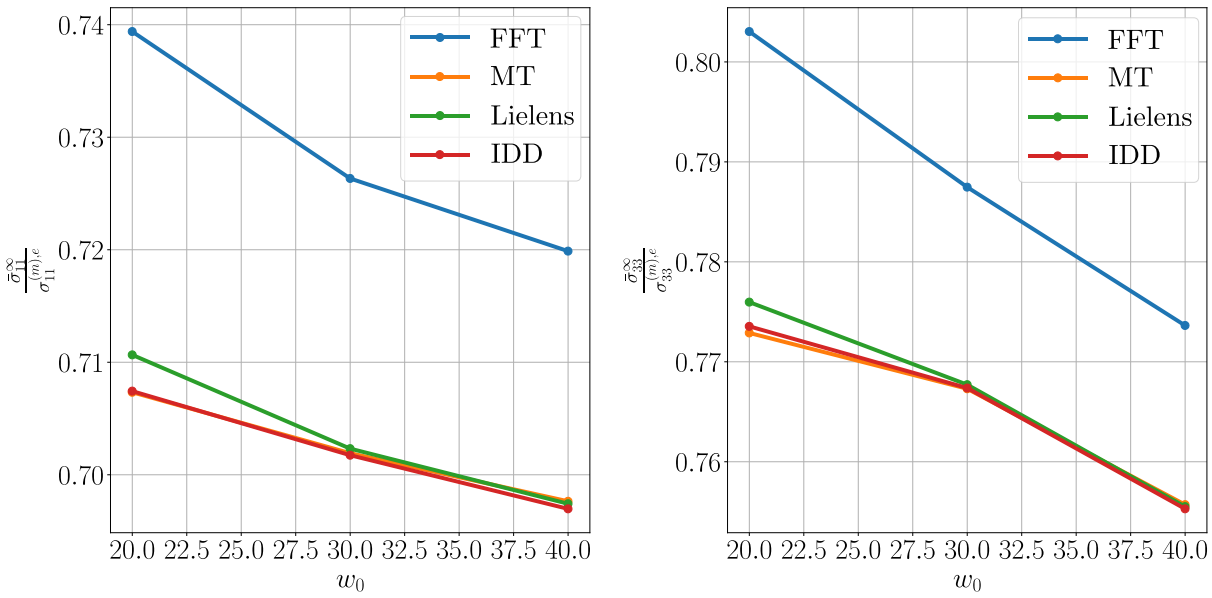

(a) On-plane residual stress (σ_{11}). (b) Filament axis residual stress (σ_{33}).

Figure 4.15: Asymptotic normalized stress vs. the Weibull's parameter w_0, computed for load case 1, Cooling time = 8.64[s], $c^{(f)} = 0.2$, $m_{\text{AT}} = 10$ and $c_w = 1.5$.

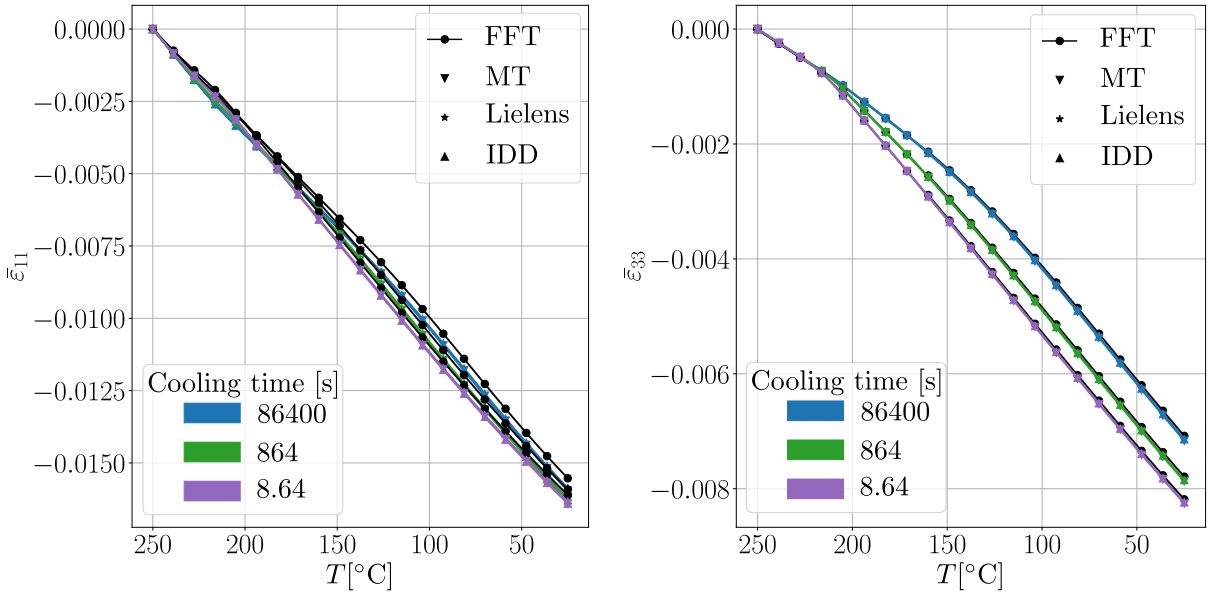

(a) On-plane residual strain (ε_{11}). (b) Filament axis residual strain (ε_{33}).

Figure 4.16: Strain vs. temperature (T), computed for load case 2, $c^{(f)} = 0.2$, $m_{\text{AT}} = 10$, $c_w = 1.5$ and $w_0 = 30$.

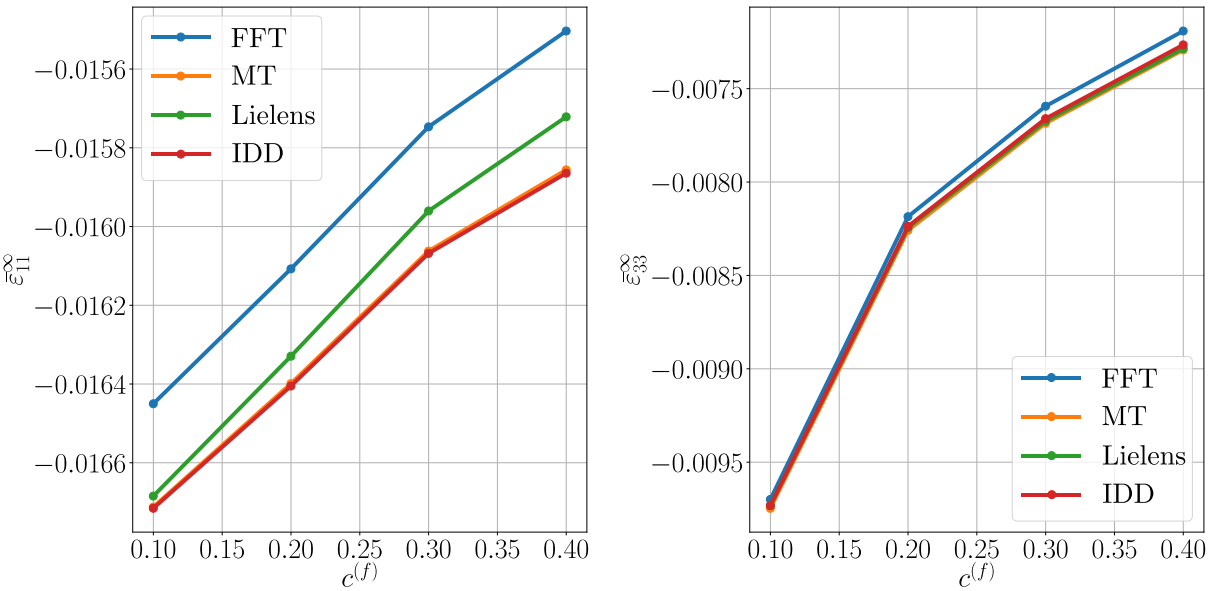

(a) On-plane residual strain (ε_{11}). (b) Filament axis residual strain (ε_{33}).

Figure 4.17: Asymptotic strain vs. the volume fraction ($c^{(f)}$), computed for load case 2, Cooling time = 8.64[s], $m_{\text{AT}} = 10$, $c_w = 1.5$ and $w_0 = 30$.

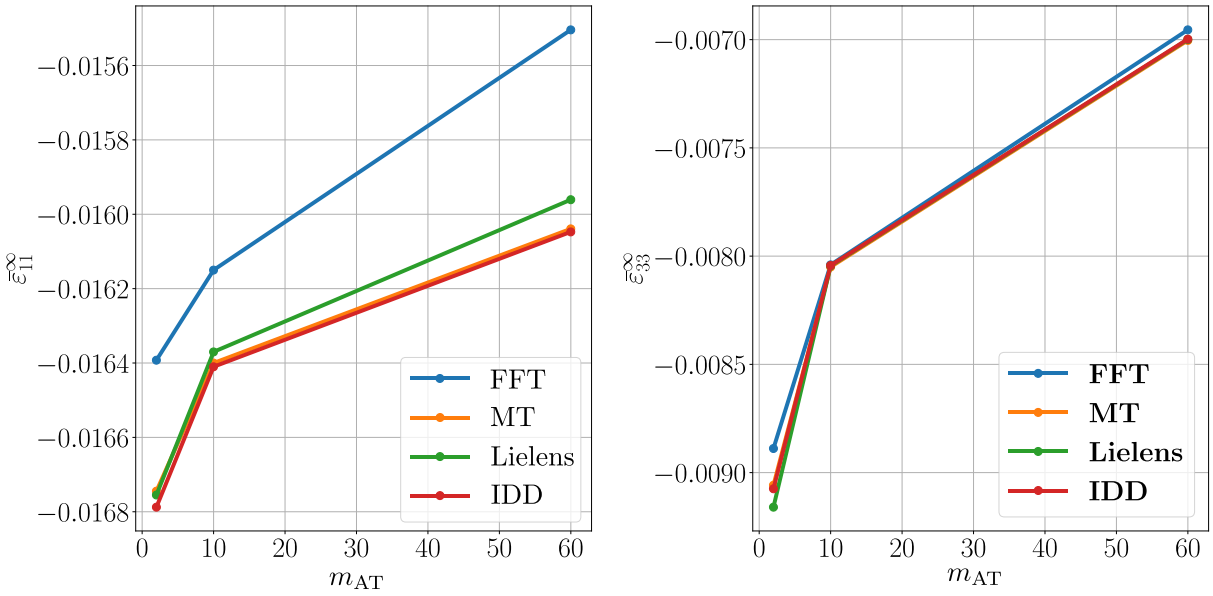

(a) On-plane residual strain (ε_{11}). (b) Filament axis residual strain (ε_{33}).

Figure 4.18: Asymptotic strain vs. the Advani-Tucker parameter (m_{AT}), computed for load case 2, Cooling time= 8.64[s], $c^{(f)} = 0.2$, $c_w = 1.5$ and $w_0 = 30$.

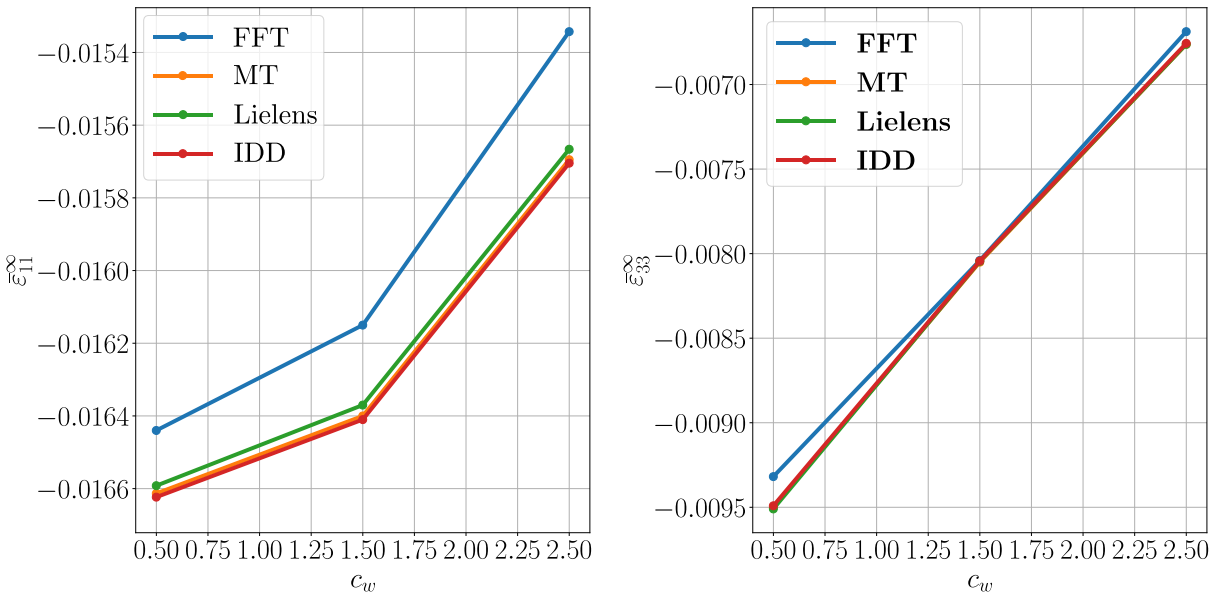

(a) On-plane residual strain (ε_{11}). (b) Filament axis residual strain (ε_{33}).

Figure 4.19: Asymptotic strain vs. the Weibull parameter c_w, computed for load case 2, Cooling time = 8.64[s], $c^{(f)} = 0.2$, $m_{\mathrm{AT}} = 10$ and $w_0 = 30$.

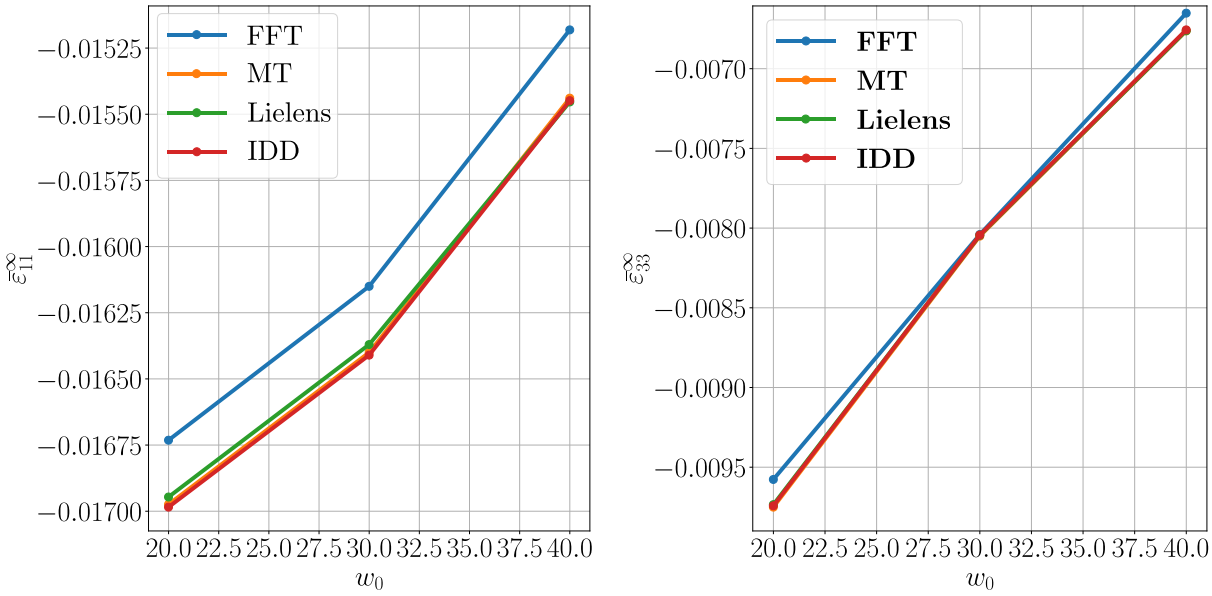

(a) On-plane residual strain (ε_{11}). (b) Filament axis residual strain (ε_{33}).

Figure 4.20: Asymptotic strain vs. the Weibull parameter w_0, computed for load case 2, Cooling time = 8.64[s], $c^{(f)} = 0.2$, $m_{\mathrm{AT}} = 10$ and $c_w = 1.5$.

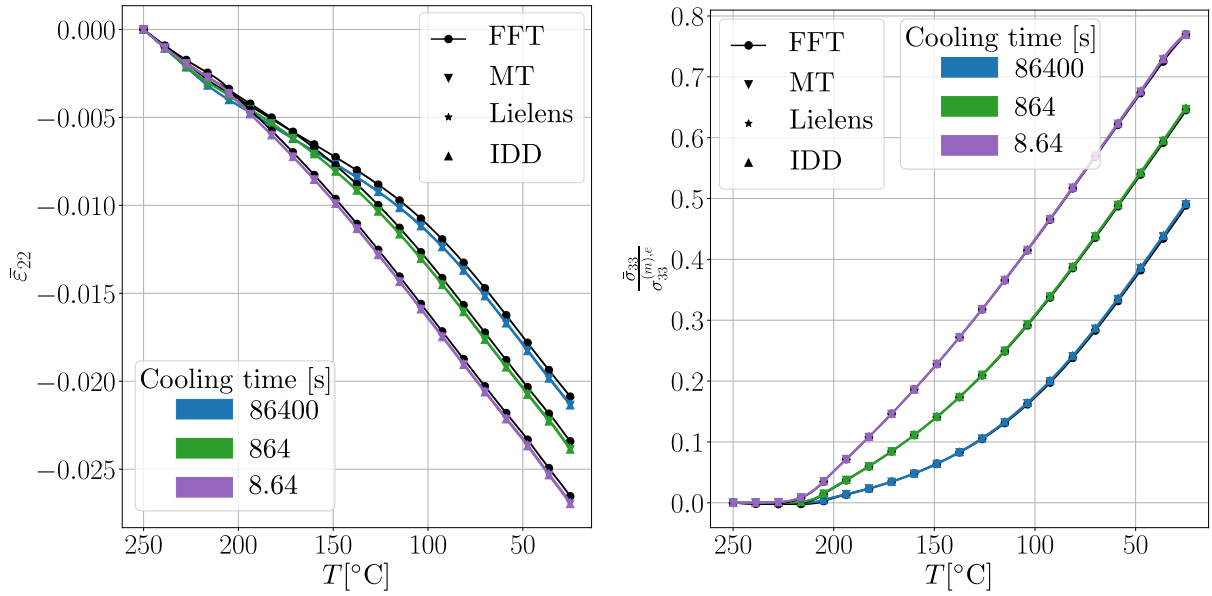

(a) On-plane residual strain (ε_{11}). (b) Filament axis residual stress (σ_{33}).

Figure 4.21: Strain and normalized stress response vs. temperature (T), computed for load case 3, $c^{(f)} = 0.2$, $m_{\mathrm{AT}} = 10$, $c_w = 1.5$ and $w_0 = 30$.

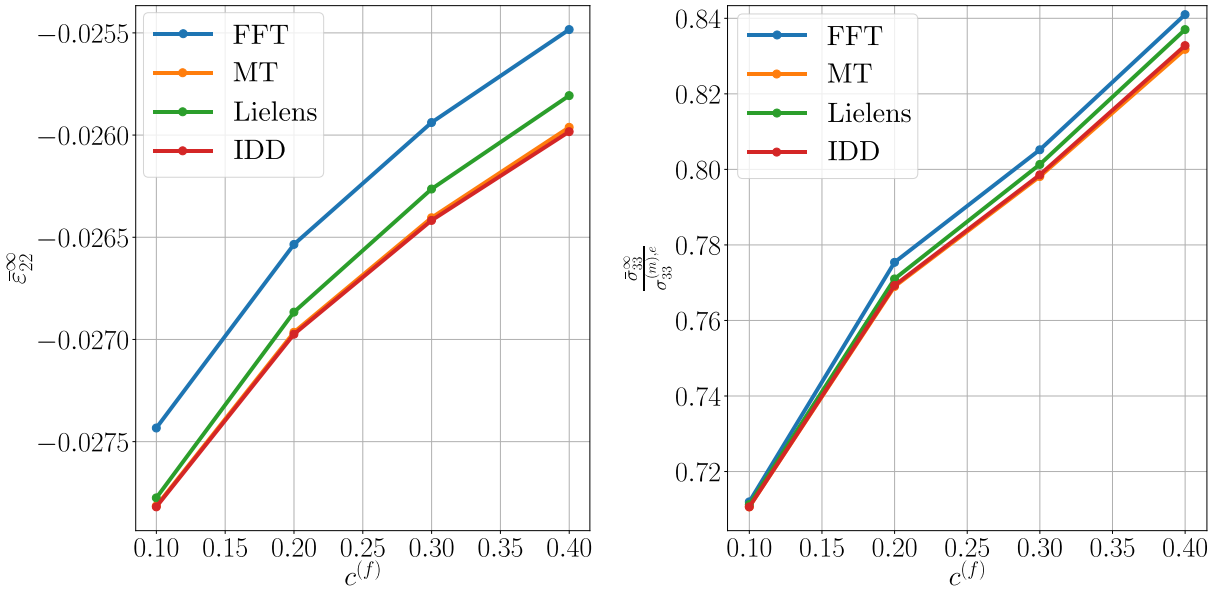

(a) On-plane residual strain (ε_{11}). (b) Filament axis residual stress (σ_{33}).

Figure 4.22: Asymptotic strain and normalized stress response vs. the volume fraction ($c^{(f)}$), computed for load case 3, Cooling time = 8.64[s], $m_{\text{AT}} = 10$, $c_w = 1.5$ and $w_0 = 30$.

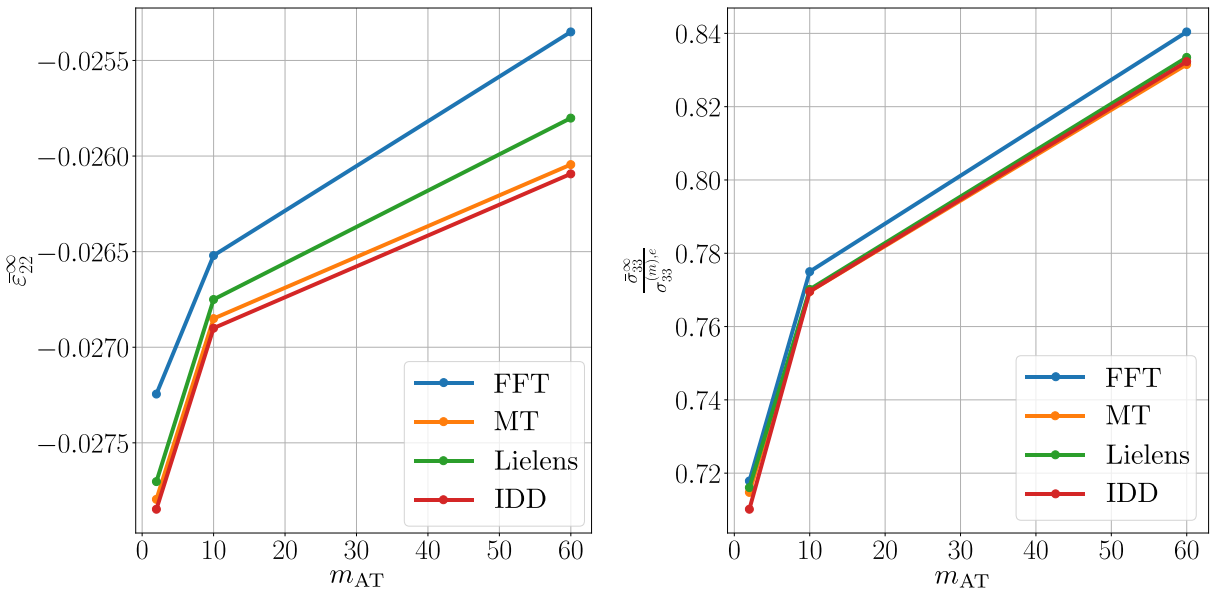

(a) On-plane residual strain (ε_{11}). (b) Filament axis residual stress (σ_{33}).

Figure 4.23: Asymptotic strain and normalized stress response vs. the Advani-Tucker parameter m_{AT}, computed for load case 3, Cooling time = 8.64[s], $c^{(f)} = 0.2$, $c_w = 1.5$ and $w_0 = 30$.

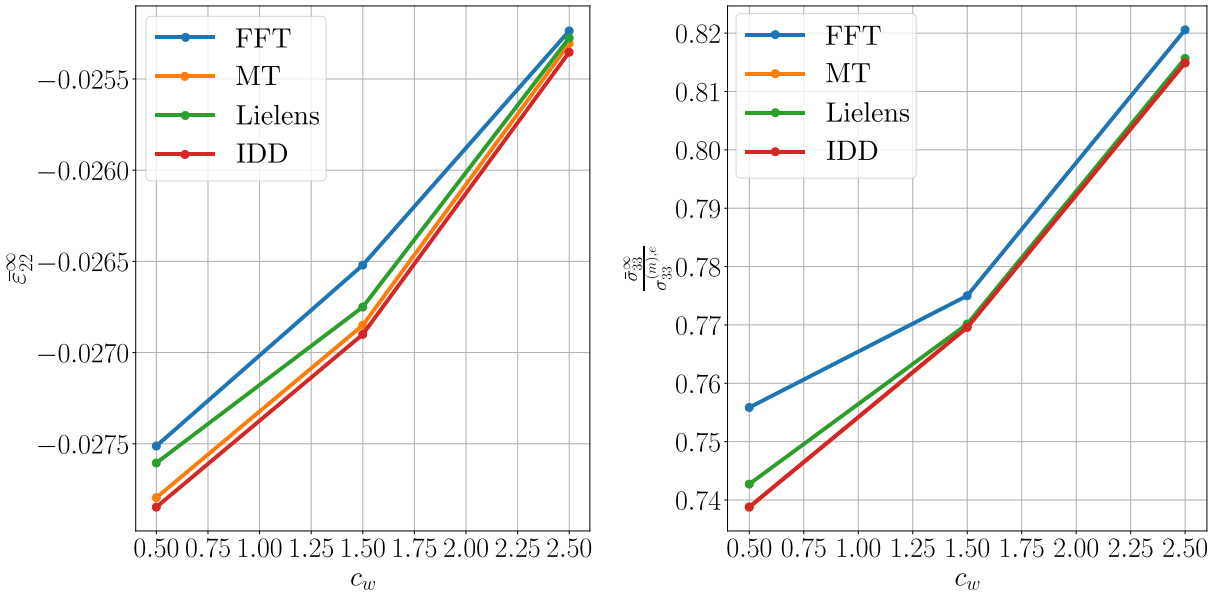

(a) On-plane residual strain (ε_{11}). (b) Filament axis residual stress (σ_{33}).

Figure 4.24: Asymptotic strain and normalized stress response vs. the Weibull's parameter c_w, computed for load case 3, Cooling time = 8.64[s], $c^{(f)} = 0.2$, $m_{\text{AT}} = 10$ and $w_0 = 30$.

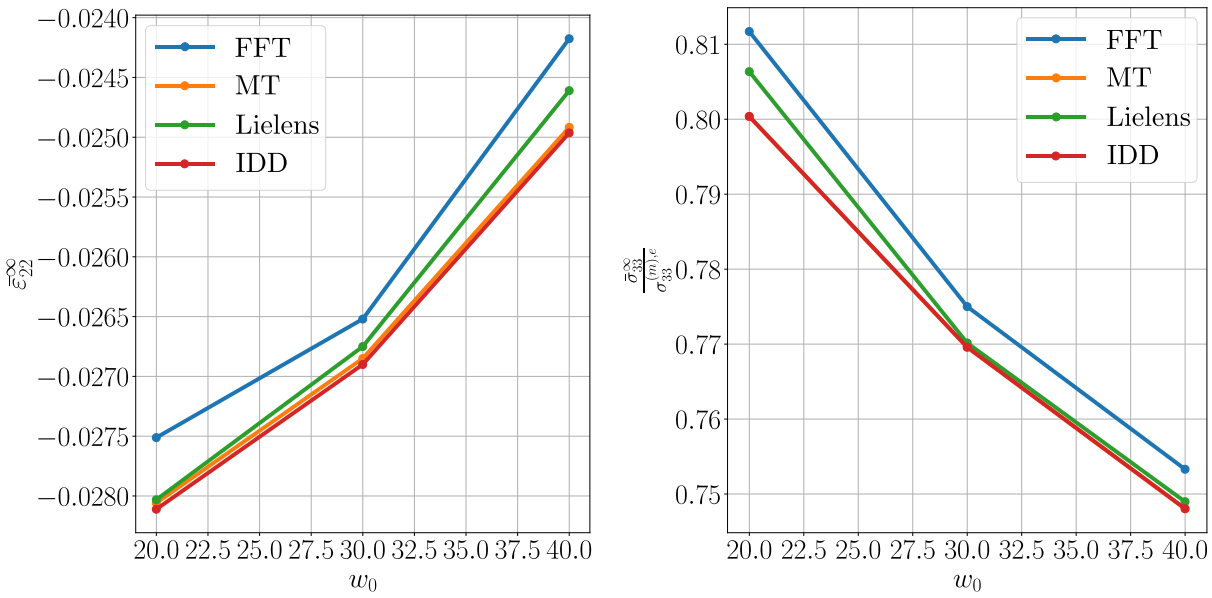

(a) On-plane residual strain (ε_{11}). (b) Filament axis residual stress (σ_{33}).

Figure 4.25: Asymptotic strain and normalized stress response vs. the Weibull's parameter w_0, computed for load case 3, Cooling time = 8.64[s], $c^{(f)} = 0.2$, $m_{\text{AT}} = 10$ and $c_w = 1.5$.

4.4 Final comments

As it was shown in the simulations section, the proposed procedure to compute the effective macroscopic behavior of an SPC filament exhibits a remarkable accuracy compared to the full-field simulations for all the different REVs that were tested. In addition, this fact confirms the validity of the probabilistic description of the fibers' microstructural parameters (i.e. length and orientation). This procedure holds consistency when computing the mechanical response (stress or strain) when different mechanical constraints are applied. The accuracy of the procedure was verified when different cooling rates are applied in the thermal history, then confirming the good agreement when considering the instantaneous or delayed components of the macroscopic mechanical responses. The highlights of the proposed methodoly are:

- Polymer matrix representation that holds thermodynamic consistency; being able to map the delayed response in terms of volume variations in function of temperature, reproducing the transitional states from rubbery to glassy behavior. This fact is indeed of primal importance, as the nature of the manufacturing process imposes the thermal strain as the main source of residual stress and dimensional instability in an HT-FRAM 3D-printed composite part.

- Concise methodology, constructed around practical and functional choices, giving to the formulation simplicity while conserving its reliability, reducing dramatically the time of computations when comparing to full-field analysis (Table. 4.2). This is achieved through the introduction of the extension of analytical homogenization in the context of thermo-viscoelasticity via the internal-time technique for the correspondence principle in continuous variations of temperature, and ensuring the mathematical representation of the composite in the same way as the matrix by introducing an identification step, able to identify optimal values of the discrete spectra when no noisy data is used.

- Efficient implementation of the estimation of the influence of the variability of length and orientations in the effective behavior by implementing probabilistic descriptions of the parameters' distributions. Giving a plus in simplicity of formulation while being a more accurate description of the general state of the composite.

- High accurate Methodology to approximate effective thermo-viscoelastic behavior in discontinuous-

fiber reinforced amorphous polymers, with high capacity of adaptation in finite elements commercial software products, as it has already been tested (Abaqus and Digimat).

In terms of perspectives, the next step will be to model the effective thermo-viscoelastic behavior of the printed part at the upper scale with the porosities due to the stacking of the filaments (mesoscale) by integrating the effective behavior model of the composite filament proposed in this paper and the topology of the porosities to solve the thermomechanical structure calculation in order to predict the warping of the HT FRAM 3D-printed part and to compare against experiments performed in simple structures.

Chapter 5

Microscale Analysis : thermorheologically complex material

In this chapter we will address a special apart to treat the thermorheologically complex solids, this is the case in which the unicity of the shift function a_T is no longer ensured, equivalently to the case in which the polymer matrix can no longer be modeled as it was presented in Chapter 1. This work is already published in the *European journal of Mechanics - A/Solids* [6]. The applicability of the mean-field homogenization in ensured through a model order reduction of the thermo-viscoelastic homogenization problem. Analytical verification is considered for exact forms derived form conventional mean-field estimates as it is demonstrated in Chapter 4. Using the same material properties of that chapter a numercial simulation section is presented to compare conventional y reduced models in the case of rigid reinforments of continuous fiber composites.

During their consolidation, reinforced polymers develop internal stresses due to the pronounced mismatch between the thermomechanical properties of the matrix and the reinforcement [123]. These so-called thermal residual stresses can significantly reduce the mechanical strength and fatigue endurance of the composite material, and can induce undesired dimensional changes of the structural element [124]. This has motivated numerous attempts to correlate the magnitude of residual stresses with material and process parameters such as matrix rheology, reinforcement shape and distribution, and cooling rate [125, 126, 127, 128, 129]. In the absence

of chemical changes —as in amorphous thermoplastics—, the problem reduces to that of estimating the macroscopic behavior and microscopic field statistics of a viscoelastic composite in terms of the thermomechanical properties and microgeometrical arrangement of its constituents. The use of mean-field descriptions derived by homogenization methods thus constitutes an effectual approach. However, given that consolidation processes often vary the temperature of the sample across the glass transition temperature of the thermoplastic matrix, the method of choice should account for the strong coupling between elastic and viscous deformation mechanisms along with the strong variation of matrix rheology with temperature. This hinders the use of most mean-field descriptions commonly employed for describing isothermal processes, especially if the matrix response is thermorheologically complex in the sense of [130]. The sections that follow present mean-field descriptions adequate for such situations.

The descriptions follow from a homogenization procedure proposed by [131] for composites undergoing isothermal deformations, recast as in [132] and generalized to non-isothermal processes. Thus, the thermo-viscoelastic response of the constituent phases is described in Section 5.1 via generalized standard models in terms of viscous deformations that play the role of microscopic internal variables. Given that the homogenized thermo-viscoelastic response of the composite then depends on the entire spatial distribution of these microscopic internal variables over a representative volume element, a variational model reduction is then employed in Section 5.2 to generate an approximate homogenized description in terms of a finite number of macroscopic internal variables identified with low-order statistics of the microscopic internal variable fields. Unlike descriptions based on the correspondence principle [59, 133], the reduced-order mean-field descriptions thus obtained can account for thermorheologically complex constitutive laws with multiple internal times —or even none— and can provide information not only on the macroscopic response but also on statistics of the microscopic mechanical fields up to second order. Furthermore, it is demonstrated that these descriptions can also accommodate a special class of hereditary laws of common use in polymer science. Simple expressions for material systems with elastically rigid but thermally dilatant reinforcements are provided in Section 5.3. In order to assess the capabilities of the reduced descriptions, results are generated in Section 5.4 for a special class of rigidly reinforced solids whose effective response can be determined exactly by means of the correspondence principle. The reduced and exact descriptions for this reinforced solids are confronted and discussed in Section 5.5. The presentation concludes with

final comments elaborated in Section 5.6.

5.1 Material description

5.1.1 Microscopic description

We consider a representative volume element of a composite material made up of N constituent phases, and denote by Ω and $\Omega^{(r)}$ $(r = 1, ..., N)$ the domains occupied by the element and the phases within it, respectively, so that $\Omega = \cup_{r=1}^{N} \Omega^{(r)}$. Also, we denote by $\chi^{(r)}(\mathbf{x})$ the characteristic function of each subdomain $\Omega^{(r)}$. Let's assume that the local viscoelastic response can be described within the framework of generalized standard materials by constitutive relations of the form [134]

$$\boldsymbol{\sigma} = \frac{\partial w}{\partial \boldsymbol{\varepsilon}}(\mathbf{x}, \boldsymbol{\varepsilon}, \boldsymbol{q}, \theta) \quad \text{and} \quad \frac{\partial w}{\partial \boldsymbol{q}}(\mathbf{x}, \boldsymbol{\varepsilon}, \boldsymbol{q}, \theta) + \frac{\partial \varphi}{\partial \dot{\boldsymbol{q}}}(\mathbf{x}, \dot{\boldsymbol{q}}, \theta) = \mathbf{0}, \tag{5.1}$$

where

$$w(\mathbf{x}, \boldsymbol{\varepsilon}, \boldsymbol{q}, \theta) = \sum_{r=1}^{N} \chi^{(r)}(\mathbf{x}) w^{(r)}(\boldsymbol{\varepsilon}, \boldsymbol{q}, \theta) \quad \text{and} \quad \varphi(\mathbf{x}, \dot{\boldsymbol{q}}, \theta) = \sum_{r=1}^{N} \chi^{(r)}(\mathbf{x}) \varphi^{(r)}(\dot{\boldsymbol{q}}, \theta). \tag{5.2}$$

In these expressions, $\boldsymbol{\varepsilon}$ and θ denote the strain and temperature change relative to a stress-free reference configuration, $\boldsymbol{q}$ is a collection of internal variables describing viscous effects, the dot over a variable denotes a time derivative, and the functions $w^{(r)}$ and $\varphi^{(r)}$ denote, respectively, the Helmholtz free-energy density and the dissipation potential of phase r. These potentials are convex functions of the mechanical fields and are bounded from below. The dissipation potentials are, at the same time, positive functions vanishing at the origin.

For our purposes, it suffices to consider viscoelastic phases characterized by generalized Maxwell rheologies with an arbitrary number of viscoelastic units. To each unit we associate a

viscous strain tensor $\boldsymbol{q}^{(u)}$ $(u = 1, ..., U)$ and write the thermodynamic potentials as

$$w^{(r)}(\boldsymbol{\varepsilon}, \boldsymbol{q}, \theta) = \sum_{u=1}^{U} \frac{1}{2} \left(\boldsymbol{\varepsilon} - \boldsymbol{\beta}^{(r)}(\theta) - \boldsymbol{q}^{(u)}\right) \cdot \mathbb{L}^{(r,u)}(\theta) \left(\boldsymbol{\varepsilon} - \boldsymbol{\beta}^{(r)}(\theta) - \boldsymbol{q}^{(u)}\right) + f^{(r)}(\theta) \quad \text{and} \tag{5.3}$$

$$\varphi^{(r)}(\dot{\boldsymbol{q}}, \theta) = \sum_{u=1}^{U} \frac{1}{2} \dot{\boldsymbol{q}}^{(u)} \cdot \mathbb{M}^{(r,u)}(\theta) \dot{\boldsymbol{q}}^{(u)}, \tag{5.4}$$

where $\mathbb{L}^{(r,u)}$ and $\mathbb{M}^{(r,u)}$ denote positive-definite tensors of elastic and viscous moduli, respectively, characterizing the u^{th} unit of the rheological model for phase r, and $\boldsymbol{\beta}^{(r)}$ is the corresponding thermal straining. The form of these potentials is motivated by a rheological model corresponding to U units of the Maxwellian type connected in parallel, along with a thermal unit connected in series, as depicted in figure 1.2. It generates constitutive relations and evolution equations of the form

$$\boldsymbol{\sigma} = \sum_{u=1}^{U} \mathbb{L}^{(r,u)}(\theta) \left(\boldsymbol{\varepsilon} - \boldsymbol{\beta}^{(r)}(\theta) - \boldsymbol{q}^{(u)}\right) \tag{5.5}$$

and

$$\mathbb{M}^{(r,u)}(\theta) \dot{\boldsymbol{q}}^{(u)} + \mathbb{L}^{(r,u)}(\theta) \boldsymbol{q}^{(r,u)} = \mathbb{L}^{(r,u)}(\theta) \left(\boldsymbol{\varepsilon} - \boldsymbol{\beta}^{(r)}(\theta)\right). \tag{5.6}$$

The elastic stiffness of the material is thus

$$\mathbb{L}^{(r)}(\theta) = \sum_{u=1}^{U} \mathbb{L}^{(r,u)}(\theta). \tag{5.7}$$

This model can accommodate any variation of material properties with instant temperature change, provided it satisfies the requirements imposed on the thermodynamic potentials.

5.1.2 Macroscopic description

The homogenized mechanical response relates the macroscopic stress $\overline{\boldsymbol{\sigma}}$ to the macroscopic strain $\overline{\boldsymbol{\varepsilon}}$ and temperature change $\overline{\theta}$, which are the averages of the local stress, strain, and temperature fields over the representative volume element. This relation can be written in terms of the

macroscopic free-energy density and dissipation potential as [134, 135]

$$\overline{\boldsymbol{\sigma}} = \frac{\partial \overline{w}}{\partial \overline{\boldsymbol{\varepsilon}}}(\overline{\boldsymbol{\varepsilon}}, \boldsymbol{q}, \overline{\theta}) \quad \text{and} \quad \frac{\delta \overline{w}}{\delta \boldsymbol{q}(\mathbf{x})}(\overline{\boldsymbol{\varepsilon}}, \boldsymbol{q}, \overline{\theta}) + \frac{\delta \overline{\varphi}}{\delta \dot{\boldsymbol{q}}(\mathbf{x})}(\dot{\boldsymbol{q}}, \overline{\theta}) = \mathbf{0}, \tag{5.8}$$

where

$$\overline{w}(\overline{\boldsymbol{\varepsilon}}, \boldsymbol{q}, \overline{\theta}) = \inf_{\boldsymbol{\varepsilon} \in \mathcal{K}(\overline{\boldsymbol{\varepsilon}})} \big\langle w(\mathbf{x}, \boldsymbol{\varepsilon}, \boldsymbol{q}, \overline{\theta}) \big\rangle \quad \text{and} \quad \overline{\varphi}(\dot{\boldsymbol{q}}, \overline{\theta}) = \big\langle \varphi(\mathbf{x}, \dot{\boldsymbol{q}}, \overline{\theta}) \big\rangle. \tag{5.9}$$

In these expressions, $\mathcal{K}(\overline{\boldsymbol{\varepsilon}})$ is the set of kinematically admissible strain fields with average $\overline{\boldsymbol{\varepsilon}}$, $\langle \cdot \rangle$ denotes volume averaging over the representative volume element, and the δ operator denotes a functional derivative. That the temperature change within the entire representative volume element is uniformly given by the macroscopic temperature change $\overline{\theta}$ has been found in multiple works with varying degrees of rigor and generality [136, 115, 137, 138] provided the local thermodynamic potentials satisfy certain mathematical properties that are assumed to hold in this work.

It is observed that the macroscopic free-energy density and dissipation potential are the volume averages of their microscopic counterparts, and are therefore functionals of the microscopic viscous strain fields and their rates. In the case of the generalized Maxwellian rheologies considered in this work, they take the forms

$$\overline{w}(\overline{\boldsymbol{\varepsilon}}, \boldsymbol{q}, \overline{\theta}) = \inf_{\boldsymbol{\varepsilon} \in \mathcal{K}(\overline{\boldsymbol{\varepsilon}})} \sum_{r=1}^{N} \sum_{u=1}^{U} c^{(r)} \left\langle \frac{1}{2} \left(\boldsymbol{\varepsilon} - \boldsymbol{\beta}^{(r)}(\overline{\theta}) - \boldsymbol{q}^{(u)} \right) \cdot \mathbb{L}^{(r,u)}(\overline{\theta}) \left(\boldsymbol{\varepsilon} - \boldsymbol{\beta}^{(r)}(\overline{\theta}) - \boldsymbol{q}^{(u)} \right) \right\rangle^{(r)} \tag{5.10}$$

and

$$\overline{\varphi}(\dot{\boldsymbol{q}}, \overline{\theta}) = \sum_{r=1}^{N} \sum_{u=1}^{U} c^{(r)} \left\langle \frac{1}{2} \dot{\boldsymbol{q}}^{(u)} \cdot \mathbb{M}^{(r,u)}(\overline{\theta}) \dot{\boldsymbol{q}}^{(u)} \right\rangle^{(r)}, \tag{5.11}$$

where the functions $f^{(r)}$ have been dropped to shorten notation, given their irrelevance to the stress response and our disinterest in the entropic response of the solid. These functionals inherit the convexity of the local potentials. Thus, homogenization preserves the generalized standard structure of the local reponse, with the microscopic viscous strain fields playing the role of macroscopic internal variables albeit of *infinite* dimension. The purpose of the approximate

scheme presented in the next section is to reduce the dimensionality of the macroscopic internal variables to a *finite* number.

5.1.3 Extension to a class of hereditary responses

Thermal strains in polymers near the glass transition temperature are time dependent and can exhibit significant differences depending on whether heating or cooling occurs. Hereditary laws are often employed to describe such behavior [50]. While the formalism presented above along with the model reduction presented below are cast in terms of internal-variable laws, they remain valid *ut stat* for more general constitutive laws of the form (5.5)-(5.6) with the dependence on temperature change θ replaced by a dependence on temperature change history θ^t up to time t as defined by $\theta^t(\tau) = \theta(t-\tau)$ for $0 \leq \tau < \infty$, provided the replacement maintains the validity of the homogenization procedure leading to the macroscopic description (5.8)-(5.9). This is because the equilibrium conditions and the evolution laws for the internal variables within such representative volume element still follow from the macroscopic potentials (5.10) and (5.11) —now functionals of the macroscopic temperature change histories $\overline{\theta}^t$—, and the incremental statement (5.13) still constitutes a valid time discretization of those evolution laws. On the other hand, the thermodynamic status of the potentials may be altered [cf., e.g., 139, 140].

5.2 Reduced-order description

5.2.1 Model reduction

Central to our purposes is the observation that the model reduction for viscoelastic composites proposed by [131] carries over to thermo-viscoelastic composites unaltered, regardless of the variation of mechanical properties with temperature. This model reduction relies on an implicit Euler discretization in time of the macroscopic evolution law $(5.8)_2$, so that the internal variables at the current instant are the solution to the algebraic equation

$$\frac{\delta \overline{w}}{\delta \boldsymbol{q}(\mathbf{x})}(\overline{\boldsymbol{\varepsilon}}, \boldsymbol{q}, \overline{\theta}) + \frac{\delta \overline{\varphi}}{\delta \dot{\boldsymbol{q}}(\mathbf{x})}\left(\frac{\boldsymbol{q} - \boldsymbol{q}_n}{\Delta t}, \overline{\theta}\right) = \mathbf{0}, \tag{5.12}$$

where $\boldsymbol{q}_n$ are the values of the internal variables in the previous instant and Δt is the time step. In view of the convexity of the macroscopic potentials, this equation is the optimality condition

of the variational problem

$$\inf_{\boldsymbol{q}} \left[\overline{w}(\overline{\boldsymbol{\varepsilon}}, \boldsymbol{q}, \overline{\theta}) + \Delta t \; \overline{\varphi} \left(\frac{\boldsymbol{q} - \boldsymbol{q}_n}{\Delta t}, \overline{\theta} \right) \right]. \tag{5.13}$$

As recently elicited by [132], the model reduction of [131] is effected upon estimating each phase average in the discretized dissipation (5.11) by Cauchy-Schwarz lower bounds. In practice, these bounds are applied on suitably chosen projections by expressing the constitutive tensors as

$$\mathbb{L}^{(r,u)}(\theta) = \sum_{b=1}^{B} \ell^{(r,u,b)}(\theta) \; \mathbb{B}^{(r,u,b)} \quad \text{and} \quad \mathbb{M}^{(r,u)}(\theta) = \sum_{b=1}^{B} m^{(r,u,b)}(\theta) \; \mathbb{B}^{(r,u,b)}, \tag{5.14}$$

where $\mathbb{B}^{(r,u,b)}$ are fourth-order symmetric tensors such that $\mathbb{B}^{(r,u,b)}\mathbb{B}^{(r,d)} = 0$ if $b \neq d$ and the moduli $\ell^{(r,u,b)}$ and $m^{(r,u,b)}$ are all positive functions of temperature [141]. For instance, within an isotropic phase use can be made of the decomposition $\mathbb{B}^{(r,1)} = \mathbb{J}$ and $\mathbb{B}^{(r,2)} = \mathbb{K}$ with $B = 2$, where $\mathbb{J}$ and $\mathbb{K}$ are the standard fourth-order, isotropic, hydrostatic and shear projection tensors, respectively. The macroscopic potentials can then be written as

$$\overline{w}(\overline{\boldsymbol{\varepsilon}}, \boldsymbol{q}, \overline{\theta}) = \inf_{\boldsymbol{\varepsilon} \in \mathcal{K}(\overline{\boldsymbol{\varepsilon}})} \sum_{r=1}^{N} \sum_{u=1}^{U} \sum_{b=1}^{B} c^{(r)} \ell^{(r,u,b)}(\overline{\theta}) \left\langle \frac{1}{2} \left(\boldsymbol{\varepsilon} - \boldsymbol{\beta}^{(r)}(\overline{\theta}) - \boldsymbol{q}^{(u)} \right) \cdot \mathbb{B}^{(r,u,b)} \left(\boldsymbol{\varepsilon} - \boldsymbol{\beta}^{(r)}(\overline{\theta}) - \boldsymbol{q}^{(u)} \right) \right\rangle^{(r)} \tag{5.15}$$

and

$$\overline{\varphi} \left(\frac{\boldsymbol{q} - \boldsymbol{q}_n}{\Delta t}, \overline{\theta} \right) = \sum_{r=1}^{N} \sum_{u=1}^{U} \sum_{b=1}^{B} c^{(r)} m^{(r,u,b)}(\overline{\theta}) \left\langle \frac{1}{2} \frac{\boldsymbol{q}^{(u)} - \boldsymbol{q}_n^{(u)}}{\Delta t} \cdot \mathbb{B}^{(r,u,b)} \frac{\boldsymbol{q}^{(u)} - \boldsymbol{q}_n^{(u)}}{\Delta t} \right\rangle^{(r)}. \tag{5.16}$$

Now, each term in this last expression for the discretized dissipation potential can be bounded from below as [132]

$$\left\langle \left(\frac{\boldsymbol{q}^{(u)} - \boldsymbol{q}_n^{(u)}}{\Delta t} \right) \cdot \mathbb{B}^{(r,u,b)} \left(\frac{\boldsymbol{q}^{(u)} - \boldsymbol{q}_n^{(u)}}{\Delta t} \right) \right\rangle^{(r)} \geq \frac{\langle \boldsymbol{q}^{(u)} \rangle^{(r)} - \langle \boldsymbol{q}_n^{(u)} \rangle^{(r)}}{\Delta t} \cdot \mathbb{B}^{(r,u,b)} \frac{\langle \boldsymbol{q}^{(u)} \rangle^{(r)} - \langle \boldsymbol{q}_n^{(u)} \rangle^{(r)}}{\Delta t} + \left(\frac{C_{\alpha}^{(r,u,b)^{1/2}} - C_{\alpha_n}^{(r,u,b)^{1/2}}}{\Delta t} \right)^2, \tag{5.17}$$

where

$$C_{\alpha}^{(r,u,b)} = \left\langle (\boldsymbol{q}^{(u)} - \langle \boldsymbol{q}^{(u)} \rangle^{(r)}) \cdot \mathbb{B}^{(r,u,b)} (\boldsymbol{q}^{(u)} - \langle \boldsymbol{q}^{(u)} \rangle^{(r)}) \right\rangle^{(r)} \tag{5.18}$$

and $C_{\alpha_n}^{(r,u,b)}$ are traces of the intraphase fluctuations of the viscous strain field $\boldsymbol{q}^{(u)}$ at each time instant. The discretized dissipation *functional* is thus approximated by the discretized dissipation *function*

$$\begin{aligned} \overline{\varphi}\left(\frac{\boldsymbol{q}-\boldsymbol{q}_n}{\Delta t}, \overline{\theta}\right) \approx & \hat{\varphi}\left(\left\{\frac{\langle \boldsymbol{q}^{(u)} \rangle^{(r)} - \langle \boldsymbol{q}_n^{(u)} \rangle^{(r)}}{\Delta t}\right\}, \left\{\frac{C_{\alpha}^{(r,u,b)^{1/2}} - C_{\alpha_n}^{(r,u,b)^{1/2}}}{\Delta t}\right\}, \overline{\theta}\right) \\ = & \frac{1}{2} \sum_{r=1}^{N} \sum_{u=1}^{U} c^{(r)} \left[\frac{\langle \boldsymbol{q}^{(u)} \rangle^{(r)} - \langle \boldsymbol{q}_n^{(u)} \rangle^{(r)}}{\Delta t} \cdot \mathbb{M}^{(r,u)}(\overline{\theta}) \frac{\langle \boldsymbol{q}^{(u)} \rangle^{(r)} - \langle \boldsymbol{q}_n^{(u)} \rangle^{(r)}}{\Delta t} + \right. \\ & \left. \sum_{b=1}^{B} m^{(r,u,b)}(\overline{\theta}) \left(\frac{C_{\alpha}^{(r,u,b)^{1/2}} - C_{\alpha_n}^{(r,u,b)^{1/2}}}{\Delta t} \right)^2 \right], \end{aligned} \tag{5.19}$$

which depends on the viscous strain fields only through their phase averages and intraphase fluctuations. Here, $\{\cdot\}$ refers to an entire collection of variables for all $r = 1, ..., N$, $u = 1, ..., U$, and $b = 1, ..., B$. Making use of this estimate in the discretized evolution law (5.13) generates the variational approximation

$$\inf_{\boldsymbol{q}} \left[\overline{w}(\overline{\boldsymbol{\varepsilon}}, \boldsymbol{q}, \overline{\theta}) + \Delta t \ \hat{\varphi}\left(\left\{\frac{\langle \boldsymbol{q}^{(u)} \rangle^{(r)} - \langle \boldsymbol{q}_n^{(u)} \rangle^{(r)}}{\Delta t}\right\}, \left\{\frac{C_{\alpha}^{(r,u,b)^{1/2}} - C_{\alpha_n}^{(r,u,b)^{1/2}}}{\Delta t}\right\}, \overline{\theta}\right) \right], \tag{5.20}$$

which, upon partitioning the infimum problem, can be written as

$$\begin{aligned} \inf_{\substack{\overline{\boldsymbol{q}}^{(r,u)} \\ \widetilde{q}^{(r,u,b)} \geq 0}} & \left[\hat{w}\left(\overline{\boldsymbol{\varepsilon}}, \left\{\overline{\boldsymbol{q}}^{(r,u)}\right\}, \left\{\widetilde{q}^{(r,u,b)}\right\}, \overline{\theta}\right) + \right. \\ & \left. \Delta t \ \hat{\varphi}\left(\left\{\frac{\langle \boldsymbol{q}^{(u)} \rangle^{(u)} - \langle \boldsymbol{q}_n^{(u)} \rangle^{(u)}}{\Delta t}\right\}, \left\{\frac{C_{\alpha}^{(r,u,b)^{1/2}} - C_{\alpha_n}^{(r,u,b)^{1/2}}}{\Delta t}\right\}, \overline{\theta}\right) \right], \end{aligned} \tag{5.21}$$

where

$$\hat{w}\left(\overline{\boldsymbol{\varepsilon}}, \left\{\overline{\boldsymbol{q}}^{(r,u)}\right\}, \left\{\widetilde{q}^{(r,u,b)}\right\}, \overline{\theta}\right) = \inf_{\boldsymbol{q} \in \mathcal{J}\left(\left\{\overline{\boldsymbol{q}}^{(r,u)}\right\}, \left\{\widetilde{q}^{(r,u,b)}\right\}\right)} \overline{w}\left(\overline{\boldsymbol{\varepsilon}}, \boldsymbol{q}, \overline{\theta}\right) \tag{5.22}$$

and

$$\mathcal{J}\left(\left\{\overline{\boldsymbol{q}}^{(r,u)}\right\},\left\{\widetilde{q}^{(r,u,b)}\right\}\right)=\Big\{\boldsymbol{q}\ :\ \left\langle \boldsymbol{q}^{(u)}\right\rangle^{(r)}=\overline{\boldsymbol{q}}^{(r,u)}\quad\text{and}\\ C_{\alpha}^{(r,u,b)^{1/2}}=\widetilde{q}^{(r,u,b)}\quad\text{for}\quad r=1,...,N,\ u=1,...,U,\ b=1,...,B\Big\}. \tag{5.23}$$

For later reference, we note that the internal variable fields $\boldsymbol{q}^{(u)}(\mathbf{x})$ minimizing the free-energy density (5.22) can be shown to be

$$\left(\boldsymbol{q}^{(u)}(\mathbf{x})-\overline{\boldsymbol{q}}^{(r,u)}\right)=\sum_{b=1}^{B}\frac{\widetilde{q}^{(r,u,b)}}{C_{\varepsilon}^{(r,u,b)^{1/2}}}\mathbb{B}^{(r,u,b)}\left(\boldsymbol{\varepsilon}(\mathbf{x})-\left\langle\boldsymbol{\varepsilon}\right\rangle^{(r)}\right)\quad\text{in}\quad\Omega^{(r)}, \tag{5.24}$$

where use has been made of the decomposition (5.14), and the symbols $C_{\varepsilon}^{(r,u,b)}=\mathbb{B}^{(r,u,b)}\cdot\mathbb{C}_{\varepsilon}^{(r)}$ have been introduced to denote traces of the fourth-order covariance tensors of the strain field within phase r as given by

$$\mathbb{C}_{\varepsilon}^{(r)}=\left\langle\left(\boldsymbol{\varepsilon}-\left\langle\boldsymbol{\varepsilon}\right\rangle^{(r)}\right)\otimes\left(\boldsymbol{\varepsilon}-\left\langle\boldsymbol{\varepsilon}\right\rangle^{(r)}\right)\right\rangle^{(r)}. \tag{5.25}$$

The infimum problem (5.21) is now seen to constitute an implicit Euler discretization of the continuous evolution laws

$$\frac{\partial\hat{w}}{\partial\overline{\boldsymbol{q}}^{(r,u)}}\left(\overline{\boldsymbol{\varepsilon}},\left\{\overline{\boldsymbol{q}}^{(r,u)}\right\},\left\{\widetilde{q}^{(r,u,b)}\right\},\overline{\theta}\right)+\frac{\partial\hat{\varphi}}{\partial\dot{\overline{\boldsymbol{q}}}^{(r,u)}}\left(\left\{\dot{\overline{\boldsymbol{q}}}^{(r,u)}\right\},\left\{\dot{\widetilde{q}}^{(r,u,b)}\right\},\overline{\theta}\right)=\mathbf{0}, \tag{5.26}$$

$$\frac{\partial\hat{w}}{\partial\widetilde{q}^{(r,u,b)}}\left(\overline{\boldsymbol{\varepsilon}},\left\{\overline{\boldsymbol{q}}^{(r,u)}\right\},\left\{\widetilde{q}^{(r,u,b)}\right\},\overline{\theta}\right)+\frac{\partial\hat{\varphi}}{\partial\dot{\widetilde{q}}^{(r,u,b)}}\left(\left\{\dot{\overline{\boldsymbol{q}}}^{(r,u)}\right\},\left\{\dot{\widetilde{q}}^{(r,u,b)}\right\},\overline{\theta}\right)=0, \tag{5.27}$$

for $r=1,...,N$, $u=1,...,U$, and $b=1,...,B$, where

$$\hat{w}\left(\overline{\boldsymbol{\varepsilon}},\left\{\overline{\boldsymbol{q}}^{(r,u)}\right\},\left\{\widetilde{q}^{(r,u,b)}\right\},\overline{\theta}\right)=\inf_{\boldsymbol{\varepsilon}\in\mathcal{K}(\overline{\boldsymbol{\varepsilon}})}\sum_{r=1}^{N}\sum_{u=1}^{U}\frac{c^{(r)}}{2}\Big[\Big(\left\langle\boldsymbol{\varepsilon}\right\rangle^{(r)}-\boldsymbol{\beta}^{(r)}(\overline{\theta})-\overline{\boldsymbol{q}}^{(r,u)}\Big)\cdot\\ \mathbb{L}^{(r,u)}(\overline{\theta})\left(\left\langle\boldsymbol{\varepsilon}\right\rangle^{(r)}-\boldsymbol{\beta}^{(r)}(\overline{\theta})-\overline{\boldsymbol{q}}^{(r,u)}\right)+\sum_{b=1}^{B}\ell^{(r,u,b)}(\overline{\theta})\left(C_{\varepsilon}^{(r,u,b)^{1/2}}-\widetilde{q}^{(r,u,b)}\right)^{2}\Big] \tag{5.28}$$

and

$$\hat{\varphi}\left(\left\{\dot{\overline{\boldsymbol{q}}}^{(r,u)}\right\},\left\{\dot{\widetilde{q}}^{(r,u,b)}\right\},\overline{\theta}\right)=\sum_{r=1}^{N}\sum_{u=1}^{U}\frac{c^{(r)}}{2}\left[\dot{\overline{\boldsymbol{q}}}^{(r,u)}\cdot\mathbb{M}^{(r,u)}(\overline{\theta})\dot{\overline{\boldsymbol{q}}}^{(r,u)}+\sum_{b=1}^{B}m^{(r,u,b)}(\overline{\theta})\;\dot{\widetilde{q}}^{(r,u,b)^2}\right]. \tag{5.29}$$

Expression (5.28) follows from expression (5.22) evaluated at the minimizing internal variable fields (5.24), while expression (5.29) follows from expression (5.19) evaluated at a vanishing time step $\Delta t \to 0$ [see 132, for details]. The main observation in the context of these expressions is that *the system of equations (5.26)-(5.27) provides a reduced-order description of the macroscopic thermo-viscoelastic evolution problem in terms of a finite set of effective internal variables identified with the first moments of the viscous strains over each phase* $\overline{\boldsymbol{q}}^{(r,u)}$ *and the second moments of their intraphase fluctuations* $\widetilde{q}^{(r,u,b)}$*, and a pair of reduced effective potentials identified with a free-energy density* $\hat{w}$ *and a dissipation potential* $\hat{\varphi}$*; in addition, the reduced free-energy density provides the estimate*

$$\overline{\boldsymbol{\sigma}}=\frac{\partial\hat{w}}{\partial\overline{\boldsymbol{\varepsilon}}}\left(\overline{\boldsymbol{\varepsilon}},\left\{\overline{\boldsymbol{q}}^{(r,u)}\right\},\left\{\widetilde{q}^{(r,u,b)}\right\},\overline{\theta}\right) \tag{5.30}$$

for the macroscopic stress.

Evaluating the various derivatives in these expressions we obtain the reduced constitutive relation

$$\overline{\boldsymbol{\sigma}}=\sum_{r=1}^{N}\sum_{u=1}^{U}c^{(r)}\mathbb{L}^{(r,u)}(\overline{\theta})\left(\overline{\boldsymbol{\varepsilon}}^{(r)}-\boldsymbol{\beta}^{(r)}(\overline{\theta})-\overline{\boldsymbol{q}}^{(r,u)}\right) \tag{5.31}$$

along with the reduced evolution equations

$$\mathbb{M}^{(r,u)}(\overline{\theta})\;\dot{\overline{\boldsymbol{q}}}^{(r,u)}+\mathbb{L}^{(r,u)}(\overline{\theta})\;\overline{\boldsymbol{q}}^{(r,u)}=\mathbb{L}^{(r,u)}(\overline{\theta})\left(\overline{\boldsymbol{\varepsilon}}^{(r)}-\boldsymbol{\beta}^{(r)}(\overline{\theta})\right) \tag{5.32}$$

$$m^{(r,u,b)}(\overline{\theta})\;\dot{\widetilde{q}}^{(r,u,b)}+\ell^{(r,u,b)}(\overline{\theta})\;\widetilde{q}^{(r,u,b)}=\ell^{(r,u,b)}(\overline{\theta})\;\widetilde{\varepsilon}^{(r,u,b)} \tag{5.33}$$

for $r=1,...,N$, $u=1,...,U$, and $b=1,...,B$, where $\overline{\boldsymbol{\varepsilon}}^{(r)}=\langle\boldsymbol{\varepsilon}\rangle^{(r)}$ and $\widetilde{\varepsilon}^{(r,u,b)}=C_{\varepsilon}^{(r,u,b)^{1/2}}$ are the phase averages and intraphase fluctuations of the strain field that minimizes the reduced free-energy density (5.28) at the prescribed macroscopic strain $\overline{\boldsymbol{\varepsilon}}$ and temperature change $\overline{\theta}$. The Euler-Lagrange equations for the minimizing strain field, along with the minimizing internal

variable fields (5.24), also imply the intraphase reduced stress statistics

$$\overline{\boldsymbol{\sigma}}^{(r)} = \langle \boldsymbol{\sigma} \rangle^{(r)} = \sum_{u=1}^{U} \mathbb{L}^{(r,u)}(\overline{\theta}) \left(\overline{\boldsymbol{\varepsilon}}^{(r)} - \boldsymbol{\beta}^{(r)}(\overline{\theta}) - \overline{\boldsymbol{q}}^{(r,u)} \right) \tag{5.34}$$

and

$$\widetilde{\sigma}^{(r,b)} = \left\langle (\boldsymbol{\sigma} - \langle \boldsymbol{\sigma} \rangle^{(r)}) \cdot \mathbb{B}^{(r,u,b)} (\boldsymbol{\sigma} - \langle \boldsymbol{\sigma} \rangle^{(r)}) \right\rangle^{(r)^{1/2}} = \left| \sum_{u=1}^{U} \ell^{(r,u,b)}(\overline{\theta}) \left(\widetilde{\varepsilon}^{(r,u,b)} - \widetilde{q}^{(r,u,b)} \right) \right|, \tag{5.35}$$

which will serve to quantify the amount of residual stresses present within each phase r of the composite.

5.2.2 Mean-field homogenization

Instrumental to the above order reduction is the fact that the reduced constitutive relation and evolution equations (5.31)-(5.33) depend on the strain field only through its first and second moments over each phase, and that these moments can be evaluated via linear homogenization techniques. This is evident by noting that, even though the minimization problem (5.28) for the strain field is *nonlinear*, the associated Euler-Lagrange equations are those of a *linear* thermoelastic comparison solid with the same microstructure as the thermo-viscoelastic composite but with piecewise uniform stiffness tensor and eigenstress field given by

$$\mathbb{L}_0^{(r)} = \sum_{u=1}^{U} \sum_{b=1}^{B} \ell_0^{(r,u,b)} \mathbb{B}^{(r,u,b)} \quad \text{and} \quad \boldsymbol{\tau}_0^{(r)} = \sum_{u=1}^{U} \mathbb{L}^{(r,u)}(\overline{\theta}) \left(\overline{\boldsymbol{\varepsilon}}^{(r)} - \boldsymbol{\beta}^{(r)}(\overline{\theta}) - \overline{\boldsymbol{q}}^{(r,u)} \right) - \mathbb{L}_0^{(r)} \overline{\boldsymbol{\varepsilon}}^{(r)}. \tag{5.36}$$

where

$$\ell_0^{(r,u,b)} = \ell^{(r,u,b)}(\overline{\theta}) \, \frac{\widetilde{\varepsilon}^{(r,u,b)} - \widetilde{q}^{(r,u,b)}}{\widetilde{\varepsilon}^{(r,u,b)}}, \tag{5.37}$$

Therefore, the minimizing strain field in (5.28) is exactly identical to that of a linear comparison problem

$$\hat{w}_0(\overline{\boldsymbol{\varepsilon}},\overline{\theta}) = \underset{\boldsymbol{\varepsilon}\in\mathcal{K}(\overline{\boldsymbol{\varepsilon}})}{\text{stat}} \sum_{r=1}^{N} c^{(r)} \left\langle \frac{1}{2}\boldsymbol{\varepsilon}\cdot\mathbb{L}_0^{(r)}\boldsymbol{\varepsilon} + \boldsymbol{\tau}_0^{(r)}\cdot\boldsymbol{\varepsilon} \right\rangle^{(r)} \tag{5.38}$$

with constitutive tensors given self-consistently by (5.36). The stationary rather than extremal character of the variational problem (5.38) is due to the fact that the tensors $\mathbb{L}_0^{(r)}$ are not necessarily positive definite. In any event, this comparison energy density can be expressed as

$$\hat{w}_0(\overline{\boldsymbol{\varepsilon}},\overline{\theta}) = \frac{1}{2}\overline{\boldsymbol{\varepsilon}}\cdot\widetilde{\mathbb{L}}_0\overline{\boldsymbol{\varepsilon}} + \widetilde{\boldsymbol{\tau}}_0\cdot\overline{\boldsymbol{\varepsilon}} + \widetilde{g}_0, \tag{5.39}$$

where $\widetilde{\mathbb{L}}_0$, $\widetilde{\boldsymbol{\tau}}_0$ and $\widetilde{g}_0$ are effective properties that can be determined with any suitable mean-field homogenization technique for N-phase linear thermoelastic solids [see, for instance, 142]. The first and second moments of the strain field within each phase can then be determined from this comparison energy by evaluating the derivatives

$$\langle\boldsymbol{\varepsilon}\rangle^{(r)} = \frac{1}{c^{(r)}}\frac{\partial\hat{w}_0}{\partial\boldsymbol{\tau}_0^{(r)}}(\overline{\boldsymbol{\varepsilon}},\overline{\theta}) \quad \text{and} \quad \langle\boldsymbol{\varepsilon}\otimes\boldsymbol{\varepsilon}\rangle^{(r)} = \frac{2}{c^{(r)}}\frac{\partial\hat{w}_0}{\partial\mathbb{L}_0^{(r)}}(\overline{\boldsymbol{\varepsilon}},\overline{\theta}) \quad \text{for} \quad r=1,...,N, \tag{5.40}$$

which follow from well-known relations for field statistics in linear heterogeneous media and, together with relations (5.36), constitute a set of algebraic non-linear equations for those moments. Whenever these equations exhibit multiple roots, the root giving the minimum value of (5.28) with positive-definite phase covariances of the strain field must be selected. In any event, the reduced free-energy density (5.22) and ensuing relations (5.31)-(5.33) are completely determined by the linear homogenization scheme of choice.

Since the stress fields associated with both variational problems agree exactly as well, the reduced constitutive relation (5.31) can also be obtained from the comparison energy density as

$$\overline{\boldsymbol{\sigma}} = \frac{\partial\hat{w}_0}{\partial\overline{\boldsymbol{\varepsilon}}}(\overline{\boldsymbol{\varepsilon}},\overline{\theta}) = \widetilde{\mathbb{L}}_0\overline{\boldsymbol{\varepsilon}} + \widetilde{\boldsymbol{\tau}}_0, \tag{5.41}$$

where the partial derivative has been taken with comparison properties $\mathbb{L}_0^{(r)}$ and $\boldsymbol{\tau}_0^{(r)}$ held fixed. Finally, relations (5.40) provide the first- and second-order intraphase statistics of the underlying

strain field, and the corresponding stress statistics follow from the identities

$$\overline{\boldsymbol{\sigma}}^{(r)} = \mathbb{L}_0^{(r)}\overline{\boldsymbol{\varepsilon}}^{(r)} + \boldsymbol{\tau}_0^{(r)} \quad \text{and} \quad \mathbb{C}_\sigma^{(r)} = \mathbb{L}_0^{(r)}\mathbb{C}_\varepsilon^{(r)}\mathbb{L}_0^{(r)}, \tag{5.42}$$

where $\mathbb{C}_\varepsilon^{(r)}$ and $\mathbb{C}_\sigma^{(r)}$ are the fourth-order covariance tensors of the strain and the stress fields, respectively, within phase r.

5.3 Specialization to rigidly reinforced solids with isotropic constituents

Viscoelastic solids containing elastically rigid reinforcements are of particular practical interest. We consider reinforced systems ($N = 2$) composed of a viscoelastic matrix phase ($r = 1$) characterized by isotropic constitutive tensors of the form

$$\begin{aligned} &\boldsymbol{\beta}^{(1)}(\theta) = \beta^{(1)}(\theta)\boldsymbol{I}, \quad \mathbb{L}^{(1,u)} = \mathbb{L}^{(u)} \quad \text{and} \quad \mathbb{M}^{(1,u)}(\theta) = \tau^{(u)}(\theta)\ \mathbb{L}^{(u)} \\ &\text{with} \quad \mathbb{L}^{(u)} = 3\kappa^{(u)}\mathbb{J} + 2\mu^{(u)}\mathbb{K} \end{aligned} \tag{5.43}$$

$u = 1, ..., U$, recalling that $\boldsymbol{I}$ denotes the second-order identity tensor, $\mathbb{J}$ and $\mathbb{K}$ denote the standard fourth-order isotropic bulk and shear projection tensors, respectively, $\kappa^{(u)}$ and $\mu^{(u)}$ represent bulk and shear elastic moduli, respectively, and the $\tau^{(u)}$ represent temperature-dependent relaxation times. These constitutive assumptions are typically employed to model the response of amorphous polymers [43]. In turn, the corresponding tensors in the reinforcement phase ($r = 2$) are all set to infinity. Thus, the reinforcements undergo purely thermal deformations given by

$$\boldsymbol{\beta}^{(2)}(\theta) = \beta^{(2)}(\theta)\boldsymbol{I}. \tag{5.44}$$

Results reported below make use of the simplest possible choice of basis tensors given by

$$\mathbb{L}^{(u)} = \ell^{(u)}\ \mathbb{B}^{(u)} \quad \text{where} \quad \ell^{(u)^2} = 9{\kappa^{(u)}}^2 + 20{\mu^{(u)}}^2 \quad \text{and} \quad \mathbb{B}^{(u)} = \frac{3\kappa^{(u)}}{\ell^{(u)}}\mathbb{J} + \frac{2\mu^{(u)}}{\ell^{(u)}}\mathbb{K}, \tag{5.45}$$

so that $\mathbb{B}^{(u)} \cdot \mathbb{B}^{(u)} = 1$. The reduced potentials (5.28) and (5.29) can then be written as

$$\hat{w}\left(\overline{\boldsymbol{\varepsilon}}, \left\{\overline{\boldsymbol{q}}^{(u)}\right\}, \left\{\widetilde{q}^{(u)}\right\}, \overline{\theta}\right) = \inf_{\boldsymbol{\varepsilon} \in \mathcal{K}_*\left(\overline{\boldsymbol{\varepsilon}} - \boldsymbol{\beta}^{(2)}(\overline{\theta})\right)} \frac{1-c}{2} \sum_{u=1}^{U} \left[\left(\frac{\overline{\boldsymbol{\varepsilon}} - \overline{\boldsymbol{\beta}}(\overline{\theta})}{1-c} - \overline{\boldsymbol{q}}^{(u)} \right) \cdot \mathbb{L}^{(u)} \left(\frac{\overline{\boldsymbol{\varepsilon}} - \overline{\boldsymbol{\beta}}(\overline{\theta})}{1-c} - \overline{\boldsymbol{q}}^{(u)} \right) + \ell^{(u)} \left(\widetilde{\varepsilon}^{(u)} - \widetilde{q}^{(u)} \right)^2 \right] \quad \text{and} \tag{5.46}$$

$$\hat{\varphi}\left(\left\{\dot{\overline{\boldsymbol{q}}}^{(u)}\right\}, \left\{\dot{\widetilde{q}}^{(u)}\right\}, \overline{\theta}\right) = \frac{1-c}{2} \sum_{u=1}^{U} \tau^{(u)}(\overline{\theta}) \left[\dot{\overline{\boldsymbol{q}}}^{(u)} \cdot \mathbb{L}^{(u)} \dot{\overline{\boldsymbol{q}}}^{(u)} + \ell^{(u)} \, \dot{\widetilde{q}}^{(u)^2} \right], \tag{5.47}$$

where $c = c^{(2)}$ is the reinforcement content, $\overline{\boldsymbol{\beta}} = c^{(1)}\boldsymbol{\beta}^{(1)} + c^{(2)}\boldsymbol{\beta}^{(2)}$ is the average thermal strain, $\overline{\boldsymbol{q}}^{(u)} \equiv \overline{\boldsymbol{q}}^{(1,u)}$ and $\widetilde{q}^{(u)} \equiv \widetilde{q}^{(1,u,1)}$ are the effective internal variables associated with the viscoelastic matrix, $\widetilde{\varepsilon}^{(u)} \equiv \widetilde{\varepsilon}^{(1,u,1)}$ is a measure of the strain fluctuations within the matrix phase given by

$$\widetilde{\varepsilon}^{(u)} = \sqrt{\mathbb{B}^{(u)} \cdot \mathbb{C}_{\varepsilon}^{(1)}} = \sqrt{\frac{2\mu^{(u)}}{\ell^{(u)}} \widetilde{\varepsilon}_d^{(1)^2} + \frac{9\kappa^{(u)}}{\ell^{(u)}} \widetilde{\varepsilon}_m^{(1)^2}} \tag{5.48}$$

in terms of the fluctuations of the mean and deviatoric parts of the strain field $\widetilde{\varepsilon}_m^{(1)^2} = \mathbb{J} \cdot \mathbb{C}_{\varepsilon}^{(1)}/3$ and $\widetilde{\varepsilon}_d^{(1)} = \mathbb{K} \cdot \mathbb{C}_{\varepsilon}^{(1)}$, respectively, and $\mathcal{K}_*(\overline{\boldsymbol{\varepsilon}} - \boldsymbol{\beta}^{(2)}(\overline{\theta}))$ is the set of kinematically admissible strain fields with average $\overline{\boldsymbol{\varepsilon}} - \boldsymbol{\beta}^{(2)}(\overline{\theta})$ that vanish identically within the reinforcing phase. In deriving this expression for the free-energy density, use has been made of the change of variables $\boldsymbol{\varepsilon} \to \boldsymbol{\varepsilon} + \boldsymbol{\beta}^{(2)}(\overline{\theta})$ for convenience; the strain fluctuations (5.48) are insensitive to this change.

Following the arguments provided in the previous subsection, and invoking well-known relations for two-phase composites derived by [121], the effective constitutive relations and intraphase strain statistics generated by (5.46) can be conveniently computed from the comparison energy density

$$\hat{w}_0(\overline{\boldsymbol{\varepsilon}}, \overline{\theta}) = \frac{1}{2}(\overline{\boldsymbol{\varepsilon}} - \boldsymbol{\beta}^{(2)}(\overline{\theta})) \cdot \widetilde{\mathbb{L}}_0(\overline{\boldsymbol{\varepsilon}} - \boldsymbol{\beta}^{(2)}(\overline{\theta})) + \boldsymbol{\tau}_0 \cdot (\overline{\boldsymbol{\varepsilon}} - \boldsymbol{\beta}^{(2)}(\overline{\theta})), \tag{5.49}$$

where $\widetilde{\mathbb{L}}_0$ is the effective elasticity tensor of a rigidly reinforced solid with the same microstructural morphology as the reinforced solid of interest but with matrix properties

$$\mathbb{L}_0 = 3\kappa_0 \, \mathbb{J} + 2\mu_0 \, \mathbb{K} \equiv \sum_{u=1}^{U} \ell_0^{(u)} \mathbb{B}^{(u)} \quad \text{and} \quad \boldsymbol{\tau}_0 = \sum_{u=1}^{U} \mathbb{L}^{(u)} \left(\frac{\overline{\boldsymbol{\varepsilon}} - \overline{\boldsymbol{\beta}}(\overline{\theta})}{1-c} - \overline{\boldsymbol{q}}^{(u)} \right) - \mathbb{L}_0 \frac{\overline{\boldsymbol{\varepsilon}} - \boldsymbol{\beta}^{(2)}(\overline{\theta})}{1-c} \tag{5.50}$$

given in terms of the comparison moduli $\ell_0^{(u)}$ defined by

$$\ell_0^{(u)} = \ell^{(u)} \frac{\widetilde{\varepsilon}^{(u)} - \widetilde{q}^{(u)}}{\widetilde{\varepsilon}^{(u)}} \quad u = 1, ..., U, \tag{5.51}$$

and determined self-consistently by the accompanying identities

$$\widetilde{\varepsilon}_d^{(1)} = \frac{1}{1-c} \sqrt{\left(\overline{\boldsymbol{\varepsilon}} - \boldsymbol{\beta}^{(2)}(\overline{\theta})\right) \cdot \left[(1-c)\frac{\partial \widetilde{\mathbb{L}}_0}{\partial(2\mu_0)} - \mathbb{K}\right] \left(\overline{\boldsymbol{\varepsilon}} - \boldsymbol{\beta}^{(2)}(\overline{\theta})\right)} \quad \text{and}$$
$$\widetilde{\varepsilon}_m^{(1)} = \frac{1}{1-c} \sqrt{\left(\overline{\boldsymbol{\varepsilon}} - \boldsymbol{\beta}^{(2)}(\overline{\theta})\right) \cdot \left[(1-c)\frac{\partial \widetilde{\mathbb{L}}_0}{\partial(9\kappa_0)} - \frac{1}{3}\mathbb{J}\right] \left(\overline{\boldsymbol{\varepsilon}} - \boldsymbol{\beta}^{(2)}(\overline{\theta})\right)}. \tag{5.52}$$

Note that expressions $(5.45)_3$ and $(5.50)_1$ imply the relations

$$\kappa_0 = \sum_{u=1}^{U} \frac{\ell_0^{(u)}}{\ell^{(u)}} \kappa^{(u)} \quad \text{and} \quad \mu_0 = \sum_{u=1}^{U} \frac{\ell_0^{(u)}}{\ell^{(u)}} \mu^{(u)}, \tag{5.53}$$

which should be invoked to express the strain fluctuations (5.52) in terms of the comparison moduli $\ell_0^{(u)}$, and with (5.51), in terms of the strain fluctuations $\widetilde{\varepsilon}^{(u)}$. Evaluation of the reduced free-energy density (5.46) requires introducing the resulting expressions into (5.48) to generate a set of equations for the quantities $\widetilde{\varepsilon}^{(u)}$ to be solved for given temperature change $\overline{\theta}$, macroscopic deformation $\overline{\boldsymbol{\varepsilon}}$ and internal variables $\widetilde{q}^{(u)}$ $(u = 1, ..., U)$. In general, the set of equations requires numerical treatment.

Differentiation of (5.49) with respect to the macroscopic deformation generates the effective constitutive relations

$$\overline{\boldsymbol{\sigma}} = \widetilde{\mathbb{L}}_0 \left(\overline{\boldsymbol{\varepsilon}} - \overline{\boldsymbol{\beta}}(\overline{\theta})\right) + \boldsymbol{\tau}_0^{(1)}, \tag{5.54}$$

while differentiation of the reduced potentials (5.46) and (5.47) with respect to the internal variables generates the evolution laws

$$\tau^{(u)}(\overline{\theta})\ \dot{\overline{\boldsymbol{q}}}^{(u)} + \overline{\boldsymbol{q}}^{(u)} = \frac{\overline{\boldsymbol{\varepsilon}} - \overline{\boldsymbol{\beta}}(\overline{\theta})}{1-c} \quad \text{and} \quad \tau^{(u)}(\overline{\theta})\ \dot{\widetilde{q}}^{(u)} + \widetilde{q}^{(u)} = \widetilde{\varepsilon}^{(u)} \quad u = 1, ..., U. \tag{5.55}$$

5.4 Exact results for a class of rigidly reinforced solids with isotropic constituents

In order to assess the capabilities of the reduced-order mean-field description proposed above, results are generated in this section for a special class of rigidly reinforced solids whose effective response can be determined exactly by means of the correspondence principle. The viscoelastic matrix is characterized by constitutive tensors of the form (5.43) with relaxation times [43]

$$\boldsymbol{\tau}^{(u)}(\theta) = \tau_{\circ}^{(u)} a_T(\theta) \quad u = 1, ..., U. \tag{5.56}$$

Thus, each rheological unit u can exhibit a viscosity characterized by a different relaxation time constant $\tau_{\circ}^{(u)}$ but the same temperature dependence through the common shift function $a_T(\theta)$; the ratio between relaxation times of different units is insensitive to temperature changes. For a given thermomechanical loading program, the constitutive relation and evolution laws within the matrix phase are then given by

$$\begin{aligned} &\boldsymbol{\sigma}(t) = \sum_{u=1}^{U} \mathbb{L}^{(u)} \left(\boldsymbol{\varepsilon}(t) - \boldsymbol{\beta}^{(1)}(\overline{\theta}(t)) - \boldsymbol{q}^{(u)}(t) \right) \quad \text{and} \\ &\tau_{\circ}^{(u)} a_T(\overline{\theta}(t)) \dot{\boldsymbol{q}}^{(u)}(t) + \boldsymbol{q}^{(u)}(t) = \boldsymbol{\varepsilon}(t) - \boldsymbol{\beta}^{(1)}(\overline{\theta}(t)) \end{aligned} \tag{5.57}$$

for $u = 1, ..., U$. This form of evolution laws motivate the introduction of an "internal" time variable defined as

$$\xi = \int_0^t \frac{\mathrm{d}\tau}{a_T\left(\overline{\theta}(\tau)\right)}, \tag{5.58}$$

so that, again with a slight abuse of notation,

$$\boldsymbol{\sigma}(\xi) = \sum_{u=1}^{U} \mathbb{L}^{(u)} \left(\boldsymbol{\varepsilon}(\xi) - \boldsymbol{\beta}^{(1)}(\xi) - \boldsymbol{q}^{(u)}(\xi) \right) \quad \text{and} \quad \tau_{\circ}^{(u)} \dot{\boldsymbol{q}}^{(u)}(\xi) + \boldsymbol{q}^{(u)}(\xi) = \boldsymbol{\varepsilon}(\xi) - \boldsymbol{\beta}^{(1)}(\xi), \tag{5.59}$$

where $\dot{(\cdot)}$ denotes differentiation with respect to ξ. Application of the Laplace-Carson transform to these expressions yields

$$\boldsymbol{\sigma}^*(p) = \mathbb{L}^*(p)\left(\boldsymbol{\varepsilon}^*(p) - \boldsymbol{\beta}^{(1)*}(p)\right) \quad \text{with} \quad \mathbb{L}^*(p) = \sum_{u=1}^{U} \frac{p}{p + \tau_\circ^{(u)^{-1}}}\mathbb{L}^{(u)}, \tag{5.60}$$

where $(\cdot)^*$ refers to a transformed function. The correspondence principle together with the Levin relations then imply the effective response

$$\overline{\boldsymbol{\sigma}}^*(p) = \widetilde{\mathbb{L}}^*(p)\left(\overline{\boldsymbol{\varepsilon}}^*(p) - \boldsymbol{\beta}^{(2)*}(p)\right) + \mathbb{L}^*(p)\left(\boldsymbol{\beta}^{(2)*}(p) - \boldsymbol{\beta}^{(1)*}(p)\right), \tag{5.61}$$

where $\widetilde{\mathbb{L}}^*(p)$ depends on the microstructural morphology of the composite. When this dependence is of the form

$$\widetilde{\mathbb{L}}^*(p) = \sum_{\rho=1}^{\mathrm{R}} \frac{p}{p + \tau_*^{(\rho)^{-1}}}\widetilde{\mathbb{A}}^{(\rho)}, \tag{5.62}$$

the inverse transform of (5.61) yields

$$\overline{\boldsymbol{\sigma}}(\xi) = \sum_{\rho=1}^{\mathrm{R}} \widetilde{\mathbb{A}}^{(\rho)} \int_0^\xi \left(\dot{\overline{\boldsymbol{\varepsilon}}}(s) - \dot{\boldsymbol{\beta}}^{(2)}(s)\right) e^{-\frac{\xi - s}{\tau_*^{(\rho)}}} \mathrm{d}s + \sum_{u=1}^{U} \mathbb{L}^{(u)} \int_0^\xi \left(\dot{\boldsymbol{\beta}}^{(2)}(s) - \dot{\boldsymbol{\beta}}^{(1)}(s)\right) e^{-\frac{\xi - s}{\tau_\circ^{(u)}}} \mathrm{d}s. \tag{5.63}$$

Two particular cases are considered next.

5.4.1 Particulate composites under hydrostatic loadings

We consider particulate composites with isotropic microstructural statistics such that the effective bulk modulus is given exactly by the Hashin-Shtrikman lower bound; thus [90]

$$3\widetilde{\kappa}^*(p) = \sum_{u=1}^{U} \frac{p}{p + \tau_\circ^{(u)^{-1}}} \frac{3\kappa^{(u)} + 4c\mu^{(u)}}{1 - c}, \tag{5.64}$$

which is of the form (5.62) with $R = U$ and $\tau_*^{(u)} = \tau_\circ^{(u)}$. The macroscopic response (5.63) for spherical deformations $\overline{\boldsymbol{\varepsilon}}(\xi) = \overline{\varepsilon}_m(\xi)\boldsymbol{I}$ is then given by

$$\overline{\sigma}_m(\xi) = \sum_{u=1}^{U} \int_0^\xi \left[\frac{3\kappa^{(u)} + 4c\mu^{(u)}}{1-c} \left(\dot{\overline{\varepsilon}}_m(s) - \dot{\beta}^{(2)}(s) \right) + 3\kappa^{(u)} \left(\dot{\beta}^{(2)}(s) - \dot{\beta}^{(1)}(s) \right) \right] e^{-\frac{\xi - s}{\tau_\circ^{(u)}}} \, \mathrm{d}s. \tag{5.65}$$

Corresponding results in the absence of thermal strains were given by [59] and [60].

5.4.2 Fiber-reinforced composites under thermal loadings

We now consider fiber-reinforced composites with transversely isotropic microstructural statistics such that the effective elasticity tensor is given exactly by the Hashin-Shtrikman lower bound; thus [90]

$$\begin{aligned} \widetilde{\mathbb{L}}^*(p) = \sum_{u=1}^{U} \frac{p}{p + \tau_\circ^{(u)^{-1}}} \Bigg[& \frac{6\kappa^{(u)} + 2(1+3c)\mu^{(u)}}{3(1-c)} \mathbb{H}_1 + \frac{(1-3c)3\kappa^{(u)} - (1+3c)2\mu^{(u)}}{3(1-c)} (\mathbb{H}_2 + \mathbb{H}_3) \\ & + 2\mu^{(u)} \frac{\sum_{v=1}^{U} \left(p + \tau_\circ^{(v)^{-1}} \right)^{-1} \left[3(1+c)\kappa^{(v)} + (7+c)\mu^{(v)} \right]}{(1-c) \sum_{v=1}^{U} \left(p + \tau_\circ^{(v)^{-1}} \right)^{-1} \left[3\kappa^{(v)} + 7\mu^{(v)} \right]} \mathbb{H}_5 + 2\mu^{(u)} \frac{1+c}{1-c} \mathbb{H}_6 \Bigg], \end{aligned} \tag{5.66}$$

where the set of tensors $\mathbb{H}_i$ corresponds to the basis for transversely isotropic tensors of [141]. This expression is of the form (5.62) with R depending on U. For a given number of units U, the parameters $\tau_*^{(\rho)}$ and corresponding tensors $\widetilde{\mathbb{A}}^{(\rho)}$ ($\rho = 1, ..., \mathrm{R}$) can be obtained by means of the methodology presented in [7] for frequency dependent responses. This procedure combines a highly accurate approximation of the discrete time spectra derived from the Nevanlinna Pick interpolation problem [143] with a conventional mean-squares procedure for the computation of the associated moduli distributions.

5.5 Sample comparisons and discussion

5.5.1 Particulate composites under hydrostatic loadings

We consider the particulate composites of Section 5.4.1 subject to spherical deformations $\overline{\boldsymbol{\varepsilon}} = \overline{\varepsilon}_m \boldsymbol{I}$. The reduced description based on effective internal variables require the effective bulk

modulus of the comparison solid, which is given by [90]

$$3\widetilde{\kappa}_0 = \frac{3\kappa_0 + 4c\mu_0}{1-c}. \tag{5.67}$$

Expression (5.52) can then be easily evaluated, and upon introducing this expression into (5.48) we obtain the expression

$$\widetilde{\varepsilon}^{(u)} = \sqrt{\frac{12c\mu^{(u)}}{\ell^{(u)}}}\frac{|\overline{\varepsilon}_m - \beta_m^{(2)}(\overline{\theta})|}{1-c} \tag{5.68}$$

for the intraphase strain fluctuations. In turn, symmetry implies that $\overline{\boldsymbol{q}}^{(u)} = \overline{q}^{(u)}\boldsymbol{I}$ for all $u = 1, ..., U$ throughout the deformation history, provided all internal variables depart from zero. The reduced effective potentials (5.46) and (5.47) are thus given by

$$\hat{w}\left(\overline{\varepsilon}_m\boldsymbol{I}, \left\{\overline{q}^{(u)}\right\}, \left\{\widetilde{q}^{(u)}\right\}, \overline{\theta}\right) = \frac{1-c}{2}\sum_{u=1}^{U}\left[9\kappa^{(u)}\left(\frac{\overline{\varepsilon}_m - \overline{\beta}(\overline{\theta})}{1-c} - \overline{q}^{(u)}\right)^2 + \ell^{(u)}\left(\sqrt{\frac{12c\mu^{(u)}}{\ell^{(u)}}}\frac{|\overline{\varepsilon}_m - \beta^{(2)}(\overline{\theta})|}{1-c} - \widetilde{q}^{(u)}\right)^2\right] \quad \text{and} \tag{5.69}$$

$$\hat{\varphi}\left(\left\{\dot{\overline{q}}^{(u)}\right\}, \left\{\dot{\widetilde{q}}^{(u)}\right\}, \overline{\theta}\right) = \frac{1-c}{2}\sum_{u=1}^{U}\tau^{(u)}(\overline{\theta})\left[9\kappa^{(u)}\dot{\overline{q}}^{(u)2} + \ell^{(u)}\,\dot{\widetilde{q}}^{(u)2}\right], \tag{5.70}$$

where $\overline{\beta} = (1-c)\beta^{(1)} + c\beta^{(2)}$. These reduced potentials are explicit and completely characterize the overall response of the composite under any hydrostatic thermomechanical loading conditions. However, while the reduced dissipation potential is a convex function of the internal variable rates, the reduced free-energy density is *not* a convex function of the macroscopic deformation and internal variables conjointly. This non-convexity is introduced by the model reduction performed in Section 5.2.1 for reasons already elicited by [132] in the context of isothermal viscoelasticity. The negative consequences on ensuing predictions for the macroscopic response have been assessed in depth by [144]. However, it was also found in that work that an efficacious convexification of this reduced free-energy could be carried out in some simple cases like the one considered here. This convexification amounts to eliminating the absolute value in the last term

of (5.69) and adopting the function

$$\hat{w}\left(\overline{\varepsilon}_m \boldsymbol{I}, \left\{\overline{q}^{(u)}\right\}, \left\{\widetilde{q}^{(u)}\right\}, \overline{\theta}\right) = \frac{1-c}{2}\sum_{u=1}^{U}\left[9\kappa^{(u)}\left(\frac{\overline{\varepsilon}_m - \overline{\beta}(\overline{\theta})}{1-c} - \overline{q}^{(u)}\right)^2 + \ell^{(u)}\left(\sqrt{\frac{12c\mu^{(u)}}{\ell^{(u)}}}\frac{\overline{\varepsilon}_m - \beta^{(2)}(\overline{\theta})}{1-c} - \widetilde{q}^{(u)}\right)^2\right] \tag{5.71}$$

as the reduced free-energy density. This function is now convex. Upon differentiating these reduced potentials we obtain the effective constitutive relation

$$\overline{\sigma}_m = \sum_{u=1}^{U}\left[3\kappa^{(u)}\left(\frac{\overline{\varepsilon}_m - \overline{\beta}(\overline{\theta})}{1-c} - \overline{q}^{(u)}\right) + \sqrt{\frac{4c\mu^{(u)}\ell^{(u)}}{3}}\left(\sqrt{\frac{12c\mu^{(u)}}{\ell^{(u)}}}\frac{\overline{\varepsilon}_m - \beta^{(2)}(\overline{\theta})}{1-c} - \widetilde{q}^{(u)}\right)\right] \tag{5.72}$$

along with the evolution laws for the internal variables

$$\tau^{(u)}(\overline{\theta})\dot{\overline{q}}^{(u)} + \overline{q}^{(u)} = \frac{\overline{\varepsilon}_m - \overline{\beta}(\overline{\theta})}{1-c} \quad \text{and} \quad \tau^{(u)}(\overline{\theta})\dot{\widetilde{q}}^{(u)} + \widetilde{q}^{(u)} = \sqrt{\frac{12c\mu^{(u)}}{\ell^{(u)}}}\frac{\overline{\varepsilon}_m - \beta^{(2)}(\overline{\theta})}{1-c}. \tag{5.73}$$

The reduced description (5.72)-(5.73) admits any choice of relaxation times $\tau^{(u)}(\overline{\theta})$. Now, it is easy to show that for the special choice (5.56), it reproduces the exact response (5.65). Indeed, in that case the Laplace-Carson transform of the evolution laws (5.73) expressed in terms of the internal time (5.58) yields

$$\overline{q}^{(u)*}(p) = \frac{1}{1+\tau_\circ^{(u)}p}\frac{\overline{\varepsilon}_m^*(p) - \overline{\beta}^*(p)}{1-c} \quad \text{and} \quad \widetilde{q}^{(u)*}(p) = \frac{1}{1+\tau_\circ^{(u)}p}\sqrt{\frac{12c\mu^{(u)}}{\ell^{(u)}}}\frac{\overline{\varepsilon}_m^*(p) - \beta^{(2)*}(p)}{1-c}, \tag{5.74}$$

and introducing these expressions into the corresponding Laplace-Carson transform of (5.72) yields

$$\overline{\sigma}_m^*(p) = \sum_{u=1}^{U}\frac{p}{p+\tau_\circ^{(u)-1}}\left[\frac{3\kappa^{(u)}+4c\mu^{(u)}}{1-c}\left(\overline{\varepsilon}_m^*(p) - \beta^{(2)*}(p)\right) + 3\kappa^{(u)}\left(\beta^{(2)*}(p) - \beta^{(1)*}(p)\right)\right], \tag{5.75}$$

whose inverse transform is precisely (5.65). This remarkable result is in line with earlier results

already reported in the context of isothermal viscoelasticity with simpler rheologies by [144] and [145]. It shows that the variational model reduction performed in Section 5.2.1 has the capability of reproducing exact thermomechanical responses for composite materials with complex local responses and microstructural morphologies, even in the presence of multiple relaxation mechanisms.

Under stress-free conditions, the reduced description (5.72)-(5.73) predicts a macroscopic strain

$$\overline{\varepsilon}_m = \overline{\beta}(\overline{\theta}) + \frac{4c\mu}{3\widetilde{\kappa}}\left(\beta^{(2)}(\overline{\theta}) - \beta^{(1)}(\overline{\theta})\right) + \sum_{u=1}^{U}\left[\frac{\kappa^{(u)}}{\widetilde{\kappa}}\overline{q}^{(u)} + \sqrt{\frac{4c\mu^{(u)}\ell^{(u)}}{27\widetilde{\kappa}^2}}\widetilde{q}^{(u)}\right] \tag{5.76}$$

and evolution laws

$$\tau^{(u)}(\overline{\theta})\dot{\overline{q}}^{(u)} + \overline{q}^{(u)} - \sum_{v=1}^{U}\left[\frac{\kappa^{(v)}}{\widetilde{\kappa}}\frac{\overline{q}^{(v)}}{1-c} + \sqrt{\frac{4c\mu^{(u)}\ell^{(u)}}{3}}\frac{\widetilde{q}^{(v)}}{1-c}\right] = \frac{c}{1-c}\frac{4\mu}{3\widetilde{\kappa}}\left(\beta^{(2)}(\overline{\theta}) - \beta^{(1)}(\overline{\theta})\right) \tag{5.77}$$

$$\tau^{(u)}(\overline{\theta})\dot{\widetilde{q}}^{(u)} + \widetilde{q}^{(u)} - \sum_{v=1}^{U}\left[\frac{\kappa^{(v)}}{\widetilde{\kappa}}\frac{\overline{q}^{(v)}}{1-c} + \sqrt{\frac{4c\mu^{(u)}\ell^{(u)}}{3}}\frac{\widetilde{q}^{(v)}}{1-c}\right] = \frac{c^{3/2}}{1-c}\frac{12\mu^{(u)}}{\ell^{(u)}}\left(\beta^{(2)}(\overline{\theta}) - \beta^{(1)}(\overline{\theta})\right). \tag{5.78}$$

Casting expressions in this form makes it plain that the source of viscous deformations within the matrix phase is solely the mismatch between microscopic thermal strains, which consequently generate a dependence of the macroscopic thermal strain on cooling or heating rate even when the microscopic thermal strains are rate insensitive.

5.5.2 Fiber-reinforced composites under monotonic cooling

We now consider the unidirectional fiber-reinforced composites of Section 5.4.2 with thermal strains within the matrix phase given by the functional [50] (see: 1)

$$\beta^{(1)}(\theta) = \int_0^{\xi} \alpha^{(1)}(\xi - s)\ \dot{\theta}(s)\mathrm{d}s, \tag{5.79}$$

where ξ is the internal time defined by (5.58), and $\alpha^{(1)}$ is a thermal creep function given by

$$\alpha^{(1)}(\xi) = \alpha_{\infty}^{(1)} - \sum_{v=1}^{V} \alpha^{(1,v)} e^{-\xi/\tau_{\alpha}^{(v)}}. \tag{5.80}$$

In this expression, $\tau_{\alpha}^{(v)}$ and $\alpha^{(1,v)}$ represent thermal relaxation times and thermal expansion coefficients, respectively, and $\alpha_0^{(1)}$ represents a thermal expansion coefficient at high temperature. With this choice, the constitutive relations (5.5)-(5.6) become hereditary laws of the single-integral type like the ones studied in [139], this is indeed the matrix model that we have used in 4 for the artificial matrix representation in preserving the same mechanical spectra but with a simplification in the thermal creep function performed by preserving its asymptotic values as they are in agreement with data found in literature and reducing the number of viscoelastic thermal branches to just a single one aiming to simplify the numerical computations. As it is shown in the previous chapter, this model takes into account the influence of heating and cooling rates on thermal expansion. On the other hand, the thermal strain within the fibers is chosen as

$$\beta^{(2)}(\theta) = \alpha^{(2)}\theta, \tag{5.81}$$

where $\alpha^{(2)}$ is a thermal expansion coefficient, which is indeed the same model used in the previous section for the case of the fiber, the difference in the present application examples is that another simplification is applied aiming to obtain a simple expression of the explicit forms, this is by considering the asymptotic case in which the fibers are too stiff compared to the matrix, and then we consider them as rigid. The composites are taken as representative of a lamina situated in the bulk of a symmetric cross-ply laminate undergoing monotonic cooling at constant pressure, as in a consolidation process. The presence of contiguous orthogonal laminae is mimicked by subjecting the composite lamina to mixed boundary conditions of the form

$$\overline{\varepsilon}_{11} = \overline{\varepsilon}_{33} = \beta^{(2)}(\overline{\theta}), \quad \overline{\sigma}_{22} = 0, \quad \overline{\varepsilon}_{12} = \overline{\varepsilon}_{13} = \overline{\varepsilon}_{23} = 0, \tag{5.82}$$

where tensor components are referred to a basis with directions 2 and 3 aligned with the directions of lamination and of the lamina fibers, respectively. Under these circumstances, the reduced description for the reinforced lamina depends on the effective in-plane bulk and shear moduli of

the comparison solid, which are given by [90]

$$\widetilde{k}_0 = \frac{2\kappa_0 + (2/3)(1+3c)\mu_0}{1-c} \quad \text{and} \quad \widetilde{m}_0 = \frac{3(1+c)\kappa_0 + (7+c)\mu_0}{3\kappa_0 + 7\mu_0}\frac{\mu_0}{1-c}, \tag{5.83}$$

respectively. Expressions (5.52) for the intraphase strain fluctuations then become

$$\widetilde{\varepsilon}_m^{(1)} = \frac{1}{1-c}\sqrt{\frac{1-c}{9}\left(\frac{\partial \widetilde{k}_0}{\partial(2\kappa_0)} + \frac{\partial \widetilde{m}_0}{\partial \kappa_0}\right) - \frac{1}{9}}\,|\overline{\varepsilon}_{22} - \beta^{(2)}(\overline{\theta})| \quad \text{and} \tag{5.84}$$

$$\widetilde{\varepsilon}_d^{(1)} = \frac{1}{1-c}\sqrt{\frac{1-c}{2}\left(\frac{\partial \widetilde{k}_0}{\partial(2\mu_0)} + \frac{\partial \widetilde{m}_0}{\partial \mu_0}\right) - \frac{2}{3}}\,|\overline{\varepsilon}_{22} - \beta^{(2)}(\overline{\theta})|, \tag{5.85}$$

which should be introduced in (5.48) to generate the set of equations for the strain fluctuations $\widetilde{\varepsilon}^{(u)}$ required to evaluate the reduced free-energy density for the boundary conditions (5.82). For a given cooling program $\overline{\theta}(t)$, the evolution laws (5.55) are discretized in time following an implicit Euler scheme and taken as additional equations which, together with the previous set of equations, are solved numerically for the quantities $\overline{\boldsymbol{q}}^{(u)}$, $\widetilde{q}^{(u)}$, $\widetilde{\varepsilon}^{(u)}$, and $\overline{\varepsilon}_{22}$. Once these quantities are determined, the macroscopic stress component $\overline{\sigma}_{11}$ is computed from (5.54), while the statistics of the stress field within the matrix phase are computed from (5.34) and (5.35).

Specific results are reported below for matrix responses described with nineteen viscoelastic units ($U = 19$) characterized by constitutive tensors of the form (5.43) with relaxation times of the form (5.56). Figure 4.2 of the precedent chapter shows the choice of elastic moduli and relaxation times $(\kappa^{(u)}, \mu^{(u)}, \tau_\circ^{(u)})$ with numerical values specified in C.2, and Fig. 4.3a shows the choice of shift factor $a_T(\theta)$. In turn, as mentioned before, we adopt only one term ($V = 1$) in (5.80) with $\alpha_\infty^{(1)} = 1.02 \times 10^{-4}\ {}^\circ C^{-1}$, $\alpha^{(1,1)} = 4.22 \times 10^{-5}\ {}^\circ C^{-1}$ and $\tau_\alpha^{(1)} = 0.2017 s$. This set of material parameters is taken to represent the thermomechanical response of an amorphous thermoplastic like polyetherimide [see 4]. In particular, it is noted that the choice of shift factor pertains to a material response that transitions from negligible elasticity at the higher temperatures to negligible viscosity at the lower temperatures. Finally, the choice $\alpha^{(2)} = 2.21 \times 10^{-5}\ {}^\circ C^{-1}$ is adopted for the thermal expansion coefficient of the fibers. A composite with reinforcement content $c = 0.3$ is subject to monotonic cooling from a processing temperature of 250 $^\circ C$ down to room temperature 25 $^\circ C$, so that the total macroscopic temperature change relative to the initial temperature is $\overline{\theta}_0 = -225\ {}^\circ C$. Various cooling rates $\dot{\overline{\theta}}$ in the wide range between $-225 \times 10^{-12}\ {}^\circ C/s$ and

-225×10^{20} $^{\circ}C/s$ are considered. These unrealistically extreme values have been chosen so that elastic deformations are negligible at the slowest rate while viscous deformations are negligible at the fastest rate. This last case is considered as representative of non-dissipative material models based on purely thermoelastic constitutive laws.

Figure 5.1 displays predictions for the macroscopic stress ($\overline{\sigma}_{11}$) and strain ($\overline{\varepsilon}_{22}$) versus temperature drop for the various cooling rates, normalized by the final stress and strain levels ($\overline{\sigma}^{e}_{11}$, $\overline{\varepsilon}^{e}_{22}$) produced by the fastest cooling rate. The main observation in the context of this figure is that the reduced and exact predictions are quantitatively indistinguishable for the entire range of temperature drops and cooling rates considered. As a consequence of the choice of shift factor, the stresses and strains at the end of the cooling process do not relax but remain as residual instead. These residual stresses and deformations increase with increasing cooling rate, as expected. The reduced description is seen to provide accurate predictions for both of these quantities. In practice, cooling rates in the order of 1 $^{\circ}C/min$ (0.017 $^{\circ}C/s$) are commonly employed. At such rates, the residual stress levels predicted by the thermo-viscoelastic model are in the order of 40% of those predicted by a purely thermoelastic model; the residual thermal shrinkages, in turn, are seen to be in the order of 80%. Also displayed in the figure are corresponding reduced predictions for the average values and fluctuations of the mean (σ_m) and deviatoric (σ_d) stresses within the matrix phase ($r = 1$). Exact results for stress fluctuations are not reported due to the well-known limitations of descriptions based on the correspondence principle to predict intraphase stress statistics of order higher than one. The reduced and exact predictions are seen to remain indistinguishable for the average stresses over the matrix phase. The predicted residual stress field within that phase is seen to exhibit fluctuation levels of about half of the average values. Once again, values for realistic cooling rates are seen to be well below the values for the fastest cooling rate. The associated evolution of the effective internal variables is provided for five representative units out of the nineteen, for the cooling rate 2.25 $^{\circ}C/s$. In all cases the internal variables are seen evolve from the outset and up to certain temperature below which they remain constant. This is a manifestation of the viscous-to-elastic transition effected by the choice of shift factor. The saturation value and temperature change of each internal variable is dictated by the associated relaxation time $\boldsymbol{\tau}^{(u)}_{\circ}$ shown in Fig. 4.2. In any event, these results suggest that purely thermoelastic analyses which neglect all viscous mechanisms will, in general, provide quite inaccurate predictions for residual stresses resulting from consolidation

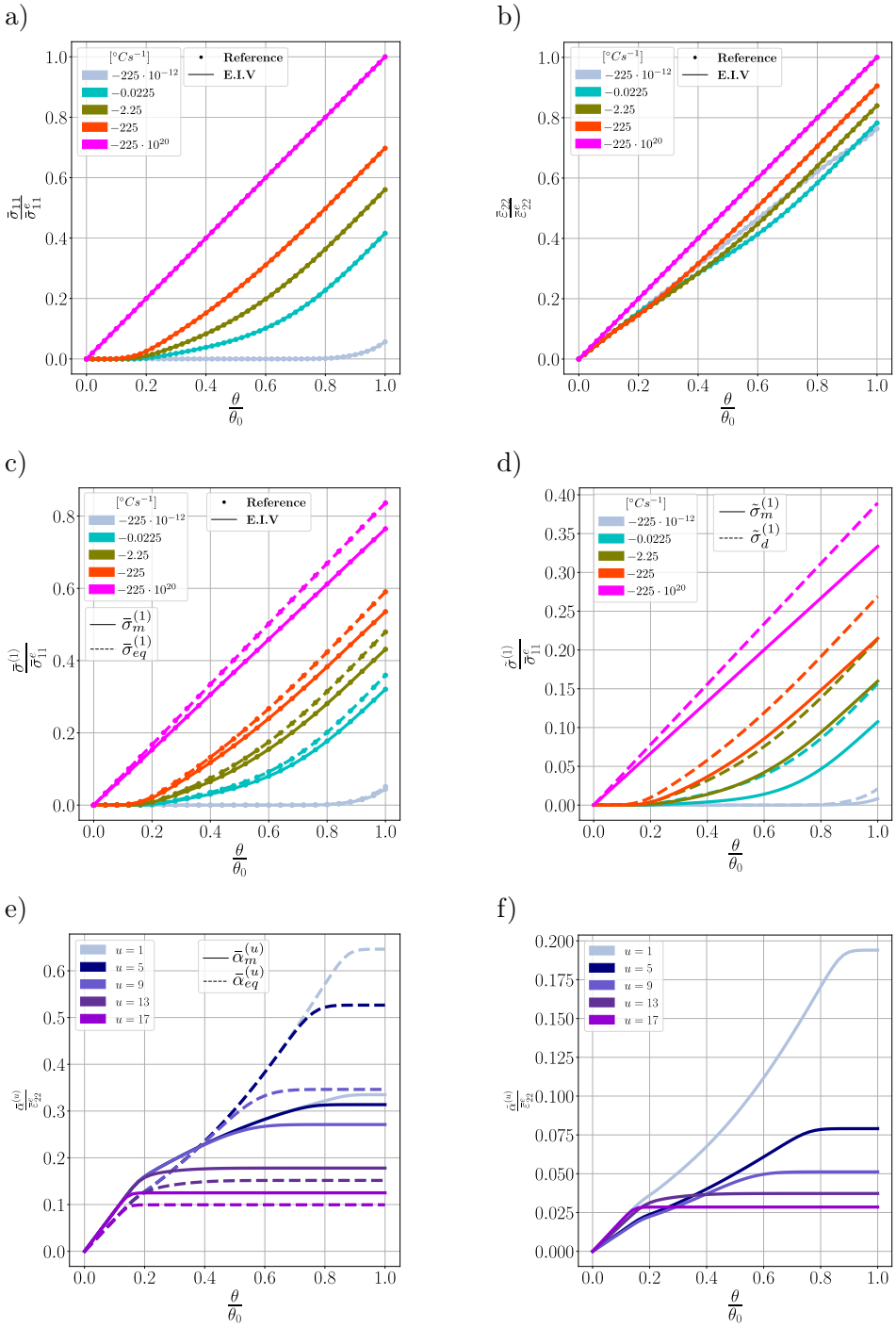

Figure 5.1: Reduced-order estimates (EIV) and exact results (Reference) versus temperature change for fiber-reinforced composites subject to monotonic cooling at various cooling rates: (a) macroscopic stress, (b) macroscopic strain, (c) and (d) average stress and stress fluctuations within the matrix phase, (e) and (f) evolution of effective internal variables for the cooling rate 2.25 $°C/s$. Stress and strain quantities are normalized, respectively, by the macroscopic residual stress and strain for the fastest cooling rate. The reinforcement content is $c = 0.3$.

processes of this sort.

We conclude this discussion by noting that the reduced free-energy density of the fiber-reinforced composite employed by this reduced description is non-convex and cannot be convexified like the reduced free-energy density of the particulate composites considered in the previous subsection. Predictions will exhibit spurious transients for certain classes of non-monotonic thermomechanical programs, for which the intraphase fluctuations of some thermodynamic forces may vanish [132, 144]. However, this is unlikely to occur during thermomechanical programs commonly employed in consolidation processes of practical interest. The reduced mean-field descriptions derived in this work are thus expected to provide a valuable tool to identify processing routes to lower residual stresses or use them to our advantage.

5.6 Final comments

A dual mean-field description wherein the mechanical fields entering the potentials are the stresses and thermodynamic forces rather than the strains and internal variables was proposed by [146] and applied to viscoelastic composites and polycrystals by [147], [145] and [148]. The predictions generated by this alternative description are different from those generated by the primal description considered in this work, and their relative merits have been discussed by [149] and [150]. This last work casts the description within an alternative formalism to that of [146] which makes the generalization of the dual description to thermorheologically complex solids mathematically similar to the one observed here for the primal description. An thorough comparison between the primal and dual versions of the reduced descriptions, along with approximate extensions of the correspondence principle to ageing behaviors [151, 152], will be reported elsewhere.

In any event, the mean-field descriptions provided in this work already apply to a large class of thermorheologically complex reinforced solids and, moreover, admit further generalizations with ease. For instance, they can incorporate nonlinear viscous mechanisms via non-quadratic dissipation potentials together with well-known linearization strategies [153, 149, 154]. More importantly, they can incoporate curing deformations arising in thermosetting composites [155] via homogenization results for well-known curing kinetic laws [137]. Future efforts will be directed towards these problems.

Chapter 6

Mesoscale Analysis : the poro-thermo-viscoelastic network

This chapter is devoted to the second upscaling. We will then take the results of chapter 4 and we will use them as the material properties of the matrix for the upper scale, that of the printed filaments arrangements in a cohesive structure exhibiting a porous network. The effective behavior is computed using the FEM framework to solve the homogenization problem in sample mesostructures presenting periodicity. This work is on preparation for publication with target journal: *Journal of Additive manufacturing*. The outputs from the computation on the effective properties are then tested to compare the macroscopic response of mesostructures lacking periodicity in the stacking direction of the printed layers. Numerical validation is initially presented for the low temperature behavior (the glassy case) to simplify the numerical cost while ensuring representativeness. Numerical thermoviscoelastic validation examples are presented for a thin plate and an experimental validation section is presented the end as final source of validation while comparing deflection in actual 3D printed non-symmetric thin plates

So far, we have been able to obtain reliable approximations for the effective behavior of the reinforced filament both for a thermorheologically complex matrix (Chapter 5) and for our reference material (Chapter 4), a thermorheologically simple matrix (i.e., PEI). Our two-step homogenization methodology is now located at the transition from the mesoscale porous network to the

macroscopic scale of the printed part, which we see as continuous to the naked eye.

It is now appropriate to summarize a bit the work we have done so far. As already mentioned, the fact that the matrix of the filament is a polymer takes the first homogenization step out of the conventional context in which it is classically applied. The mechanical behavior is defined as thermo-viscoelastic, which means that the properties of the material are a function of time and temperature. With respect to the linear theory of classical viscoelasticity, the analytical homogenization is performed using the correspondence principle, a mathematical strategy based on the Laplace-Carson transform [59], which allows to implement the analytical homogenization in an equivalent way as it is done for linear thermoelasticity. This technique was introduced by Eshelby [1, 3, 2], fully developed and presented in [60] with explicit forms for the Hashin-Shtrikman estimate in the case of isotropic distributions of isotropic spheres in a linear viscoelastic matrix. The temperature dependence of the properties was not considered in that work. We dealt with the thermo-viscoelastic behavior by extending the correspondence principle to continuous temperature variations by means of the internal time technique, an extension of the time-temperature superposition principle for thermo-rheologically simple materials. This work has already been published in [4] and presented in Chapter 4. In this paper, the effective thermo-mechanical behavior of short fiber reinforced polymer filament is calculated using three different approaches: Mori-Tanaka scheme, Lielens scheme [117] and Interaction Direct Derivative (IDD) scheme [119], showing the closeness of these estimates in calculating the stress response to a thermo-mechanical load. The diversity in the orientations and lengths of the fibrous inclusions was accounted for by considering probabilistic distributions. Finally, the heterogeneous filament is exchanged for its continuous version to serve as the matrix material for the calculation of the effective behavior of the porous layered structure. And again, it is at this point that we are, at the second upscaling.

When the 3D printed part is growing inside the printing chamber, layers of material are deposed by extruding the cylindrical filament and promoting the consolidation of their lateral interphases by juxtaposing them while ensuring their contact. In principle, this technology allows an arbitrary combination of trajectories serving to obtain the part. If for instance we see Fig. 2 of the introduction, the pattern shown is a consequence of a particular choice of the printing trajectories which represents the simplest one, and this is in fact our choice as starting point for characterizing the mesostructure in Section 6.1.1. By choosing the same direction for all trajectories of the printing head, we obtain this pattern in which the cross-section of the

elongated porosities are represented by curved diamonds.

Of course this choice of trajectories will influence the macroscopic behavior of the part, as from the precedent homogenization step, the presence of isotropic short glass fibers embedded in an isotropic amorphous polymer matrix gave us an effective behavior of the composite filament that is transverse isotropic, represented by the presence of a longitudinal symmetry axis in the material properties. Therefore, the printing direction will create an arrangement of oriented transverse isotropic cylinders within a distribution of porosities. The present study considers printing layers conserving the same printing direction at least each couple of layers, lying in oriented porosities shapes that are close to the ideal geometry presented in Fig. 6.2. The particularity of such microstructures is the presence of periodicity. If one aims to solve analytically such problems, the inconvenient raises when choosing an analytical representation of the elongated curved diamond necessary to define the explicit form of the localization tensor $\mathbb{A}$ as we did in Chapter 4 where we represented the glass fibers as oriented prolate ellipsoids. We work around this issue by addressing the computation of the effective behavior at the mesoscale by means of full-field estimates implementing numerical homogenization of periodic microstructures [156, 157], as is presented in Section 6.1. Similarly to Chapter 4, in Section 6.1.2 here we use the correspondance principle to reformulate the homogenization problem in the Laplace-Carson domain to immediately identify this problem as equivalent to the steady state response to a harmonic loading, allowing us to implement homogenization again analogically as it is performed for composites with thermoelastic constituents.

The implementation of the computation of the effective thermo-mechanical behavior at this scale is computed using finite element commercial solver Abaqus®, a full-field estimate. The parametric characterization of the REV is also presented in this section (Section 6.1.1). In Section 6.2 to assess the effectiveness of the chosen methodology, the effective thermo-elastic response is considered instead of the thermo-viscoelastic response, due to the fact that the homogenization procedure is carried out in the Laplace-Carson domain (an analogy of the steady-state response in the frequency domain), in consequence the thermo-elastic response is enough to perform the comparative analysis between the homogenized and full heterogeneous response, avoiding the large amount of computations of the discretized frequency space. Discretization convergence studies are presented as well for both the homogenized and reference solutions.

In Section 6.2.3 the volume fraction of the porosities is chosen to be approximately 0.05, the

macroscopic effective response is computed using the REV of the precedent section, and tested in two different models. These are, a 10mm $\times$ 10mm $\times$ 10mm cube, and a 100mm $\times$ 100mm $\times$ 2mm plate. In the case of the homogenized cube response, it is compared with two 2D generalized plane strain simulations, these are, a homogeneous plate which properties are the same as the cube, and a heterogeneous plate with 0.05 of porosity. For the homogenized 3D plate model, it is compared with a heterogeneous 3D plate with the same volume fraction of porosity and a 2D shell model under plane stress. The loading conditions for the simulation cases are: i) distributed bending, ii) uniaxial traction and iii) free-load cooling.

In section 6.2.4, the macroscopic response for an oriented stacking of printed layers is considered, the stacking is done in a way that a layer is defined as two sublayers with a same single printing trajectory (ensuring the validity of the cavities idealized geometry), which is a 100mm $\times$ 100mm $\times$ 4mm plate for two different volume fractions of porosity, 0.05 and 0.15. 3D homogenized models and 2D homogenized laminate models are compared with 3D heterogeneous reference solutions for three cases of the stacking orientation, two asymmetric cases, $[0, 0, 90, 90]$ and $[0, 90, 0, 90]$, and a symmetric stacking $[0, 90, 90, 0]$. The simulations consider the cooling under load-free conditions, comparing the deflection of the models. The objective here is to propose a simplified model for the warping of built-up parts.

Finally, a last verification study is presented in in Section 6.3, one of the key points of the present work that is to face the proposed methodology against experiments. To do so, an experimental procedure is proposed. The object of the comparisons is the deflection exhibit by a 3D printed thin plate made of composite filament with 30% of short glass fibers and a polymeric matrix in Ultem® 1010. A full report of results and further discussion is presented in this section. This chapter closes with a local set of final comments in Section **??**.

6.1 Effective behavior of the layered structure

We start here with the first step of any homogenization procedure, the representation. We must then be able to give an appropriate geometrical and material description of the phases that coexist in the heterogeneous domain. As we can see in the microphotograph (Fig. 6.1), there are two clear phases, filaments and voids, we then identify this composite material in the simplest category of a binary composite. In terms of material properties, we already have

a suitable mathematical description for the continuous phase, the matrix, which in our case consists of a transversely isotropic thermo-viscoelastic material (obtained from Chapter 4). The voids are assumed to have negligible constant mechanical properties. Further comments on the implications of this will be presented later in this section. For now, we will first consider the geometric representation of the Representative Elementary Volume (REV).

6.1.1 Choice of the REV

As we have just said, we will address homogenization in this step by considering a restricted scenario of unidirectional printing trajectories. Figure 6.1 shows a microphotograph of the cross-section of such mesostructure from [158], which is the reference geometry for the present work. As can be observed in this figure, the predominant shape is a curved diamond like shape. To

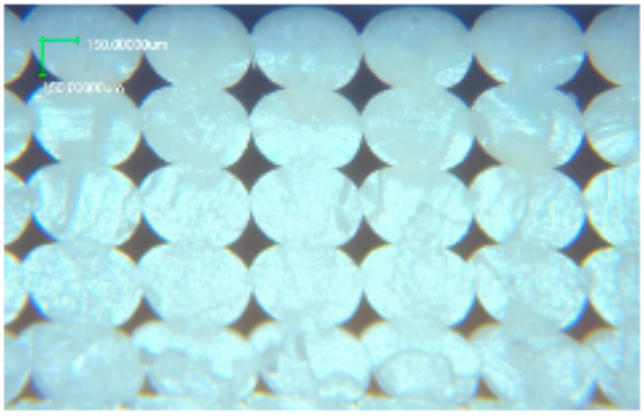

Figure 6.1: Microphotography of the cross-section of the layered structure.

model this, we consider an idealized mesoscructure assuming that this predominant shape is extended uniformly in the whole volume of the printed part (see Fig. 6.2). Here, the simplest geometrical representation of the porosity shape is sought, in other words the choice will be done in a way that the generation of the geometry is achieved by using a parametric representation with the lowest number of parameters. As we have already mentioned, the REV is chosen based on the observations reported by [158] (Fig. 6.1). In this work, the authors represent the filaments as hexagonal prisms, in consequence, the porosity cross-section takes the shape of a diamond. In [159], the authors assimilate the printed filaments as elliptical cylinders, in consequence the porosity cross-section's shape is a curved diamond. For the present work, the latter representation is taken as it is more realistic. Moreover, a supplementary assumption is

made for the sake of simplicity in the porosity parametrization for the first round of numerical tests, this is, the equal length of the semi-axes of the curved-diamonds, obtained by considering circular cylinder shaped filaments with some degree of overlapping, or equivalently, rounded rectangular or square cylinders with no overlapping. As can be noted in Fig. 6.2, the volume of the cavities is defined as a function of the degree of overlapping of the neighboring filaments [159, 160]. It must be recalled that this representation is an idealization of the mesostructure since the real situation does not hold the symmetry of a curved-diamond. Indeed, other assumptions are made to be able to characterize the REV as the hypothesis of translation symmetry in the normal direction of the cross-section of the mesostructure and perfect interphases in the contact zones of the neighboring filaments.

Parametric characterization of the porosity

The idealized mesostructure is presented in Fig. 6.2. In consequence of the foregoing assumptions, the mesostructure can be characterized as a periodic medium with periodicity vectors being collinear to the principal orthogonal directions of the symmetry plane ($\boldsymbol{e}_1$ and $\boldsymbol{e}_2$) and geometrical invariance in the normal direction ($\boldsymbol{e}_3$). The REV is then characterized by a unit square cell of side $l = 1$ with a centered curved-diamond shaped porosity. The parametrization of the porosity is obtained by considering the given volume fraction of porosity v_f of the part, that due to the geometrical invariance in the normal direction is identical to the surface fraction of the cross-section, to calculate the surface parameters of the curved diamond of the single porosity in the REV that serve as inputs in the geometry generation of the computational domain. By considering equal lengths of the two semi-axis of the curved-diamond, the explicit form of the volume fraction of the porosity is presented as follows:

$$v_f = \left(\frac{a}{l}\right)^2 (1 - \frac{\pi}{4}). \tag{6.1}$$

The volume fraction space of the porosity for the present study is set to $v_f = \{0.05, 0.075, 0.1, 0.125, 0.15\}$, these values were chosen considering the experimental measurements reported in [161]. As mentioned above, this shape for the centered porosity of the REV will be the subject of our numerical validation experiments. In the experimental validation section, the choice of the appropriate shape will be considered from the observations of the actual printed parts used for comparisons.

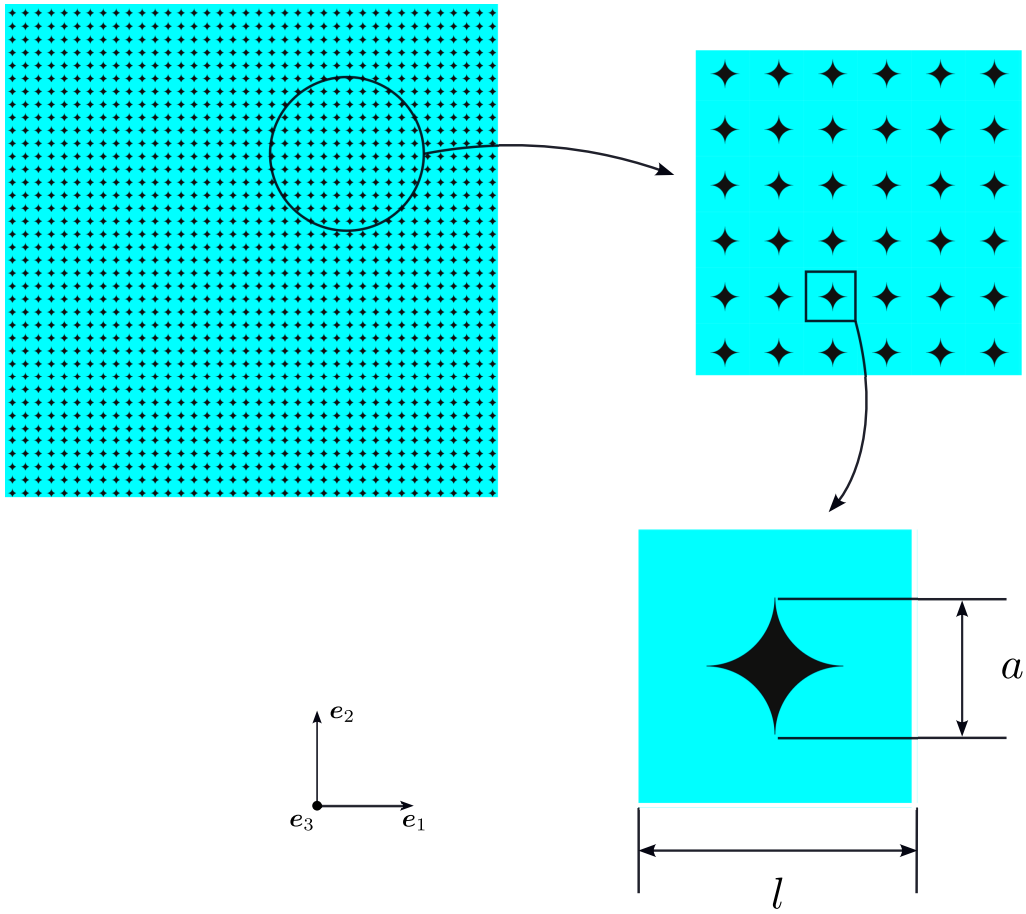

Figure 6.2: Idealized mesostructure with periodic REV.

In any case, if one wants to address the case of the squeezed curved diamond, the geometric representation will be defined by two parameters a_1 and a_2, which are the lengths of its semi-axis, as shown in the figure below:

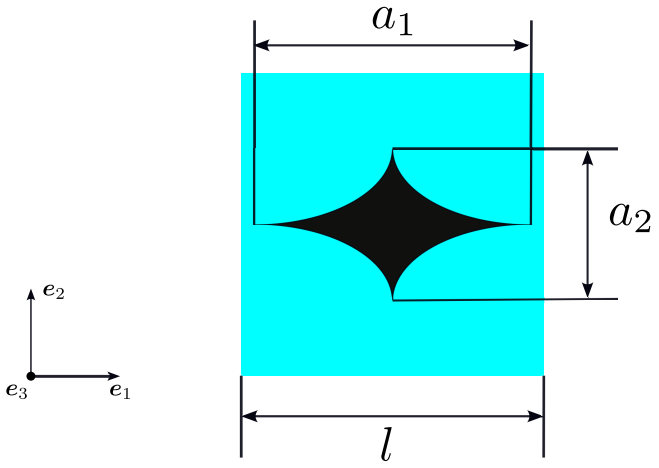

Figure 6.3: The squeezed porosity REV.

With this two parameters, the expression relating them to the volume fraction of the porous network becomes

$$v_f = \frac{a_1 a_2}{l^2}(1 - \frac{\pi}{4}). \tag{6.2}$$

6.1.2 Homogenization procedure

Having defined the suitable representation for the REV, we now pass to formulate the homogenization problem that is solved numerically by means of the conventional finite elements method. At the beginning of the section when referring to the material properties of the phases we have said that the mechanical properties of the porosities are assumed to be always negligible compared to those of the matrix and constant in function of time and temperature. We are then in a similar situation to the one in Chapter 4; a thermo-viscoelastic matrix with inclusions presenting constant mechanical properties. This implies the applicability of the Correspondence principle as it is done in Section 4.2, as we still maintain the uniqueness of the shift factor a_T since at this scale we are also in the case of a single polymer composite (SPC) whose matrix is thermorheologically simple. Before going into the details of the implementation, we will present a supplementary simplification. To illustrate it, we consider the Levin relations [121, 120, 91] for binary composites, recalling the analogy of the thermoelastic problem in virtue of the aforementioned principle. For a given thermomechanical properties of the porous phase, $\mathbb{L}^{(\mathrm{p})}$, and $\boldsymbol{\alpha}^{(\mathrm{p})}$ with volume fraction v_f, and the matrix thermomechanical properties, $\mathbb{L}^{(\mathrm{m})}$ and $\boldsymbol{\alpha}^{(\mathrm{m})}$, with volume fraction, $1-v_f$, the Levin relation (see Chapter 4) for $\widetilde{\boldsymbol{\alpha}}$ for the case of a porous media is obtained by considering the fact of the nullity of the mechanical properties of the porous phase, therefore, $\mathbb{L}^{(\mathrm{p})} = 0\mathbb{I}$, with $0\mathbb{I}$ the fourth order tensor with all elements equal to zero, the Levin relation for a biphasic composite with porous inclusions becomes:

$$\begin{aligned}
\widetilde{\mathbb{L}} \cdot \widetilde{\boldsymbol{\alpha}} =& [(1-v_f)\mathbb{L}^{(\mathrm{m})} \cdot \boldsymbol{\alpha}^{(\mathrm{m})}] + [\widetilde{\mathbb{L}} - (1-v_f)\mathbb{L}^{(\mathrm{m})}] \cdot [-\mathbb{L}^{(\mathrm{m})}]^{-1} \cdot [-\mathbb{L}^{(\mathrm{m})} \cdot \boldsymbol{\alpha}^{(\mathrm{m})}] \\
=& (1-v_f)\mathbb{L}^{(\mathrm{m})} \cdot \boldsymbol{\alpha}^{(\mathrm{m})} + \widetilde{\mathbb{L}} \cdot \boldsymbol{\alpha}^{(\mathrm{m})} - (1-v_f)\mathbb{L}^{(\mathrm{m})} \cdot \boldsymbol{\alpha}^{(\mathrm{m})} \\
=& \widetilde{\mathbb{L}} \cdot \boldsymbol{\alpha}^{(\mathrm{m})}.
\end{aligned} \tag{6.3}$$

The above expressions are a sufficient proof of, $\widetilde{\boldsymbol{\alpha}} = \boldsymbol{\alpha}^{(\mathrm{m})}$, and then, no further computations are addressed to the effective tensor of thermal creep functions as we will be using for the macroscopic

behavior the same obtained from the first homogenization step and computed in Chapter 4. After this simplification of the computation of the effective macroscopic behavior, which is reduced to the computation of the effective fourth relaxation tensor $\widetilde{\mathbb{L}}$ at the mesoscale, and recalling from Chapter 4 that the macroscopic shift factor of an SPC remains the same as the thermo-viscoelastic matrix, the homogenization procedure is then reduced to compute numerically the effective viscoelastic behavior at the reference temperature T_r using the correspondance principle. After this initial considerations reducing the complexity of the homogenization problem at the mesoscale, we can now continue on its formulation.

A periodic microstructure exhibits invariance of geometry along the periodicity vectors; for the mesostructure considered in the present work (Fig. 6.2), the periodicity vectors are those of the principal directions of the porosity cross-section (i.e., $\boldsymbol{e}_1$ and $\boldsymbol{e}_2$). For such mesostructure, the solution of a homogenization problem considering macroscopic homogeneous fields ($\bar{\boldsymbol{\varepsilon}}$ and $\bar{\boldsymbol{\sigma}}$) introduced in Chapter 3, the local fields, $\boldsymbol{\varepsilon}(\boldsymbol{x})$ and $\boldsymbol{\sigma}(\boldsymbol{x})$, are in the same way invariant by translation with period lengths equal to the sides of the REV. Indeed, it is possible to decompose the local fields in a mean and fluctuant part, for instance the strain field: $\boldsymbol{\varepsilon}(\boldsymbol{x}) = \bar{\boldsymbol{\varepsilon}} + \boldsymbol{\varepsilon}(\boldsymbol{u}'(\boldsymbol{x}))$. Where $\bar{\boldsymbol{\varepsilon}} = \langle \boldsymbol{\varepsilon}(\boldsymbol{x}) \rangle = \frac{1}{|\Omega|} \int_\Omega \boldsymbol{\varepsilon}(\boldsymbol{x}) d\Omega$ by construction, and $\boldsymbol{u}'(\boldsymbol{x})$ stands for the periodic fluctuation of the displacement field $\boldsymbol{u}(\boldsymbol{x})$ whose associated strain field $\boldsymbol{\varepsilon}' = \boldsymbol{\varepsilon}(\boldsymbol{u}'(\boldsymbol{x}))$ vanishes at the macroscopic scale in consequence of its periodicity $\langle \boldsymbol{\varepsilon}'(\boldsymbol{x}) \rangle = \mathbf{0}$. The strong form of the homogenization problem presented in Chapter 3 can be rewritten for the case of a periodic REV (Ω) as follows:

$$\begin{cases} \nabla \cdot \boldsymbol{\sigma}(\boldsymbol{x}, t) = \mathbf{0} & \forall \boldsymbol{x} \in \Omega, \\ \boldsymbol{\sigma}(\boldsymbol{x}, t) = \left[\mathbb{L}(\boldsymbol{x}, \cdot) \circledast \boldsymbol{\varepsilon}(\boldsymbol{x}, \cdot) \right](t) & \forall \boldsymbol{x} \in \Omega, \\ \boldsymbol{\varepsilon}(\boldsymbol{x}, t) = \bar{\boldsymbol{\varepsilon}} + \boldsymbol{\varepsilon}'(\boldsymbol{x}, t) & \forall \boldsymbol{x} \in \Omega, \\ \boldsymbol{u}'(\boldsymbol{x}, t) & \Omega\text{-periodic}, \end{cases} \tag{6.4}$$

Again, as it is done in Chapter 4 we use the Laplace-Carson transform to rewrite the viscoelastic

problem above as a symbolic analogy of the elastic problem in the Laplace-Carson domain:

$$\begin{cases} \nabla \cdot \boldsymbol{\sigma}^*(\boldsymbol{x}, p) = \mathbf{0} & \forall \boldsymbol{x} \in \Omega, \\ \boldsymbol{\sigma}^*(\boldsymbol{x}, p) = \mathbb{L}^*(\boldsymbol{x}, p) \cdot \boldsymbol{\varepsilon}(\boldsymbol{x}, p) & \forall \boldsymbol{x} \in \Omega, \\ \boldsymbol{\varepsilon}^*(\boldsymbol{x}, p) = \bar{\boldsymbol{\varepsilon}}^* + \boldsymbol{\varepsilon}'^*(\boldsymbol{x}, p) & \forall \boldsymbol{x} \in \Omega, \\ \boldsymbol{u}'^*(\boldsymbol{x}, p) & \Omega\text{-periodic.} \end{cases} \tag{6.5}$$

As we aim to solve this problem numerically, we will now identify this problem to be equivalent to the steady state dynamic problem when harmonic loads are considered. This is done by considering the change of variable $p = j\omega$, with $j\omega$ being the complex angular frequency. This equivalency is already presented in [5, 35], where the local fields solving the problem above have to satisfy the same equations of a boundary value problem on an elastic body, with application examples including more recent publications in [45, 162]. The above linear problem is rewritten in the frequency space as:

$$\begin{cases} \nabla \cdot \boldsymbol{\sigma}^*(\boldsymbol{x}, j\omega) = \mathbf{0} & \forall \boldsymbol{x} \in \Omega, \\ \boldsymbol{\sigma}^*(\boldsymbol{x}, j\omega) = \mathbb{L}^*(\boldsymbol{x}, j\omega) \cdot \boldsymbol{\varepsilon}(\boldsymbol{x}, j\omega) & \forall \boldsymbol{x} \in \Omega, \\ \boldsymbol{\varepsilon}^*(\boldsymbol{x}, j\omega) = \bar{\boldsymbol{\varepsilon}}^* + \boldsymbol{\varepsilon}'^*(\boldsymbol{x}, p) & \forall \boldsymbol{x} \in \Omega, \\ \boldsymbol{u}'^*(\boldsymbol{x}, j\omega) & \Omega\text{-periodic.} \end{cases} \tag{6.6}$$

In the constitutive equation of the stress in the above problem, the Laplace-Carson transform of the relaxation moduli tensor $\mathbb{L}^*(p)$ is now identified as the *complex moduli* fourth order tensor $\mathbb{L}^*(jw)$. This complex moduli are identified in practice from dynamical mechanical experiments, as we did for the identification of the mechanical properties of the PEI in Chapter 4. This experiment is performed by applying harmonic displacements or forces in samples under controlled boundary conditions, the DMA, a common procedure in rheology and often preferred instead of relaxation or creep experiments. For the sake of clarity, we will present explicitly the correspondence of both forms starting from the frequency domain experience.

The response of the polymer in the case of steady-state oscillations of the form $\boldsymbol{\varepsilon}(t) = \boldsymbol{\varepsilon}_0 e^{j\omega t} = \boldsymbol{\varepsilon}(j\omega t)$. First, $\boldsymbol{\varepsilon}(t)$ is substituted in the integral form of the constitutive equation of the stress in

Eq. (6.4):

$$\boldsymbol{\sigma}(j\omega t) = \left(j\omega \int_{-\infty}^{t} \mathbb{L}(t-\tau) e^{j\omega t} d\tau \right) : \boldsymbol{\varepsilon}_0, \tag{6.7}$$

now we perform the change of variable $u = t - \tau$:

$$\boldsymbol{\sigma}(j\omega t) = \left(j\omega \int_{0}^{\infty} \mathbb{L}(u) e^{-j\omega u} du \right) : \boldsymbol{\varepsilon}_0 e^{j\omega t} = \mathbb{L}^*(j\omega) : \boldsymbol{\varepsilon}(j\omega t). \tag{6.8}$$

Then the equivalence is given by changing the complex angular frequency $j\omega$ by the Laplace-Carson variable p in $\mathbb{L}^*(j\omega)$:

$$\mathbb{L}^*(p) = p \int_{0}^{\infty} \mathbb{L}(u) e^{-pu} du = p\mathcal{L}\{\mathbb{L}\}(p) = \mathcal{LC}\{\mathbb{L}\}(p) \tag{6.9}$$

A complex relaxation moduli tensor $\mathbb{L}^*(j\omega)$ is then identical to the Laplace-Carson transform of the relaxation moduli tensor in Eq. (4.3) and Eq. (4.4), this is why the same notation is used. Similarly, as it is done in practice during experiments, we will solve the homogenization problem for a set of constant frequencies $\{\omega_n\}$ describing the service conditions of the material in terms of time and temperature, computing the numerical values of the effective complex moduli tensor by solving numerically for each ω_n, the homogenization problem defined above by imposing six elementary harmonic loads as virtual experiments of traction and shear deformation necessary to fill the elements in $\widetilde{\mathbb{L}}^*(j\omega_n)$. Precision about how we actually do this will be given after formulating a weak form of the linear elastic like problem with complex coefficients.

The macrohomogenity condition imposes the nullity of the volume average of the strain fluctuation, $\langle \boldsymbol{\varepsilon}'^*(\boldsymbol{x}) \rangle = 0$. First, consider the decomposition of all plane boundaries enclosing Ω as, $\partial\Omega = \cup_{d=1}^{D} \partial\Omega^{(d)}$. The periodicity condition of the displacement fluctuation is traduced by its equality on the boundaries concerned by the periodicity vectors. This can be interpreted as follows : Consider the set of periodicity vectors $\boldsymbol{v}^{(b)}, b \in \{1, ..., B\}$, a subset of $\boldsymbol{n}^{(d)}$, the set of all outer normal vectors of the surfaces enclosing the REV (Ω). Let $l^{(b)}$ be the set of characteristic lengths representing the normal distance between each reference periodic boundary and its correspondent. To derive the weak form of the homogenization problem, the periodicity constraint can be introduced in the definition of the appropriate Sobolev space $\mathcal{S}$ in which the solution to the homogenization problem exist by considering the decomposition of the displacement field

$\boldsymbol{u}^*(\boldsymbol{x}) = \bar{\boldsymbol{\varepsilon}}^* \cdot \boldsymbol{x} + \boldsymbol{u}'^*$.

$$\boldsymbol{u}^* \in \mathcal{S}(\Omega) = \{\boldsymbol{u}^* \in \mathbb{R}^3(\Omega) \ : \ \boldsymbol{u}^*(\boldsymbol{x} + l^{(b)}\boldsymbol{v}^{(b)}) - \boldsymbol{u}^*(\boldsymbol{x}) = l^{(b)}\bar{\boldsymbol{\varepsilon}}^* \cdot \boldsymbol{v}^{(b)} \ \forall \boldsymbol{x} \in \partial\Omega^{(b)}\} \tag{6.10}$$

In practice, to define $\mathcal{S}$ for numerical applications, multipoint constraints are imposed on the periodic boundaries $\partial\Omega^{(b)}$. To define this easily on discretized domains, a periodic mesh is generated, that is, a mesh with outer boundaries with matching nodes on the corresponding opposite boundary. The formulation of the variational problem is equivalent to the conventional formulation of the linear elastic body, starting from the equilibrium equation. The index notation is used in the following steps:

$$\sigma^*_{ij,j} = 0_i \tag{6.11}$$

This traduces the nullity of each element in the three-dimensional vector resulting from the divergence of the stress in each material point $\boldsymbol{x} = x_i$. Assuming that this is hold, the introduction of the weighting function $\boldsymbol{w}^* \in \mathcal{V}$ (with $\mathcal{V}$ being the vector space holding the homogeneous Dirichlet boundary conditions) does not affect the previous statement.

$$w^*_i\sigma^*_{ij,j} = 0 = \left(w^*_i\sigma^*_{ij}\right)_{,j} - w^*_{i,j}\sigma^*_{ij}. \tag{6.12}$$

Integrating in Ω the foregoing expression and by means of the Green's theorem, the global equilibrium equation reads:

$$\int_\Omega w^*_{i,j}\sigma^*_{ij}d\Omega = \int_\Omega \left(w^*_i\sigma^*_{ij}\right)_{,j} d\Omega = \int_{\partial\Omega} w^*_i\sigma^*_{ij}n_j d\partial\Omega \tag{6.13}$$

The homogenization problem is formulated by imposing the macroscopic homogeneous strain field $\bar{\varepsilon}^*_{ij}$, this is traduced by an absence of any kind of external stress loading on the boundaries. In consequence, the right-hand side of the above equation vanishes. By using the constitutive equation, the global equilibrium equation takes the following form considering here that this linear problem is solved for each frequency ω_n, the fourth order complex moduli tensor L^*_{ijkl}

corresponds to $L^*_{ijkl}(\omega_n)$,

$$\int_\Omega w^*_{i,j} L^*_{ijkl} u^*_{k,l} d\Omega = 0. \tag{6.14}$$

Finally, the weak form of the variational formulation of the homogenization problem for periodic microstructures reads:

$$\begin{aligned} &\text{Find } u^*_i \in \mathcal{S}(\Omega) \text{ such that:} \\ &\int_\Omega w^*_{i,j} L^*_{ijkl} u^*_{k,l} d\Omega = 0, \qquad \forall w^*_i \end{aligned} \tag{6.15}$$

6.1.3 FEM based periodic homogenization

As pointed out before, to solve numerically the above set of problems, we use conventional finite elements method [156, 157]. The computation of the effective behavior under the framework of composite materials with periodic microstructures is carried out using the commercial software Abaqus® through the home plugin HomTools [163]. This plugin allows to easily impose periodic boundary conditions in periodic meshes and macroscopic fields for both $\bar{\boldsymbol{\varepsilon}}^*$ and $\bar{\boldsymbol{\sigma}}^*$, here, we use the first which correspond to the elements in $\widetilde{\mathbb{L}}^*$. After solving for $\boldsymbol{u}$ the problem in Eq. (6.15) these elements are computed in a post-processing procedure by considering the volume average of the strain and stress fields in Ω.

Numerical implementation with Abaqus®

In our case, this procedure combines the implementation of material's subroutine (UMAT) for transverse isotropic thermo-viscoelasticity in the frequency domain, the imposition of periodicity constraints with the aid of the home plugin HomTools and the parametric study utility of Abaqus® (.psf script), launching the series of steady state dynamics simulations and then executing the first post-processing by extracting the frequency series of the elements of the 4th order effective relaxation tensor ($\widetilde{\mathbb{L}}^*$). A general description of the implementation of the numerical homogenization procedure is given below:

i. REVs are generated using Abaqus CAE (see Fig. 6.6), including: material properties defined by choosing the user material option of the properties dialog, pointing to the UMAT subroutine. The mesh generation must ensure matching nodes between correspondent

surfaces in the periodicity directions (a periodic mesh).

ii. Using HomTools we impose periodic kinematic boundary conditions on the periodic boundaries, constraining the solution space corresponding to Eq. (6.10).

iii. During the step definition, a steady state dynamics simulation is defined within a set of discrete frequencies ω_n that matches with the space of the frequency spectrum characterizing the mechanical properties of the matrix. Finally, boundary conditions are initialized on reference points that must be defined during the imposition of the periodic boundary conditions, this kinematic boundary conditions are used to impose the macroscopic test fields for the estimation of the elements of the effective relaxation tensor for each frequency. After this, no further operations are needed on the graphical CAE, and we generate an input file for the simulations.

iv. Now we modify the input file to introduce the values of the complex moduli using a python script, these are the coefficients of the Prony series of the matrix mechanical properties to be passed as inputs for the UMAT subroutine. Then we introduce some lines in the input file to change the parameters for the above initialized boundary conditions imposed on the reference points, these parameters will be modified internally by means of an Abaqus parametric study file.

v. The UMAT subroutine serve to compute the fourth order complex moduli tensor for a given frequency defined in the input file; to do so, we read the frequency step of the dynamic study, then we read the mechanical properties that we just have introduced before in the input file, and we give the corresponding value of the complex coefficients of $\mathbb{L}^{(\mathrm{m})*}(\omega_n)$. If one wants to address a different set of frequencies for the simulations, a linear interpolation is performed if the given frequency is within the frequency range of the material properties.

vi. In the parametric study that takes the form of a .psf script, we write the instructions to copy and modify the parameters of a generic input file (the one that we have just created), then we use it to automatically launch the six dynamic simulations switching boundary conditions corresponding to the six elementary kinematic loads (see Fig. 6.5), that solves the linear problem in Eq. (6.15) for each frequency defined in the input files.

vii. Having the set of output database files (.odb) after the simulations, a python script post-process the results computing and collecting the values of the nine complex orthotropic coefficients of the effective behavior $\widetilde{\mathbb{L}}^{(\mathrm{m})*}(\omega_n)$ and giving as output a .csv file.

The last step is to use the obtained frequency data to estimate the best set of parameters for each Prony series representing each coefficient of the 4th order relaxation tensor, following the Krerin-Nuddleman method from [7] and already implemented in Chapter 4. In the following section, we will perform a first set of numerical experiments to evaluate the pertinence of such approximation for our application context. In Fig. 6.4 an example of the outputs used for the numerical validation examples in the present work is presented.

6.2 Primal comparative analysis

The study of the reliability of the homogenization procedure chosen to estimate the macroscopic behavior will be performed by considering that the matrix-material is linear elastic, i.e., only the glassy effective behavior will be considered for this first set of numerical comparisons [164]. The justification of this comes from recalling the fact that the effective behavior is computed in the frequency domain by using the correspondence principle [5, 44]. In practice, this is achieved by using the analogy of the steady-state oscillations simulations, as we have already mentioned.

6.2.1 Phases properties for comparative analysis

The properties are taken from [4] considering a composite filament with 20% of short glass fiber inclusions with a representative choice of length and orientation distributions, that is : the Advani-Tucker axisymmetric coefficient $m_{\mathrm{AT}} = 60$ representing the tendency of the fibers to follow the direction of the filament length, and the Weibull coefficients $c_w = 2.5$ and $w_0 = 30$ with a population of fibers whose length is concentrated around its mean value. Therefore, the matrix-material is transverse isotropic with the symmetry axis being normal to the filament's cross-section and is represented using the Hill basis notation [46, 4] (see A.5). The thermomechanical

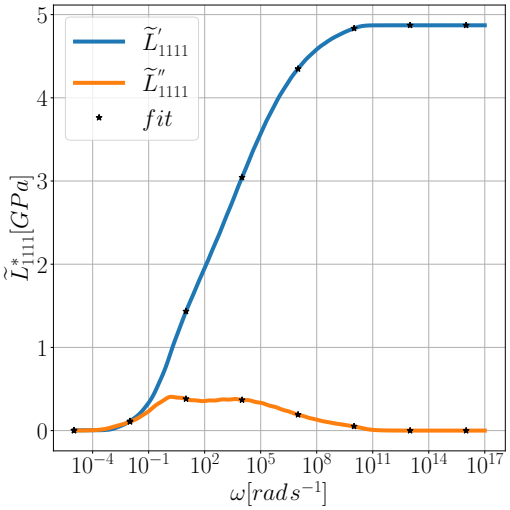

(a) $\widetilde{L}^*_{1111}$

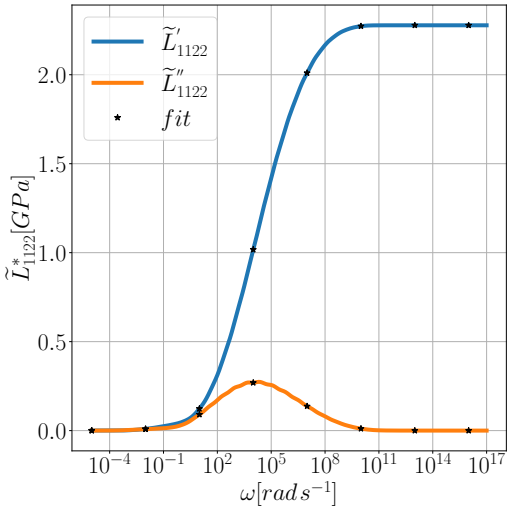

(b) $\widetilde{L}^*_{1122}$

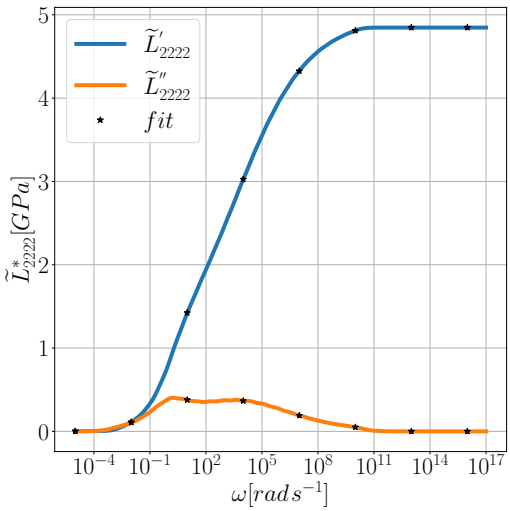

(c) $\widetilde{L}^*_{2222}$

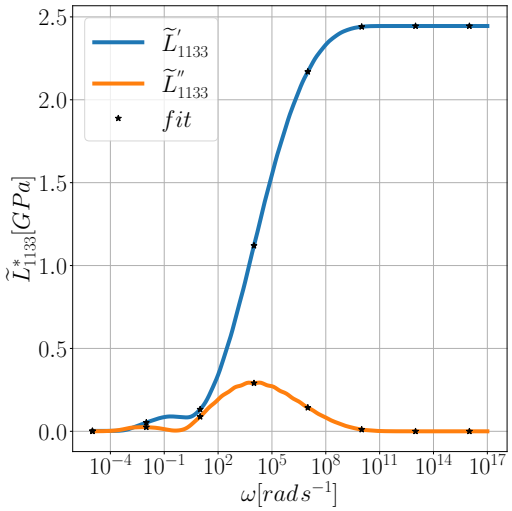

(d) $\widetilde{L}^*_{1133}$

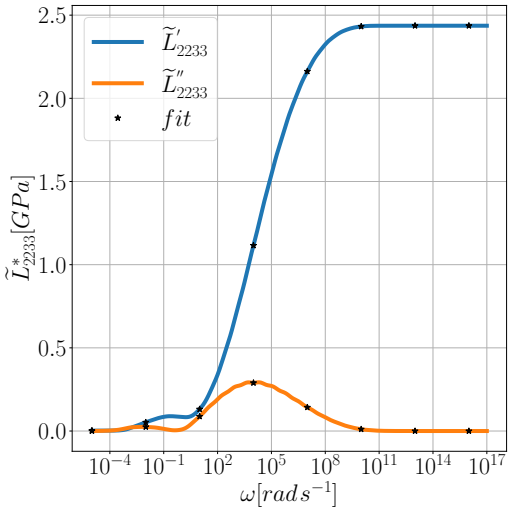

(e) $\widetilde{L}^*_{2233}$

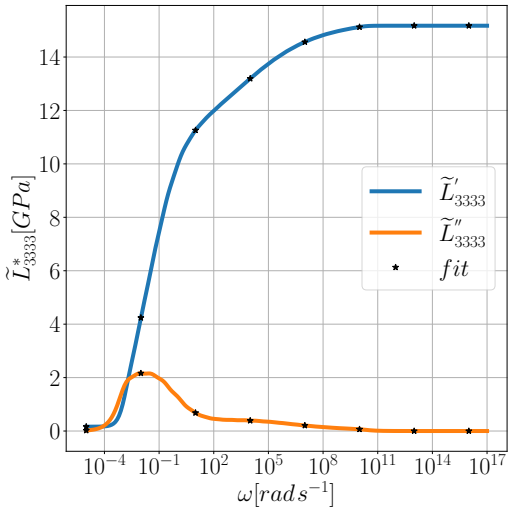

(f) $\widetilde{L}^*_{3333}$

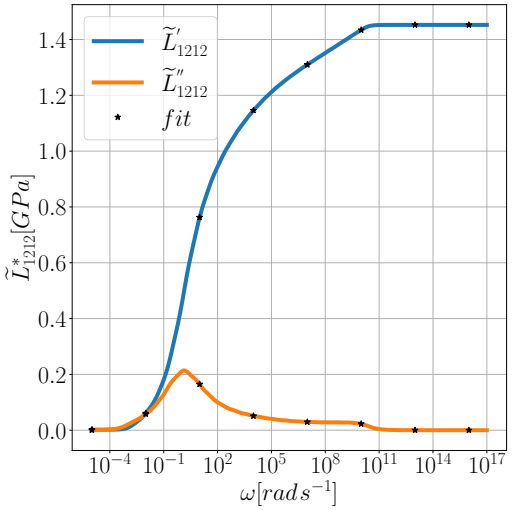

(g) $\widetilde{L}^*_{1212}$

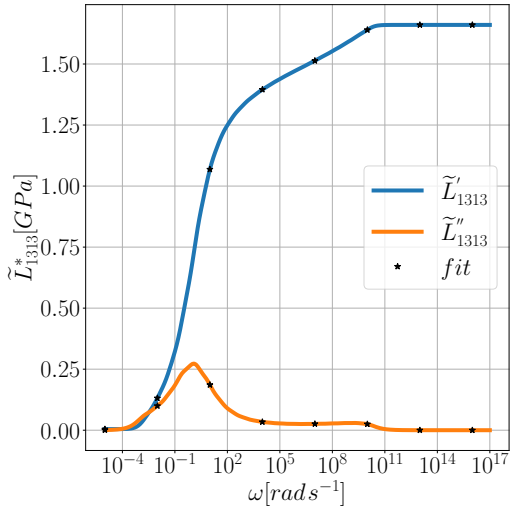

(h) $\widetilde{L}^*_{1313}$

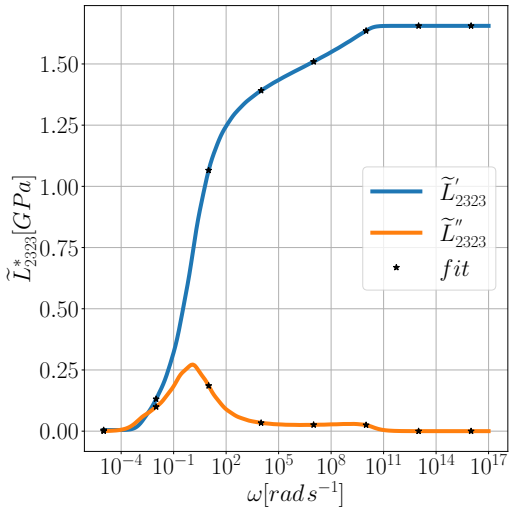

(i) $\widetilde{L}^*_{2323}$

Figure 6.4: Output example of the effective orthotropic thermo-viscoelastic behavior of the mesoscale, $v_f = 0.05$.

properties are presented below.

$$\mathbb{L}^{(\mathrm{m})} = 2\kappa_{\mathrm{t}}^{(\mathrm{m})}\mathbb{H}^{(1)} + \ell^{(\mathrm{m})}(\mathbb{H}^{(2)} + \mathbb{H}^{(3)}) + n^{(\mathrm{m})}\mathbb{H}^{(4)} + 2\mu_{\mathrm{t}}^{(\mathrm{m})}\mathbb{H}^{(5)} + 2\mu_{\mathrm{l}}^{(\mathrm{m})}\mathbb{H}^{(6)} = \sum_{b=1}^{6} l^{(\mathrm{m},b)}\mathbb{H}^{(b)}.$$

$$\boldsymbol{\alpha}^{(\mathrm{m})} = \alpha_{\mathrm{t}}^{(\mathrm{m})}\boldsymbol{\Theta} + \alpha_{\mathrm{l}}^{(\mathrm{m})}\boldsymbol{\mathcal{N}}, \tag{6.16}$$

with κ_{t}, μ_{t} and α_{t} being the in-plane modulus of compressibility, shear and thermal expansion respectively, μ_{l} and α_{l} are the longitudinal shear and thermal expansion modulus respectively,

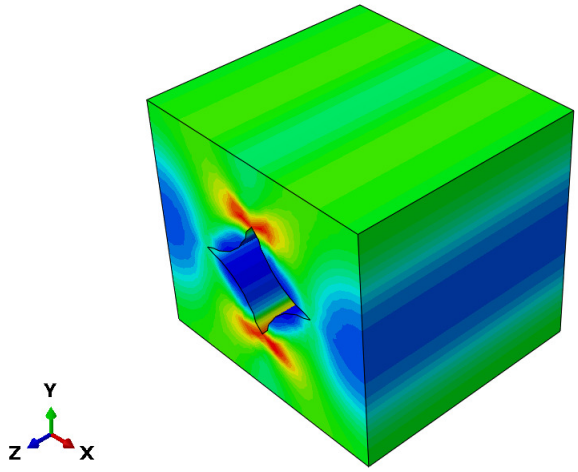

(a) elementary case traction in direction $\boldsymbol{e}_1$

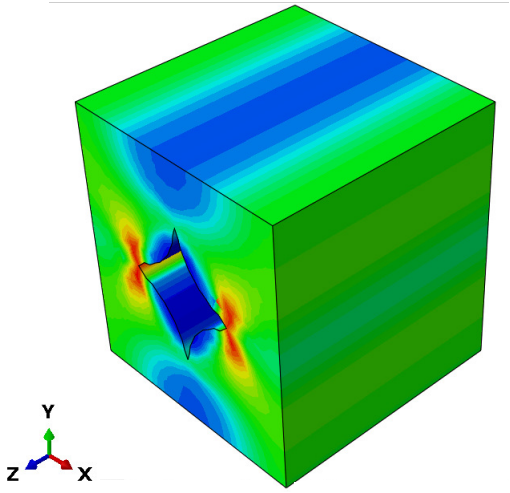

(b) elementary case traction in direction $\boldsymbol{e}_2$

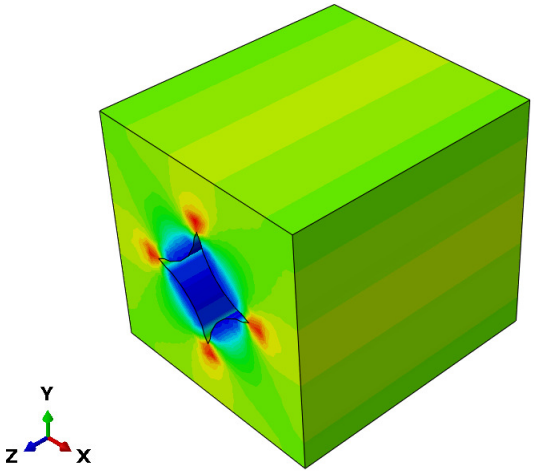

(c) elementary case traction in direction $\boldsymbol{e}_3$

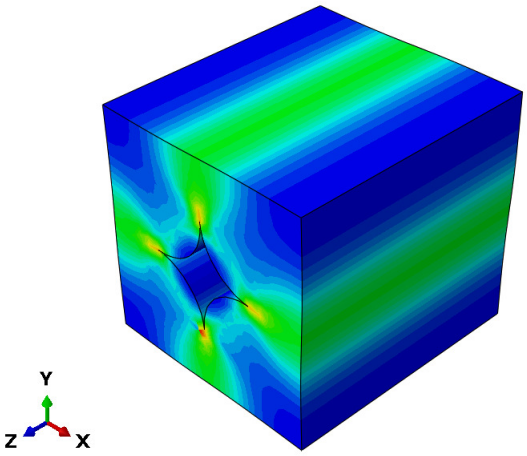

(d) elementary case shear on plane $\boldsymbol{e}_1 \times \boldsymbol{e}_2$

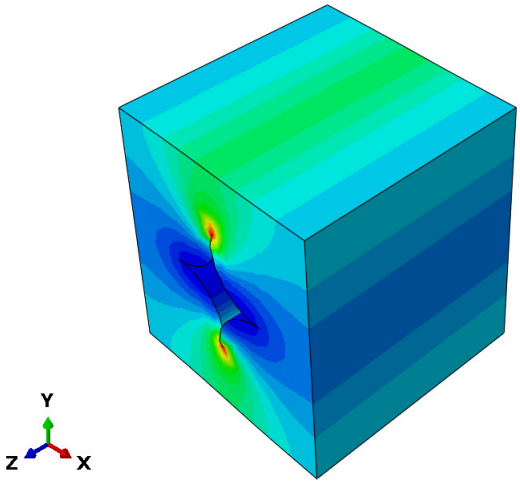

(e) elementary case shear on plane $\boldsymbol{e}_1 \times \boldsymbol{e}_3$

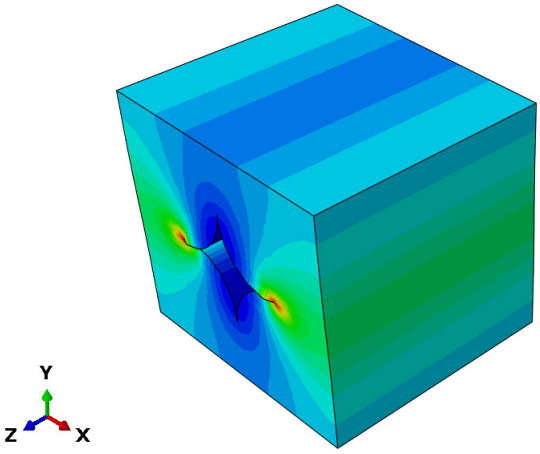

(f) elementary case shear on plane $\boldsymbol{e}_2 \times \boldsymbol{e}_3$

Figure 6.5: Equivalent stress distribution of numerical homogenization simulations for the set of elementary loads, $v_f = 0.05$.

finally, n is related to the axial response and ℓ relating the on-plane and longitudinal responses [4, 46]. Numerical values are presented in Table. 6.1. The fourth order tensor basis $\mathbb{H}^{(b)}$, stands for the Hill's transverse isotropic basis, $\boldsymbol{\mathcal{N}}$ is the second order orientation tensor obtained as the tensor product of the symmetry axis (for instance $\boldsymbol{e}_3$) by itself, and $\boldsymbol{\Theta} = \boldsymbol{I} - \boldsymbol{\mathcal{N}}$ is the second order tensor characterizing the symmetry plane, for instance $\boldsymbol{e}_1 \times \boldsymbol{e}_2$.

Parameter	κ_t [GPa]	ℓ [GPa]	n [GPa]	μ_t [GPa]	μ_l [GPa]	α_t [1/K]	α_l [1/K]
Values	5.42	3.80	13.07	1.53	1.66	0.0000617	0.0000329

Table 6.1: Thermo-mechanical properties of the matrix-material for the glassy cases.

Convergence study

As pointed out before because the effective thermo-viscoelastic behavior can be interpreted as a symbolic thermoelastic behavior by means of the correspondance principle, the present study is limited to classic thermoelastic simulations. Computationally speaking, some differences should be considered when one wants to discuss the pertinence of such studies on the actual behavior. First, the computation of the effective thermoelastic behavior can be observed as one step of a series of steps in the frequency domain with moduli holding a null imaginary part; therefore, the greatest differences are i) the computational time: if one fixes the discretization of the frequency domain, and suppose numerical stability regarding the material properties (difficult to ensure due to high contrast in the frequency sweep), an initial approximation of the ratio between the thermoelastic and thermo-viscoelastic simulations is N_f, the scalar representing the number of steps of the discrete frequency interval whose limits are a function of the operating conditions of the material. ii) inverting complex matrices : considering the symbolic problem, the coefficients associated to the fourth order stiffness tensor of each frequency step are no longer real numbers but complex, as can be inferred, to invert complex valued systems is indeed more difficult than to invert real valued systems. The numerical cost of the actual behavior is then greater. This study considers the latter comments to choose the best combination of discretization parameters, giving an accurate approximation while conserving a reasonable numerical cost as a starting point to study the computation of the frequency series for the effective poro-thermo-viscoelastic behavior that will be presented in Section 6.3.

This section aims to present the numerical setting established for the computation of the

Effective behavior by solving the problem of Eq. (6.15) in the representative elementary volume (REV). The simulations were performed using the HPC services of the university of Luxembourg. Parallel computations were carried out by using intel MPI v2020b libraries in conjunction with Abaqus® 2021.HF11. As can be inferred, the convergence studies are limited by the access to computational resources (i.e., maximum number of nodes / licences) and the upper limit of execution time; an example of such compromise in the cost is presented in Fig. 6.8b, where the memory requirement is plotted as a function of the number of degrees of freedom N_{dof}. The observed values were fitted to a polynomial function of third order with positive coefficients, ensuring the strictly increasing behavior of the memory requirement, allowing an estimation of a possible minimum of h_{max} for the convergence study. Quadratic tetrahedral elements were used when defining the function space. The controlled meshing parameter is h_{max}, representing the maximum distance between each couple of principal degrees of freedom. Convergence analysis for the effective behavior simulations is performed only in the extreme values of the volume fraction range chosen for this study (i.e. $\{0.05, 0.15\}$, see the figure below).

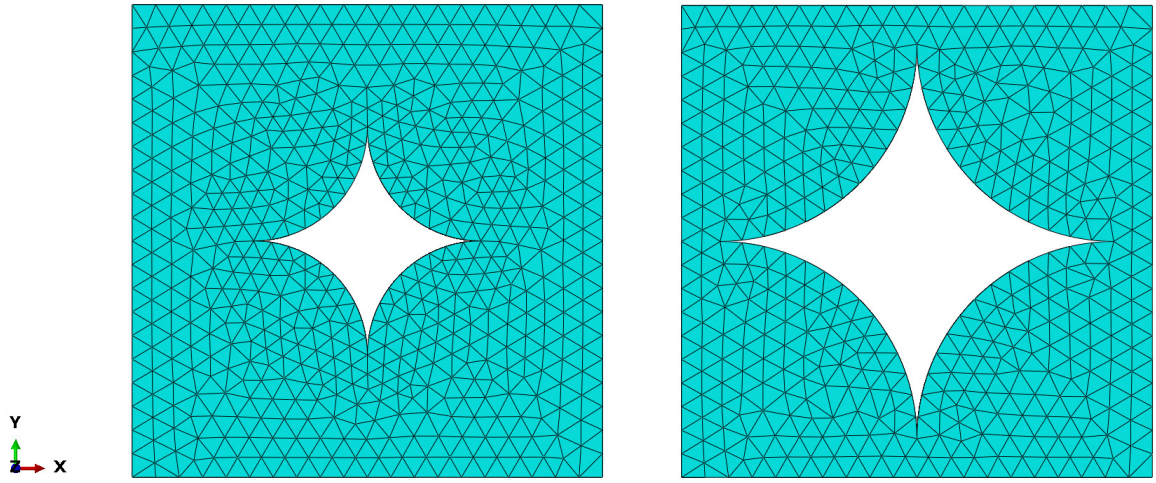

Figure 6.6: Example of the meshed REV's for the convergence study. From left to right, volume fractions of 0.05 and 0.15.

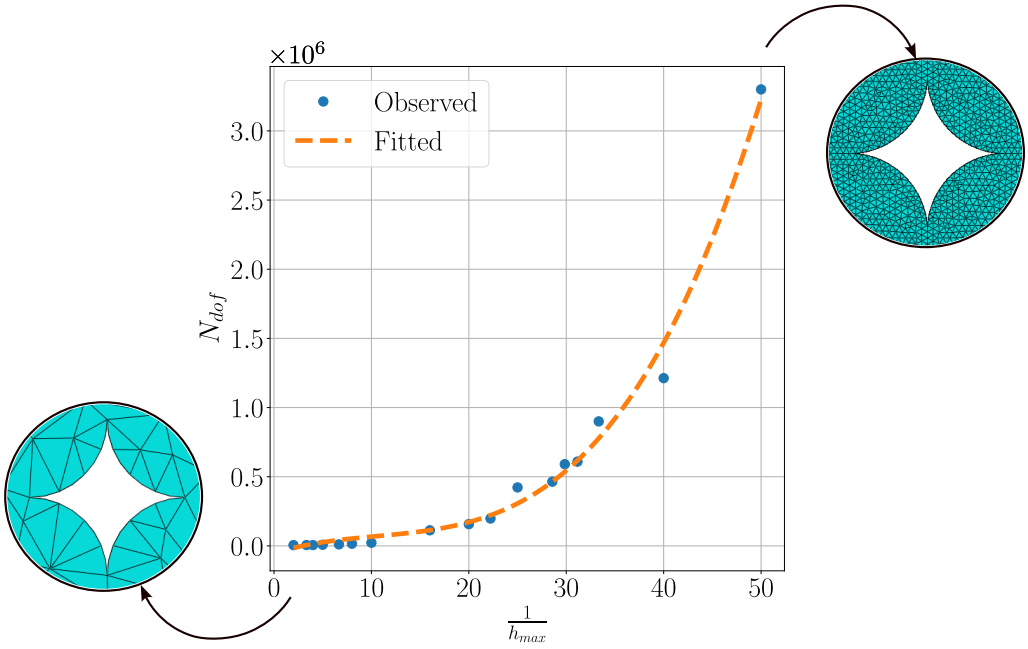

Figure 6.7: Relation between the meshing parameter h_{max} and the total number of degrees of freedom N_{dof}.

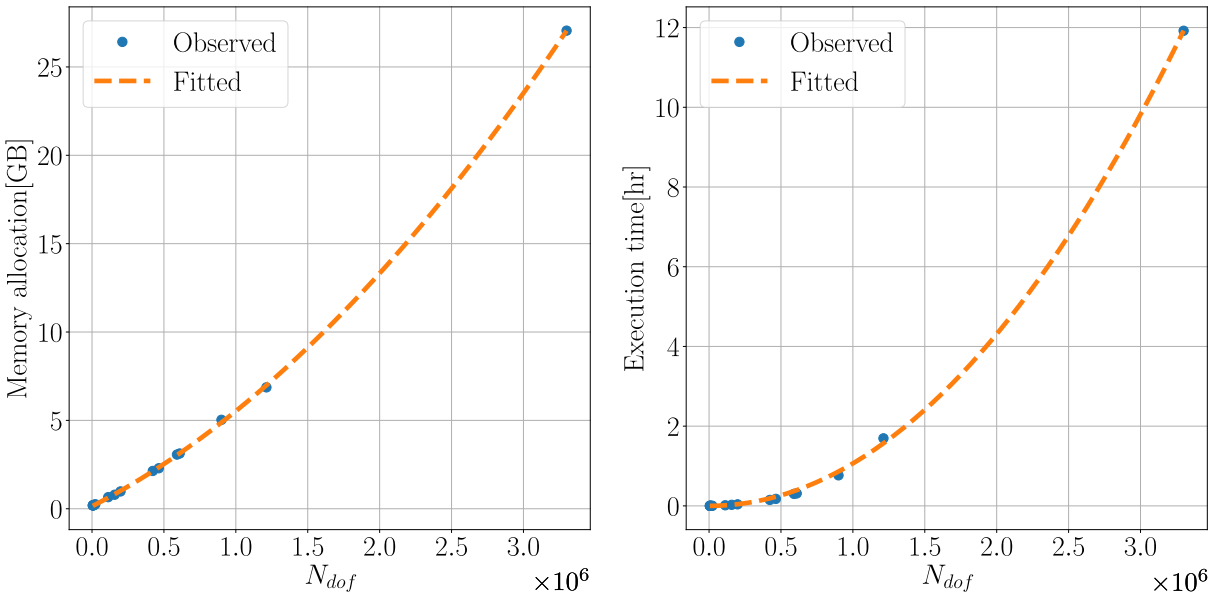

(a) Simulation cost in terms of memory allocation.

(b) Simulation cost in terms of execution time.

Figure 6.8: REV with $v_f = 0.05$: Number of degrees of freedom N_{dof} vs. Computational efficiency parameters.

Considering the measure of the convergence rates, the relative error is measured taking as reference the finest mesh simulation, concerning the comparisons, two norms are considered: the L_2-norm and the L_∞-norm with explicit forms for the error e of a one dimensional vector $\boldsymbol{v} = \{v^{(1)}, ..., v^{(i)}, ..., v^{(dim(\boldsymbol{v}))}\}$:

$$||e(\boldsymbol{v})||_{L_2} = \sqrt{\frac{\sum_{i=1}^{i=\dim(\boldsymbol{v})} \left(v_{\text{ref}}^{(i)} - v^{(i)}\right)^2}{\sum_{i=1}^{i=\dim(\boldsymbol{v})} \left(v_{\text{ref}}^{(i)}\right)^2}}, \qquad ||e(\boldsymbol{v})||_{L_\infty} = \max_{i=1,dim(\boldsymbol{v})} \frac{\left|v_{\text{ref}}^{(i)} - v^{(i)}\right|}{\left|v_{\text{ref}}^{(i)}\right|}. \tag{6.17}$$

The latter are presented in Fig. 6.9. One can note that the L_2-norm is always lower than L_∞-norm for a given number of degrees of freedom N_{dof}, this can be explained from the different order of magnitudes regarding the orthotropic coefficients. Therefore, the maximum relative error norm (L_∞-norm) should be considered as the main referent to choose the appropriate meshing parameter. However, as pointed out before, the scope of the convergence study is limited by the computational resources available.

Finally, in Fig. 6.10 one can observe the evolution of the independent coefficients of the orthotropic fourth order elasticity tensor by means of the normalized graph. To compute the vertical axis values, each effective coefficient is divided by the correspondent value in the matrix, this corresponds to the contrast of each effective orthotropic coefficient of the composite with respect to the corresponding values for its matrix, the mechanical contrast vector :

$$\boldsymbol{\gamma} = \frac{\widetilde{L}_{ijkl}}{L_{ijkl}^{(\text{m})}} = \left\{ \frac{\widetilde{L}_{1111}}{L_{1111}^{(\text{m})}}, \frac{\widetilde{L}_{1122}}{L_{1122}^{(\text{m})}}, \frac{\widetilde{L}_{2222}}{L_{2222}^{(\text{m})}}, \frac{\widetilde{L}_{1133}}{L_{1133}^{(\text{m})}}, \frac{\widetilde{L}_{2233}}{L_{2233}^{(\text{m})}}, \frac{\widetilde{L}_{3333}}{L_{3333}^{(\text{m})}}, \frac{\widetilde{L}_{1212}}{L_{1212}^{(\text{m})}}, \frac{\widetilde{L}_{1313}}{L_{1313}^{(\text{m})}}, \frac{\widetilde{L}_{2323}}{L_{2323}^{(\text{m})}} \right\}.$$

and then the vector $\boldsymbol{\gamma}$ is normalized to get closer the different curves of the evolution of its elements in function of the N_{dof}, this allows to observe more clearly the rate of convergence of each of these values :

$$\hat{\boldsymbol{\gamma}} = \frac{\boldsymbol{\gamma}}{(\boldsymbol{\gamma} \cdot \boldsymbol{\gamma})^{1/2}},$$

note that in the figure in question, we use the index of the independent coefficients to refer to the corresponding elements in $\hat{\boldsymbol{\gamma}}$ for the legends.

From this figure, one can note the similar evolution of the coefficients, in special the almost superposition of the evolution of the coefficients that takes the same values in transverse-isotropic symmetry. In fact, the implications of the symmetric curved diamond impose the effective behavior of the mesoscale to remain transverse isotropic, the differences observed in the outputs (i.e., 1111≠2222, 1133≠2233 and 1313≠2323) are originated due to the asymmetric distribution of the elements in the representative elementary volume, since the only constraints applied to the meshing generation was to ensure periodic boundaries.

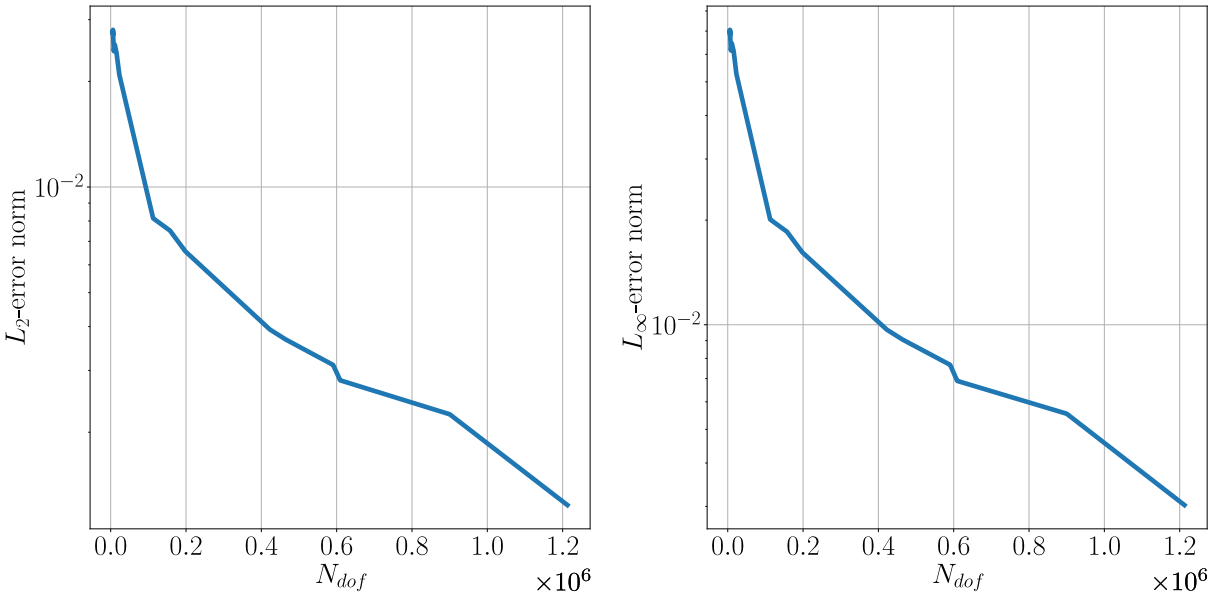

(a) L_2 norm of error

(b) L_∞ norm of error

Figure 6.9: REV with $v_f = 0.05$: Relative error vs. the number of degrees of freedom N_{dof}.

6.2.2 Influence of the porosity volume fraction

Effective properties have been computed for the above specified discrete interval of characteristic volume fractions at the observed scale. Numerical results are presented in the Table. 6.2. The evolution of the different elastic independent coefficients as a function of the volume fraction is shown in Fig. 6.11, where the legends stand for the indexes of the observed elements of the stiffness tensor. In this figure, the curves “1111” and “2222” appears to be almost superposed, suggesting a conservation of these two coefficients, characterizing the on-plane response and a consequence of the symmetry exhibit by the voids’ shape. In the same fashion, “1313” and “2323” are almost superposed and then suggesting this conservation but in the outer plane shear behavior, finally, the same situation can be observed when comparing “1133” and “2233” related

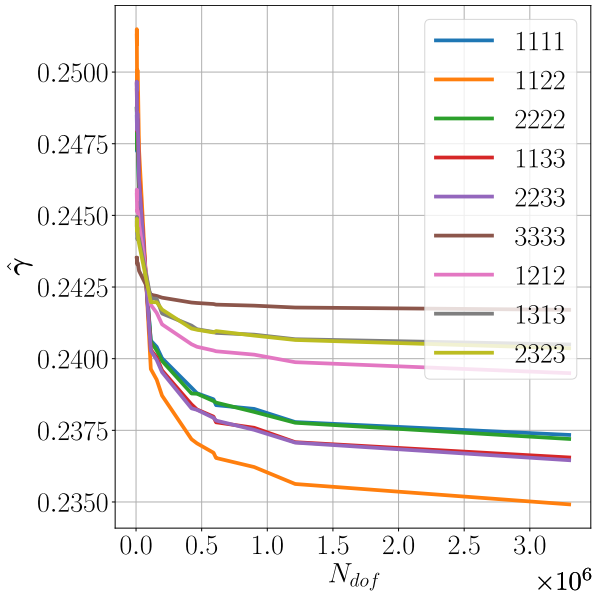

Figure 6.10: Normalized evolution of the contrast in orthotropic independent coefficients $\hat{\gamma}$ vs. number of degrees of freedom N_{dof}.

to the second Lamé coefficient λ. The foregoing affirmations are indeed confirmed when observing the numerical values in the aforementioned table. Regarding the loss of stiffness, "1122", "1133", "2233" and "1212" are found below half of it correspondent matrix magnitude. As mentioned before, in general, one can conclude that, due to the symmetry of the porosity, the effective behavior should be transverse isotropic, but it appears as an orthotropic behavior which is a subtle deviation of a perfect transverse isotropic behavior in consequence of the mesh used to solve the periodic problem numerically.

v_f	$\widetilde{L}_{1111}$	$\widetilde{L}_{1122}$	$\widetilde{L}_{2222}$	$\widetilde{L}_{1133}$	$\widetilde{L}_{2233}$	$\widetilde{L}_{3333}$	$\widetilde{L}_{1212}$	$\widetilde{L}_{1313}$	$\widetilde{L}_{2323}$
0.000	6.96	3.89	6.95	3.80	3.80	13.07	1.53	1.66	1.66
0.050	4.26	2.04	4.25	2.20	2.20	11.42	1.25	1.36	1.36
0.075	3.44	1.49	3.44	1.73	1.73	10.84	1.12	1.23	1.23
0.100	2.81	1.09	2.81	1.37	1.37	10.32	0.98	1.11	1.11
0.125	2.30	0.78	2.30	1.08	1.08	9.86	0.86	0.98	0.98
0.150	1.87	0.55	1.86	0.85	0.84	9.43	0.73	0.86	0.86

Table 6.2: Effective elastic (i.e., glassy) constants in GPa for different volume fractions of porosity.

The validation of the computed estimations of the effective behavior will be carried through comparisons of the macroscopic responses regarding different geometries affecting the periodicity of the REV. Three different simulation scenario will be presented: i) the distributed bending

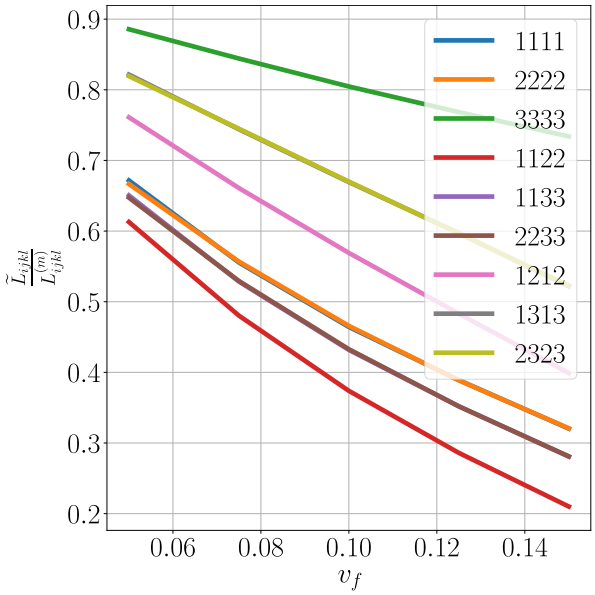

Figure 6.11: Effective orthotropic constants normalized by its correspondent matrix value ($\frac{\widetilde{L}_{ijkl}}{L^{(m)}_{ijkl}}$) vs. volume fraction ($v_f$).

case (Fig. 6.12a) in which the body will exhibits a deflection u_2 in the negative second principal direction (i.e. $-\boldsymbol{e}_2$). ii) The distributed horizontal traction case (Fig. 6.12b) with load direction $\boldsymbol{e}_1$ and comparison field u_1. and iii) The pure thermoelastic case (Fig. 6.12c) with comparison variable still u_1 and magnitude of the temperature variation $\Delta T = 200°C$. One could claim that the pertinent comparison variable should be the displacement norm as this case causes a volume variation of the body, the issue to consider such variable is that in some simulations geometrical simplifications are made then some elements of the displacement vector could be missing. It must be noted that in all simulations the same kind of Dirichlet boundary conditions are applied. Finally, regarding the comparisons when the error is referred, it corresponds to the $\boldsymbol{L^2}$-relative error norm expressed in percentage.

6.2.3 2D periodic mesostructures

Here, some validation tests are performed to ensure the reliability compared to full field simulations with massive structures compared to the REV. For this study, only the lower porosity volume fraction will be considered (i.e. $v_f = 0.05$). The periodicity of the mesostructures is the one proposed from the model of the REV (i.e. periodicity conserved in $\boldsymbol{e}_1$ and $\boldsymbol{e}_2$). Therefore, these tests are equivalent to consider a unidirectional printing trajectory program in each layer which is constant in the stacking direction $\boldsymbol{e}_2$.

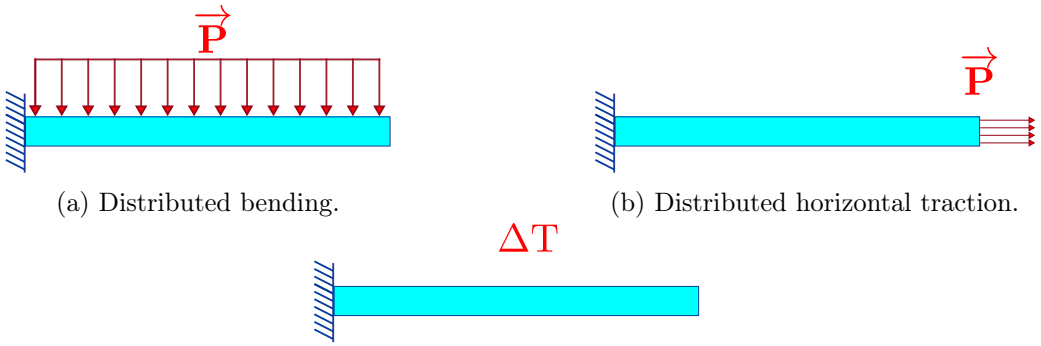

(a) Distributed bending.

(b) Distributed horizontal traction.

(c) Thermoelastic case.

Figure 6.12: Load cases for the benchmarking examples

Cube

For these simulations, a 3D cube with sides $10 \times 10 \times 10$ mm is considered. The comparisons are made by considering the displacement response obtained in a linear section that is collinear to the symmetry axis of the symmetry plane of the mesostructure. The mechanical cases consider the same uniaxial pressure $\|\vec{P}\| = 1$ MPa. Three different simulation approaches are implemented. First, a full homogeneous 3D cube with mechanical properties being the effective properties previously computed ($v_f = 0.05$) and reported in Table. 6.2. The second is a heterogeneous domain simulated under the framework of plane strains, with the plane being coplanar to the symmetry plane of the voids' geometry (i.e. $\boldsymbol{e}_1 \times \boldsymbol{e}_2$). The last one is a plane strain simulation of the symmetry plane but instead of the heterogeneous domain, a homogenized uniform one is considered.

Distributed bending:

The deflection u_2 is used for comparisons. Regarding the reported results in Fig. 6.13a, one can note the closeness of the computed responses along the middle line, compared to the reference solution (in green on Fig. 6.13a) the error is considerably small, with reported values: 0.6% with respect to the 3D homogeneous and 0.9% compared to 2D homogeneous simulation. This shows, as expected, a good agreement between the full heterogeneous simulations and the homogenized responses that appears to be almost superposed.

Horizontal traction:

The observed field for comparisons is the horizontal displacement u_1 along the middle line of

the top surface of the cube. Results are reported in Fig. 6.13b. Similarly to the latter case, the uniaxial traction simulations show a good agreement between the computed responses with an error of 0.99% with respect to the 3D homogeneous and 0.38% compared to 2D homogeneous simulation, what is indeed close to the error reported from the bending simulations. Therefore, the error is consistent when regarding different effective moduli involved in each elementary loading. The computer errors are very small as expected, and the horizontal displacement appears as in the above case to be almost superposed when comparing the three cases.

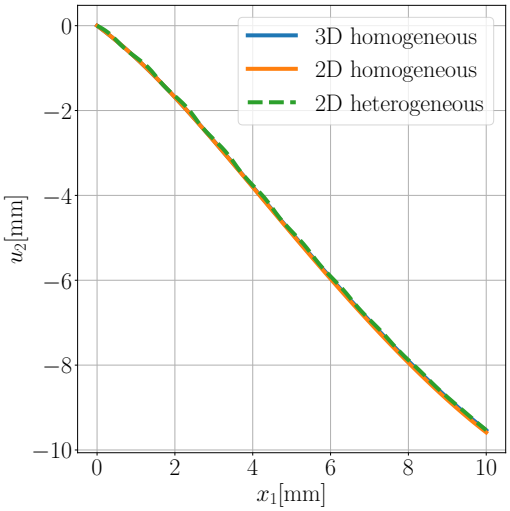

(a) Vertical displacement u_2, distributed bending case

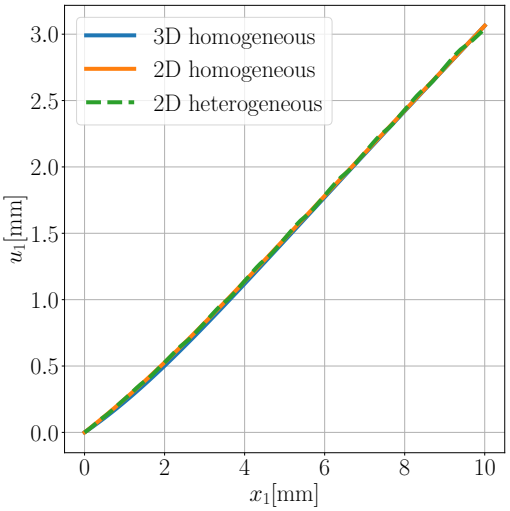

(b) Horizontal displacement u_1, distributed traction case

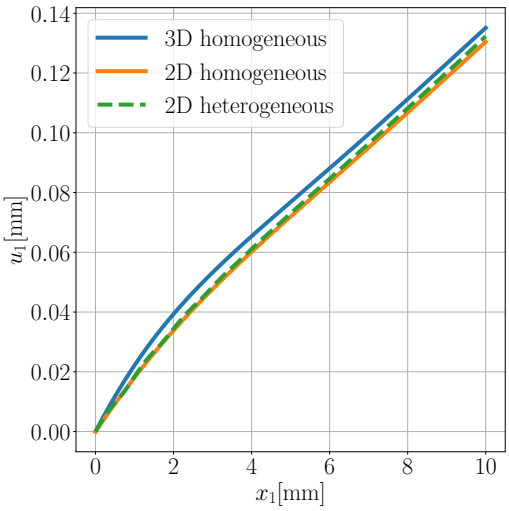

(c) Horizontal displacement u_1, distributed thermoelastic case

Figure 6.13: Observed responses of the cube's middle line: Displacement vs. horizontal coordinate x_1

Thermoelastic response:

This is the case of an evaluation of the response in function to a variation of temperature. The thermal expansion moduli for the matrix and composite are presented in the Table. 6.1, recalling from Section 6.1.2 that when porosities are considered as inclusions, the effective thermal expansion behavior remains the same as the matrix-material of the porous mesoscale. The considered temperature variation is set to $T = 200°\text{C}$.Results are reported in Fig. 6.13c. From this figure, one can note the good agreement between the computed responses, with maximum L2 relative error norm of 4.61% reported for the 3D case, which confirms the reliability of the homogenization approach on the computation of the volume variations due to a variation in temperature. Indeed, one can note from the graph that the greater gaps are presented between the two simulation scenarios (3D vs. 2D) rather than between homogenized vs. heterogeneous, in which, such comparison between the two 2D models give a relative error of 1.4%. In conclusion, this result allows then to sustain and give a favorable conclusion about the accuracy on the estimation of the macroscopic response.

6.2.4 Non-periodic mesostructures

This study considers the case in which a loss of periodicity is observed. This corresponds to the case of printing a thin plate or an arrangement of "bi-layers" in which the printing trajectories are constant every two layers. As can be inferred, the periodicity in the vertical direction ($\boldsymbol{e}_2$) is no longer hold. However, the effective properties considered for comparisons against full heterogeneous bodies are the same of the precedent 2D periodic examples, the only change is made on the magnitude of the uniform distributed pressure, here $\|\overrightarrow{\mathrm{P}}\| = 1$ Pa. Therefore, the main goal is to validate the reliability of those estimations in the present case.

Thin plate

This is the case of a printed thin plate with dimensions $100 \times 100 \times 2$ mm as it is shown in Fig. 6.15, that can be interpreted as a printed part obtained by superposition of four layers with the same printing trajectories. Due to the separation of scales between the magnitudes in $\boldsymbol{e}_1$ and $\boldsymbol{e}_2$, the periodicity in $\boldsymbol{e}_2$ is lost. The simulation scenarios considered in this section are the same of the precedent cases; the distributed bending and traction, and the thermoelastic case.

Distributed bending:

The computed vertical displacements u_2 for the different simulation approaches are presented in Fig. 6.14a. From this figure, one can note the marked gap between the reference (heterogeneous) and homogenized displacement fields. The homogeneous simulations seem to almost overlap for both 2D and 3D simulations. Concerning the heterogeneous models, the gap between them is smaller, suggesting a good validation of the 2D simplifications. The error of the 3D simulation is 3.31%, The error of the 2D shell simulation is 2.73% and for the plane strain simulation, an error of 2.71%.

Distributed traction:

The computed displacements u_1 are reported in Fig. 6.14b. Again, The homogeneous simulations seem to almost overlap for both 2D and 3D simulations, as well as the heterogeneous fields. The computed results for the homogeneous simulation show a good agreement. The error of the 3D simulation is 1.84%, The error of the 2D shell simulation is 1.87% and for the plane strain simulation, an error of 2%. The errors in this case are still in an order of magnitude that makes the approach a good candidate for a simplification, considering the computational cost of the full heterogeneous examples in which the quotient between the times of simulation is on the order of 10^3.

Thermoelastic response:

The observed fields are presented in Fig. 6.14c. The compared responses are still in a good agreement with the greater error of 3.97% from the shell model, an error of $9.13 \cdot 10^{-2}$% for the 3D homogeneous simulation, and an error of $3.59 \cdot 10^{-3}$ % in the case of 2D homogeneous simulation. In contrast to the pure mechanical cases, the computed heterogeneous responses do not seem to overlap, showing an error of 4.09% for the 2D generalized plane strain heterogeneous simulation.

Laminates arrangements

This section considers different arrangement of oriented orthotropic layers, this is, a laminate with dimensions $100 \times 100 \times 4$ mm. First, let's admit that a "layer" in the present context implies the printing of two "sublayers" with the same uniaxial printing direction (which preserves

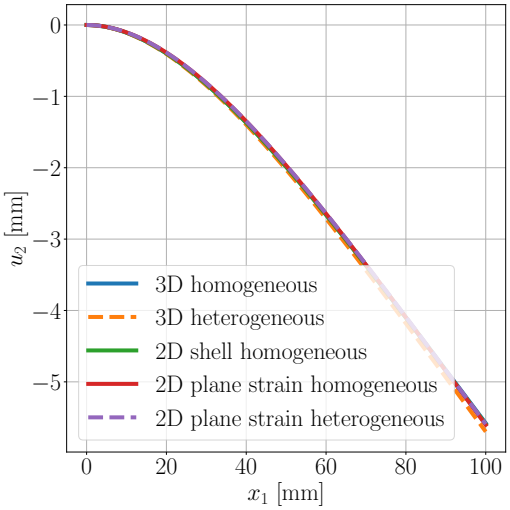

(a) Vertical displacement u_2, distributed bending

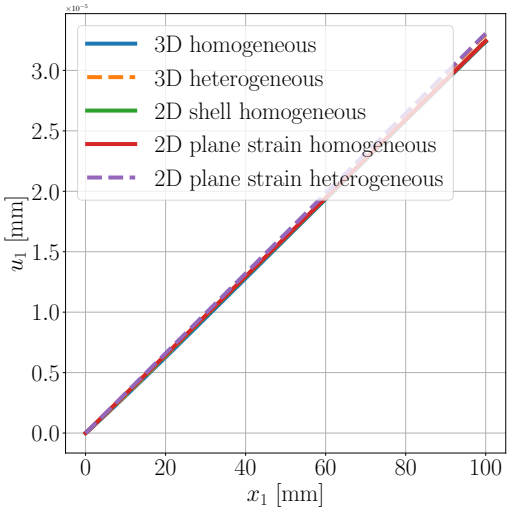

(b) Horizontal displacement u_1, distributed traction

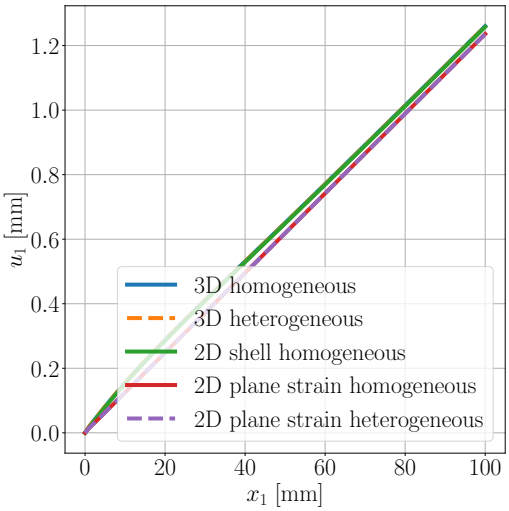

(c) Horizontal displacement u_1, thermal

Figure 6.14: Mechanical response of the unidirectional laminate's middle line: Displacement vs. horizontal coordinate x_1

the geometry of the REV). The combinations of tested layers are among, which in laminates theory is called symmetric and non-symmetric arrangements. Results and conclusions will be presented for each combination considered. In contrast with the precedent simulations, here only the thermoelastic load case will be considered as is the one giving the higher error magnitudes, allowing to observe the computed responses in the more critical scenario while the numerical cost is reduced. Indeed, the fact that now the laminate has doubled its thickness and considering the necessary fine meshes around the heterogeneity, the computation time of reference solutions becomes too important. Anyway, for the sake of comparisons and validations the thermoelastic case is enough to appropriate analyze the pertinence of the proposed estimation in such cases.

Results are presented in two forms: the concerned fields for comparisons are plotted for each arrangement considered in two different locations at the sides of the middle plane of the laminate located at the vertical coordinate $x_2 = 2$ mm. The "front side" locate at the coordinate $x_1 = 100$mm relatively placed in the opposite side of the clamped side. And the lateral side, one of the free sides and located at the coordinate $x_3 = 100$ mm. The results presented in this section correspond to two cases of volume fraction, the limits of the interval given in the Section. 6.1.1.

The results for the case of $v_f = 0.05$ are presented in the Fig. 6.19 for the symmetric arrangement $[0, 90, 90, 0]$ (see Fig. 6.16), and Figs 6.20 - 6.21 for the non-symmetric cases $[0, 90, 0, 90]$ (see Fig. 6.17) and $[0, 0, 90, 90]$ (see Fig. 6.18) respectively. Furthermore, in Table. 6.3 an accumulated of L2 relative errors in percentage form is presented.

When observing the plotted fields in conjunction with the errors table, one can note the good agreement in most of the computed fields. The non-symmetric arrangements exhibit an almost superposition of the displacement when regarding the lateral side ($x_3 = 100$) with a maximum error of 3.05% reported by the case $[0, 90, 0, 90]$. Similar behavior is observed in the displacement u_3 of the front side, where the maximum error of 1.32% for the $[0, 90, 0, 90]$ case. The displacement fields u_1 and u_2 exhibit notable differences when regarding the plots, anyway this observed differences are low considering the scaling of the vertical axis in the plots, this is confirmed when the errors are computed which its maximum is 0.83% reported by the laminate $[0, 90, 0, 90]$. Considering the comparisons between the Laminate simulation (2D) and the homogeneous 3D simulation, in most of the cases the computed responses are almost superposed, nevertheless, 2D simulations are always closer to the referent solutions suggesting an underestimation of some effective orthotropic coefficients.

Concerning the symmetric arrangement, as in the cases of the non-symmetric laminates most of the computed fields show a good agreement, the zero vertical displacement fields u_2 in both lateral and front sides in both, 3D and 2D simulations is a consequence of such arrangements that prevents the vertical deflection of the laminate during the thermal treatment. For the rest of the fields, the errors reported are similar to those of the non-symmetric cases, with a maximum error of 1.69% in the u_1 field located in the lateral side.

For the case of volume fraction $v_f = 0.15$, the upper bound of the interval, all cases exhibit a similar agreement in comparison to the lower bound (i.e., $v_f = 0.05$). In most of the cases,

Cases			Displacement error [%]					
Laminates		Location	u_1		u_2		u_3	
			2D	3D	2D	3D	2D	3D
Symmetric	[0,90,90,0]	x_1=100	0.20	0.22	-	-	1.30	1.33
		x_3=100	1.38	1.69	-	-	0.43	1.13
Non-Symmetric	[0,90,0,90]	x_1=100	0.22	0.08	0.23	3.05	1.32	1.30
		x_3=100	0.50	0.11	0.69	3.05	0.20	0.17
	[0,0,90,90]	x_1=100	0.17	0.06	0.20	1.22	1.20	1.20
		x_3=100	0.52	0.08	0.83	1.20	0.35	0.10

Table 6.3: L2-relative norm of error for observed fields in laminates arrangements with volume fraction $v_f = 0.05$.

the error reported in the upper bound is greater, suggesting a decrease of the reliability of the periodic approximation as the porosity characteristic size increases. Fig. 6.22 presents the computed fields for the symmetric arrangement, and Figs. 6.23 - 6.24 for the non-symmetric cases. Equivalently Table. 6.4 presents a compilation of the errors obtained from the comparison between the approximations and the reference solutions.

As pointed out before, when observing the vertical displacement fields $u_2(\boldsymbol{x})$ for the symmetric arrangements, the approximation shows the nullity of it, a consequence of the disposition of layers (Fig. 6.22a and Fig. 6.22d) a suitable combination in laminates manufacturing preventing the residual vertical deformation in the plate, the warping. The rest of the fields in all cases show a good agreement for both, the 2D and 3D cases. However, as can be inferred considering the later comment, the higher magnitudes of the L^2-relative norm of error are presented always in the vertical displacement u_2 with the highest values in the non-symmetrical arrangement $[0, 90, 0, 90]$ of the intercalated layers with a maximum error of 11.8% as can be corroborated in Table. 6.4. Concerning the relative position of 2D and 3D simulations in the plotted figures, the same situations are hold; in most of the cases, the 2D simulations are closer to the reference solutions and still suggesting an underestimation of some orthotropic coefficients.

One can note that the approximations obtained by means of the periodic homogenization framework causes a loss of accuracy as the volume fraction increases. Indeed, if the volume fraction tends to zero (i.e., approaching to a homogeneous solid) the solution will converge to the

exact solution. In contrast, as the volume fraction of voids increases the heterogeneous nature of the solid increases and then, the method is less reliable in predictions. However, regarding the interval of interest, the relative error computed from the output fields can be considered as a good approximation of the actual behavior for engineering applications. This conclusion will be faced against experiments in further sections.

Cases			Displacement error [%]					
Laminates		Location	u_1		u_2		u_3	
			2D	3D	2D	3D	2D	3D
Symmetric	[0,90,90,0]	x_1=100	1.38	1.25	-	-	1.53	1.49
		x_3=100	1.26	1.36	-	-	1.15	0.85
Non-Symmetric	[0,90,0,90]	x_1=100	0.98	1.22	8.06	11.80	1.91	1.87
		x_3=100	1.00	1.26	7.13	10.81	1.53	1.62
	[0,0,90,90]	x_1=100	0.43	0.55	1.79	3.25	1.37	1.38
		x_3=100	0.34	0.57	1.13	2.58	1.19	0.92

Table 6.4: L2-relative norm of error for observed fields in laminates arrangements with volume fraction $v_f = 0.15$.

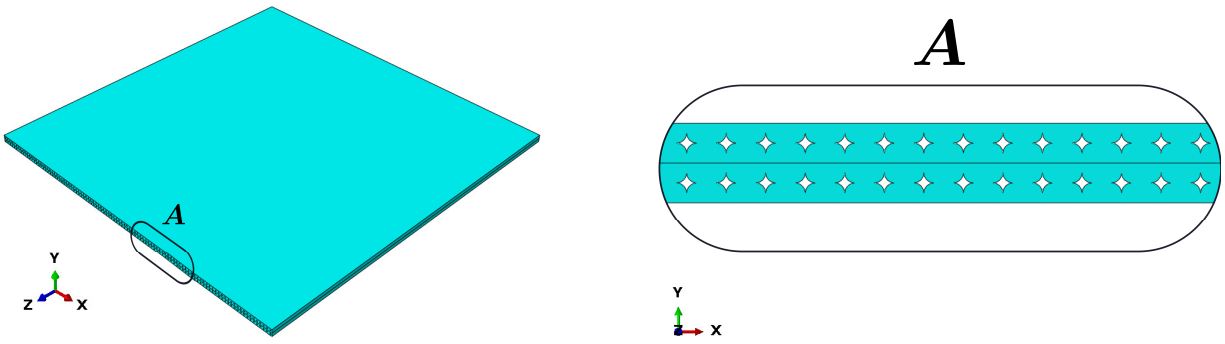

Figure 6.15: Thin plate Abaqus geometry $v_f = 0.05$.

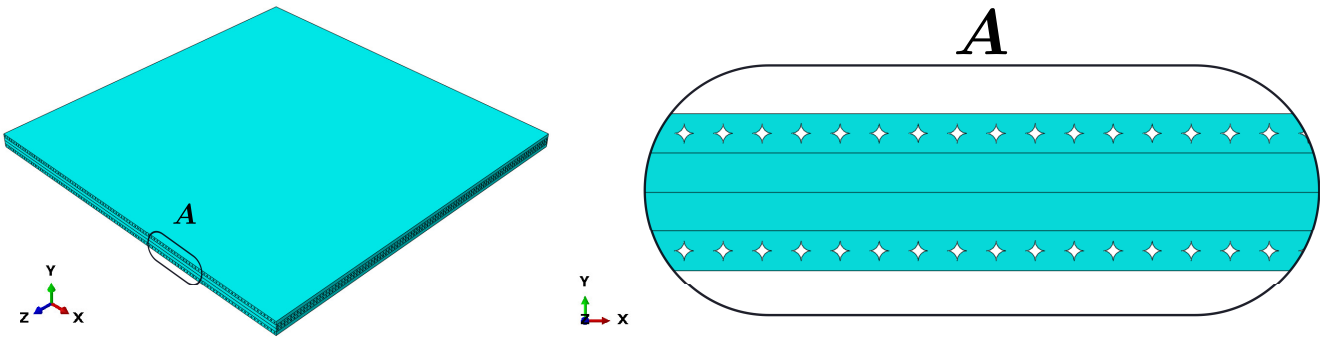

Figure 6.16: Plate $[0, 90, 90, 0]$ Abaqus geometry $v_f = 0.05$.

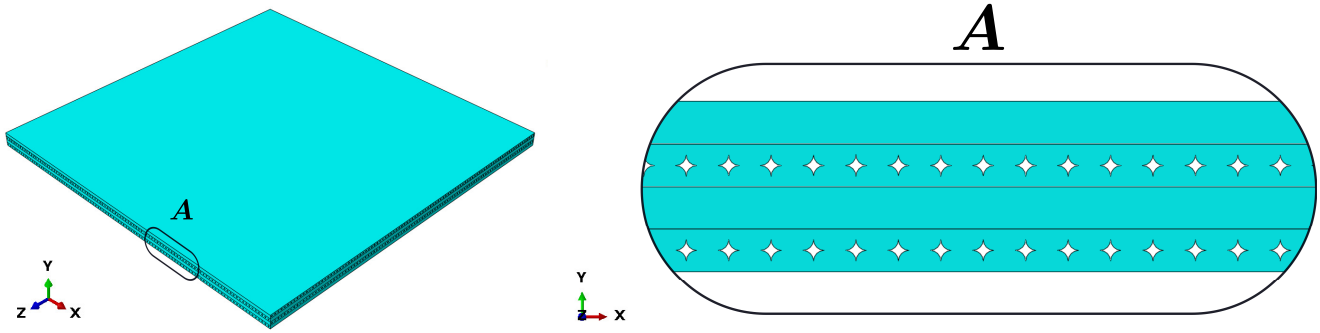

Figure 6.17: Plate $[0, 90, 0, 90]$ Abaqus geometry $v_f = 0.05$.

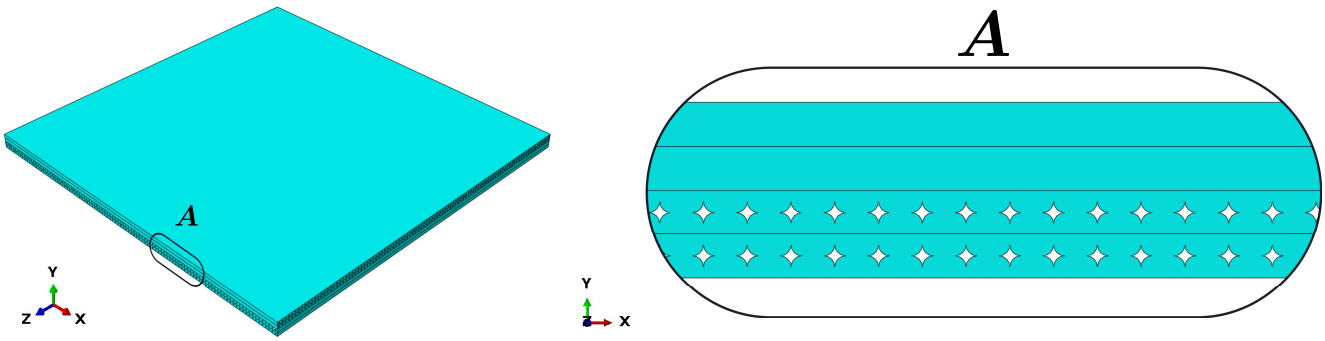

Figure 6.18: Plate $[0, 0, 90, 90]$ Abaqus geometry $v_f = 0.05$.

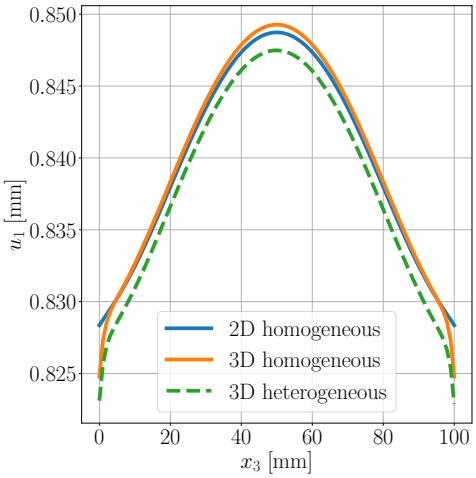

(a) u_1 vs. x_3, front face

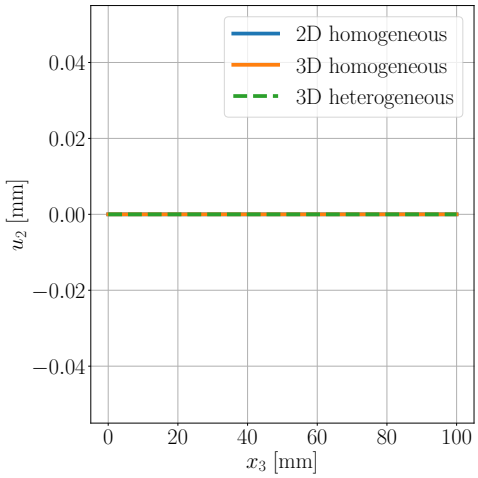

(b) u_2 vs. x_3, front face

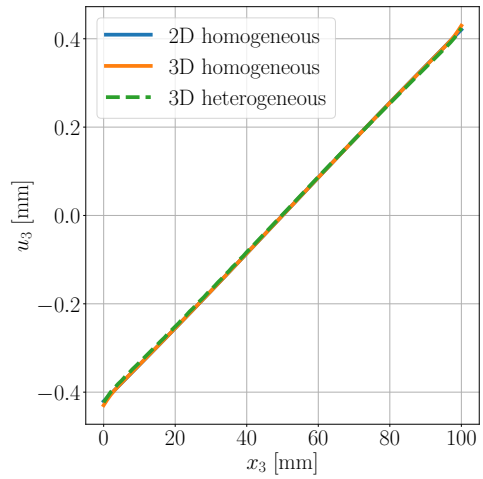

(c) u_3 vs. x_3, front face

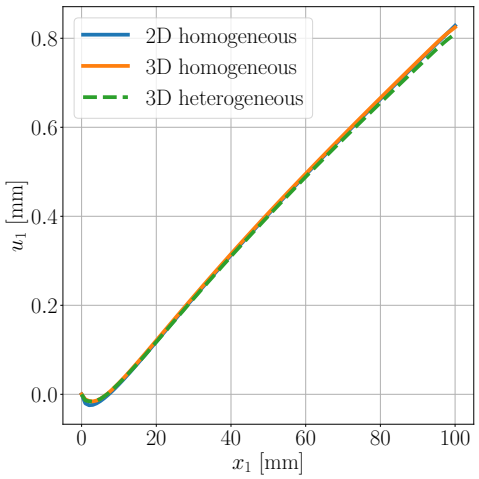

(d) u_1 vs. x_1, lateral face

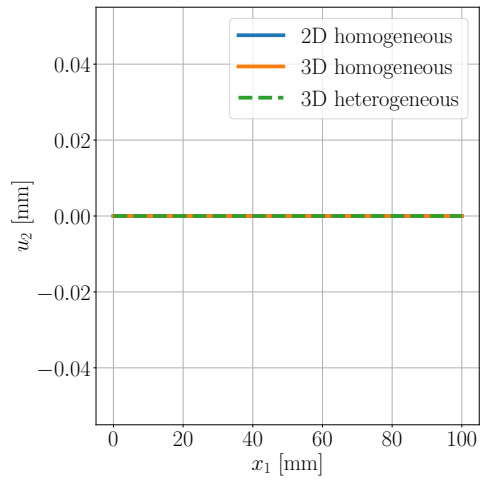

(e) u_2 vs. x_1, lateral face

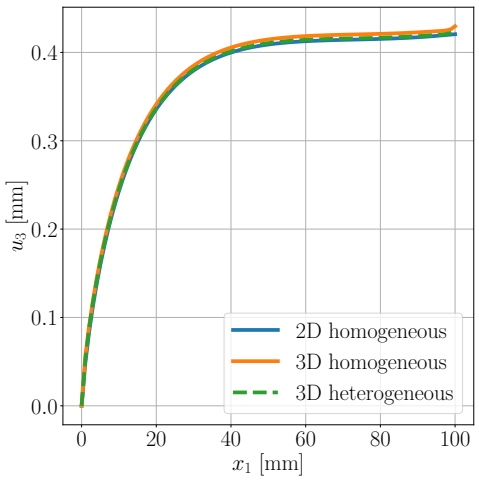

(f) u_3 vs. x_1, lateral face

Figure 6.19: displacement fields, symmetric laminate $[0, 90, 90, 0]$, $v_f = 0.05$.

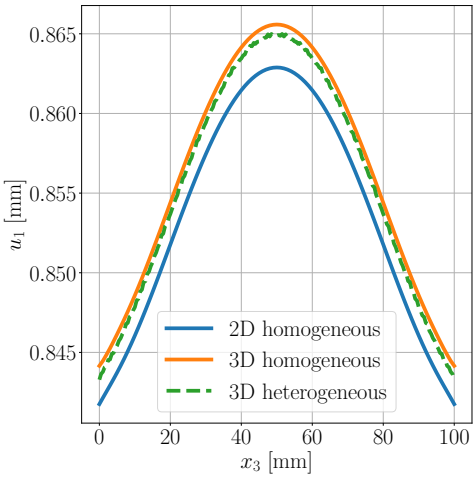

(a) u_1 vs. x_3, front face

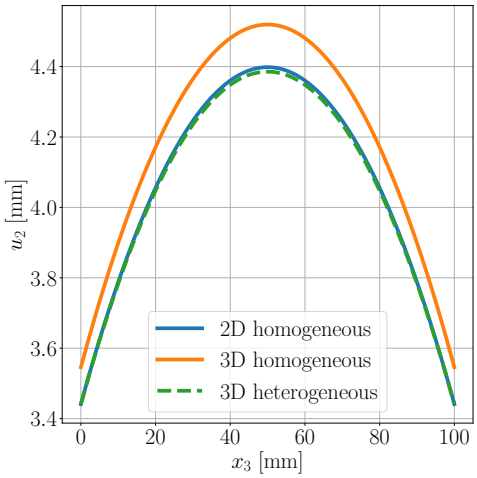

(b) u_2 vs. x_3, front face

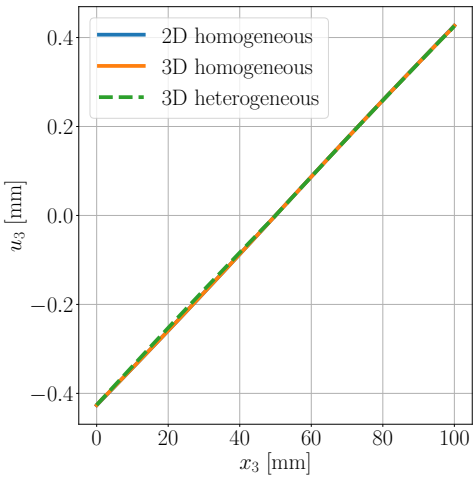

(c) u_3 vs. x_3, front face

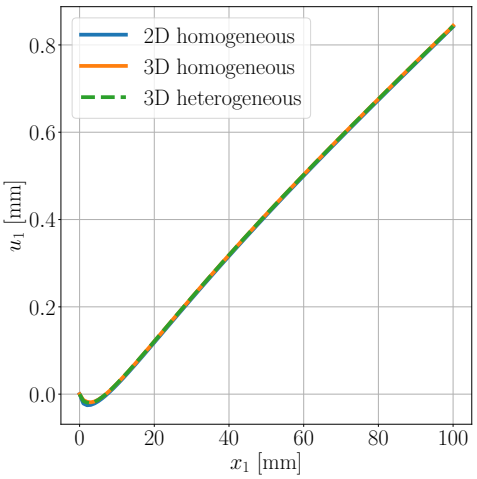

(d) u_1 vs. x_1, lateral face

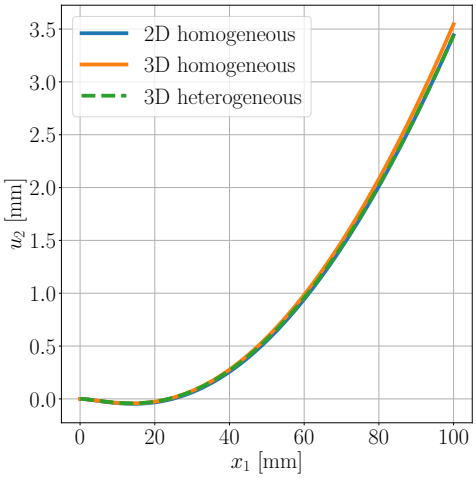

(e) u_2 vs. x_1, lateral face

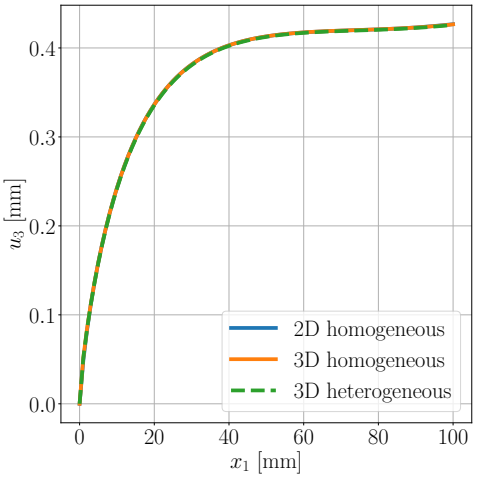

(f) u_3 vs. x_1, lateral face

Figure 6.20: displacement fields, non-symmetric laminate $[0, 90, 0, 90]$, $v_f = 0.05$.

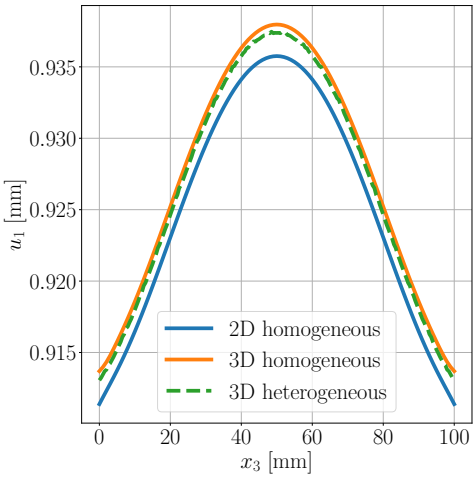

(a) u_1 vs. x_3, front face

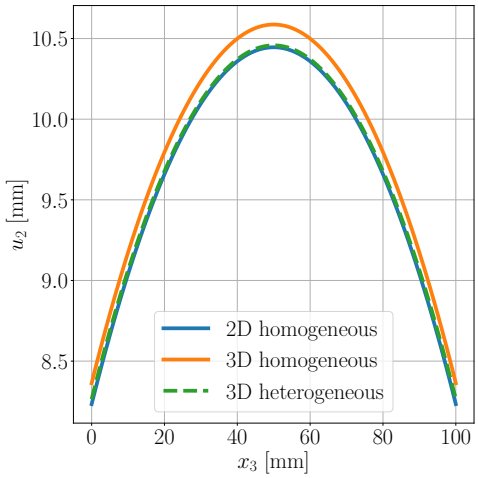

(b) u_2 vs. x_3, front face

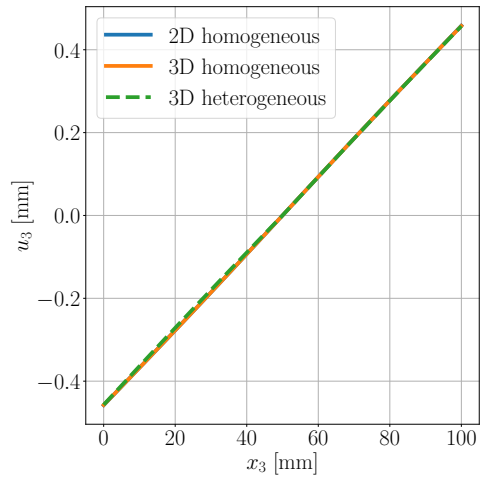

(c) u_3 vs. x_3, front face

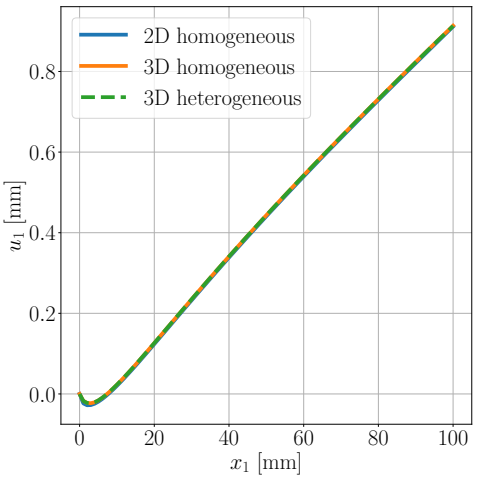

(d) u_1 vs. x_1, lateral face

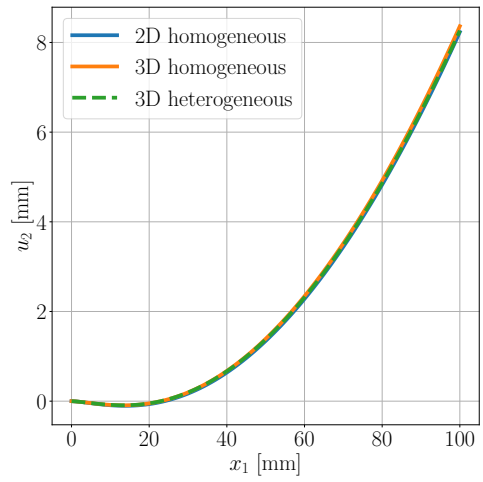

(e) u_2 vs. x_1, lateral face

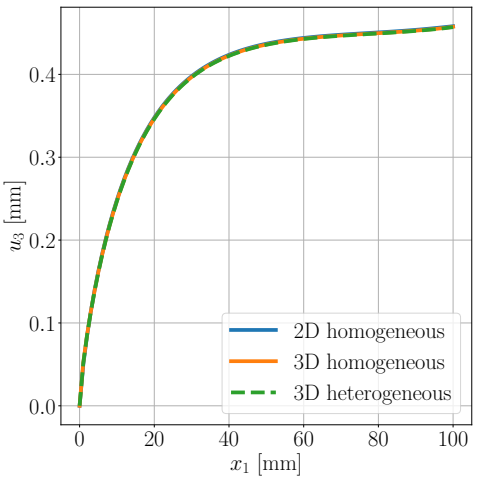

(f) u_3 vs. x_1, lateral face

Figure 6.21: displacement fields, non-symmetric laminate $[0, 0, 90, 90]$, $v_f = 0.05$.

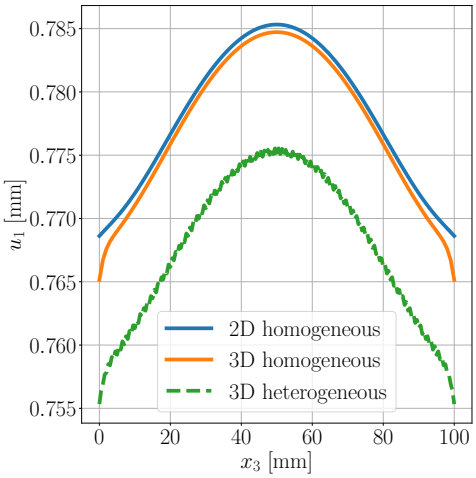

(a) u_1 vs. x_3, front face

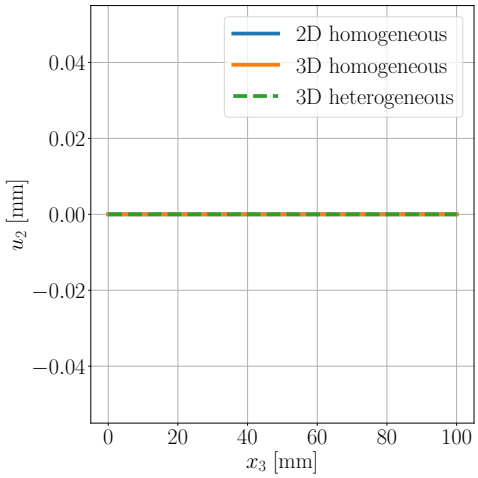

(b) u_2 vs. x_3, front face

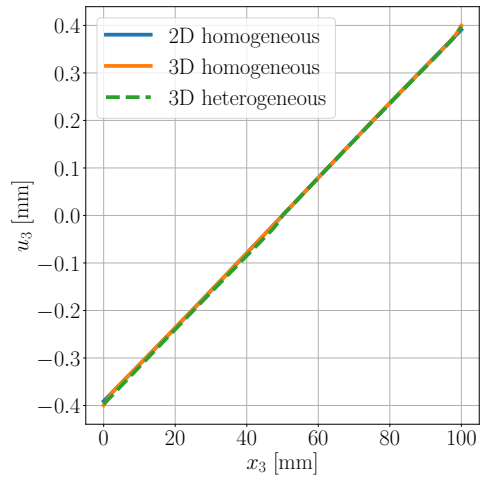

(c) u_3 vs. x_3, front face

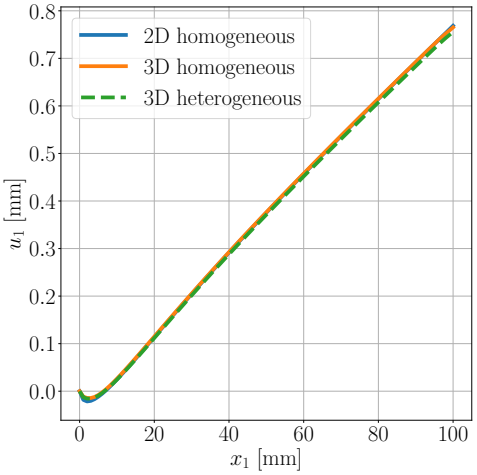

(d) u_1 vs. x_1, lateral face

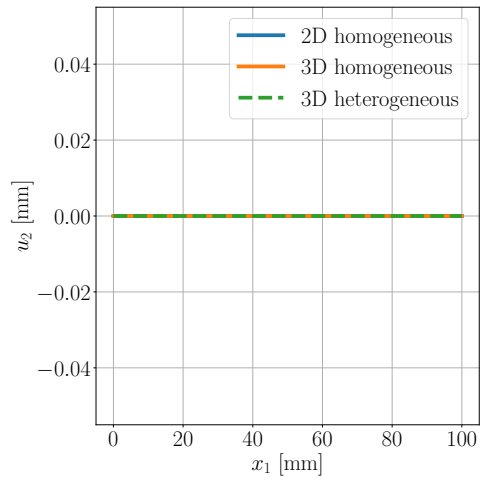

(e) u_2 vs. x_1, lateral face

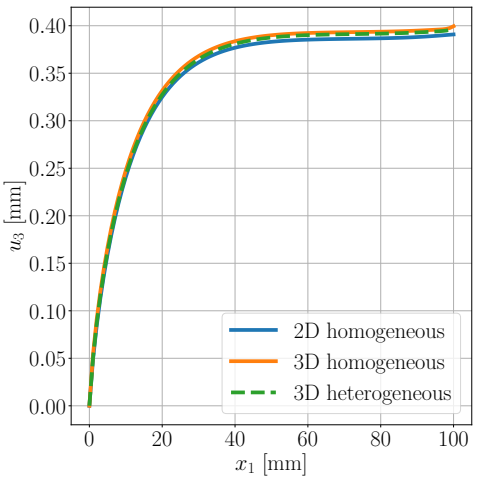

(f) u_3 vs. x_1, lateral face

Figure 6.22: displacement fields, symmetric laminate $[0, 90, 90, 0]$, $v_f = 0.15$.

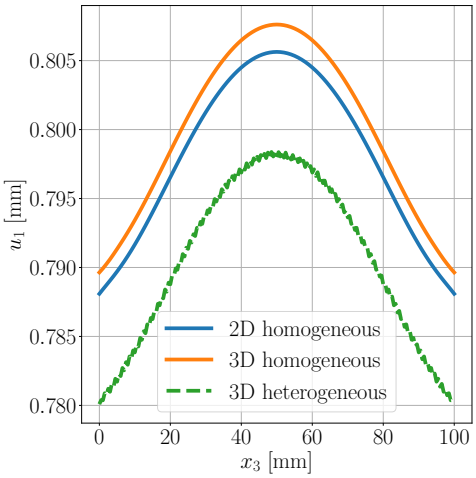

(a) u_1 vs. x_3, front face

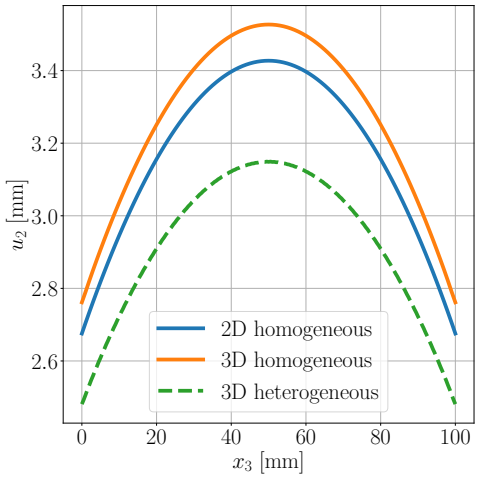

(b) u_2 vs. x_3, front face

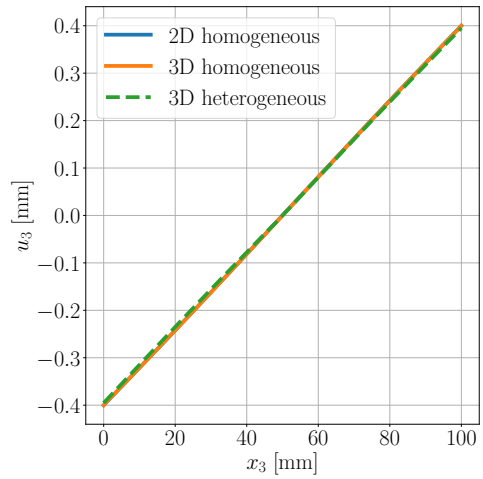

(c) u_3 vs. x_3, front face

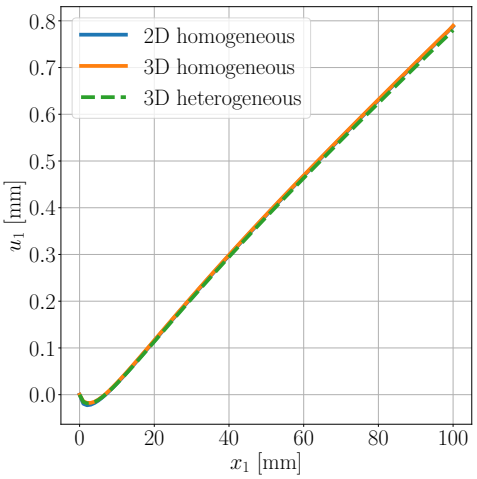

(d) u_1 vs. x_1, lateral face

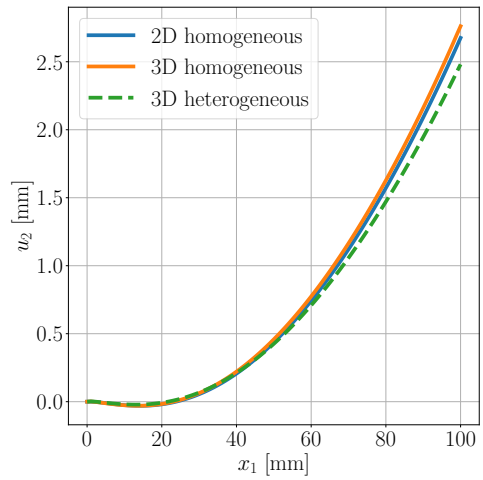

(e) u_2 vs. x_1, lateral face

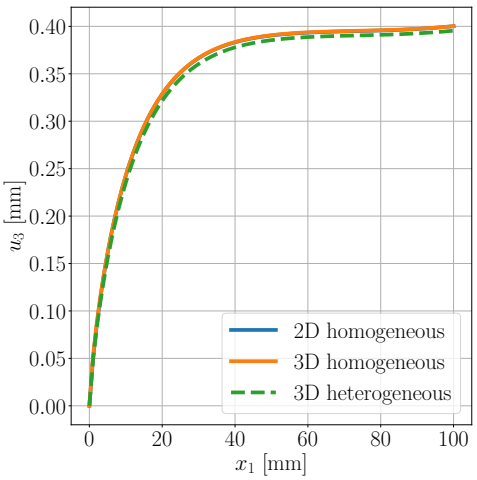

(f) u_3 vs. x_1, lateral face

Figure 6.23: displacement fields, non-symmetric laminate $[0, 90, 0, 90]$, $v_f = 0.15$.

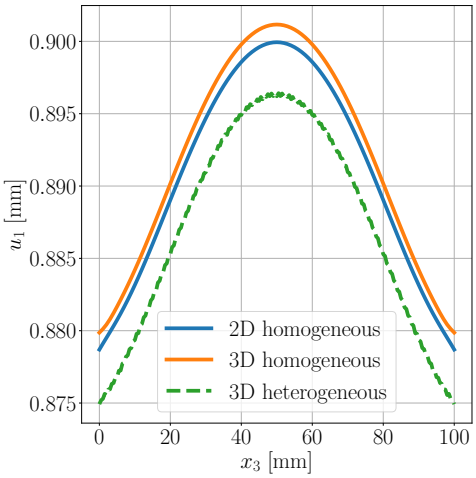

(a) u_1 vs. x_3, front face

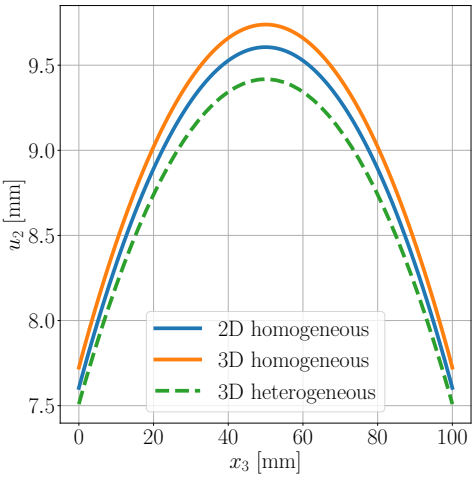

(b) u_2 vs. x_3, front face

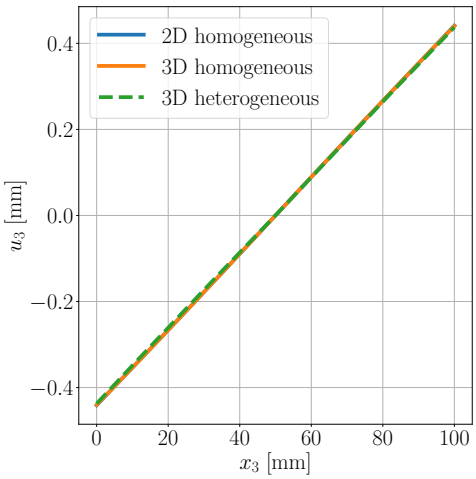

(c) u_3 vs. x_3, front face

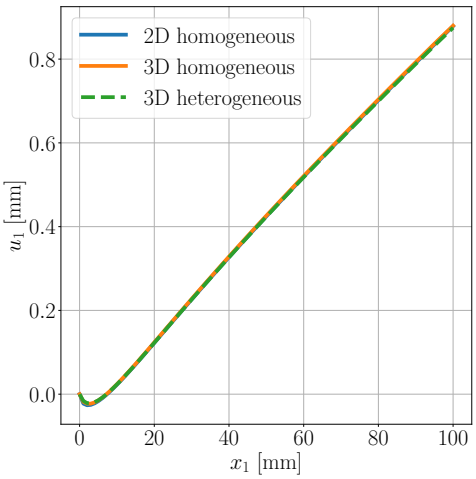

(d) u_1 vs. x_1, lateral face

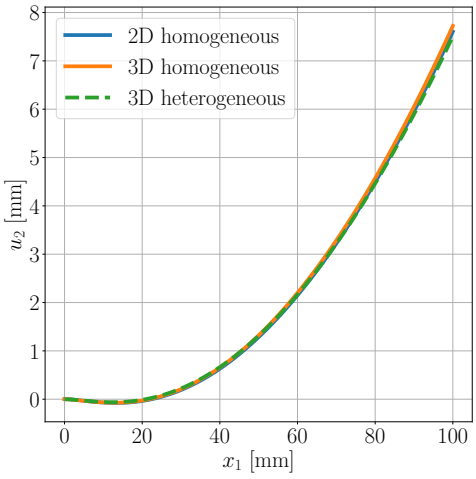

(e) u_2 vs. x_1, lateral face

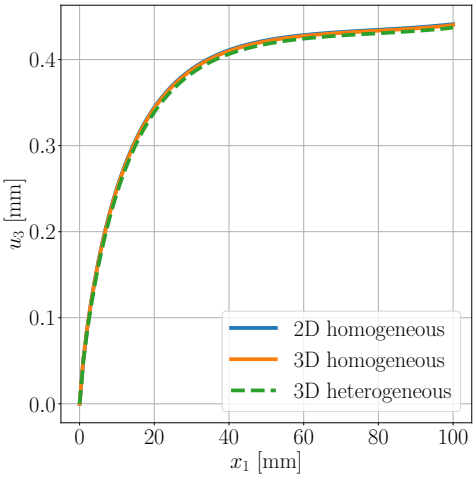

(f) u_3 vs. x_1, lateral face

Figure 6.24: displacement fields, non-symmetric laminate $[0, 0, 90, 90]$, $v_f = 0.15$.

6.3 Thermo-viscoelastic macroscopic response

This section presents an application case considering the full thermo-viscoelastic behavior. The computational model considers layer-oriented mesostructure. First, a numerical exploration is envisaged.

6.3.1 Numerical settings

This section considers the cooling of a 3D printed plate under controlled variation of temperature inside the printing chamber. The printing temperature of the reference material, the commercial high performance thermoplastic Ultem®1010, is around 355°C. As this primal experience is purely numerical, the starting temperature of the simulations is set to $T(0) = 250$°C that corresponds to $\mathrm{T}_g + 30$°C, 30°C above the glass transition temperature T_g. The study of this interval is still representative of the cooling, as we already have shown in [4]. For the sake of simplicity, only one quart of the plates will be studied traduced by symmetry conditions on the symmetry surfaces with normal vectors on the plane of the printing bed. In terms of boundary conditions the started point consider a plate that is completely relaxed over the surface of the printing bed, traduced by a zero displacement in the direction of the outed normal of the printing bed, further time steps allows the displacement in every direction while holding the zero vertical displacement in one of the edges of the bottom plane of the thin plate, allowing to capture the deflection of the plate until it reaches room temperature.

A first virtual experiment: two computational domains

In this section, a first source of validation is given. This will consider the simulation of an idealized heterogeneous domain as a reference solution. As the head of the section specifies, here the actual behavior of the printed part is considered for simulation, in other words the thermo-viscoelastic case. the microscale properties taken are representative of a real material, yet they're artificial, and these properties are indeed characterized by the fitted thermoviscoelastic laws presented in Fig. 6.4. The pores volume fraction is set to 5%. The thin plate cooling considers the plate as a unique domain of simulation, the presence of other elements in the real context is represented on the boundary conditions presented above. The total variation of temperature is maintained too, and the evolution from the start to the ending temperature is defined as linear, with cooling rate

of $2.25°C/s$. As can be inferred, this experience allows evaluating the validity of the meso-macro scale transition on the predictions of the target phenomena.

In Figs. 6.25-6.26 we can observe the distributions of the vertical displacement (i.e., deflection) in both, the heterogeneous, being the reference solution, and the homogenized model in which we use the output from Section 6.1.3. Both distributions look very similar, with marked differences close to the place in which we impose the boundary conditions (close to the bottom edge is easily observed). The distributions shown below are those of the final step of the 100 seconds simulations of the cooling of the part.

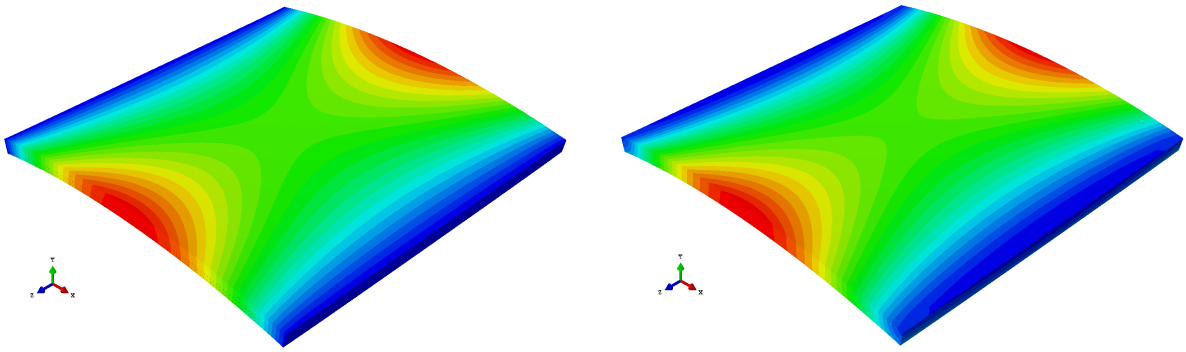

(a) Heterogeneous model. (b) Homogenized model.

Figure 6.25: Vertical displacement distribution u_2, isometric view.

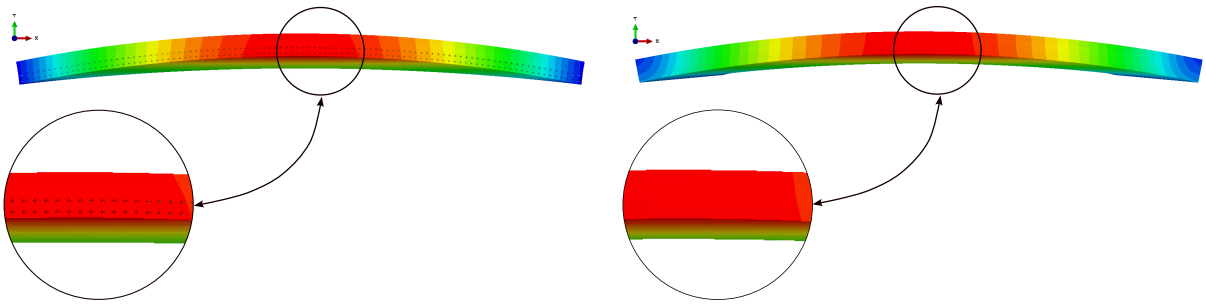

(a) Heterogeneous model. (b) Homogenized model.

Figure 6.26: Vertical displacement distribution u_2, front view.

In Fig. 6.27 we can observe the differences between the vertical displacement of the middle line on the front plane of the plate, which is indeed representative of the whole interval of the vertical displacement. The curves are very close with a L_2 error of 4.29% and a maximum gap of 0.21 mm at the center of the middle line, recalling that this gap is a consequence of the mechanical estimation of the macroscopic behavior as the thermal dilatation behavior is preserved in the meso-macro transition due to the presence of the porous phase at the mesoscale (see Section

6.1.2). These observations validate the pertinence of such simulations on homogenized models instead of the full heterogeneous, considering that the separation of scales in the size of the porosity compared to the length of the edge of the plate (approx. 1/100) imposes a high number of elements for the discretization task, affecting the total time of the simulation. The heterogeneous domain with around 3×10^6 elements and an execution time of 76 hrs, computations performed on HPC services on 2 nodes with a total RAM of 256 GB and 100 cores. while the homogeneous domain with 5×10^3 elements and an execution time of 41 mins, computation of a local machine with 128 GB of RAM and 16 cores. We can see the drastic decrease on time of computation of the homogeneous computations that is about 111 times lower with a compromise of 4.29% on the accuracy. We then can conclude that this virtual experiment successfully show the advantage of the homogenization process and considering that we have started from a homogeneous matrix at the mesoscale, indeed the computation of the full multiscale plate would be much more expensive.

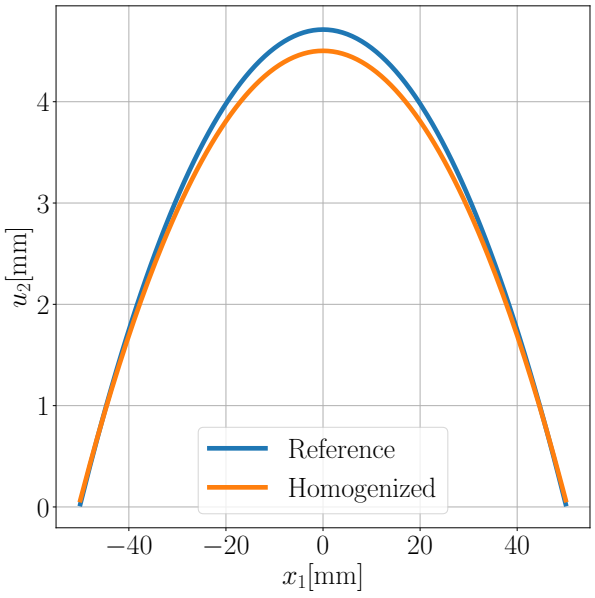

Figure 6.27: Comparison vertical displacement u_2, middle line of the front plane.

6.3.2 Experimental validation

This final section is in fact our first trial testing the methodology presented in the previous content in a real but controlled scenario. In summary, we will attempt to predict the deflection of a 3D printed thin plate made of glass fiber reinforced PEI Ultem 1010 with matrix properties identified in Chapter 2. The argument behind the thin plate verification test is that the hypothesis of uniform temperature distribution during the printing program is still admissible, which simplifies the need to calculate the temperature field for each material point during the printing simulations restricting the computation of the residual stress to the solution of the thermomechanical boundary value problem. The reader is maybe concern about how this assumption will at some point obscure the objective analysis of the approximation given by our methodology, since the errors will contain information not only about the deviation of the estimated behavior with respect to actual observations, but also about the deviation caused by this physical assumption. We recognize this concern and we in fact feel the same; but as we were limited by the experimental facilities and the experimental data, there was indeed not other choice to achieve such a first attempt, arguing that this is one of the most exciting parts of this kind of activities, when we can confront our predictions with nature.

Materials and Methods

As we have just said before, the material used in the experiments is the PEI Ultem 1010 from Sabic®, and we have devoted an entire chapter, Chapter 2, to the experimental identification of the target properties needed to describe the thermo-viscoelastic behavior of an amorphous polymer that follows the mathematical structure presented in Chapter 1. For now, the only information concerning the microstructure description of the reinforced filament is the volume fraction given by the supplier, which is 30% of short glass fibers. The glass fibers properties are extracted from literature and data sheets as its properties remain constant in the range of temperatures at which the polymer matrix is functional for engineering applications, this can be confirmed by considering that the glass transition temperature is close to 1000 °C compared to 216 °C of the polymer matrix.

About the 3D printer that we use to obtain the thin plate, the machine is a high temperature

3D printer from QUALUP SAS, the Qu3 HT[1] (see Fig. 6.28), from the vendors we know that this machine is specially designed to print parts with high performance polymers, the PEI included. a picture of the printer is shown below.

(a) (b)

Figure 6.28: Picture of 3D printer used to obtain the thin. On the left side (a) the closed view, and (b) the open view showing the indoor retractable printing chamber in red.

This specialized 3D printer is able to print up to 500 °C, has a chamber temperature able to hold up to 270 °C and a printing bed holding up to 250 °C. Other special features include a drying chamber controlling the amount of water in the air surrounding the filament and offering a drying program to be set before printing to prevent hygroscopic strains during the printing and high resolution. If the reader is interested in more information about the hardware of this machine, the Qualup website presents an interactive environment that allows a virtual observation of the components in detail.

As we have been discussing throughout the present work, the nature of the constitutive material of the printed part being the composite filament, and due to the manufacturing process itself, the printed part exhibits multiple scales of heterogeneity (see Fig. 2). Regarding the prediction of residual stresses, if we aim to solve such multiscale problem numerically, the computation cost of such operation is too important and grows exponentially with the volume of the printed part. We then use the fact that in an engineering context, at the macroscopic scale at which we measure events, the local fluctuations of the fields are mostly negligible compared to the mean

[1] https://qualup.com

macroscopic observable behavior, suggesting the pertinence of continuum approximations of such material fields supporting the idea of implementing a homogenization procedure to find an appropriate continuum substitute of the actual material that exhibits an equivalent macroscopic response. Recalling this, we then need to compute this homogeneous equivalent material, and this is what we have done in the previous chapters, represented by a two-step homogenization methodology. Here we follow Chapter 4 for the estimation of the effective behavior of the composite filament (the microscale) and the previous content of the present chapter dedicated to the estimation of the effective behavior of the mesoscale using as input the homogenized version of the reinforced thermoplastic filament.

The effective behavior of the reinforced filament

The first step of the homogenization procedure is to give an appropriate mathematical description of the microstructural parameters, according to Chapter 4 this is done by estimating the distributions of the orientations and lengths of the glass fibers. To do this, we need to zoom in on the filament samples and map the state of each fiber in the sample. as can be inferred, we can not perform these observations with common tools, we then use 3D reconstruction of CT-scans acquisitions performed on the fiber reinforced filament with a voxel size of 2.67 μm. The imager has a resolution of 1920 $\times$ 1536 pixels. The device used is the EasyTom XL Ultra 150/160 (μCT) manufactured by RX Solutions[2]. This is in fact the same scanner that we used in Chapter 4, in earlier observations of the filaments. These specifications show that this device is sufficient to map the heterogeneities in the filament, as the size of a single fiber with respect to the short axis is about 10μm.

At this point we should discuss an important fact: if we consider that the target material is that of a 3D printed part, with this logic, a 3D printed part is not made of raw filaments but printed filaments. Our previous observations were focused on raw filaments, which opens the possibility that perhaps the analytical distributions previously chosen in Chapter 4 are no longer suitable to describe the new distribution of microstructural parameters in the printed filament and, first, to verify that there is indeed an actual important variation in such distributions. let's take a look at how these two filaments look like. The figure below is an example of a sectional view of a 3D reconstruction of a couple of filaments samples before and after passing through

[2]https://www.rx-solutions.com

the printing nozzle.

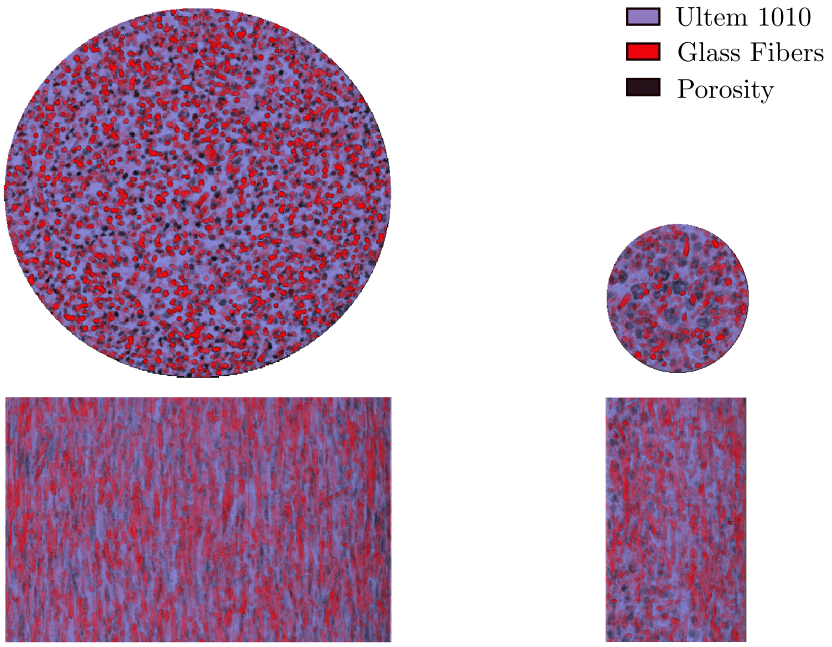

(a) Raw filament.

(b) Extruded filament.

(c) Perspective views.

Figure 6.29: Sectional views of the 3D reconstruction of filament samples.

There are several things that we can say from Fig. 6.29: i) There is a non-negligible reduction in the diameter of the filament (≈1.75 mm), in fact the nozzle diameter is about 2.5 times smaller compared to the raw filament's diameter. ii) On the left side, looking at the raw filament, we can clearly see that the axial direction of the filament is indeed the predominant direction that the fibers follow, in the transverse view (on top) we see the fibers almost as points ergo in the axial view (bottom) they appear almost aligned with the long axis. This is no longer the case when we look at the image of the right side, in the transverse view we no longer see points, but

short lines, suggesting a higher level of disorder, which is confirmed in the axial view, where the population of "aligned" fibers decreases. iii) A third phase appears, this is that of porosity. In fact the observation of the presence of porosity has been observed in the previous scans, but in a first time this was addressed as a purely technological problem in the context of the present project expecting to improve the filament fabrication avoiding the presence of porosity in the filament as it causes loss of rigidity ("what we earn with fibers is lost in porosity"). In the end this difficulty has not been overcome, then we are forced to consider this phase at this scale. It should be noted that the presence of the porous phase is also true for non-reinforced filaments, of course the presence of the fibers has an influence on the porosity volume fraction and distribution, unfortunately these observations were not made during this project and our observation were restricted to only two samples. In the following table, we present the volume fraction data extracted from the post-processing of the scans.

	Raw filament	Extruded Filament
Glass fibers	0.28	0.25
Porosity	0.07	0.09

Table 6.5: Computed phase's volume fraction of the reinforced filament 3DXTECH PEI Ultem1010 30% GF

In the Table 6.5, we observe a decrease in the concentration of the fibers and an increase of the porosity. We could explain this by the fact that there is this important reduction of diameter during the extrusion of the filament. In fact, as the filament is pushed out of the nozzle at some given printing velocity, that consequence of the pressure exerted on the filament by the printer head, the trajectory of the filaments can be modified, in any case, since this fused filament holds a non-negligible viscosity at the printing temperature this variation should not be important, the most important variation in the trajectory of the fibers is indeed the geometry of the nozzle itself, which will force the fibers to move from the nice initial filament aligned direction. This change in trajectories will also affect the porosities, which will easily flow inside the filament forming clusters, giving in consequence bigger porosities in the printed filament compared to the group of porosities of the raw filament which max diameter is close to the fibers short axis (see Fig. 6.29). Let's now take a look at the distribution of the lengths. In the same fashion of Chapter 4 the length distribution is analyzed through the aspect ratio $w = l/d$, with l being the

length of the fiber and d its diameter. The distributions are presented in the form of probability density (or relative frequency) histograms PDF, and the cumulative frequency plots or CDF.

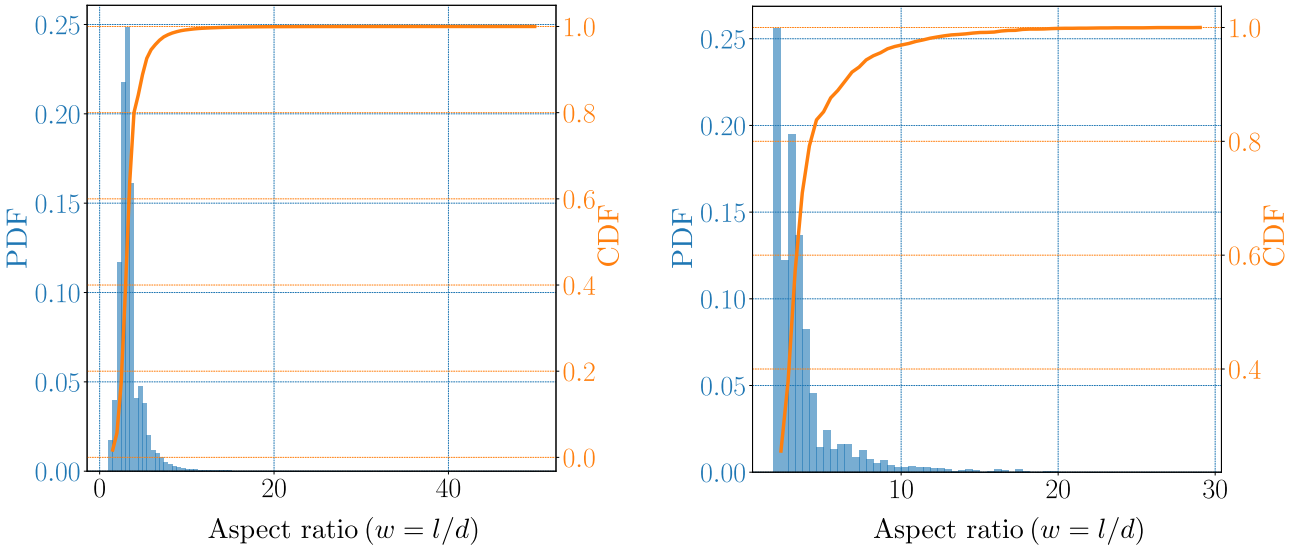

(a) Raw filament.

(b) Extruded filament.

Figure 6.30: Aspect ratio distributions.

From Fig. 6.30 we can see how the population of intermediate values of w decreases from left to right, the maximum relative frequency (PDF histograms) is now located in the lower interval. In addition, we observe how the population of high aspect ratio is drastically reduced in the extruded filament, represented by a jump in the relative frequency on the right side of the histogram; in fact, the population of aspect ratios greater than 30 completely disappears, this can be directly observed in the cumulative plots (in orange) looking at the maximum of the curves. We could think about a possible breaking event of some fibers while crossing the nozzle length, that could be generated by the intersection of fibers close to the outside due to the reduction of diameter, which at some point will block their displacement, forcing them to break as a consequence of the pressure applied by the extruder. What we can say that is similar in the two graphs is that the majority of fibers are located in the interval with a maximum value of $w = 20$. The other microstructural parameter, completing the microstructure description of the glass fibers.

In Fig. 6.31 above, we confirm the observations in the Fig. 6.29, the peak of the relative frequencies are around $\theta = 0°, \phi = 0°$ which reflects that the majority of fibers are aligned with the long axis of the filament. If we now look at the figure on the right side, the distribution of orientations of the extruded filament appears to have a significant deviation with respect to the

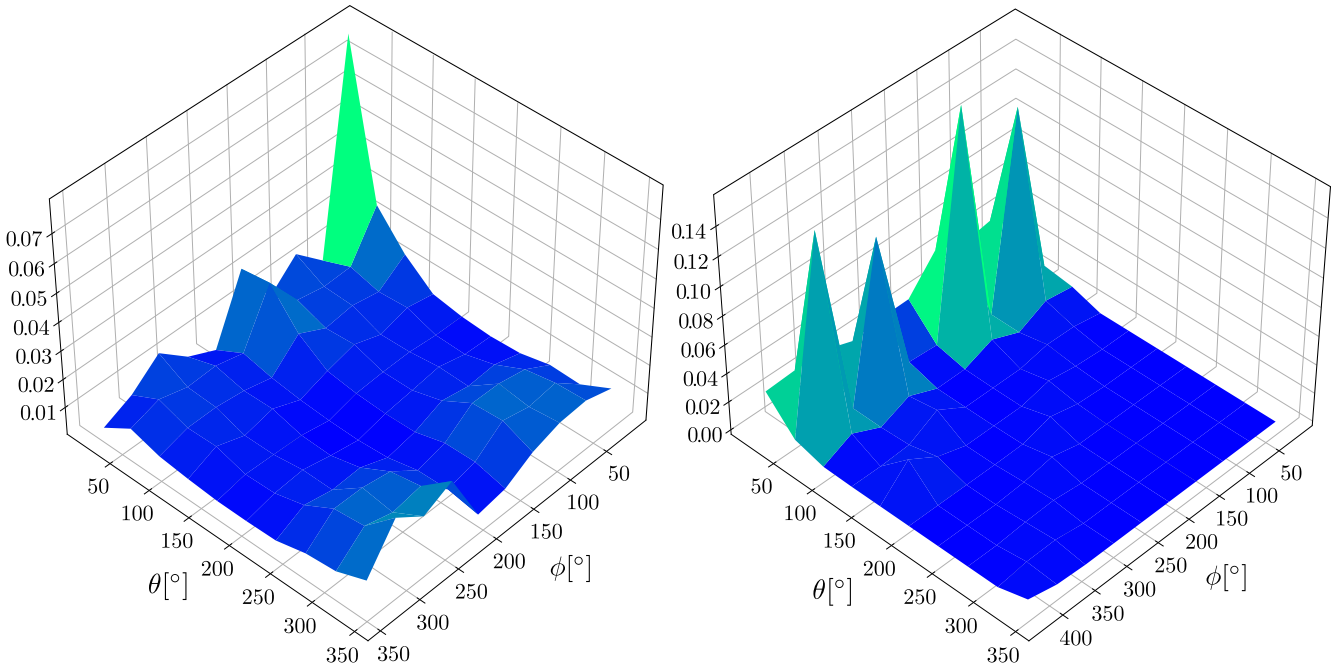

(a) Raw filament.

(b) Extruded filament.

Figure 6.31: PDF for orientation distributions.

altitude angle ϕ, and a slight deviation for the azimuth angle θ, then for the extruded filaments we see a population with fibers preserving a single degree of alignment with respect to the long axis of the filaments reflecting that during the printing process the fibers locally rotate in planes that are parallel to the median plane of the filament.

With this, we close the microstructural description of the fibers. The reader is maybe wondering about the identification of the appropriate candidate for the analytical representation of the above presented distributions; in fact, since the data we have analyzed was obtained from a single observation there is no statistical meaning of such distributions as it lacks of trial redundancy. In any case, as we aim to present an example of an approach to a real case, the pertinence of such tests remains in force. Then, instead of fitting an analytical distribution, we will perform numerical integration for the computation of the distribution averaged localization tensor $\mathbb{A}_\star^{*(f)}$ from Chapter 4, necessary for the computation of the effective fourth order relaxation tensor $\widetilde{\mathbb{L}}^*$, and the effective second order tensor of thermal creep functions $\widetilde{\boldsymbol{\alpha}}^*$, by means of a mean-field homogenization procedure recalling that this is performed in the context of the extension of the correspondence principle to continuous variations of temperature presented in the aforementioned chapter and published in [4].

Considering that Chapter 4 contains enough information for the homogenization procedure of the reinforced filament and considering the microstructural description presented before, we will not make any more comments on this part, and we will directly present the predictions of the effective behavior obtained using for the material properties of the matrix those identified in chapter 2.

Experimental protocol

In this part, we address the comparison of the proposed methodology in actual 3D printed parts using a standard printing velocity of 60 mm/min with a nozzle temperature of 350°C. As we have pointed out above, the target scenario considers thin plates. The printed chamber allows controlling the cooling of the part, this experience considered three different linear cooling programs (from 220°C to 25°C) for three different plates, the first case considers a rapid cooling, the second a medium cooling of 4 hours and the last one a very slow cooling of 3 days expected to be the one exhibiting the lower deflection. The dimensions of the printed plates are $200 \times 200 \times 1.6$ mm. The plates' printing directions are equivalent to those presented in the previous virtual experiments, i.e., the non-symmetric $[0, 0, 90, 90]$ plate. The experimental measurement was conducted using the Aramis 3D-DIC facility to determine the deflection of the middle line of the front plane of the plate. In Fig. 6.32 we can observe the good agreement of the simulations compared to the experimental observations with a maximum error of 12.8%, 7.86% and 13.5% for the three cases.

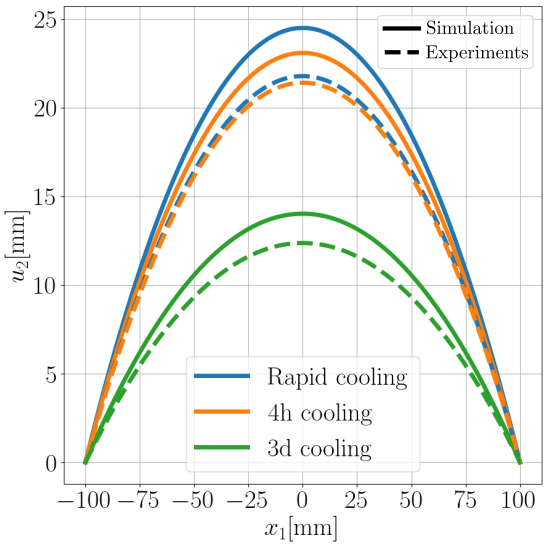

Figure 6.32: Comparison vertical displacement u_2, middle line of the front plane.

Conclusion

In general, at the end of each chapter we have presented a set of local conclusions, considering this, we will address the last comments regarding the last chapter in conjunction with the previous ones as this last section include an experimental validation of the entire methodology, that is indeed the one giving the first information about the actual applicability of the proposed workflow for the estimation of the residual stress distribution in a 3D printed composite part.

To be able to compute the effective behavior at the macroscale we need to be able to describe mathematically each target property. Since the heterogeneous medium is characterized by three phases: a polymer matrix, short glass fibers and voids, the only non-trivial behavior to describe was the matrix material, considered as thermo-viscoelastic. In chapter 2 we have presented the outputs from the experimental identification of such properties.

Most observations happened to be in coherence with industrial datasheets and experimental observations conducted by external sources. Despite this apparent coherence, we observe some difficulties during confined compression tests and dilatation tests, first trials were performed by external contractors who failed to perform such measurement on injection molded plates. These measurements are not overcame challenges and were limited by budget and the lack of expertise available to perform it. We therefore conclude that it is pertinent to design an appropriate standard procedure to measure such properties in the context of FDM 3D printing, in addition properties as shear and tensile time-temperature dependent behavior should be considered as being affected by the manufacturing process used to obtain the samples and the direct application must be judged considering its influence.

Chapter 4, and chapter 5 presents the methodology to derive the effective properties of the microscale, i.e., the scale of the composite filament reinforced with elastic fibers for both, a thermorheologically simple and a thermorheologically complex polymer, showing a good agreement

with respect to the proposed reference solutions, and a clear advantage in terms on computation cost. In terms of contextualization of the application envisaged here, chapter 4 considers short fibers properties distributions fed from micro-CT scans, which allows ensuring a high fidelity description of the fibers phase since the target material for validation experiments is a thermorheologically simple polymer (PEI Ultem 1010). In this chapter we have done a couple of observations that deserve to be mention:

First, when considering SPC or single polymer composites in which the other phases exhibit invariance of properties in the range of temperature of the study, the time temperature superposition principle (represented by the shift factor a_T) for the composite will remain the same as the matrix, this is currently validated by experimental campaign that we are preparing for publication.

Second, in chapter 2 we have chosen a non-trivial representation of the isotropic thermal dilatation coefficient of the polymer matrix, this representation can be observed as an analogy of a compliance coefficient, this representation is more appropriate as it describes better the real behavior of the polymer. Considering the homogenization procedure followed, it turns out that despite the choice made for the dilatation coefficient (elastic or viscoelastic-like) the behavior of the effective dilatation coefficients of the transverse isotropic thermo-viscoelastic medium will always match the mathematical structure chosen in this work, this validates partially the pertinence of such choice on the identification of properties for the experiments.

Finally, in chapter 6 we perform the second upscaling. We must mention that, this step of the upscaling could become really difficult to handle in function of the printing program in terms of the distribution of plane trajectories serving to obtain the 3D volume of the printed part. In the present thesis, we have chosen a simplified scenario that allows us to conduct validation experiments of the proposed method, we then consider unidirectional plane trajectories allowed to change each layer. Moreover, we chose some combinations of this plane trajectories lying in variations of 90° with respect to the first deposed layer. This allowed us to study the 3D printing part, as we used to do in the case of stratified materials in the classic thermoset plies. Numerical comparisons shown the good agreement of the homogenized behavior when comparing against heterogeneous computational domains.

Furthermore, experiments shown an additional argument to the pertinence of these approximations. The computed values happened to be very close to its real counterparts. This primal observation encourages the justification of the extension of the present study, trying to describe better the physical parameters to obtain better approximations, since these results suggests that the mathematical structure of the thermo-viscoelasticity theory in conjunction with the homogenization theory by means of the correspondance principle is a suitable description for predicting deformation and stresses in 3D printed parts in the context of mechanical engineering.

Extension to arbitrary plane directions is the next step for improving the upscaling procedure. In general, the methodology introduced here represents a clear advantage for the virtual prototyping of 3D printed parts in mechanical design, presenting a reasonable simulation scenario for parts that gives the possibility of optimization of parts without implying the waste of materials and production time.

Appendix A

Mathematical tools

A.1 Convolution Product

The convolution product is a mathematical operation that combines two functions into a single function, often used in the context of signal processing, system response analysis, and probability theory. Given two functions $f(t)$ and $g(t)$, their convolution, denoted by $(f * g)(t)$, is defined as follows:

$$[f * g](t) = \int_{-\infty}^{\infty} f(\tau)g(t-\tau)\,d\tau \tag{A.1}$$

The variable τ is a dummy variable of integration. The convolution operation possesses several important mathematical properties, including:

1. **Commutativity:**

$$[f * g](t) = [g * f](t) \tag{A.2}$$

2. **Associativity:**

$$[(f * g) * h](t) = [f * (g * h)](t) \tag{A.3}$$

3. **Distributivity:**

$$[f * (g + h)](t) = [f * g](t) + [f * h](t) \tag{A.4}$$

4. **Scalar Multiplication:**

$$[c(f * g)](t) = [cf * g](t) = [f * cg](t) \tag{A.5}$$

A.2 Stieltjes Convolution Product

Stieltjes convolution is a mathematical concept related to functional analysis and probability theory. The Stieltjes convolution arises from the combination of a non-decreasing function, typically a distribution function of a probability measure, and another function. The concept is named after the Dutch mathematician Thomas Joannes Stieltjes, who made significant contributions to various fields of mathematics in the late 19th century. The Stieltjes convolution of a non-decreasing function F (usually a cumulative distribution function) and a function g is defined as:

$$[f \circledast g](t) = \int_{-\infty}^{\infty} f(\tau) dg(t - \tau) \tag{A.6}$$

Stieltjes convolution is often encountered in probability theory, where F represents the cumulative distribution function of a probability measure, and g represents a function related to the problem at hand. In such cases, the Stieltjes convolution is used to analyze the sum of independent random variables or the behavior of certain stochastic processes. If we consider for instance the Stieltjes convolution product as the derivative of the conventional convolution, we can write:

$$[f \circledast g](t) = \frac{d}{dt} \int_{-\infty}^{\infty} f(\tau) g(t - \tau) d\tau = \int_{-\infty}^{\infty} f(\tau) \frac{dg(t - \tau)}{dt} d\tau = \int_{-\infty}^{\infty} f(\tau) dg(t - \tau) \tag{A.7}$$

by means of the commutativity property of the convolution product this definition is sufficient proof to transfer the rest of the properties of the classic convolution product to the Stieltjes convolution product these are:

1. **Commutativity:**

$$[f \circledast g](t) = [g \circledast f](t) \tag{A.8}$$

2. **Associativity:**

$$[(f \circledast g) \circledast h](t) = [f \circledast (g \circledast h)](t) \tag{A.9}$$

3. **Distributivity:**

$$[f \circledast (g + h)](t) = [f \circledast g](t) + [f \circledast h](t) \tag{A.10}$$

4. **Scalar Multiplication:**

$$[c(f \circledast g)](t) = [cf \circledast g](t) = [f \circledast cg](t) \tag{A.11}$$

where c is a constant scalar.

A.2.1 Derivative Properties of Stieltjes Convolution

Differentiation under the integral sign

When dealing with the derivatives of Stieltjes convolution, it is essential to consider differentiating under the integral sign. Suppose f and g differentiable functions, and its partial derivative with respect to t exists and is continuous. Then, using Leibniz's rule for differentiation under the integral sign, we can differentiate the Stieltjes convolution with respect to t:

$$\frac{d[f \circledast g](t)}{dt} = \int_{-\infty}^{\infty} f(\tau) \frac{d^2 g(t-\tau)}{dt^2} d\tau = \int_{-\infty}^{\infty} \frac{df(t-\tau)}{dt} \frac{dg\tau}{d\tau} d\tau \tag{A.12}$$

General properties of the derivative of Stieltjes convolution

Some general properties of the derivative of Stieltjes convolution. If f, g , and h are continuous differentiable functions, then:

1. Linearity:

$$\frac{d}{dt}\left[(f + h) \circledast h\right](t) = \frac{d[f \circledast g](t)}{dt} + \frac{d[g \circledast h](t)}{dt} \tag{A.13}$$

2. Commutativity:

$$\frac{d[f \circledast h](t)}{dt} = \frac{d[h \circledast f](t)}{dt} \tag{A.14}$$

3. Chain rule:

$$\frac{d[f \circledast (g \circledast h)](t)}{dt} = [f \circledast \frac{d(g \circledast h](t)}{dt}) \tag{A.15}$$

These properties can be helpful in simplifying expressions and solving problems involving the derivatives of Stieltjes convolutions. The Stieltjes convolution operation can be also interpreted as a measure of the interaction or overlap between the two functions $f(t)$ and $g(t)$. In the context of probability theory, the Stieltjes convolution of two cumulative distribution functions represents the cumulative distribution function of the sum of two independent random variables. The properties of the Stieltjes convolution mentioned above also hold for the discrete case, with the integral replaced by a summation:

$$(f \circledast g)(n) = \sum_{m=0}^{n} f(m)\Delta g(n-m) \tag{A.16}$$

where $\Delta g(n-m) = g(n-m) - g(n-m-1)$.

A.3 Laplace-Carson Transform

A.3.1 Introduction

The Laplace-Carson transform is an extension of the classic Laplace transform. It is widely used in the analysis of linear time-invariant systems and the solving of ordinary and partial differential equations.

A.3.2 Classic Laplace Transform

The classic Laplace transform is defined as:

$$\mathcal{L}\{f(t)\}(p) = \int_0^\infty e^{-pt} f(t) dt \tag{A.17}$$

where $f(t)$ is a given function of time t, and p is a complex variable.

A.3.3 Laplace-Carson Transform

The Laplace-Carson transform is defined as:

$$\mathcal{LC}\{f(t)\}(p) = p\int_0^\infty e^{-pt}f(t)dt \tag{A.18}$$

A.3.4 Connection to the Classic Laplace Transform

$$\mathcal{LC}\{f(t)\}(p) = p\mathcal{L}\{gf(t)\}(p) \tag{A.19}$$

A.3.5 Properties of the Laplace-Carson Transform

1. Linearity: The Laplace-Carson transform is a linear operation. If $f(t)$ and $g(t)$ are functions with Laplace-Carson transforms $F(p)$ and $G(p)$, respectively, and a and b are constants, then:

$$\mathcal{LC}\{af(t) + bg(t)\}(s) = aF(p) + bG(p) \tag{A.20}$$

2. Time scaling: If a is a positive constant, then:

$$\mathcal{LC}\{f(at)\}(p) = \frac{1}{a}F\left(\frac{p}{a}\right) \tag{A.21}$$

3. Frequency scaling: If a is a positive constant, then:

$$\mathcal{LC}\{e^{at}f(t)\}(p) = F(p-a) \tag{A.22}$$

4. Time shifting: If t_0 is a constant, then:

$$\mathcal{LC}\{f(t-t_0)\}(s) = e^{-pt_0}F(p) \tag{A.23}$$

5. Differentiation in the time domain: If $f'(t)$ is the derivative of $f(t)$ with respect to time t, then:

$$\mathcal{LC}\{f'(t)\}(p) = pF(p) - f(0^-) \tag{A.24}$$

6. Integration in the time domain: If $F(p)$ is the Laplace-Carson transform of $f(t)$, then the Laplace-Carson transform of the integral of $f(t)$ is given by:

$$\mathcal{LC}\left\{\int_{-\infty}^{t} f(\tau)d\tau\right\}(p) = \frac{F(p)}{p} \tag{A.25}$$

7. Convolution theorem: If $f(t)$ and $g(t)$ are functions with Laplace-Carson transforms $F(p)$ and $G(p)$, respectively, then the Laplace-Carson transform of their Stieltjes convolution is given by:

$$\mathcal{LC}\{[f \circledast g](t)\}(p) = F(p)G(p) \tag{A.26}$$

These properties of the Laplace-Carson transform can be helpful in simplifying expressions and solving problems in various fields, such as control theory, signal processing, and differential equations.

A.4 Decomposition of Fourth-Order Tensors Using Orthogonal Fourth-Order Projectors

In the context of continuum mechanics and material science, fourth-order tensors are often used to describe the elastic properties of materials. To simplify the analysis and computation involving fourth-order tensors, it's helpful to decompose them using orthogonal fourth-order projectors. In this appendix, we will discuss the decomposition of a fourth-order tensor A_{ijkl} into its isotropic and deviatoric parts using the fourth-order identity tensor I_{ijkl} and orthogonal projectors J_{ijkl} and K_{ijkl}. First, let's define the fourth-order identity tensor I_{ijkl} as follows:

$$I_{ijkl} = \frac{1}{2}(\delta_{ik}\delta_{jl} + \delta_{il}\delta_{jk}) \tag{A.27}$$

where δ_{ij} is the Kronecker delta. Now, let's define the orthogonal projectors J_{ijkl} and K_{ijkl}:

$$J_{ijkl} = \frac{1}{3}\delta_{ij}\delta_{kl}, \tag{A.28}$$

$$K_{ijkl} = I_{ijkl} - J_{ijkl}. \tag{A.29}$$

The projector J_{ijkl} projects the tensor onto its hydrostatic part, while the projector K_{ijkl} projects it onto its deviatoric part. Using these projectors, we can decompose the fourth-order tensor A_{ijkl} into its hydrostatic and deviatoric parts:

$$A_{ijkl} = a_h J_{ijkl} + a_d K_{ijkl}. \tag{A.30}$$

Here, a_h and a_d are scalar coefficients representing the hydrostatic and deviatoric contributions of the tensor A_{ijkl}. They can be computed as follows:

$$a_h = \frac{1}{9} A_{ijij}, \tag{A.31}$$

$$a_d = A_{ijkl} - a_h J_{ijkl}. \tag{A.32}$$

In summary, the decomposition of a fourth-order tensor using orthogonal projectors allows us to separate the isotropic and deviatoric parts, simplifying the analysis and computation involving these tensors.

A.5 Transversely isotropic elasticity tensors and matrix representation

The explicit form of the Hill basis tensors for a given symmetry axis orientation ($\boldsymbol{n}$) is presented below.

$$\begin{aligned}
&\boldsymbol{\mathcal{N}} = \boldsymbol{n} \otimes \boldsymbol{n}, \quad \boldsymbol{\Theta} = \boldsymbol{I} - \boldsymbol{\mathcal{N}}, \\
&\mathbb{H}^{(1)}(\boldsymbol{n}) = \frac{1}{2}\boldsymbol{\Theta} \otimes \boldsymbol{\Theta}, \quad \mathbb{H}^{(2)}(\boldsymbol{n}) = \boldsymbol{\Theta} \otimes \boldsymbol{\mathcal{N}}, \quad \mathbb{H}^{(3)}(\boldsymbol{n}) = \boldsymbol{\mathcal{N}} \otimes \boldsymbol{\Theta}, \quad \mathbb{H}^{(4)}(\boldsymbol{n}) = \boldsymbol{\mathcal{N}} \otimes \boldsymbol{\mathcal{N}}, \\
&\mathbb{H}^{(5)}(\boldsymbol{n}) = \frac{1}{2}\left(\Theta_{ik}\Theta_{lj} + \Theta_{il}\Theta_{kj} - \Theta_{ij}\Theta_{kl}\right), \\
&\mathbb{H}^{(6)}(\boldsymbol{n}) = \frac{1}{2}\left(\Theta_{ik}\mathcal{N}_{lj} + \Theta_{il}\mathcal{N}_{kj} + \Theta_{jk}\mathcal{N}_{li} + \Theta_{jl}\mathcal{N}_{ki}\right).
\end{aligned} \tag{A.33}$$

With $\otimes$ representing the tensor product.

Transversely isotropic elasticity tensors are written in Hill basis as:

$$\mathbb{L} = 2K\mathbb{H}^1 + \ell(\mathbb{H}^2 + \mathbb{H}^3) + n\mathbb{H}^4 + 2m\mathbb{H}^5 + 2\mu\mathbb{H}^6 = \sum_{b=1}^{6} l^{(b)}\mathbb{H}^{(b)}, \tag{A.34}$$

where:

- K is the plane strain bulk modulus.
- m is the transverse shear modulus: ($m = G_{23}$ if $\boldsymbol{n} = \boldsymbol{e}_1$).
- μ is the longitudinal shear modulus: ($\mu = G_{12} = G_{13}$ if $\boldsymbol{n} = \boldsymbol{e}_1$).
- ℓ and n can be linked to the "engineering" constants, e.g if $\boldsymbol{n} = \boldsymbol{e}_1$:

$$\ell/2K = \nu_{12}, \qquad n - \ell^2/K = E_1. \tag{A.35}$$

In 6×6 matrix representation (Voigt notations), taking $\boldsymbol{n} = \boldsymbol{e}_1$, one has [165]

$$\boldsymbol{L}_{\text{Voigt}} = \begin{bmatrix} L_{11} & L_{12} & L_{12} & 0 & 0 & 0 \\ L_{12} & L_{22} & L_{23} & 0 & 0 & 0 \\ L_{12} & L_{23} & L_{22} & 0 & 0 & 0 \\ 0 & 0 & 0 & (L_{22} - L_{23})/2 & 0 & 0 \\ 0 & 0 & 0 & 0 & L_{55} & \\ 0 & 0 & 0 & 0 & 0 & L_{55} \end{bmatrix} = \begin{bmatrix} n & \ell & \ell & 0 & 0 & 0 \\ \ell & K+m & K-m & 0 & 0 & 0 \\ \ell & K-m & K+m & 0 & 0 & 0 \\ 0 & 0 & 0 & m & 0 & 0 \\ 0 & 0 & 0 & 0 & \mu & 0 \\ 0 & 0 & 0 & 0 & 0 & \mu \end{bmatrix}. \tag{A.36}$$

Using "engineering" coefficients (e.g. $(E_1, E_2, \nu_{12}, G_{12}, G_{23})$) the associated compliance matrix is:

$$\boldsymbol{S}_{\text{Voigt}} = \begin{bmatrix} \frac{1}{E_1} & -\frac{\nu_{12}}{E_2} & -\frac{\nu_{12}}{E_2} & 0 & 0 & 0 \\ -\frac{\nu_{21}}{E_1} & \frac{1}{E_2} & -\frac{\nu_{32}}{E_2} & 0 & 0 & 0 \\ -\frac{\nu_{21}}{E_1} & -\frac{\nu_{32}}{E_2} & \frac{1}{E_2} & 0 & 0 & 0 \\ 0 & 0 & 0 & \frac{1}{G_{23}} & 0 & 0 \\ 0 & 0 & 0 & 0 & \frac{1}{G_{12}} & 0 \\ 0 & 0 & 0 & 0 & 0 & \frac{1}{G_{12}} \end{bmatrix}, \tag{A.37}$$

where ν_{21} is determined by the symmetry requirement $\nu_{21}/E_1 = \nu_{12}/E_2$.

For completely isotropic materials, one has:

$$\boldsymbol{L}_{\text{Voigt}} = \begin{bmatrix} \lambda+2\mu & \lambda & \lambda & 0 & 0 & 0 \\ \lambda & \lambda+2\mu & \lambda & 0 & 0 & 0 \\ \lambda & \lambda & \lambda+2\mu & 0 & 0 & 0 \\ 0 & 0 & 0 & \mu & 0 & 0 \\ 0 & 0 & 0 & 0 & \mu & 0 \\ 0 & 0 & 0 & 0 & 0 & \mu \end{bmatrix}, \quad \text{so that} \quad \begin{cases} K = \lambda+\mu & = \kappa + \dfrac{1}{3}\mu \\ \ell = \lambda & = \kappa - \dfrac{2}{3}\mu \\ n = \lambda+2\mu & = \kappa + \dfrac{4}{3}\mu \\ m = \mu \end{cases} \tag{A.38}$$

where we used $\lambda = \kappa - 2\mu/3$.

A.5.1 Products of tensors in Hill basis

Double product ":"	$\boldsymbol{\mathcal{N}}$	$\boldsymbol{\Theta}$
$\mathbb{H}^{(1)}$	$\mathbf{0}$	$\boldsymbol{\Theta}$
$\mathbb{H}^{(2)}$	$\boldsymbol{\Theta}$	$\mathbf{0}$
$\mathbb{H}^{(3)}$	$\mathbf{0}$	$2\boldsymbol{\mathcal{N}}$
$\mathbb{H}^{(4)}$	$\boldsymbol{\mathcal{N}}$	$\mathbf{0}$
$\mathbb{H}^{(5)}$	$\mathbf{0}$	$\mathbf{0}$
$\mathbb{H}^{(6)}$	$\mathbf{0}$	$\mathbf{0}$

Table A.1: Product between fourth-order Hill basis tensor and second-order tensor of the natural basis of transverse isotropic tensors.

By Table. A.1, the product between fourth- and second-order transverse isotropic tensors is:

$$\boldsymbol{T} : \boldsymbol{t} = (T_4 t_1 + 2T_3 t_2)\boldsymbol{\mathcal{N}} + (T_2 t_1 + T_1 t_2)\boldsymbol{\Theta}. \tag{A.39}$$

A.5.2 Orientation averaged Hill basis

By Eq. (A.33) it is noted that the orientation averaging of the Hill basis is reduced to the computation of the second and fourth order orientation tensors, interpreted as the second and fourth order moments of the orientation distribution respectively [110]. the expressions of the orientation tensors are presented below.

$$\boldsymbol{\eta}_2 = \int_S f_{\boldsymbol{n}}(\boldsymbol{n})(\boldsymbol{n}\otimes\boldsymbol{n})dS, \quad \boldsymbol{\eta}_4 = \int_S f_{\boldsymbol{n}}(\boldsymbol{n})(\boldsymbol{n}\otimes\boldsymbol{n}\otimes\boldsymbol{n}\otimes\boldsymbol{n})dS. \tag{A.40}$$

The explicit forms of the orientation averaged Hill basis reads

$$\begin{aligned}
&\mathbb{H}_{\star}^{(1)} = \frac{1}{2}\left[\boldsymbol{I}_2 \otimes \boldsymbol{I}_2 - \boldsymbol{I}_2 \otimes \boldsymbol{\eta}_2 - \boldsymbol{\eta}_2 \otimes \boldsymbol{I}_2 + \boldsymbol{\eta}_4\right], \quad \mathbb{H}_{\star}^{(2)} = \boldsymbol{I}_2 \otimes \boldsymbol{\eta}_2 - \boldsymbol{\eta}_4, \quad \mathbb{H}_{\star}^{(3)} = \boldsymbol{\eta}_2 \otimes \boldsymbol{I}_2 - \boldsymbol{\eta}_4 \\
&\mathbb{H}_{\star}^{(4)} = \boldsymbol{\eta}_4, \quad \mathbb{H}_{\star}^{(5)} = \frac{1}{2}\left[2\boldsymbol{I}_4 - \boldsymbol{\lambda} - \boldsymbol{I}_2 \otimes \boldsymbol{\eta}_2 + \boldsymbol{I}_2 \otimes \boldsymbol{\eta}_2 + \boldsymbol{\eta}_2 \otimes \boldsymbol{I}_2 + \boldsymbol{\eta}_4\right], \quad \mathbb{H}_{\star}^{(6)} = \frac{1}{2}\boldsymbol{\lambda} - 2\boldsymbol{\eta}_4 \\
&\lambda_{ijkl} = (I_2)_{ik}(\eta_2)_{jl} + (\eta_2)_{ik}(I_2)_{jl} + (I_2)_{il}(\eta_2)_{jk} + (\eta_2)_{il}(I_2)_{jk}.
\end{aligned} \tag{A.41}$$

A.6 Orientation tensors for Advani-Tucker law

By Eq.A.40, the orientation tensors in matrix notation corresponding to the Advani-Tucker law for the axisymmetric distribution, can be computed as follows:

$$\boldsymbol{\eta}_2 = \frac{1}{m_{\mathrm{AT}}+3}\begin{bmatrix} m_{\mathrm{AT}}+1 & 0 & 0 \\ 0 & 1 & 0 \\ 0 & 0 & 1 \end{bmatrix}$$

$$\boldsymbol{\eta}_4 = \frac{1}{(m_{\mathrm{AT}}+3)(m_{\mathrm{AT}}+5)}\begin{bmatrix} (m_{\mathrm{AT}}+1)(m_{\mathrm{AT}}+3) & (m_{\mathrm{AT}}+1) & (m_{\mathrm{AT}}+1) & 0 & 0 & 0 \\ (m_{\mathrm{AT}}+1) & 3 & 1 & 0 & 0 & 0 \\ (m_{\mathrm{AT}}+1) & 1 & 3 & 0 & 0 & 0 \\ 0 & 0 & 0 & 1 & 0 & 0 \\ 0 & 0 & 0 & 0 & (m_{\mathrm{AT}}+1) & 0 \\ 0 & 0 & 0 & 0 & 0 & (m_{\mathrm{AT}}+1) \end{bmatrix} \tag{A.42}$$

A.7 Parameters identification

The Laplace-Carson transform of a relaxation moduli tensor $\boldsymbol{L}^*$, gives the steady-state response to a harmonic loading by considering the change of variable $p = j\omega$, with ω being the circular velocity of the harmonic loading [45, 122]. This is why identification methods developed for this kind of harmonic loading (e.g. DMA tests) are implemented to estimate the coefficients of an equivalent Prony-series representing the effective thermo-viscoelastic behavior from the generated data.

Let $m(t)$ be a given relaxation modulus (an element of $\boldsymbol{L}(t)$), and $m^*(p)$ its correspondent Laplace-Carson transform. The identification of the coefficients of $m(t)$ begins with the approximation of the discrete characteristic time distribution. This is achieved by using the Krein-Nudelman method [7]. After this, the associated coefficients are computed from a classic mean-squares procedure. The methodology to approximate Prony-series is presented as follows:

Given the frequency data: $\{\omega_i, \hat{m}_i\}$, with $m_i^* = m_i' + jm_i''$, and its conjugate form $\hat{m}_i$, with $i \in [1, I]$. Find an approximation for τ_n, N_τ and m_n, that are the discrete time distribution and its size, and the coefficients associated to each characteristic time, respectively:

- Build the following square matrices:

$$M_{kl}^1 = j\frac{\hat{m}_k - m_l^*}{\omega_k + \omega_l}, \qquad M_{kl}^2 = \frac{\frac{\hat{m}_k}{\omega_k} + \frac{m_l^*}{\omega_l}}{\omega_k + \omega_l}. \tag{C.1}$$

- Compute the eigenvectors $\boldsymbol{\lambda}^1$ and $\boldsymbol{\lambda}^2$ associated to the null space of $\boldsymbol{M}^1$ and $\boldsymbol{M}^2$, then compute the following two functions:

$$f_1(s) = \sum_{i=1}^{I} \frac{\lambda_i^1}{s + j\omega_i}, \qquad f_2(s) = \sum_{i=1}^{I} \frac{\lambda_i^2}{s + j\omega_i}. \tag{C.2}$$

- Discretize f_1 and f_2 considering s as a frequency variable lying in the same range of $\{\omega_i/2\pi\}$. Then, find numerically the common real positive zeros (s_n) corresponding to the discrete characteristic times of the relaxation modulus $m(t)$:

$$\tau_n = (s_n)^{-1}, \quad n \in [1, N_\tau] \tag{C.3}$$

- Build the following rectangular matrices:

$$A^1_{in} = \frac{(\omega_i \tau_n)^2}{1 + (\omega_i \tau_n)^2}, \qquad A^2_{in} = \frac{\omega_i \tau_n}{1 + (\omega_i \tau_n)^2} \tag{C.4}$$

- The associated moduli are computed by solving the following minimization problem:

$$\{m_n\} = \text{argmin} \left(||\boldsymbol{A}^1.\{m_n\} - \{m'_i\}|| + ||\boldsymbol{A}^2.\{m_n\} - \{m''_i\}|| \right) \tag{C.5}$$

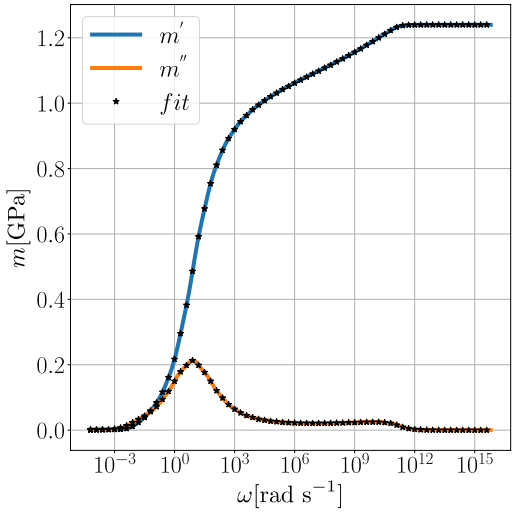

(a) On-plane shear relaxation modulus.

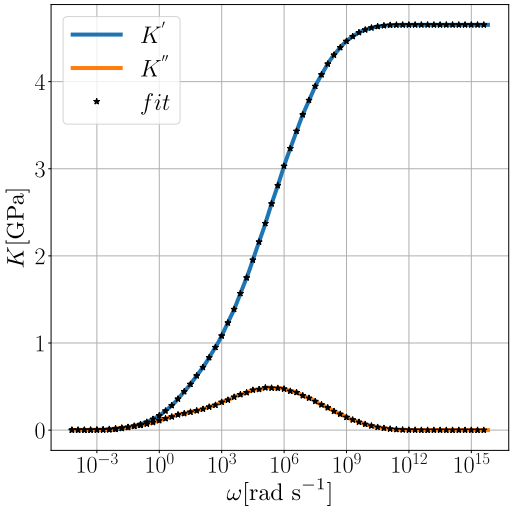

(b) On-plane compressibility relaxation modulus.

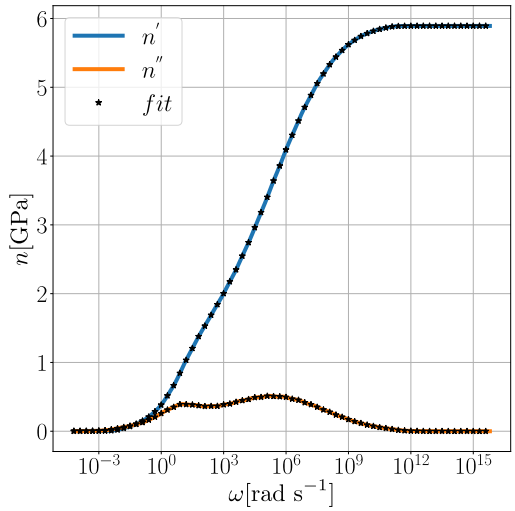

(c) relaxation modulus related with the axial behavior n.

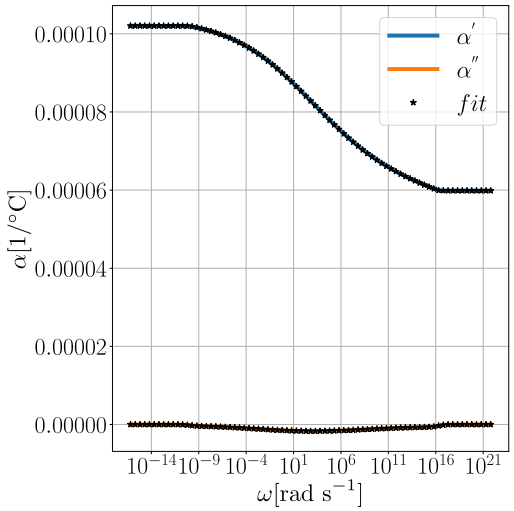

(d) On-plane thermal creep function.

Figure A.1: Identification examples using Krein-Nudelman method.

Appendix B

Formulations

B.1 State equations

The following derivations of a linear theory of thermo-viscoeslasticity are obtained from Suquet 2003 [65] and Christensen 1982 [43] expressed locally for a given point of the continuous medium. Let's start by introducing the first principle of thermodynamics for continuum mechanics, expressed locally and called the local balance of energy equation with time derivatives in Newton's notation:

$$\rho \dot{e} = \boldsymbol{\sigma} \cdot \dot{\boldsymbol{\varepsilon}} - \nabla \cdot \boldsymbol{q}^{th} + r, \tag{C.1}$$

with e the internal energy, $\boldsymbol{\sigma}$ is the second order stress tensor, the heat flux vector $\boldsymbol{q}^{th}$ and an external heat source r, and ∇ the nabla differential operator. Now we write the entropy inequality from the second principle of thermodynamics :

$$\rho T \dot{s} + \nabla \cdot \boldsymbol{q}^{th} - \boldsymbol{q}^{th} \frac{\nabla T}{T} - r \geq 0, \tag{C.2}$$

with s the entropy, and $T > 0$ the positive temperature. Finally, we rewrite this equation by introducing the Helmholtz free energy $w = e - Ts$ and Eq.C.1:

$$\boldsymbol{\sigma} \cdot \dot{\boldsymbol{\varepsilon}} - \rho(\dot{w} + \dot{T}s) - \boldsymbol{q}^{th} \frac{\nabla T}{T} \geq 0. \tag{C.3}$$

As the free energy is not only a functional of the strain history, but the temperature history too, then it can not be considered as a linear functional. For a suitable form of the free energy for a thermo-viscoelastic transformation, we use the form proposed by Christensen. For continuous smooth real functions $\boldsymbol{\varepsilon}(t)$ and $T(t)$, with asymptotic values defined as $\boldsymbol{\varepsilon}(t) \to \mathbf{0}$ and $T(t) \to T_0$ as $t \to -\infty$. Applying the Stone-Weierstrass theorem, a real functional $w(t)$ of $\boldsymbol{\varepsilon}(\tau)$ and $T(\tau)$ $\in -\infty < \tau \leq t$, may be uniformly approximated by a polynomial in a set of real linear continuous functionals. Finally, by means of the Riesz representation theory, the linear functionals are expressed in terms of Stieltjes integrals with bounded integrating functions. Similarly to [5] these functionals are built as it is done in the case of the stress functionals in the isothermal viscoelastic case. Introducing $\theta(t)$ as the instantaneous variation of temperature with respect to a reference state T_0, and assuming infinitesimal variations of $\boldsymbol{\varepsilon}(\tau)$ and $\frac{\theta(t)}{T_0}$, the polynomial expansion to the second order, presented similarly in [166] give the following form with all material properties being causal functions:

$$\rho w = \rho w_0 + \boldsymbol{\sigma}_0 \cdot \boldsymbol{\varepsilon} - \rho s_0 \theta + \frac{1}{2}\mathbb{L} \circledast \boldsymbol{\varepsilon} \circledast \boldsymbol{\varepsilon} - \mathbb{L} \circledast \boldsymbol{\alpha} \circledast \boldsymbol{\varepsilon} \circledast \theta - \frac{1}{2} m \circledast \theta \circledast \theta, \tag{C.4}$$

with w_0 the mean free energy, $\boldsymbol{\sigma}_0$ the initial stress, s_0 the initial entropy, $\mathbb{L}$ the fourth order relaxation tensor, $\boldsymbol{\alpha}$ the second order thermal expansion coefficient tensor and m the heat capacity. By using Eq.C.4 in Eq.C.3, and noting $\dot{\theta}(t) = \dot{T}(t)$, the entropy inequality becomes:

$$(\boldsymbol{\sigma} - \boldsymbol{\sigma}_0 + \mathbb{L} \circledast \boldsymbol{\varepsilon} + \mathbb{L} \circledast \boldsymbol{\alpha} \circledast \theta) \cdot \dot{\boldsymbol{\varepsilon}} + (\rho s - \rho s_0 + \mathbb{L} \circledast \boldsymbol{\alpha} \circledast \boldsymbol{\varepsilon} + m \circledast \theta)\, \dot{\theta} + \phi - \boldsymbol{q}^{th} \frac{\nabla T}{T} \geq 0. \tag{C.5}$$

With ϕ being the dissipation potential. As the above inequality must hold for arbitrary values of $\dot{\boldsymbol{\varepsilon}}$ and $\dot{\theta}$, the terms associated to them in Eq.C.5 must vanish and the inequality takes the following form:

$$\phi - \boldsymbol{q}^{th} \frac{\nabla T}{T} \geq 0, \tag{C.6}$$

with the explicit form of the dissipation potential :

$$\phi = -\frac{1}{2}\dot{\mathbb{L}} \circledast \boldsymbol{\varepsilon} \circledast \boldsymbol{\varepsilon} + \mathbb{L} \dot{\circledast} \boldsymbol{\alpha} \circledast \boldsymbol{\varepsilon} \circledast \theta + \frac{1}{2}\dot{m} \circledast \theta \circledast \theta. \tag{C.7}$$

Now, we introduce a suitable constitutive law for the heat flux $\boldsymbol{q}^{th}$ using the Fourier law of heat conduction in a hereditary form without doing any prior assumption about the form of the second order conductivity tensor $\boldsymbol{\lambda}$:

$$\boldsymbol{q}^{th} = -\boldsymbol{\lambda} \circledast \nabla\theta. \tag{C.8}$$

The constitutive equations of stress and entropy become:

$$\boldsymbol{\sigma} = \boldsymbol{\sigma}_0 + \mathbb{L} \circledast \boldsymbol{\varepsilon} - \mathbb{L} \circledast \boldsymbol{\alpha} \circledast \theta \tag{C.9}$$

$$\rho s = \rho s_0 + \mathbb{L} \circledast \boldsymbol{\alpha} \circledast \boldsymbol{\varepsilon} + m \circledast \theta. \tag{C.10}$$

Considering the last expressions we can rewrite C.1, the balance of energy equation in a suitable form to be integrated in a code, noting that as it is indicated in the linear theory the second order terms are neglected (i.e., the dissipation ϕ takes no role in the balance of energy equation), this expression reads:

$$\rho r - T_0 \frac{\partial}{\partial t}[\mathbb{L} \circledast \boldsymbol{\alpha} \circledast \boldsymbol{\varepsilon} + m \circledast \theta] + \nabla \cdot (\boldsymbol{\lambda} \circledast \nabla T) = 0. \tag{C.11}$$

B.2 Mean-field models

Here, the explicit forms of the localization tensors $\mathbb{A}^{*(r)}$ used in the computation of its distribution averaged form $\mathbb{A}_\star^{*(f)}$ after Eqs. (4.10)-(4.13), are presented. Recalling the explicit form of the latter:

$$\mathbb{A}_\star^{*(f)} = \int_S \int_{w_{min}}^{w_{max}} f_w(w) f_{\boldsymbol{n}}(\boldsymbol{n}) \mathbb{A}^{(r)}(w, \boldsymbol{n}) dw dS \tag{C.12}$$

Localization tensors for the implemented mean-field schemes:

All mean-fields approximations are based on Eshelby's equivalent inclusion method, whose results and notations are summarized. Consider an ellipsoidal domain $\Omega^{(r)}$ embedded in an infinite matrix with elastic tensor $\boldsymbol{L}^{(\mathrm{m})}$, supporting a constant internal stress (or *polarization*) $\boldsymbol{\tau}$ so that

the total stress is $\boldsymbol{\sigma}^{(r)} = \mathbb{L}^{(\mathrm{m})} : \boldsymbol{\varepsilon}^{(r)} + \tau$, where $\boldsymbol{\varepsilon}^{(r)}$ is the total strain inside the inclusion. Then this strain is found to be constant and equal to:

$$\boldsymbol{\varepsilon}^{(r)} = -\mathbb{P}_0^{(r)} : \boldsymbol{\tau} \tag{C.13}$$

where $\mathbb{P}_0^{(r)}$ is *Hill's tensor*, and depends on the matrix moduli and the inclusion's shape. Now consider that the domain $\Omega^{(r)}$ supports an *inhomogeneity* characterized by the elastic tensor $\mathbb{L}^{(r)}$, and is submitted to a strain field $\boldsymbol{\varepsilon}_0$ uniform at infinity. Then, writing $\boldsymbol{\sigma}^{(r)} = \mathbb{L}^{(r)} : \boldsymbol{\varepsilon}^{(r)} = \mathbb{L}^{(\mathrm{m})} : \boldsymbol{\varepsilon}^{(r)} + (\mathbb{L}^{(r)} - \mathbb{L}^{(\mathrm{m})}) : \boldsymbol{\varepsilon}^{(r)}$, i.e. introducing the polarization $\boldsymbol{\tau} = (\mathbb{L}^{(r)} - \mathbb{L}^{(\mathrm{m})}) : \boldsymbol{\varepsilon}^{(r)}$, applying the previous formula (C.13) one obtains by superposition

$$\boldsymbol{\varepsilon}^{(r)} = \boldsymbol{\varepsilon}_0 - \mathbb{P}_0^{(r)} : (\mathbb{L}^{(r)} - \mathbb{L}^{(\mathrm{m})}) : \boldsymbol{\varepsilon}^{(r)} \tag{C.14}$$

and finally,

$$\boldsymbol{\varepsilon}^{(r)} = \mathbb{A}_0^{(r)} : \boldsymbol{\varepsilon}_0, \qquad \mathbb{A}_0^{(r)} = \left[\mathbb{I} + \mathbb{P}_0^{(r)} : (\mathbb{L}^{(r)} - \mathbb{L}^{(\mathrm{m})})\right]^{-1}. \tag{C.15}$$

where $\mathbb{A}_0^{(r)}$ is the *localization tensor* of the inclusion $\Omega^{(r)}$ embedded in the matrix $\mathbb{L}_0$. Both Hill and localization tensors' expressions are given in [46] for a wide variety of inclusion shapes. The localization tensor $\mathbb{A}_0^{(r)}$ is used in the dilute approximation, or Eshelby's model, valid only for very low volume fractions of inclusions where interactions between inclusions are negligible. For higher volume fractions, these interactions must be accounted for, as proposed by various authors.

Mori–Tanaka (MT) model: As reformulated by [116], in this model the mean inclusion strain is linked to the mean matrix strain (rather than the total mean strain) through Eshelby's method. This results in the following localization tensor:

$$\mathbb{A}_{\mathrm{MT}}^{(r)} = \mathbb{A}_0^{(r)} : \left[(1 - \sum_{r=2}^{R} c^{(r)})\mathbb{I} + \sum_{r=2}^{R} c^{(r)}\mathbb{A}_0^{(r)}\right]^{-1}, \tag{C.16}$$

where $c^{(r)}$ is the inclusion's volume fraction.

Lielens' model: This model, introduced in [117], results from an interpolation between two bounds of the effective properties: (i) the lower Hashin and Shtrikman bound (corresponding to the MT model), and (ii) an upper bound, obtained by inverting the properties and geometries of matrix and fibers. The resulting localization tensor is:

$$\mathbb{A}_{\text{Lie}}^{(r)} = \overline{\mathbb{A}}^{(r)} : \left[(1-\sum_{r=2}^{R} c^{(r)})\mathbb{I}+\sum_{r=2}^{R} c^{(r)}\overline{\mathbb{A}}^{(r)}\right]^{-1}, \text{ where } \overline{\mathbb{A}}^{(r)} = \left[(1-\eta_L)\left[\mathbb{A}_0^{(r)}\right]^{-1} + \eta_L\left[\mathbb{A}_{\text{inv}}^{(r)}\right]^{-1}\right]^{-1}, \tag{C.17}$$

where $\mathbb{A}_{\text{inv}}^{(r)}$ is the tensor given by Eq. (C.15) by inverting the matrix' and inclusion properties, and η_L being the interpolation factor depending on the volume fraction. Lielens proposes to use:

$$\eta_L = \frac{1}{2}c^{(r)}(1+c^{(r)}), \tag{C.18}$$

a choice that was validated by subsequent studies.

Interaction direct derivative (IDD) model: This model, introduced by [119, 118], comes from a double inclusion approach whereas a micromechanical analysis is performed by considering a matrix cell $\Omega_D^{(r)}$ of ellipsoidal geometry surrounding each inclusion $\Omega^{(r)}$, itself surrounded by the effective medium. After some simplifications, the resulting concentration tensor for an inclusion is:

$$\mathbb{A}_{\text{IDD}}^{(r)} = \mathbb{A}_0^{(r)} : \left[\mathbb{I} - \sum_{r=2}^{R} c^{(r)}\mathbb{P}_0^{(\text{D},r)} : (\mathbb{L}^{(r)} - \mathbb{L}^{(\text{m})}) : \mathbb{A}_0^{(r)}\right]^{-1}, \tag{C.19}$$

As pointed out by [119] and recently recalled by [109], the IDD model is in fact a general formulation that embeds (i) the MT model when each cell has the same geometry as its related inclusion (i.e. $\mathbb{P}_0^{(\text{D},r)} = \mathbb{P}_0^{(r)}$), and (ii) the Ponte-Castañeda and Willis (PCW) model from [167] when all cells are identical and their shape characterizes the distribution of inclusions' centers (i.e. $\mathbb{P}_0^{(\text{D},r)} = \mathbb{P}_0^{(\text{D})}$).

Appendix C

Material properties

C.1 Coefficients Prony series PEI

Shear asymptotic modulus: $\mu_\infty = 2.15144\text{E}-3$[GPa]

$\tau^{(s)}$[s]	$\mu^{(s)}$[GPa]	$\tau^{(s)}$[s]	$\mu^{(s)}$[GPa]
$1.86106\text{E}-16$	$5.50504\text{E}-3$	$1.60598\text{E}-5$	$1.09662\text{E}-2$
$2.65620\text{E}-15$	$2.72850\text{E}-2$	$3.22285\text{E}-5$	$6.54471\text{E}-2$
$2.70558\text{E}-14$	$2.18342\text{E}-2$	$6.85867\text{E}-5$	$1.62457\text{E}-3$
$1.42154\text{E}-13$	$1.73939\text{E}-2$	$2.17260\text{E}-4$	$3.02228\text{E}-2$
$8.59014\text{E}-13$	$2.06096\text{E}-2$	$5.43851\text{E}-4$	$8.85832\text{E}-2$
$5.18800\text{E}-12$	$1.99604\text{E}-2$	$1.15473\text{E}-3$	$6.12456\text{E}-3$
$1.28381\text{E}-11$	$7.59394\text{E}-2$	$3.27703\text{E}-3$	$1.33240\text{E}-2$
$3.85035\text{E}-11$	$1.91562\text{E}-3$	$6.64477\text{E}-3$	$1.22330\text{E}-2$
$1.20921\text{E}-10$	$1.32797\text{E}-2$	$2.99903\text{E}-2$	$1.57701\text{E}-1$
$3.73680\text{E}-10$	$2.20416\text{E}-2$	$7.03850\text{E}-2$	$1.00220\text{E}-1$
$9.81748\text{E}-10$	$9.86862\text{E}-2$	$1.41247\text{E}-1$	$1.39123\text{E}-1$
$2.08930\text{E}-9$	$2.42285\text{E}-3$	$2.98868\text{E}-1$	$5.97401\text{E}-2$
$4.81393\text{E}-9$	$1.17004\text{E}-2$	$5.89495\text{E}-1$	$2.14813\text{E}-1$
$1.28086\text{E}-8$	$2.62035\text{E}-2$	$2.75728\text{E}+0$	$7.07200\text{E}-2$
$5.93937\text{E}-8$	$2.80566\text{E}-2$	$3.76461\text{E}+1$	$4.31203\text{E}-3$
$2.55706\text{E}-7$	$2.05670\text{E}-2$	$4.58902\text{E}+2$	$1.67077\text{E}-3$
$1.01681\text{E}-6$	$1.67201\text{E}-2$	$4.40271\text{E}+3$	$1.09030\text{E}-3$
$4.51066\text{E}-6$	$1.51982\text{E}-2$	$1.62263\text{E}+4$	$3.35492\text{E}-4$

Tensile asymptotic modulus: $E_\infty = 5.47523\text{E}-5[\text{GPa}]$

$\tau^{(s)}$[s]	$E^{(s)}$[GPa]	$\tau^{(s)}$[s]	$E^{(s)}$[GPa]
$1.33536\text{E}-7$	$6.96934\text{E}-1$	$1.46363\text{E}-1$	$2.19751\text{E}-1$
$2.74057\text{E}-6$	$2.54842\text{E}-1$	$3.93581\text{E}-1$	$2.46437\text{E}-1$
$1.89461\text{E}-5$	$3.30656\text{E}-1$	$6.60085\text{E}-1$	$1.27470\text{E}-1$
$5.32907\text{E}-5$	$1.69354\text{E}-1$	$2.43162\text{E}+0$	$5.43388\text{E}-2$
$1.46561\text{E}-4$	$2.84952\text{E}-1$	$2.03044\text{E}+1$	$1.36716\text{E}-2$
$3.50631\text{E}-4$	$1.54908\text{E}-1$	$1.24321\text{E}+2$	$2.86498\text{E}-3$
$9.42875\text{E}-4$	$4.23297\text{E}-1$	$2.68082\text{E}+3$	$2.59890\text{E}-3$
$2.65207\text{E}-3$	$1.88516\text{E}-1$	$2.00954\text{E}+4$	$2.22848\text{E}-3$
$6.78747\text{E}-3$	$4.00527\text{E}-1$	$1.25839\text{E}+5$	$1.89358\text{E}-3$
$1.74495\text{E}-2$	$2.77064\text{E}-1$	$6.61267\text{E}+5$	$3.93338\text{E}-4$
$4.95245\text{E}-2$	$3.98659\text{E}-1$	$4.35087\text{E}+6$	$3.08895\text{E}-5$

C.2 Material properties: Study of the effective properties of the microscale

Fibers' mechanical properties are assumed to be constant: $\kappa = 39.733$[GPa], $\mu = 29.05$[GPa] and

$\alpha = 2.21\text{E}-5[1/^\circ\text{C}]$.

Matrix coefficients for the reference master-curves are presented below:

Glassy moduli: $\kappa_g = 4.23879$[GPa], $\mu_g = 1.23968$[GPa]

$\tau^{(u)}$[s]	$\kappa^{(u)}$[GPa]	$\mu^{(u)}$[GPa]
1.4211E − 11	0.0284181	0.0284181
7.2697E − 11	0.0341941	0.0273223
3.7188E − 10	0.0920182	0.0255737
1.9024E − 9	0.172648	0.0237469
9.7315E − 9	0.268286	0.0222851
4.9782E − 8	0.366893	0.0214578
2.5466E − 7	0.452075	0.0214489
1.3027E − 6	0.505714	0.0224768
6.6640E − 6	0.514237	0.0249357
3.4089E − 5	0.47587	0.0296341
1.7439E − 4	0.402704	0.0383457
8.9208E − 4	0.314523	0.055318
4.5634E − 3	0.229389	0.0917189
0.0233442	0.158053	0.174055
0.119418	0.103904	0.274284
0.610883	0.0656627	0.187685
3.12498	0.040106	0.0904041
15.9858	0.0237646	0.0485919
81.7757	0.0136966	0.0302413

Glassy modulus: $\alpha_g = 5.98536\text{E}-5[1/^\circ\text{C}]$

$\tau^{(s)}$[s]	$\alpha^{(s)}$[1/°C]	$\tau^{(s)}$[s]	$\alpha^{(s)}$[1/°C]
1.09402E − 16	6.43788E − 7	1.48477E − 3	1.63691E − 6
4.96202E − 16	6.54383E − 7	6.73427E − 3	1.62182E − 6
2.25056E − 15	6.74554E − 7	3.05438E − 2	1.59023E − 6
1.02075E − 14	7.03568E − 7	1.38533E − 1	1.54303E − 6
4.62970E − 14	7.40899E − 7	6.28327E − 1	1.48174E − 6
2.09983E − 13	7.86106E − 7	2.84982	1.40840E − 6
9.52393E − 13	8.38741E − 7	12.9255	1.32544E − 6
4.31964E − 12	8.98259E − 7	58.6247	1.23550E − 6
1.95920E − 11	9.63950E − 7	265.896	1.14129E − 6
8.88601E − 11	1.03487E − 6	1205.99	1.04541E − 6
4.03035E − 10	1.10980E − 6	5469.85	9.50225E − 7
1.82799E − 9	1.18721E − 6	24808.9	8.57797E − 7
8.29098E − 9	1.26525E − 6	112522	7.69789E − 7
3.76043E − 8	1.34181E − 6	510353	6.87463E − 7
1.70557E − 7	1.41451E − 6	2.31474E + 6	6.11684E − 7
7.73572E − 7	1.48087E − 6	1.04987E + 7	5.42952E − 7
3.50859E − 6	1.53837E − 6	4.76174E + 7	4.81461E − 7
1.59134E − 5	1.58461E − 6	2.15972E + 8	4.27147E − 7
7.21765E − 5	1.61749E − 6	9.79554E + 8	3.79766E − 7
3.27361E − 4	1.63530E − 6	4.44283E + 9	3.38943E − 7

Appendix D

Scripts

D.1 MFTVEH_Pkg : Mathematica package for mean-field Homogenization of thermo-viscoelastic SPC composites

D.2 Linear Thermo-viscoelasticity: Abaqus subroutines

Bibliography

[1] Michel Bornert, T. Bretheau, and P. Gilormini. Homogénéisation en mécanique des matériaux Tome 1. Hermes science, 2001.

[2] Toshio Mura. "Micromechanics of defects in solids". In: 3 (1987).

[3] Graeme W Milton. The theory of composites. Cambridge University Press, May 2002, p. 748. ISBN: ISBN 0521781256.

[4] C. A. Suarez-Afanador et al. "Effective thermo-viscoelastic behavior of short fiber reinforced thermo-rheologically simple polymers: An application to high temperature fiber reinforced additive manufacturing." In: Eur. J. Mech. A Solids. 1.2 (2022), p. 18.

[5] J. Mandel. Cours de Mécanique des milieux continus. Gauthier–Villars, 1966.

[6] Camilo A. Suarez-Afanador, Noel Lahellec, and Martín I. Idiart. "Mean-field descriptions for the viscoelastic response of thermorheologically complex reinforced solids". In: Eur. J. Mech. A Solids. 98 (2023), p. 104859. ISSN: 0997-7538.

[7] D. Jalocha, A. Constantinescu, and R. Neviere. "Revisiting the identification of generalized Maxwell models from experimental results". In: Int. J. Solids. Struct. 67-68 (2015), pp. 169–181. ISSN: 0020-7683.

[8] Camilo Suarez Afanador et al. "Mean-Field Approximations in Effective Thermo-viscoelastic Behavior for Composite Parts Obtained via Fused Deposition Modeling Technology". In: AIP Conference Proceedings 2425 (1 Apr. 2022).

[9] Abid Haleem, Mohd Javaid, and Shanay Rab. "Impact of additive manufacturing in different areas of Industry 4.0". In: Int. J. Logist. Syst. Manag. 37 (2020), pp. 239–251.

[10] Jian-Yuan Lee, Jia An, and Chee Kai Chua. "Fundamentals and applications of 3D printing for novel materials". In: Appl. Mater. Today. 7 (2017), pp. 120–133.

[11] Arit Das et al. "Current understanding and challenges in high temperature additive manufacturing of engineering thermoplastic polymers". In: Additive Manufacturing 34 (2020), p. 101218.

[12] Hideo Kodama. "Automatic method for fabricating a three-dimensional plastic model with photo-hardening polymer". In: Rev. Sci. Instrum. 52.11 (1981), pp. 1770–1773.

[13] HULL C. W. "Apparatus for Production of Three-Dimensional Objects by Stereolithography". In: USA Patent, Appl., No. 638905, Filed (1984).

[14] Wikipedia contributors. Self-replicating machine — Wikipedia, The Free Encyclopedia. [Online; accessed 26-March-2023]. 2023.

[15] Kwang-Hee Cheon et al. "Construction of tantalum/poly(ether imide) coatings on magnesium implants with both corrosion protection and osseointegration properties". In: Bioact. Mater. 6.4 (2021), pp. 1189–1200. ISSN: 2452-199X.

[16] Amit Lopes, Eric Macdonald, and Ryan Wicker. "Integrating Stereolithography and Direct Print Technologies for 3D Structural Electronics Fabrication". In: Rapid Prototyp. J. 18 (Mar. 2012), pp. 129–143.

[17] Chad E. Duty et al. "Structure and mechanical behavior of Big Area Additive Manufacturing (BAAM) materials". In: Rapid Prototyp. J. 23.1355-2546 (2017), pp. 181–189.

[18] Nurul Amira Binti Nordin et al. In: 226.1 (Aug. 2017), p. 012176.

[19] Guo Dong Goh et al. "Recent Progress in Additive Manufacturing of Fiber Reinforced Polymer Composite". In: Adv. Mater. Technol. 4 (2019), p. 1800271.

[20] Pedram Parandoush and Dong Lin. "A review on additive manufacturing of polymer-fiber composites". In: Compos. Struct. 182 (2017), pp. 36–53.

[21] John Ryan C. Dizon et al. "Mechanical characterization of 3D-printed polymers". In: Addit. Manuf. 20 (2018), pp. 44–67.

[22] Guoguang Chen et al. "Simulating and Predicting the Part Warping in Fused Deposition Modeling by Thermal-Structural Coupling Analysis". In: 3D Print. Addit. Manuf. (2021).

[23] Patricia P Parlevliet, Harald EN Bersee, and Adriaan Beukers. "Residual stresses in thermoplastic composites—A study of the literature—Part I: Formation of residual stresses". In: Compos. Part A Appl. Sci. 37.11 (2006), pp. 1847–1857.

[24] E-Xstream. Digimat Software for additive manufacturing. Dec. 2021.

[25] DassaultSystèmes. 3DS Simulia simulation pour la fabrication additive. Dec. 2021.

[26] Maurice A. Biot. Mechanics of incremental deformations. Wiley, 1965.

[27] P Sreejith, K Kannan, and KR Rajagopal. "A thermodynamic framework for additive manufacturing, using amorphous polymers, capable of predicting residual stress, warpage and shrinkage". In: Int. J. Eng. Sci. 159 (2021), p. 103412.

[28] J. Oliver et al. "Reduced order modeling strategies for computational multiscale fracture". In: Comput. Methods Appl. Mech. Eng. 313 (2017), pp. 560–595. ISSN: 0045-7825.

[29] Todd Arbogast. Numerical Analysis of Multiscale Problems. Springer Berlin Heidelberg, 2012.

[30] "A class of simple solids with fading memory". In: Int. J. Eng. Sci. 7 (12 Dec. 1969), pp. 1173–1198. ISSN: 0020-7225.

[31] Ronald L. Bagley. "The thermorheologically complex material." In: J. Acoust. Soc. Am 90 (4 Oct. 1991), pp. 2292–2293.

[32] James Clerk Maxwell. "IV. On the dynamical theory of gases". In: Philos. Trans. R. Soc. A 157 (1867), pp. 49–88.

[33] W. Voigt. "Ueber die Beziehung zwischen den beiden Elasticitätsconstanten isotroper Körper". In: Ann. Phys. 274.12 (1889), pp. 573–587.

[34] Clarence Zener. "Theory of the Elasticity of Polycrystals with Viscous Grain Boundaries". In: Phys. Rev. 60 (12 Dec. 1941), pp. 906–908.

[35] B. GROSS and E. L. da FONSECA. Mathematical structure of the theories of viscoelasticity. Actualités Scientifiques et Industrielles, 1953.

[36] R. L. Bagley and P. J. Torvik. "A Theoretical Basis for the Application of Fractional Calculus to Viscoelasticity". In: J. Rheol. 27.3 (1983), pp. 201–210.

[37] Malcolm L. Williams, Robert F. Landel, and John D. Ferry. "The Temperature Dependence of Relaxation Mechanisms in Amorphous Polymers and Other Glass-forming Liquids". In: J. Am. Chem. Soc. 77.17 (1955), pp. 3701–3707.

[38] M A Biot. "Linear thermodynamics and the mechanic of solids". In: (June 1958).

[39] S. C. Hunter. "Tentative equations for the propagation of stress, strain, and temperature fields in viscoelastic solids". In: J. Mech. Phys. Solids 9 (1 Feb. 1961), pp. 39–51. ISSN: 0022-5096.

[40] R. A. Schapery. "Application of Thermodynamics to Thermomechanical, Fracture, and Birefringent Phenomena in Viscoelastic Media". In: Journal of Applied Physics 35 (5 July 1964), p. 1451. ISSN: 0021-8979.

[41] R. M. Christensen and P. M. Naghdi. "Linear non-isothermal viscoelastic solids". In: Acta Mechanica 3 (1 Mar. 1967), pp. 1–12. ISSN: 00015970.

[42] "Linearized thermoviscoelasticity with high temperature variations and related periodic problems". In: Int. J. Eng. Sci. 16.10 (1978), pp. 681–705.

[43] R. M. Christensen. Theory of viscoelasticity. Dover Publications Inc., 1982.

[44] Jean Salençon. Viscoelastic modeling for structural analysis. Wiley, 2019.

[45] D. Gutierrez-Lemini. Engineering viscoelasticity. Springer, 2014.

[46] Parnell William J. "The Eshelby, Hill, Moment and Concentration Tensors for Ellipsoidal Inhomogeneities in the Newtonian Potential Problem and Linear Elastostatics". In: J. Elast. 125 (2016), pp. 231–294.

[47] A. J. Kovacs. "Transition vitreuse dans les polymères amorphes. Etude phénoménologique". In: Fortschritte Der Hochpolymeren-Forschung. Berlin, Heidelberg: Springer Berlin Heidelberg, 1964, pp. 394–507. ISBN: 978-3-540-37073-4.

[48] A. J. Kovacs et al. "Isobaric volume and enthalpy recovery of glasses. II A transparent multiparameter theory." In: J. Polym. Sci. B Polym. Phys. 34 (1979).

[49] W.G. Knauss and I.J. Emri. "Non-linear viscoelasticity based on free volume consideration". In: Computers Structures 13.1 (1981), pp. 123–128. ISSN: 0045-7949.

[50] W. G. Knauss and I. Emri. "Volume change and the nonlinearly thermo-viscoelastic constitution of polymers". In: Polym. Eng. Sci. 27.1 (1987), pp. 86–100.

[51] Ba Nghiep Nguyen et al. "Fiber Length and Orientation in Long-Fiber Injection-Molded Thermoplastics — Part I: Modeling of Microstructure and Elastic Properties". In: J. Compos. Mater. 42.10 (2008), pp. 1003–1029.

[52] Thao. D. Nguyen et al. "Modeling the Relaxation Mechanisms of Amorphous Shape Memory Polymers". In: Adv. Mater. 22.31 (2010), pp. 3411–3423.

[53] Xiang Chen and Thao. D. Nguyen. "Influence of thermoviscoelastic properties and loading conditions on the recovery performance of shape memory polymers". In: Mech. Mater. 43.3 (2011), pp. 127–138. ISSN: 0167-6636.

[54] M. J. Crochet and P. M. Naghdi. "On 'Thermo-Rheologically Simple' Solids". In: Thermoinelasticity. Ed. by Bruno A. Boley. Vienna: Springer Vienna, 1970, pp. 59–86.

[55] R. D. Andrews and A. V. Tobolsky. "Elastoviscous properties of polyisobutylene. IV. Relaxation time spectrum and calculation of bulk viscosity". In: J. Polym. Sci. 7.2-3 (1951), pp. 221–242.

[56] H. Leaderman. "Elastic and Creep Properties of Filamentous Materials and Other High Polymers". In: Textile Foundation, Washington, D.C (1943), p. 175.

[57] John D. Ferry. “Mechanical Properties of Substances of High Molecular Weight. VI. Dispersion in Concentrated Polymer Solutions and its Dependence on Temperature and Concentration”. In: J. Am. Chem. Soc. 72 (1950), pp. 3746–3752.

[58] Robert L. Taylor, Karl S. Pister, and Gerald L. Goudreau. “Thermomechanical analysis of viscoelastic solids”. In: Int. J. Numer. Methods. Eng. 2.1 (1970), pp. 45–59.

[59] Zvi Hashin. “Viscoelastic Behavior of Heterogeneous Media”. In: J. Appl. Mech. 32.3 (Sept. 1965), pp. 630–636.

[60] Jean-Marc Ricaud and Renaud Masson. “Effective properties of linear viscoelastic heterogeneous media: Internal variables formulation and extension to ageing behaviours”. In: Int J Solids Struct 46.7 (2009), pp. 1599–1606. ISSN: 0020-7683.

[61] J. Hristov. “Response functions in linear viscoelastic constitutive equations and related fractional operators”. In: J. EMath. Model. Nat. Phenom. 14 (2019).

[62] Yonggang Shangguan et al. “New Insight into Time-Temperature Correlation for Polymer Relaxations Ranging from Secondary Relaxation to Terminal Flow: Application of a Universal and Developed WLF Equation”. In: Polymers 9.11 (2017). ISSN: 2073-4360.

[63] Arthur Q Tool. “Viscosity and the Extraordinary Heat Effects in Glass”. In: (1946).

[64] Habibou Maitournam. “Matériaux et structures anélastiques”. In: (2006).

[65] Pierre. Suquet. “Rupture et plasticité”. In: (2003).

[66] J. Belana et al. “Physical ageing studies in polyetherimide ULTEM 1000”. In: Polym. Int. 46.1 (1998), pp. 29–32.

[67] Musa Yilmaz, Necip Fazil Yilmaz, and Mahmut Furkan Kalkan. “Rheology, Crystallinity, and Mechanical Investigation of Interlayer Adhesion Strength by Thermal Annealing of Polyetherimide (PEI/ULTEM 1010) Parts Produced by 3D Printing”. In: J. Mater. Eng. 31 (12 Dec. 2022), pp. 9900–9909.

[68] Pu Han et al. “An approach to improve interface healing in FFF-3D printed Ultem 1010 using laser pre-deposition heating”. In: Procedia Manufacturing 34 (Jan. 2019), pp. 672–677.

[69] “Fabrication and Characterization of Polyetherimide Electrospun Scaffolds Modified with Graphene Nano-Platelets and Hydroxyapatite Nano-Particles”. In: Int. J. Mol. Sci. 21 (2 Jan. 2020), p. 583.

[70] J. E. Harris and L. M. Robeson. “Miscible blends of poly(aryl ether ketone)s and polyetherimides”. In: J. Appl. Polym. Sci. 35.7 (1988), pp. 1877–1891. (Visited on 05/27/2016).

[71] Andy Goodwin and Robert Marsh. “Dielectric and dynamic mechanical relaxation of poly(ether ether ketone)/poly(etherimide) blends below the glass transition”. In: Macromol Rapid Comm 17.7 (1996), pp. 475–480.

[72] Laurence W. McKeen. “The Effect of Creep and Other Time Related Factors on Plastics and Elastomers”. In: Elsevier (2009), pp. 373–381.

[73] Albrto Schiraldi. “Comparison between WLF and VTF expressions and related physical meaning”. In: Amorphous Food and Pharmaceutical Systems. Ed. by Harry Levine. Cambridge: R. Soc. Chem., 2002, pp. 131–136.

[74] J.J. Fontanella et al. “Effect of pressure on the water relaxation in glassy polyetherimide”. In: J. Non-Cryst. Solids 353.47-51 (2007), pp. 4528–4532.

[75] F Biddlestone et al. “The relaxation spectrum and physical ageing of polyetherimide”. In: Polymer 32.17 (1991), pp. 3119–3125.

[76] Sindee L. Simon et al. “Physical aging of a polyetherimide: Volume recovery and its comparison to creep and enthalpy measurements”. In: J. Polym. Sci. B: Polym. Phys. 35.6 (1997), pp. 929–936.

[77] N. M. Alves et al. “Viscoelastic Behavior of Poly(methyl methacrylate) Networks with Different Cross-Linking Degrees”. In: Macromolecules 37.10 (2004), pp. 3735–3744.

[78] Bernhard Wunderlich. Thermal analysis of polymeric materials. Berlin Heidelberg: Springer, 2005.

[79] R. Greiner and F. R. Schwarzl. “Thermal contraction and volume relaxation of amorphous polymers”. In: Rheologica Acta 23 (4 July 1984), pp. 378–395.

[80] M. G. Krein and A. A. Nudelman. “An interpolation problem in the class of stieltjes functions and its connection with other problems”. In: Integral Equ. Oper. Theory 30.3 (1998), pp. 251–278.

[81] J. Honerkamp and J. Weese. “Tikhonovs regularization method for ill-posed problems”. In: Contin. Mech. Thermodyn. 2.1 (1990), pp. 17–30.

[82] A. Einstein. “Über die von der molekularkinetischen Theorie der Wärme geforderte Bewegung von in ruhenden Flüssigkeiten suspendierten Teilchen”. In: Annalen der Physik 322.8 (1905), pp. 549–560.

[83] M. von Smoluchowski. “Zur kinetischen Theorie der Brownschen Molekularbewegung und der Suspensionen”. In: Annalen der Physik 326.14 (1906), pp. 756–780.

[84] John Douglas Eshelby and Rudolf Ernst Peierls. “The determination of the elastic field of an ellipsoidal inclusion, and related problems”. In: Proc. R. Soc. 241.1226 (1957), pp. 376–396.

[85] “Elastic properties of reinforced solids: Some theoretical principles”. In: J. Mech. Phys. Solids 11 (5 Sept. 1963), pp. 357–372.

[86] Zvi Hashin. “The Elastic Moduli of Heterogeneous Materials”. In: J. Appl. Mech. 29 (1 Mar. 1962), pp. 143–150.

[87] Z. Hashin and S. Shtrikman. “A variational approach to the theory of the elastic behaviour of polycrystals”. In: J. Mech. Phys. Solids 10.4 (1962), pp. 343–352.

[88] Ekkehart Kröner. “Statistical Continuum Mechanics”. In: 92 (1971). DOI: 10.1007/978-3-7091-2862-6.

[89] J. R. Willis. “Variational and Related Methods for the Overall Properties of Composites”. In: Adv. Appl. Mech. 21 (C Jan. 1981), pp. 1–78.

[90] J.R. WILLIS. “Elasticity Theory of Composites”. In: Mechanics of Solids (Jan. 1982), pp. 653–686.

[91] J.R. Willis. “Bounds and self-consistent estimates for the overall properties of anisotropic composites”. In: J. Mech. Phys. Solids. 25.3 (1977), pp. 185–202. ISSN: 0022-5096.

[92] Pierre Suquet. “Elements of homogenization for inelastic solid mechanics”. In: (1985).

[93] E. Sanchez-Palencia. “Non-Homogeneous Media and Vibration Theory”. In: (1980).

[94] H. Moulinec and P. Suquet. “A fast numerical method for computing the linear and nonlinear mechanical properties of composites”. In: Comptes rendus de l’Academie des sciences. Serie II. 318.11 (1994), pp. 1417–1423.

[95] H. Moulinec and P. Suquet. “A numerical method for computing the overall response of nonlinear composites with complex microstructure”. In: Comput. Methods. Appl. Mech. Eng. 157.1 (1998), pp. 69–94. ISSN: 0045-7825.

[96] J. Dirrenberger, S. Forest, and D. Jeulin. “Towards gigantic RVE sizes for 3D stochastic fibrous networks”. en. In: Int. J Solids Struct. 51.2 (Jan. 2014), pp. 359–376. ISSN: 00207683.

[97] Boris Burgarella et al. “Effective viscoelastic behavior of short fibers composites using virtual DMA experiments”. In: Mech. Time Depend. Mater. 23.3 (2019), pp. 337–360.

[98] Boris Burgarella et al. “Modeling the effective viscoelastic properties of PEEK matrix reinforced by arbitrary oriented short glass fibers”. In: Mech. Time Depend. Mater. (2020), pp. 1–29.

[99] R. Masson and A. Zaoui. “Self-consistent estimates for the rate-dependentelastoplastic behaviour of polycrystalline materials”. en. In: J Mech. Phys. Solids 47.7 (June 1999), pp. 1543–1568. ISSN: 00225096. (Visited on 03/20/2017).

[100] Y. Rougier, C. Stolz, and A. Zaoui. “Spectral analysis of linear viscoelastic inhomogeneous materials”. In: Comptes rendus de l’Académie des sciences. Série II 316.11 (1993), pp. 1517–1522.

[101] R.M. Christensen and K.H. Lo. “Solutions for effective shear properties in three phase sphere and cylinder models”. In: J. Mech. Phys. Solids 27 (4 Aug. 1979), pp. 315–330.

[102] T. Mori and K. Tanaka. “Average stress in matrix and average elastic energy of materials with misfitting inclusions”. In: Acta Metallurgica 21 (5 May 1973), pp. 571–574. ISSN: 0001-6160. DOI: 10.1016/0001-6160(73)90064-3.

[103] G. P. Tandon and G. J. Weng. “The effect of aspect ratio of inclusions on the elastic properties of unidirectionally aligned composites”. In: Polym. Compos. 5 (4 1984), pp. 327–333.

[104] Y. Benveniste. “A new approach to the application of Mori-Tanaka’s theory in composite materials”. In: Mech. Mater. 6 (2 June 1987), pp. 147–157.

[105] S. Kammoun et al. “Micromechanical modeling of the progressive failure in short glass–fiber reinforced thermoplastics – First Pseudo-Grain Damage model”. en. In: Compos. Part A Appl. Sci. 73 (June 2015), pp. 166–175. ISSN: 1359835X.

[106] Nicolas Despringre et al. “Micromechanical modeling of damage and load transfer in particulate composites with partially debonded interface”. en. In: Compos. Struct. 155 (Nov. 2016), pp. 77–88. ISSN: 02638223. (Visited on 03/20/2017).

[107] Martin Lévesque et al. “Numerical inversion of the Laplace–Carson transform applied to homogenization of randomly reinforced linear viscoelastic media”. en. In: Comput. Mech. 40.4 (June 2007), pp. 771–789. ISSN: 0178-7675, 1432-0924. (Visited on 03/20/2017).

[108] Ankit Gupta et al. “Homogenized modeling approach for effective property prediction of 3D-printed short fibers reinforced polymer matrix composite material”. In: Int. J. Adv. Manuf. (2021), pp. 1–18.

[109] Patrick Arthur Hessman et al. “On mean field homogenization schemes for short fiber reinforced composites: Unified formulation, application and benchmark”. In: Int. J. Solids. Struct. 230-231 (2021), p. 111141. ISSN: 0020-7683.

[110] Suresh G. Advani and Charles L. Tucker. “The Use of Tensors to Describe and Predict Fiber Orientation in Short Fiber Composites”. In: J. Rheol. 31.8 (1987), pp. 751–784.

[111] Anastasia H Muliana. “A micromechanical model for predicting thermal properties and thermo-viscoelastic responses of functionally graded materials”. In: Int. J Solids Struct. 46.9 (2009), pp. 1911–1924.

[112] Noël Lahellec and Pierre Suquet. "Effective response and field statistics in elasto-plastic and elasto-viscoplastic composites under radial and non-radial loadings". en. In: Int. J. Plast. 42 (Mar. 2013), pp. 1–30. ISSN: 07496419.

[113] L. Brassart et al. "Homogenization of elasto-(visco) plastic composites based on an incremental variational principle". en. In: Int. J. Plast. 36 (Sept. 2012), pp. 86–112. ISSN: 07496419. (Visited on 03/20/2017).

[114] SABIC. ULTEM™ Resin 1000 - Americas. TDS-4195-en. UL Prospector from UL LLC. 2018.

[115] Qing Yu and Jacob Fish. "Multiscale asymptotic homogenization for multiphysics problems with multiple spatial and temporal scales: a coupled thermo-viscoelastic example problem". In: Int. J. Solids Struct. 39.26 (2002), pp. 6429–6452. ISSN: 0020-7683.

[116] Y. Benveniste. "A new approach to the application of Mori-Tanaka's theory in composite materials". In: Mech. Mater. 6.2 (1987), pp. 147–157. ISSN: 0167-6636.

[117] G. Lielens et al. "Prediction of thermo-mechanical properties for compression moulded composites". In: Compos. - A: Appl. Sci. Manuf. 29.1 (1998). Selected Papers Presented at the Fourth International Conference on Flow Processes in Composite Material, pp. 63–70. ISSN: 1359-835X.

[118] Q.-S. Zheng and D.-X. Du. "An explicit and universally applicable estimate for the effective properties of multiphase composites which accounts for inclusion distribution". In: J. Mech. Phys. 49.11 (2001). The Jean-Paul Boehler Memorial Volume, pp. 2765–2788. ISSN: 0022-5096.

[119] D. -X. Du and Q. -S. Zheng. "A further exploration of the interaction direct derivative (IDD) estimate for the effective properties of multiphase composites taking into account inclusion distribution". In: Acta Mech. 157 (2002), pp. 61–80.

[120] B.Walter Rosen and Zvi Hashin. "Effective thermal expansion coefficients and specific heats of composite materials". In: Int. J. Eng. Sci. 8.2 (1970), pp. 157–173. ISSN: 0020-7225.

[121] VM Levin. "Thermal expansion coefficients of heterogeneous materials". In: Mech. Solids. 2 (1967), pp. 58–61.

[122] Valentin Gallican and Renald Brenner. "Homogenization estimates for the effective response of fractional viscoelastic particulate composites". In: Contin. Mech. Thermodyn. 31 (2019), pp. 823–840.

[123] Patricia P. Parlevliet, Harald E.N. Bersee, and Adriaan Beukers. "Residual stresses in thermoplastic composites—A study of the literature—Part I: Formation of residual stresses". In: Compos. - A: Appl. Sci. 37 (11 Nov. 2006), pp. 1847–1857.

[124] Patricia P. Parlevliet, Harald E.N. Bersee, and Adriaan Beukers. "Residual stresses in thermoplastic composites – a study of the literature. Part III: Effects of thermal residual stresses". In: Compos. - A: Appl. Sci. 38 (6 June 2007), pp. 1581–1596. ISSN: 1359-835X.

[125] Chun Lu et al. "Thermal residual stress distribution in carbon fiber/novel thermal plastic composite". In: Appl. Compos. Mater. 15 (3 May 2008), pp. 157–169.

[126] Anxin Ding et al. "A three-dimensional thermo-viscoelastic analysis of process-induced residual stress in composite laminates". In: Compos. Struct. 129 (Oct. 2015), pp. 60–69.

[127] Anxin Ding et al. "A thermo-viscoelastic model of process-induced residual stresses in composite structures with considering thermal dependence". In: Compos. Struct. 136 (Feb. 2016), pp. 34–43.

[128] Weijia Chen and Dianyun Zhang. "Improved prediction of residual stress induced warpage in thermoset composites using a multiscale thermo-viscoelastic processing model". In: Compos. - A: Appl. Sci 126 (Nov. 2019), p. 105575.

[129] Qi Wu, Nobuhiro Yoshikawa, and Hongzhou Zhai. "Composite forming simulation of a three-dimensional representative model with random fiber distribution". In: Comput. Mater. Sci. 182 (Sept. 2020), p. 109780.

[130] B. D. Harper and Y. Weitsman. "Characterization Method for a Class of Thermorheologically Complex Materials". In: Journal of Rheology 29 (1 July 1985), p. 49.

[131] Noël Lahellec and Pierre Suquet. "Effective behavior of linear viscoelastic composites: A time-integration approach". In: Int. J. Solids Struct. 44 (2 Jan. 2007), pp. 507–529.

[132] Martín I. Idiart, Noel Lahellec, and Pierre Suquet. "Model reduction by mean-field homogenization in viscoelastic composites. I. Primal theory". In: Proc. R. Soc. 476 (2242 Oct. 2020).

[133] R. A. Schapery. "Stress Analysis of Viscoelastic Composite Materials". In: J. Compos. Mater. 1 (3 July 1967), pp. 228–267.

[134] Quoc Son Nguyen, Pierre Suquet, and P Germain. "Continuum thermodynamics ASME Gradient models View project". In: J. Appl. Mech. 105 (1983).

[135] P. M. Squet. "Local and Global Aspects in the Mathematical Theory of Plasticity". In: Plasticity Today (1985).

[136] Gilles A. Francfort. "Homogenization and Linear Thermoelasticity". In: SIAM J. Math. Anal 14 (4 July 1983), pp. 696–708.

[137] Andrey Amosov et al. "Homogenization of a thermo-chemo-viscoelastic Kelvin-Voigt model". In: J. Math. Phys. 54 (8 Aug. 2013), p. 081501.

[138] "Periodic homogenization for fully coupled thermomechanical modeling of dissipative generalized standard materials". In: Int. J. Plast. 81 (June 2016), pp. 18–39.

[139] Morton E Gurtin and William J Hrusa. "On the thermodynamics of viscoelastic materials of single-integral type". In: Quarterly of Applied Mathematics XLIX (1 1991), pp. 67–85.

[140] Djaffar Boussaa. "Effective thermoelastic properties of composites with temperature-dependent constituents". In: Mech. Mater. 43 (8 Aug. 2011), pp. 397–407.

[141] "Fourth-rank tensors of the thirty-two crystal classes: multiplication tables". In: Proc. R. Soc. Lond. 391 (1800 Jan. 1984), pp. 149–179.

[142] Pedro Ponte Castañeda and Pierre Suquet. "Nonlinear Composites". In: Adv. Appl. Mech. 34 (C Jan. 1997), pp. 171–302.

[143] C. I. Byrnes and A. Lindquist. "On the Duality between Filtering and Nevanlinna-Pick Interpolation". In: SIAM J. Control Optim. 39 (3 July 2006), pp. 757–775.

[144] Martín I. Idiart, Noel Lahellec, and Pierre Suquet. "Model reduction by mean-field homogenization in viscoelastic composites. II. Application to rigidly reinforced solids". In: Proc. R. Soc. 476 (2242 Oct. 2020), p. 20200407.

[145] José Cotelo, Shuvrangsu Das, and Pedro Ponte Castañeda. "A differential homogenization method for estimating the macroscopic response and field statistics of particulate viscoelastic composites". In: Int. J. Solids Struct. 204-205 (Nov. 2020), pp. 199–219.

[146] Noël Lahellec and Pierre Suquet. "Effective response and field statistics in elasto-plastic and elasto-viscoplastic composites under radial and non-radial loadings". In: Int. J. Plast. 42 (Mar. 2013), pp. 1–30.

[147] Claudiu Badulescu, Noel Lahellec, and Pierre Suquet. "Field statistics in linear viscoelastic composites and polycrystals". In: Eur. J. Mech. A Solids 49 (Jan. 2015), pp. 329–344.

[148] Shuvrangsu Das and Pedro Ponte Castañeda. "Differential variational estimates for the macroscopic response and field statistics of elasto-viscoplastic polycrystals". In: J. Mech. Phys. Solids 147 (Feb. 2021), p. 104202.

[149] Martín I. Idiart and Noel Lahellec. "Estimates for the overall linear properties of pointwise heterogeneous solids with application to elasto-viscoplasticity". In: J. Mech. Phys. Solids 97 (Dec. 2016), pp. 317–332.

[150] "Model reduction by mean-field homogenization in viscoelastic composites. III. Dual theory". In: Proc. R. Soc. 477 (2249 May 2021).

[151] Renaud Masson, Renald Brenner, and Olivier Castelnau. "Incremental homogenization approach for ageing viscoelastic polycrystals". In: Comptes Rendus Mécanique 340 (4-5 Apr. 2012), pp. 378–386.

[152] Q. H. Vu et al. "A self-consistent estimate for linear viscoelastic polycrystals with internal variables inferred from the collocation method". In: Model. Simul. Mater. Sci. Eng. 20 (2 Feb. 2012), p. 024003.

[153] Noël Lahellec and Pierre Suquet. "On the effective behavior of nonlinear inelastic composites: I. Incremental variational principles". In: J. Mech. Phys. Solids 55 (9 Sept. 2007), pp. 1932–1963.

[154] Julien Boudet et al. "An incremental variational formulation for the prediction of the effective work-hardening behavior and field statistics of elasto-(visco)plastic composites". In: Int. J. Solids Struct. 83 (Apr. 2016), pp. 90–113. ISSN: 0020-7683.

[155] Travis A. Bogetti and John W. Gillespie. "Process-Induced Stress and Deformation in Thick-Section Thermoset Composite Laminates". In: J. Compos. Mater. 26 (5 Mar. 1992), pp. 626–660.

[156] Martin Philip Bendsøe and Noboru Kikuchi. "Generating optimal topologies in structural design using a homogenization method". In: Comput. Methods Appl. Mech. Eng. 71.2 (1988), pp. 197–224. ISSN: 0045-7825.

[157] J.C. Michel, H. Moulinec, and P. Suquet. "Effective properties of composite materials with periodic microstructure: a computational approach". In: Comput. Methods Appl. Mech. Eng. 172.1 (1999), pp. 109–143. ISSN: 0045-7825.

[158] M. Somireddy and A. Czekanski. "Mechanical characterization of additively manufactured parts by FE modeling of mesostructure". In: J. manuf. mater. 1.2 (2017), p. 18.

[159] G. Alaimo et al. "Influence of meso-structure and chemical composition on FDM 3D-printed parts". In: Compos. B. Eng. 113 (2017), pp. 371–380.

[160] S. Garzon-Hernandez et al. "Design of FDM 3D printed polymers: An experimental-modelling methodology for the prediction of mechanical properties". In: Mater. Des. 188 (2020), p. 108414.

[161] L. G. Blok et al. "An investigation into 3D printing of fibre reinforced thermoplastic composites". In: Addit. Manuf. 22 (2018), pp. 176–186.

[162] Severino P. C. Marques and G. J. Creus. Computational Viscoelasticity. Springer, 2012.

[163] Stéphane Lejeunes and Stéphane Bourgeois. "Une Toolbox Abaqus pour le calcul de propriétés effectives de milieux hétérogènes". In: (May 2011), CSMA 2011.

[164] Pierre Suquet. “Four exact relations for the effective relaxation function of linear viscoelastic composites”. In: Comptes Rendus Mécanique 340 (4-5 Apr. 2012), pp. 387–399.

[165] J. C. Halpin Affdl and J. L. Kardos. “The Halpin-Tsai equations: A review”. In: Polym. Eng. 16.5 (1976), pp. 344–352.

[166] R. Bouc and G. Geymonat. “Periodic Problems in Thermoviscoelasticity”. In: Materials with Memory (2010), pp. 5–51.

[167] P.Ponte Castañeda and J.R. Willis. “The effect of spatial distribution on the effective behavior of composite materials and cracked media”. In: J. Mech. Phys. 43.12 (1995), pp. 1919–1951. ISSN: 0022-5096.